

GUIDED-WAVE STRUCTURAL HEALTH MONITORING

by

Ajay Raghavan

A dissertation submitted in partial fulfillment
of the requirements for the degree of
Doctor of Philosophy
(Aerospace Engineering)
in The University of Michigan
2007

Doctoral Committee:

Associate Professor Carlos E. Cesnik, Chair
Professor Karl Grosh
Professor Anthony M. Waas
Assistant Professor Jerome P. Lynch

“If we knew what it was we were doing, it would not be called research, would it?”

– *Albert Einstein* (1879-1955)

© Ajay Raghavan 2007

To Achan, Amma and my brothers, Arun and Ashwin.

ACKNOWLEDGMENTS

There are many people whose support and assistance played a very important role in the realization of this dissertation. First and foremost, a huge “obrigado” to Prof. Carlos Cesnik, who I am really glad to say, was not just my thesis advisor, but is also a great mentor and friend. He has believed in me from day one, motivated me to excel and always provided all the resources and guidance to keep me going. I am very grateful to him for everything. I greatly appreciate the time and dedication of the rest of my thesis committee: Prof. Anthony Waas, Prof. Jerome Lynch and Prof. Karl Grosh. Their advice, support and encouragement over my five-year stay here have been very helpful. I would like to acknowledge all the faculty members under whom I have learnt at Michigan (including Profs. Cesnik, Waas and Grosh): their excellent exposition of the fundamentals in structural/wave mechanics, signal/image processing and complex analysis during my graduate courses has played a key role in the analytical developments in this thesis. I am also grateful to Prof. Daniel Inman from Virginia Tech for his encouragement during my interactions with him at the Pan-American advanced study institute (PASI) on damage prognosis and various conferences.

Next, I would like to acknowledge the support of the technical center in the Aerospace Engineering Department, especially David McLean and Thomas Griffin. Their vast hands-on experience and knowledgebase was extremely useful in setting up and troubleshooting experimental setups. Thanks to my undergraduate research assistants for help in setting up some of the experiments: Kwong-Hoe Lee, Jason Banker, Monika Patel, Danny Lau and Jeremy Hollander. I appreciate suggestions from Dr. Christopher Dunn (University of Michigan, now at Metis Design Corporation) for some model validation experiments done in this thesis. The useful feedback of our NASA PoCs, Dr. William Prosser (NASA LaRC), Lance Richards and Larry Hudson (NASA DFRC),

and John Lassiter (NASA MSFC) on the design guidelines and during annual project review meetings also helped considerably. Thanks are due to Robert Littrell and Kevin King (Vibrations and Acoustics Laboratory, University of Michigan) for aiding with setting up the laser vibrometer experiment. The support of Dr. Keats Wilkie (NASA JPL) in providing the macro fiber composite transducers for the experimental tests is sincerely appreciated. Assistance from Dr. Joseph Rakow (now at Exponent) and Amit Salvi from the Composites Research Laboratory, University of Michigan, for some of the initial thermal experiments is also gratefully acknowledged.

I have immensely benefited from technical discussions and interacting with my past and present colleagues at the Active Aeroelasticity and Structures Research Laboratory: Dr. Rafael Palacios (now at Imperial College, UK), Ruchir Bhatnagar (now working for General Electric, India), Smith Thepvongs, Ji Won Mok, Dr. Christopher Shearer (now at AFIT), Satish Chimakurthi, Ken Salas, Weihua Su, Andy Klesh, Major Wong Kah Mun (now with the Singapore Air Force), Xong Sing Yap, Anish Parikh and Matthias Wilke (now working for Boeing). Thanks to all my friends at Michigan: Fortunately or unfortunately, I have too many to list everyone, but I must particularly mention my apartment mates, Ajay Tannirkulam, Shidhartha Das, Siddharth D'Silva, and Harsh Singhal for tolerating me and making my stay here enjoyable all these years. And last but certainly not least, the support and encouragement of my parents, my brothers Arun and Ashwin played an important role in the completion of this dissertation.

This thesis was supported by the Space Vehicle Technology Institute under Grant No. NCC3-989 jointly funded by NASA and DoD within the NASA Constellation University Institutes Project, with Claudia Meyer as the project manager. This support is greatly appreciated.

TABLE OF CONTENTS

DEDICATION	ii
ACKNOWLEDGMENTS	iii
LIST OF FIGURES	x
LIST OF TABLES	xvi
LIST OF APPENDICES	xvii
ABSTRACT	xviii
CHAPTER	
I. INTRODUCTION AND LITERATURE REVIEW	1
I.1 Motivation and Background	1
I.2 Fundamentals of Guided-waves	5
I.2.A Early Developments	5
I.2.B Guided-wave Analysis	6
I.3 Transducer Technology	9
I.3.A Piezoelectric Transducers	10
I.3.B Piezocomposite Transducers	11
I.3.B Other Transducers	13
I.4 Developments in Theory and Modeling	15
I.4.A Developments Motivated by NDE/NDT	15
I.4.B Models for SHM Transducers	18
I.5 Signal Processing and Pattern Recognition	21
I.5.A Data Cleansing	22
I.5.B Feature Extraction and Selection	22

I.5.C	Pattern Recognition	28
I.5.D	Excitation Signal Tailoring	29
I.6	GW SHM System Development	30
I.6.A	Packaging	30
I.6.B	Integrated Solutions	31
I.6.C	Robustness to Different Service Conditions	33
I.7	Application Areas	36
I.7.A	Aerospace Structures	36
I.7.B	Civil Structures	37
I.7.C	Other Areas	38
I.8	Integration with Other SHM Approaches	39
I.9	Summary and Scope of this Thesis	41
II.	GUIDED-WAVE TRANSDUCTION BY PIEZOS IN ISOTROPIC STRUCTURES	43
II.1	Actuation Mechanisms of Piezos and APTs	43
II.2	Plane Lamb-wave Excitation by 3-3 APTs in Rectangular-Sectional Beams	45
II.3	Axisymmetric GW Excitation by 3-3 APTs in Hollow Cylinders	47
II.4	3-D GW Excitation in Plates	52
II.4.A	Rectangular Piezo	57
II.4.B	Rectangular APT	60
II.4.C	Ring-shaped Piezo	62
II.5	Numerical Verification for Circular Piezos on Plates	67
II.6	Piezo-sensor Response Derivation	68
II.6.A	Piezo-sensor Response in GW Fields due to Circular Piezos	70
II.6.B	Piezo-sensor Response in GW Fields due to Rectangular Piezos	70

II.7	Setups for Experimental Validation and Results	71
II.7.A	Beam Experiment for Frequency Response Function of MFCs	72
II.7.B	Plate Experiments for Frequency Response Function of Piezos and MFCs	72
II.7.C	Laser Vibrometer Experiment	74
II.8	Discussion and Sources of Error	79
II.8.A	Frequency Response Function Experiments	79
II.8.B	Laser Vibrometer Experiment	82
II.9	Optimal Transducer Dimensions	83
II.9.A	Circular Piezo-Actuators on Plates	83
II.9.B	Rectangular Actuators	85
II.9.C	Piezo-sensors	86
III.	DESIGN GUIDELINES FOR THE EXCITATION SIGNAL AND PIEZO-TRANSDUCERS IN ISOTROPIC STRUCTURES	89
III.1	Excitation Signal	90
III.1.A	Center Frequency/GW Mode	90
III.1.B	Number of Cycles	91
III.1.C	Modulation Window	91
III.1.D	Consideration for Comb Array Configurations	92
III.2	Piezo-Transducers	94
III.2.A	Configuration/Shape Selection	94
III.2.B	Actuator Size	95
III.2.C	Sensor Size	101
III.2.D	Transducer Material	102
IV.	A NOVEL SIGNAL PROCESSING ALGORITHM USING CHIRPLET MATCHING PURSUITS AND MODE IDENTIFICATION	104
IV.1	Issues in GW Signal Processing	104

IV.2	Conventional Approaches to GW Signal Processing	107
IV.3	Chirplet Matching Pursuits	109
IV.4	Proposed Algorithm for Isotropic Plate Structures	112
	IV.4.A Database Creation	112
	IV.4.B Processing the Signal for Damage Detection and Characterization	115
IV.5	Demonstration of the Algorithm's Capabilities	117
	IV.5.A FEM Simulations	117
	IV.5.B Experimental Results	119
IV.6	Triangulation in Isotropic Plate Structures	123
V.	EFFECTS OF ELEVATED TEMPERATURE	127
V.1	Temperature Variation in Internal Spacecraft Structures	127
V.2	Bonding Agent Selection	128
V.3	Modeling the Effects of Temperature Change	132
V.4	Damage Characterization at Elevated Temperatures	137
VI.	GUIDED-WAVE EXCITATION BY PIEZOS IN COMPOSITE LAMINATED PLATES	147
VI.1	Theoretical Formulation	147
	VI.1.A Bulk Waves in Fiber-reinforced Composites	149
	VI.1.B Assembling the Laminate Global Matrix from the Individual Layer Matrices	152
	VI.1.C Forcing Function due to Piezo-actuator	155
	VI.1.D Spatial Fourier Integral Inversion	156
VI.2	Implementation of the Formulation and Slowness Curve Computation	158
VI.3	Results and Comparison with Numerical Simulations	160
VII.	CONCLUDING REMARKS, KEY CONTRIBUTIONS AND PATH FORWARD	166

VII.1 Key Contributions	167
VII.2 Path Forward	169
APPENDICES	173
REFERENCES	236

LIST OF FIGURES

Fig. 1: The four essential steps in GW SHM	4
Fig. 2: The 2-D plate for which dispersion relations are derived	6
Fig. 3: Dispersion curves for Lamb modes in an isotropic aluminum plate structure: (a) Phase velocity and (b) group velocity.	9
Fig. 4: Piezos (PZT and PVDF) of various shapes and sizes	11
Fig. 5: The macro fiber composite (MFC) transducer [44]	13
Fig. 6: Denoising using discrete wavelet transform: Raw GW signal reflected from a dent in a metallic plate averaged over 64 samples (left) and signal denoised using Daubechies wavelet	23
Fig. 7: (a) Configuration of 3-3 APT surface-bonded on an isotropic beam with rectangular cross-section and (b) modeled representation	45
Fig. 8: (a) Configuration of 3-3 APT surface-bonded on a hollow cylinder and modeled representation	(b) 48
Fig. 9: Contour integral in the complex ξ -plane to invert the displacement integrals using residue theory	51
Fig. 10: Infinite isotropic plate with arbitrary shape surface-bonded piezo actuator and piezo sensor and the three specific configurations considered: (1) Rectangular piezo (2) Rectangular MFC and (3) Ring-shaped piezo	54
Fig. 11: Harmonic radiation field (normalized scales) for out-of-plane surface displacement (u_3) in a 1-mm thick aluminum alloy ($E = 70$ GPa, $\nu = 0.33$, $\rho =$ 2700 kg/m ³) plate at 100 kHz, A_0 mode, by a pair of (a) 0.5-cm \times 0.5-cm square piezos (uniformly poled, in gray, center); (b) 0.5-cm diameter circular actuators (in gray, center); (c) 0.5 cm \times 0.5 cm square 3-3 APT (in grey stripes) with the fibers along the vertical direction and (d) 3-element comb array of 0.5 cm \times 0.5 cm square 3-3 APT (in grey stripes) with the fibers along the vertical direction, excited in phase	65

Fig. 12: Frequency content of unmodulated and modulated (Hann window) sinusoidal tonebursts	67
Fig. 13: Comparison of theoretical and FEM simulation results for the normalized radial displacement at $r = 5$ cm at various frequencies for: (a) S_0 mode and (b) A_0 mode	69
Fig. 14: Illustration of thin aluminum strip instrumented with MFCs	73
Fig. 15: Theoretical and experimental normalized sensor response over various frequencies in the beam experiment for: (a) S_0 mode and (b) A_0 mode	73
Fig. 16: Experimental setups for frequency response validation of: (a) circular actuator model and (b) rectangular actuator model	75
Fig. 17: Experimental setup for frequency response validation of model for surface-bonded APTs on plates	75
Fig. 18: Comparison between experimental and theoretical sensor response amplitudes in the circular actuator experiment at different center frequencies for: (a) S_0 mode and (b) A_0 mode	76
Fig. 19: Comparison between experimental and theoretical sensor response time domain signals for the circular actuator experiment: (a) S_0 mode for center frequency 300 kHz and (b) A_0 mode for center frequency 50 kHz	76
Fig. 20: Comparison between experimental and theoretical sensor response amplitudes in the rectangular actuator experiment at different center frequencies for: (a) S_0 mode and (b) A_0 mode	77
Fig. 21: Comparison between experimental and theoretical sensor response time domain signals for the circular actuator experiment: (a) S_0 mode for center frequency 150 kHz and (b) A_0 mode for center frequency 50 kHz	77
Fig. 22: Comparison between experimental and theoretical sensor response amplitudes in the rectangular MFC experiment at different center frequencies for: (a) S_0 mode and (b) A_0 mode	78
Fig. 23: Comparison between experimental and theoretical sensor response time domain signals for the frequency response experiment with rectangular MFCs: (a) S_0 mode for center frequency 300 kHz and (b) A_0 mode for center frequency 50 kHz	78
Fig. 24: Normalized surface plots showing out-of-plane velocity signals over a quarter section of the plate spanning 20 cm \times 20 cm. The MFC is at the upper left corner	

(the striped rectangle), and its fibers along the vertical: (a) Experimental plots obtained using laser vibrometry and (b) theoretical plots obtained using the developed model for APTs	80
Fig. 25: Amplitude variation of sensor response and power drawn to excite the GW field due to change in actuator radius for a 1-mm thick Aluminum plate driven harmonically in the S_0 mode at 100 kHz	84
Fig. 26: Comparison between experimental and theoretical sensor response amplitudes in the variable sensor length experiment	88
Fig. 27: Tree diagram of parameters in GW SHM (numbers above/below the boxes indicate section numbers for the corresponding parameter)	89
Fig. 28: The Kaiser window and its Fourier transform	93
Fig. 29: Illustration of comb configurations: (a) using ring elements and (b) using rectangular elements	93
Fig. 30: Comparison of harmonic induced strain in A_0 mode between an 8-array piezo comb transducer and that of a single piezo-actuator (power is kept constant).	94
Fig. 31: Parameters and design space for circular actuator dimension optimization	98
Fig. 32: Parameters and coordinate axes for rectangular actuator	99
Fig. 33: Choice of a_2 for rectangular actuator	99
Fig. 34: Possible optimal choices of a_1 for rectangular actuator in two possible cases	100
Fig. 35: From top-left, clockwise: (a) 2-D plate structure with one notch; (b) 2-D plate structure with two notches; (c) surface axial strain waveform at the center for structure in (b) and (d) surface axial strain at the center for structure in (a)	105
Fig. 36: The Lamb-wave dispersion curves with circles marking the excitation center frequency for the FEM simulations: (a) phase velocity and (b) group velocity	105
Fig. 37: WVD of two linear modulated chirps	110
Fig. 38: Spectrogram of the signal in Fig. 35 (d)	110
Fig. 39: A stationary Gaussian atom and its WVD	112
Fig. 40: A Gaussian chirplet and its WVD	112
Fig. 41: Flowchart of proposed signal processing algorithm	118

Fig. 42: (a) Portion of signal in Fig. 35 (c) with overlapping multimodal reflections and corrupted with artificial noise; (b) Spectrogram of the signal in (a); (c) Interference-free WVD of constituent chirplet atoms for the signal in (a)	119
Fig. 43: (a) Schematic of experimental setup and (b) Photograph of experimental setup	121
Fig. 44: (a) Difference signal between pristine and “damaged” states; (b) Spectrogram of the signal in (a) and (c) Interference-free WVD of constituent chirplet atoms for the signal in (a)	123
Fig. 45: (a) Approach for locating and characterizing damage sites in the plane of plate structures using multimodal signals and (b) Experimental results for in-plane damage location in plate structures using unimodal GW signals	125
Fig. 46: Schematic of specimen for tests with Epotek 301	130
Fig. 47: Variation of sensor 2 response amplitude (peak-to-peak) and associated error bars with temperature over three thermal cycles (for tests with Epotek 301)	130
Fig. 48: Sensor 2 signal at room temperature before and after each of the three thermal cycles (for tests with Epotek 301; EMI \equiv electromagnetic interference from the actuation)	131
Fig. 49: Variation of sensor response amplitude (peak-to-peak) with temperature for tests with epoxy 10-3004 – the curve hits the noise floor at 100°C while heating and does not recover	131
Fig. 50: Schematic of specimen for tests with Epotek 353ND (Damage introduced later and discussed in Section).	131
Fig. 51: GW signal sensed by sensor 2 (bonded using Epotek 353ND) before and after a thermal cycle	131
Fig. 52: Labeled photograph of setup and autoclave for controlled thermal experiments (TC \equiv thermocouple).	133
Fig. 53: Typical time-temperature curve for experiments done in the computer-controlled autoclave	133
Fig. 54: GW signals recorded by sensor 2 (averaged over 30 samples) while heating	133
Fig. 55: GW signals recorded by sensor 2 (averaged over 30 samples) while cooling	133
Fig. 56: Variation of Young’s moduli ([223]-[225])	135

Fig. 57: Variation of $d_{31} \times g_{31}$ of PZT-5A [222]	135
Fig. 58: Combined effect of changing aluminum elastic modulus (static) and thermal expansion on phase velocity	135
Fig. 59: Variation in time-of-flight of first transmitted S_0 mode received by sensor 2	135
Fig. 60: Variation in response amplitude (peak-to-peak) of first transmitted S_0 mode received by sensor 2	139
Fig. 61: Signal read by sensor 1 at 20°C and 110°C (cycle 1) for pristine condition	139
Fig. 62: Sensor 1 response during cycles 1 and 2 for pristine condition at 120°C (heating)	140
Fig. 63: Sensor 1 response during cycles 1 and 2 for pristine condition at 60°C (cooling)	140
Fig. 64: Photographs of damage introduced: (a) indentation and (b) through-hole.	141
Fig. 65: Sensor 1 response for pristine and indented specimens, along with the signal difference at: (a) 20°C (before thermal cycle) ; (b) 60°C while heating; (c) 140°C while heating and (d) 40°C while cooling	141
Fig. 66: Sensor 1 response for pristine and thru-hole specimens, along with the signal difference at: (a) 20°C (before thermal cycle) ; (b) 70°C while heating; (c) 150°C while heating and (d) 50°C while cooling	144
Fig. 67: Infinite multilayered composite plate with arbitrary shape surface-bonded piezo actuator	148
Fig. 68: Illustration of solution procedure	149
Fig. 69: (a) Relation between group velocity and slowness curve and (b) “Steering” in anisotropic media	159
Fig. 70: Slowness curves for (a) 1-mm unidirectional plate at 500 kHz and (b) quasi-isotropic laminate at 200 kHz of layup $[0/45/-45/90]_s$, each ply being 0.11-mm thick	160
Fig. 71: Geometry of FEM models for: (a) 1-mm unidirectional plate and (b) quasi-isotropic plate of layup $[0/45/-45/90]_s$, each ply being 0.11 mm thick.	162
Fig. 72: Surface out-of-plane displacements at different time instants for the unidirectional composite excited in the antisymmetric mode (by the piezo, in	

gray) with a 3.5-cycle Hanning windowed toneburst at 200 kHz obtained using: (a) FEM (b) the developed model.	163
Fig. 73: Surface out-of-plane displacements at different time instants for the quasi-isotropic composite excited symmetrically (by the piezo, in gray) with a 3.5-cycle Hanning windowed toneburst at 200 kHz obtained using: (a) FEM (b) the developed model.	164
Fig. 74: Schematic of arrangement to cut piezos to size	175
Fig. 75: Photograph of specimen with cable stand in the autoclave for thermal experiments	178
Fig. 76: Illustration of solder joints: (a) Preferable configuration for strong connections and (b) Undesirable configuration	179
Fig. 77: Agilent 33220A front view	182
Fig. 78: Infiniium 54831B oscilloscope front view	184
Fig. 79: Current measurement circuit using operational amplifier [236]	186
Fig. 80: Experimental setup for EM impedance measurements of bolt torque	186
Fig. 81: Results from preliminary experiments done for bolt torque detection (FFT \equiv fast Fourier transform)	187
Fig. 82: (a) Thermocouple module and (b) data acquisition system	188
Fig. 83: Front panel showing inputs for Labview program	189
Fig. 84: Portion of the block diagram of the LABVIEW program	191

LIST OF TABLES

Table 1: Simulated notch damage in FEM simulation	120
Table 2: Experimental results of isotropic plate with simulated damage	122
Table 3: Summary of results showing trends in thermal experiment for damage characterization with indented specimen	143
Table 4: Summary of results showing trends in thermal experiment for damage characterization using specimen with thru-hole	145

LIST OF APPENDICES

A.	NOTES ON EXPERIMENTAL PROCEDURES AND SETUPS	173
A.1	Cutting Piezoceramics and MFCs to Size	173
A.2	Bonding Piezos to Plates	175
A.3	Soldering Wires to Piezos	177
A.4	Configuring the Function Generator	179
A.5	Setting the Oscilloscope Up for Reading and Saving Signals	181
A.6	Using an Oscilloscope for Electromechanical Impedance Measurements	185
A.7	Notes on the Labview-based Setup for Automated Thermal Experiments	187
B.	SOFTWARE CODE AND COMMANDS	192
B.1	Abaqus Code for FEM Simulations	192
B.2	Maple Code for Theoretical Model Implementation	197
B.3	Fortran 90 Code for Implementing GW Excitation Models in Composites	205
B.4	Matlab Code for Generating Images/Movies and Waveform Files	224
B.5	Using LastWave 2.0 for Chirplet Matching Pursuits	234

ABSTRACT

Guided-wave (GW) approaches have shown potential in various initial laboratory demonstrations as a solution to structural health monitoring (SHM) for damage prognosis. This thesis starts with an introduction to and a detailed survey of this field. Some critical areas where further research was required and those that were chosen to be addressed herein are highlighted. Those were modeling, design guidelines, signal processing and effects of elevated temperature. Three-dimensional elasticity-based models for GW excitation and sensing by finite dimensional surface-bonded piezoelectric wafer transducers and anisotropic piezocomposites are developed for various configurations in isotropic structures. The validity of these models is extensively examined in numerical simulations and experiments. These models and other ideas are then exploited to furnish a set of design guidelines for the excitation signal and transducers in GW SHM systems. A novel signal processing algorithm based on chirplet matching pursuits and mode identification for pulse-echo GW SHM is proposed. The potential of the algorithm to automatically resolve and identify overlapping, multimodal reflections is discussed and explored with numerical simulations and experiments. Next, the effects of elevated temperature as expected in internal spacecraft structures on GW transduction and propagation are explored based on data from the literature incorporated into the developed models. Results from the model are compared with experiments. The feasibility of damage characterization at elevated temperatures is also investigated. An extension of the modeling effort for GW excitation by finite-dimensional piezoelectric wafer transducers to composite plates is also proposed and verified by numerical simulations. At the end, future directions for research to make this technology more easily deployable in field applications are suggested.

CHAPTER I

INTRODUCTION AND LITERATURE REVIEW

This chapter offers an introduction to the field of guided-wave (GW) structural health monitoring (SHM), starting with some background and basic concepts. It then delves into the constitutive elements of GW SHM system and reviews efforts by various groups in each of those aspects. Some crucial gaps in the literature are pointed out and the scope of this thesis in addressing those is defined.

I.1 Motivation and Background

In recent years, there has been an increasing awareness of the importance of damage prognosis systems in aerospace, civil and mechanical structures. It is envisaged that a damage prognosis system in a structure would apprise the user of the structure's health, inform the user about any incipient damage in real-time and provide an estimate of the remaining useful life of the structure. In the aerospace community, it is also referred to as integrated systems health management (ISHM, usually for spacecraft and space habitats) or integrated vehicle health management (IVHM, typically for aircraft) in the literature. The potential benefits that would accrue from such a technology are enormous. The maintenance procedures for structures with such systems could change from being schedule-driven to condition-based, thereby cutting down on the time period for which structures are offline and correspondingly resulting in cost-savings and reducing their labor requirements. Operators could also possibly establish leasing arrangements that charge by the amount of system life used during the lease instead of

charging simply by the time duration of the lease. And most significantly, the confidence levels in operating structures would increase sharply due to the new safeguards against unpredictable structural system degradation, particularly so for ageing structures. Moreover, most importantly, the safety of the users of the structure is better ensured. Such systems will also be important for NASA's plans to return astronauts to the Moon, and eventually, longer-term missions to Mars. ISHM will help in transitioning from low-earth orbit missions with continuous ground support to more autonomous long-term missions [1]. The ISHM system will manage all the critical spacecraft functions and systems. It will apprise astronauts on changes in vehicle systems' integrity and functionality requiring action as well as provide the crew with the capability to forecast potential problems and schedule repairs.

Another growing trend in aerospace structures is the increasing popularity of composites, particularly multilayered fiber-reinforced ones. The primary advantage of using composites is their higher stiffness-to-mass ratio compared to metals, which translates into significant fuel and operational-cost savings for aerospace vehicles. In addition, they have better corrosion resistance and can be tailored for preferentially bearing loads along specific directions. However, they are more susceptible to impact damage in the form of delaminations or cracks, which could reduce load-bearing capability and potentially lead to structural failure. The capability of damage prognosis could increase confidence in the use of composite structures by alerting operators about damage from unexpected impact events.

SHM is a key component of damage prognosis systems. SHM is the component that examines the structure for damage and provides information about any damage that is detected. A SHM sub-system typically consists of an onboard network of sensors for data acquisition and some central processor to evaluate the structural health. It may utilize stored knowledge of structural materials, operational parameters, and health criteria. The schemes available for SHM can be broadly classified as active or passive depending on whether or not they involve the use of actuators, respectively. Examples of passive schemes are acoustic emission (AE) and strain/loads monitoring, which have been demonstrated with some success ([2]-[9]). However, they suffer from the drawback

of requiring high sensor densities on the structure. They are typically implemented using fiber optic sensors and, for environments that are relatively benign, foil strain gages.

Unlike passive methods, in active schemes the structure can be excited in a prescribed, repeatable manner using actuators and it can be examined for damage quickly, where and when required. Guided-wave testing has emerged as a very prominent option among active schemes. It can offer an effective method to estimate the location, severity and type of damage, and it is a well-established practice in the Non-Destructive Evaluation and Testing (NDE/NDT) industry. There, GWs are excited and received in a structure using handheld transducers for scheduled maintenance. They have also demonstrated suitability for SHM applications having an onboard, preferably built-in, sensor and actuator network to assess the state of a structure during operation. The actuator-sensor pair in GW testing has a large coverage area, resulting in fewer units distributed over the structure.

GWs can be defined as stress waves forced to follow a path defined by the material boundaries of the structure. For example, when a beam is excited at high frequency, stress waves travel in the beam along its axis away from the excitation source, i.e., the beam “guides” the waves along its axis. Similarly, in a plate, the two free surfaces of the plate “guide” the waves within its confines. In GW SHM, an actuator generating GWs is excited by some high frequency pulse signal (typically a modulated sinusoidal toneburst of some limited number of cycles). In general, when a GW field is incident on a structural discontinuity (which has a size comparable to the GW wavelength), it scatters GWs in all directions. The structural discontinuity could be damage in the structure such as a crack or delamination, a structural feature (such as a stiffener) or boundary. Therefore, to be able to distinguish between damage and structural features, one needs prior information about the structure in its undamaged state. This is typically in the form of a baseline signal obtained for the “healthy state” to use as reference for comparison with the test case. There are two approaches commonly used in GW SHM, pulse-echo and pitch-catch. In the former, after exciting the structure with a narrow bandwidth pulse, a sensor collocated with the actuator is used to sense echoes of the pulse coming from discontinuities. Since the boundaries and the wave speed for a

given center actuation frequency of the toneburst are known, the signals from the boundaries can be filtered out (or alternatively one could subtract the test signal from the baseline signal). One is then left with signals from damage sites (if present). From these signals, damage sites can be located using the wavespeed. In the pitch-catch approach, a pulse signal is sent across the specimen under interrogation and a sensor at the other end of the specimen receives the signal. From various characteristics of the received signal, such as delay in time of transit, amplitude, frequency content, etc., information about the damage can be inferred. Thus, the pitch-catch approach cannot be used to locate the damage site unless a dense network of transducers is used. In either approach, damage-sensitive features are extracted from the signal using some signal-processing algorithm, and then a pattern recognition technique is required to classify the damage and estimate its severity. These steps involved in GW SHM are illustrated in Fig. 1. Another crucial point to note is that GW SHM always involves the use of some threshold value to decide whether damage is present in the structure or not. The choice of the threshold is usually application-dependent and typically relies on some false-positive probability estimation.

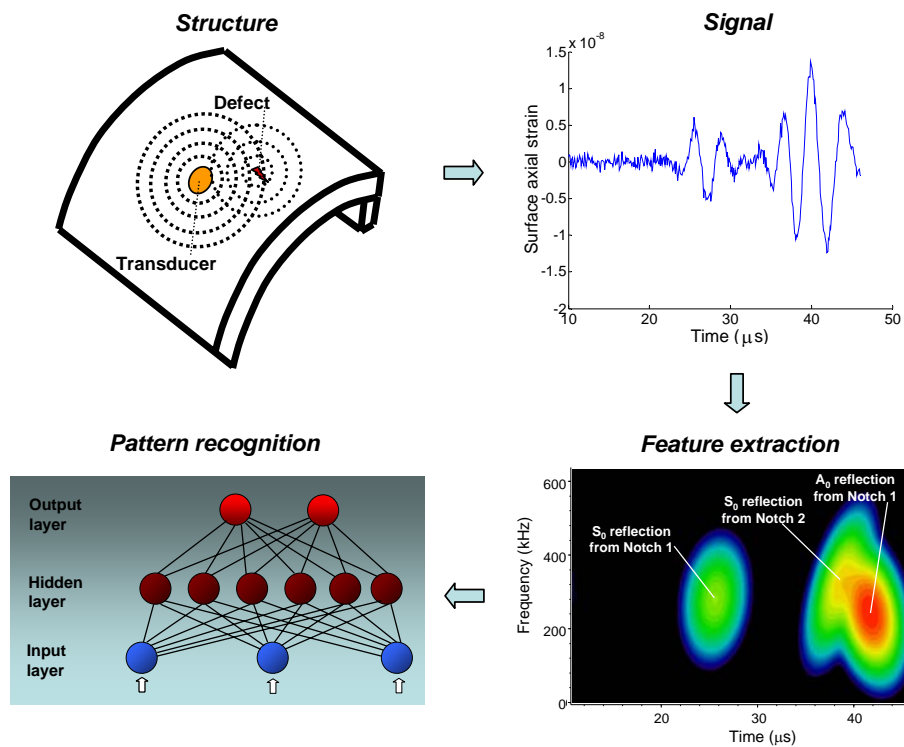


Fig. 1: The four essential steps in GW SHM

The critical elements of GW SHM are the transducers, the relevant theory, the signal processing methodology, the arrangement of the transducer network to scan the structure, and the overall SHM architecture (i.e., issues related to supporting electronics, robustness and packaging). In this chapter, each of these aspects is scrutinized and a review of the efforts by various researchers is presented. Some examples of field applications where GW SHM has been implemented are discussed. The compatibility of GW SHM with other schemes is then explored. The chapter concludes with a summary and a discussion on developments desirable in this area. However, before these elements are broached, it is useful to consider some background and basics of GWs.

I.2 Fundamentals of Guided-waves

I.2.A Early Developments

There are several application areas for guided elastic waves in solids such as seismology, inspection, material characterization, delay lines, etc. and consequently they have been a subject of much study ([10]-[12]). A very important class among these is that of Lamb waves, which can propagate in a solid plate (or shell) with free surfaces. Due to the abundance of plate- and shell-like structural configurations, this class of GWs has been the subject of much scrutiny. Another class of GW modes is also possible in plates, i.e., the horizontally polarized shear or SH-modes. Other classes of GWs have also been examined in the literature. Among them is that of Rayleigh waves, which propagate close to the free surface of elastic solids. Other examples are Love [14], Stoneley [15] and Scholte [16] waves that travel at material interfaces. Lamb waves were first predicted mathematically and described by Horace Lamb [17] about a century ago. Gazis ([18], [19]) developed and analyzed the dispersion equations for GWs in cylinders. However, neither was able to produce GWs experimentally. This was first done by Worlton [20], who was probably also the first person to recognize the potential of GWs for NDE.

I.2.B Guided-wave Analysis

To understand GW propagation in a structure, it is useful to briefly consider a simple configuration, i.e., an isotropic plate. Assume harmonic GW propagation along the plate x_1 -axis, shown in Fig. 2. Since the plate is 2-D, variations along the 3-axis (normal to the plane of the page) are ignored ($\partial/\partial x_3 = 0$). Furthermore, displacements along the 3-axis are also assumed zero. The governing equation of motion is:

$$(\lambda + \mu)\nabla\nabla\cdot\mathbf{u} + \mu\nabla^2\mathbf{u} = \rho\ddot{\mathbf{u}} \quad (1)$$

where \mathbf{u} is the displacement vector, and λ and μ are Lamé's constants for the isotropic plate material, while ρ is the material density. ∇ is the gradient operator and the $\ddot{\cdot}$ over a variable indicates the derivative with respect to time. Using Helmholtz's decomposition:

$$\mathbf{u} = \nabla\phi + \nabla\times\mathbf{H} \quad \text{and} \quad \nabla\cdot\mathbf{H} = 0, \quad (2)$$

splitting the displacement vector into the Helmholtz components, i.e., the scalar potential ϕ and vector potential \mathbf{H} . The equations of motion in terms of the Helmholtz components can be shown to be:

$$\nabla^2\phi = \frac{1}{c_p^2}\ddot{\phi} \quad \text{and} \quad \nabla^2\mathbf{H}_3 = \frac{1}{c_s^2}\ddot{\mathbf{H}}_3 \quad (3)$$

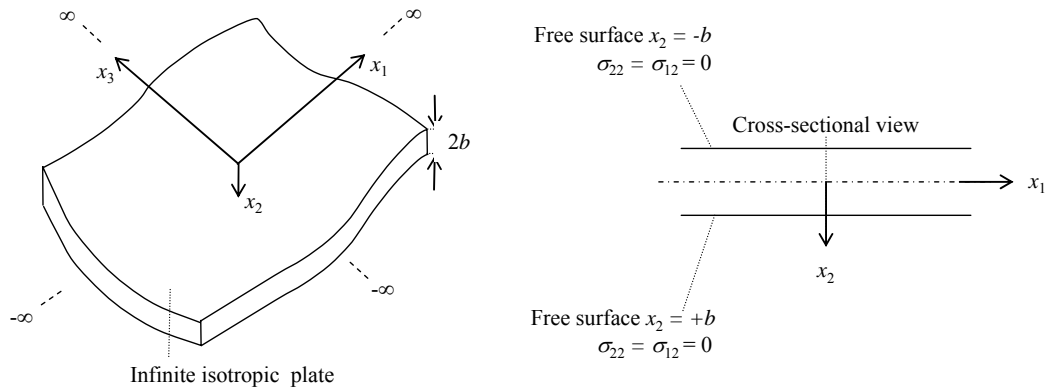


Fig. 2: The 2-D plate for which dispersion relations are derived

The other Helmholtz vector components H_1 and H_2 turn out to be zero. Here $c_p = \sqrt{(\lambda + 2\mu)/\rho}$ and $c_s = \sqrt{\mu/\rho}$ correspond to the bulk longitudinal (or ‘‘P,’’ with the characteristic of displacements along the wave propagation direction) and shear (or ‘‘S,’’ with the characteristic of displacements normal to the wave propagation direction) wave speeds, respectively. Since harmonic GW propagation along the x_1 -axis is considered, say at angular frequency ω , solutions will be of the form (assuming ξ is the wavenumber):

$$\phi = f(x_2)e^{i(\xi x_1 - \omega t)} \quad \text{and} \quad H_3 = h_3(x_2)e^{i(\xi x_1 - \omega t)} \quad (4)$$

This leads to the following differential equations for f and h_3 :

$$\frac{d^2 f}{dx_2^2} + \alpha^2 f = 0 \quad \text{and} \quad \frac{d^2 h_3}{dx_2^2} + \beta^2 h_3 = 0 \quad (5)$$

where:

$$\alpha^2 = \frac{\omega^2}{c_p^2} - \xi^2 \quad \text{and} \quad \beta^2 = \frac{\omega^2}{c_s^2} - \xi^2 \quad (6)$$

The solutions to these differential equations are:

$$f(x_2) = A \sin \alpha x_2 + B \cos \alpha x_2 \quad \text{and} \quad h_3(x_2) = C \sin \beta x_2 + D \cos \beta x_2 \quad (7)$$

where A , B , C and D are constants. Since the boundaries at $x_2 = \pm b$ are free, traction-free conditions must be imposed. Thus:

$$\sigma_{22} = \sigma_{21} = 0 \quad \text{at} \quad x_2 = \pm b \quad (8)$$

The tractions in terms of the Helmholtz components are:

$$\sigma_{22} = (\lambda + 2\mu)\nabla^2 \phi - 2\mu \left(\frac{\partial^2 \phi}{\partial x_1^2} + \frac{\partial^2 H_3}{\partial x_1 \partial x_2} \right) \quad (9)$$

$$\sigma_{21} = \mu \left(2 \frac{\partial^2 \phi}{\partial x_1 \partial x_2} + \frac{\partial^2 H_3}{\partial x_2^2} - \frac{\partial^2 H_3}{\partial x_1^2} \right) \quad (10)$$

From Eqs. (4),(7) and (8)-(10), one obtains:

$$\begin{aligned} \begin{bmatrix} -(\xi^2 - \beta^2) \cos \alpha b & 2i\xi\beta \cos \beta b \\ -2i\xi\alpha \sin \alpha b & (\xi^2 - \beta^2) \sin \beta b \end{bmatrix} \begin{bmatrix} B \\ C \end{bmatrix} &= \begin{bmatrix} 0 \\ 0 \end{bmatrix} \\ \begin{bmatrix} -(\xi^2 - \beta^2) \sin \alpha b & -2i\xi\beta \sin \beta b \\ 2i\xi\alpha \cos \alpha b & (\xi^2 - \beta^2) \cos \beta b \end{bmatrix} \begin{bmatrix} A \\ D \end{bmatrix} &= \begin{bmatrix} 0 \\ 0 \end{bmatrix} \end{aligned} \quad (11)$$

For these matrix equations to be true for nontrivial values of the constants, the determinants of the two matrices must vanish. These lead to the Rayleigh-Lamb equations for the plate, which are:

$$\frac{\tan \beta b}{\tan \alpha b} = \left(\frac{-4\alpha\beta\xi^2}{(\xi^2 - \beta^2)^2} \right)^{\pm 1} \quad (12)$$

where the positive exponent corresponds to the symmetric Lamb modes, while the negative one corresponds to the antisymmetric Lamb modes. The Rayleigh-Lamb equations yield relations between the excitation angular frequency ω and the phase velocity c_{ph} ($= \omega/\xi$) of the GW in the plate. This is called the phase velocity dispersion curve. It is plotted in Fig. 3a for an aluminum alloy plate. Thus, at any excitation frequency, there are at least two modes possible for this structure, viz., the fundamental symmetric (S_0) and anti-symmetric (A_0) modes. Then, as one moves higher up along the frequency axis, additional higher Lamb modes are possible. The equations for SH-waves in a plate can be derived by relaxing the constraint of zero displacements along the 3-axis. Another important characteristic is the group velocity curve (see Fig. 3b). The group velocity (denoted c_g) is defined as the derivative of the angular frequency with respect to the wavenumber ξ . For an isotropic medium, it gives a very good approximation to the speed of the peak of the modulation envelope of a narrow frequency bandwidth pulse. This approximation improves in accuracy as the pulse moves further away from the source or if the GW mode becomes less dispersive. The procedure above, although for a

simple structure, can be generalized to complex structures. Further details on the fundamentals of GW propagation can be found in texts such as Auld [10] and Graff [11].

I.3 Transducer Technology

GW testing is quite common in the NDE/NDT industry for material characterization and offline structural inspection. The most commonly used transducers are angled piezoelectric wedge transducers [21]-[22], comb transducers [23] and electromagnetic acoustic transducers (EMATs) [24]. These transducers can be used to excite specific GW modes by suitably designing them (e.g., in angled wedge transducers this is done by judicious selection of the wedge angle). Other options that have been explored in recent years for NDE are Hertzian contact transducers [25] and lasers [26]. However, while these types of transducers function well for maintenance checks when the structure is offline for service, they are not compact enough to be permanently onboard the structure during its operation as required for SHM. This is particularly true in aerospace structures, where the mass and space penalties associated with the additional transducers on the structure should be minimal.

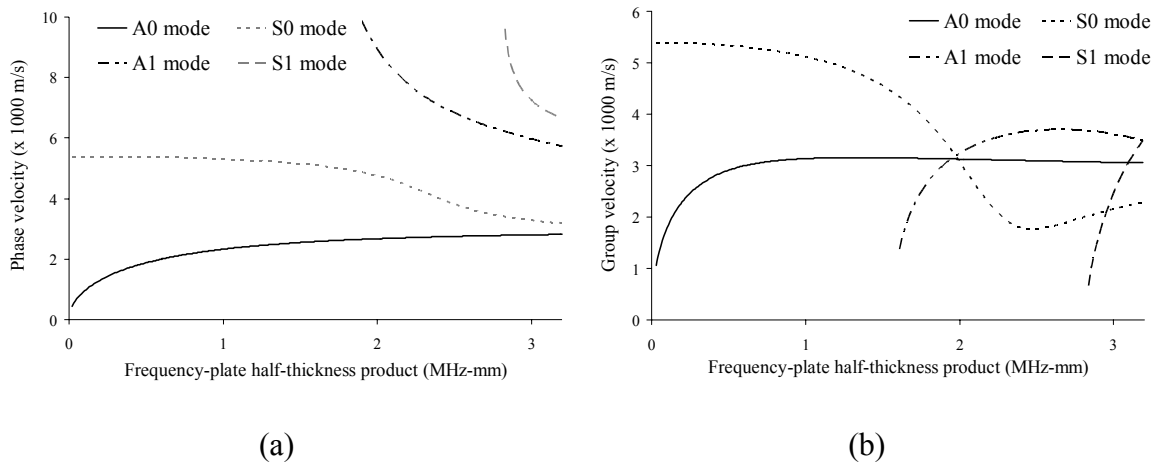


Fig. 3: Dispersion curves for Lamb modes in an isotropic aluminum plate structure: (a) Phase velocity and (b) group velocity.

I.3.A Piezoelectric Transducers

The most commonly used transducers for SHM are embedded or surface-bonded piezoelectric wafer transducers (hereafter referred to as “piezos”). Piezos are inexpensive and are available in very fine thicknesses (0.1 mm for ceramics and 9 μm for polymer film), making them very unobtrusive and conducive for integration into structures. Piezos operate on the piezoelectric and inverse piezoelectric principles that couple the electrical and mechanical behavior of the material. An electric charge is collected on the surface of the piezoelectric material when it is strained. The converse effect also happens, that is, the generation of mechanical strain in response to an applied electric field. Hence, they can be used as both actuators and sensors. The most commonly available materials are lead zirconium titanate ceramics (known as PZT) and polyvinylidene fluoride (PVDF), which is a polymer film (see Fig. 4a). Both of these are usually poled through the thickness (normally designated the 3-direction), which is also the direction in which the voltage is applied or sensed. Uniformly poled piezos are typically used in the “1-3 coupling” configuration, where the sensing/actuation effect is along the thickness or 3-direction while the actuation/sensing effect is in the plane of the piezo, normal to the poling axis. When used as an actuator, the high frequency voltage signal causes waves to be excited in the structure. In the sensor configuration, the in-plane strain over the sensor area causes a voltage signal across the piezo. Piezoceramics are quite brittle and need to be handled with care. In contrast, polymer films are very flexible and easy to handle. Monkhouse et al. ([27], [28]) designed PVDF films with copper backing layers to improve its response characteristics. An interdigitated electrode pattern was deposited using printed circuit board (PCB) techniques for modal selectivity and the transducers were able to detect simulated defects. However, due to its weaker inverse piezoelectric properties and its high compliance, the performance of PVDF based transducers as actuators and sensors is poorer. In addition, PVDF films cannot be embedded into composite structures due to the loss of piezoelectric properties under typical composite curing conditions. Therefore, PZT is the more popular choice for the transducer material among GW SHM researchers (see for example, [29]-[33]). Some researchers have examined design of arrays of actuators to enable inspection of a structure from a central point. The idea is to have each sector scanned by the actuator within that sector. Wilcox

et al. [34] investigated the use of circular and linear arrays using piezoceramic-disc actuators and linear arrays using square shear piezoceramics for long-range GW SHM in isotropic plate structures. The field of vision for the linear arrays was restricted to about 36° on either side of the array due to the interference of side lobes. Interestingly, the ratio of the area of the plate inspected to the area of the circular transducer array was about 3000:1. This gives an indication of the long-range scanning capabilities achievable with actuator arrays. Wilcox [35] proposed the idea of a circular array of six PVDF curved finger interdigitated transducers (IDTs), so that each element would generate a divergent beam, which enables the inspection of a pie-slice shaped area of the plate. Thus, the six IDTs together would have a 360° field of vision about themselves.

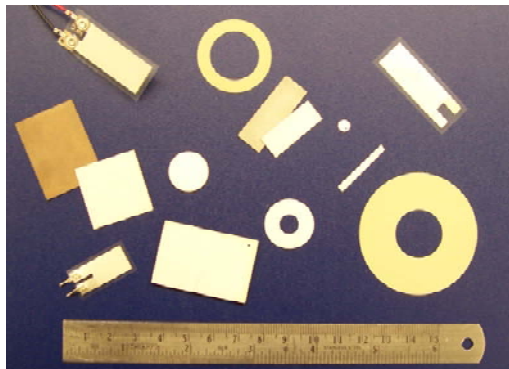


Fig. 4: Piezos (PZT and PVDF) of various shapes and sizes

I.3.B Piezocomposite Transducers

In order to overcome the disadvantage of PZT in terms of brittleness, and also to allow for easier surface conformability in curved shell structures, different types of piezocomposite transducers have been investigated. Badcock and Birt [36] used PZT powder incorporated into an epoxy resin (base material) to form poled film sheets, which were used as transducer elements for GW generation and sensing. These were shown to be much superior to PVDF piezo elements of same dimensions tested on the same host plate under similar conditions, but inferior to a pure PZT piezo element of same dimensions. Egusa and Iwasawa [37] developed a piezoelectric paint using PZT powder

as pigment and epoxy resin as binder. They successfully tested its ability to function as a vibration sensor up to 1 MHz. This makes it an attractive candidate as a structurally-integrated GW sensor. Hayward et al. [38] designed IDTs with “1-3 coupling” piezocomposite layers, consisting of modified lead titanate ceramic platelets held together by a passive soft-set epoxy polymer, and sandwiched between two PCBs for wavenumber and modal selectivity. However, these too compared unfavorably to pure PZT piezos in tests. Culshaw et al. [39] developed an acoustic/ultrasonic based structural monitoring system for composite structures. A low profile acoustic transducer (LPAS) similar in construction to angled wedge ultrasonic transducers (used for offline NDT) was used in [39] to generate the GWs. An appreciable reduction in size was achieved over traditional ultrasonic transducers, raising the possibility of their use as on-board SHM transducers. The LPAS used a “1-3” actuation mode piezo-composite layer as the active phase and two flexible printed circuit boards (PCB) with interdigitated electrode patterns as the upper and lower electrodes. A key advantage in such an angled wedge configuration is modal selectivity, which can be achieved by judicious selection of the wedge angle. A similar low-profile wedge transducer (using an array of piezos) was developed by Gordon and Braunling [40] for on-line corrosion monitoring. Active fiber composite (AFC) transducers were developed by Bent and Hagood [41]. AFCs are constructed using extruded piezoceramic fibers or ribbons embedded in an epoxy matrix with interdigitated electrodes that are symmetric on the top and bottom surfaces of the matrix. Kapton sheets on the outer surfaces electrically insulate the sensor/actuator and make it rugged. The fibers are poled along their length, and the sensing/actuation effect is primarily along the same axis. The fine ceramic fibers provide increased specific strength over monolithic materials, allowing conformability to curved surfaces. Compositing the ceramic provides alternate load path redundancy, increasing robustness to damage. It was shown that these types of actuators have significantly higher energy densities than monolithic piezoceramics in planar actuation for quasi-static applications [41]. In AFCs, by using the mode of actuation along the fiber direction (unlike in the uniformly poled piezo), the actuation authority can be approximately three times higher than that of a monolithic wafer (since the 3-3 piezoelectric constant d_{33} is typically three times larger than the 3-1 piezoelectric constant d_{31}). In addition, when used as a sensor, the more

powerful converse effect causes its response to be stronger than that of a monolithic wafer (again, roughly by three times). Thus, MFCs provide the added advantage of being power efficient. Furthermore, due to the orientation of fibers along a particular direction, AFCs can be used to excite directionally focused GW fields in structures, as well as be insensitive to GWs incident normal to the fiber direction as sensors. Finally, by suitably tailoring their interdigitated electrode pattern, they can be tuned to excite particular wavelengths, and thereby achieve GW modal selectivity. AFCs have been investigated for use in GW based SHM applications by Schulz et al. [42]. Wilkie et al. [43] developed a similar piezoceramic fiber-matrix transducer, called the macro fiber composite (MFC, see Fig. 5). These use rectangular piezoceramic fibers, which are cut from piezoceramic wafers using a computer-controlled dicing saw, and hence significantly reducing the small-batch manufacturing costs compared to AFCs. *However, few researchers have attempted using AFCs/MFCs for GW SHM and their potential as GW SHM transducers remains to be tapped.*

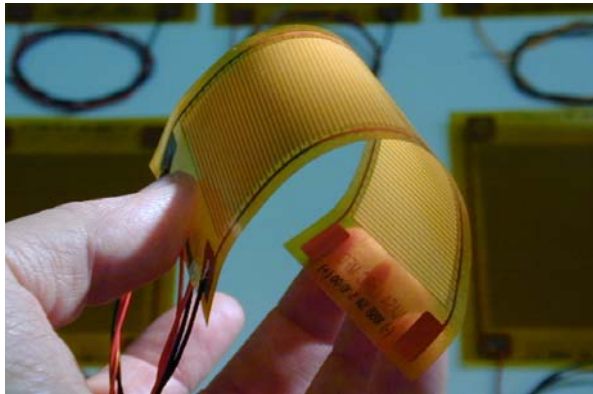


Fig. 5: The macro fiber composite (MFC) transducer [44]

I.3.C Other Transducers

Some non-piezoelectric transducers have also been explored for GW SHM. Fiber optic sensors have been explored for a wide variety of smart structures applications, GW SHM being included. The advantages of fiber optic sensors are their size (diameter as

fine as 0.2 mm), flexible structural integration (embedding/surface bonding), and the possibility of vast networks of multiplexed sensors. Culshaw et al. [39] used an embedded fiber optic sensor in the Mach Zehnder configuration to sense GWs with the characteristics of such fiber optic sensors compared to those of conventional piezo sensors. An important advantage highlighted by those authors was the higher bandwidth capability of fiber optic sensors (can go up to 25 MHz) due to the absence of mechanical resonances. Betz et al. [45] used fiber Bragg gratings in a strain rosette configuration to sense Lamb waves as well as to extract the direction from which they emanate. However, one major drawback with fiber optic sensors is the high cost involved in acquiring the associated support equipment.

Another non-piezoelectric transducer that has been developed for GW SHM is a flat magnetostrictive sensor for surface bonding or embedding into structures by Kwun et al. [46]. The transducer consists of a thin nickel foil with a coil placed over it and can be permanently bonded to the surface of a structure. It is rugged and inexpensive, and can be used as both a GW sensor and actuator. However, little work has been done to characterize this new type of transducer. Developments in Micro Electro Mechanical Systems (MEMS) and nanotechnology have affected many engineering disciplines in today's world, and GW SHM is no exception - some researchers have initiated involving these technologies for GW SHM transducer development. Varadan [47] developed MEMS technology based micro-IDTs for GW SHM, which were either micromachined, etched or printed on special cut piezoelectric wafers or on certain piezoelectric film deposited on silicon using standard microelectronics fabrication techniques and microstereolithography. Neumann et al. [48] fabricated capacitive and piezoresistive MEMS sensors for use as strain sensors for GW applications. Their performance was compared and it was concluded that piezoresistive sensors were far superior. The size of these transducers was of the order of 100 μm . Schulz et al. [49] discussed the potential of nanotubes as GW transducers for SHM. A key advantage of using carbon and boron nanotubes for actuation is that they are also load bearing due to their property of superelasticity. In this sense, the use of nanotubes provides great potential for health monitoring of structures because the structure is also the sensor. However, various

problems, including high cost, must be solved before smart nanocomposites can become practical.

I.4 Developments in Theory and Modeling

I.4.A Developments Motivated by NDE/NDT

The theory of free GW propagation in isotropic, anisotropic, and layered plates and shells is well-documented ([10], [11]). Lowe [50] has reviewed various techniques for obtaining dispersion curves in generic multilayered plates and cylinders. As pointed out in [50], the two major approaches for computing dispersion curves for multilayered structures are the transfer matrix and the global matrix. The former is computationally efficient, but suffers from precision problems at high frequencies. On the other hand, the latter is robust even at high frequencies, but can be slower computationally. Several computationally efficient numerical routines have been implemented in Disperse [51], which is commercial software, to generate analytical dispersion curves (plots of wavespeed versus frequency) and mode shapes for various configurations with or without damping. More recently, Adamou and Craster [52] presented an interesting alternative to root finding of the dispersion equations obtained by solving the underlying differential equations. Their approach uses a numerical scheme based on spectral elements, which is computationally more efficient for complex structural configurations. However, while a large body of literature exists for plates and shells, relatively less work has addressed GW propagation in beam-like structures. This is because analytical solutions of the GW propagation problem using three-dimensional (3-D) elasticity in beams are very difficult, if not impossible. In fact, in the literature, 3-D elasticity solutions exist only for hollow cylindrical ([18], [19]) and rectangular [53] cross-sections. Wilcox et al. [54] used a finite element method (FEM)-based technique for computing the properties of GWs that can exist in an isotropic straight or curved beam of arbitrary cross-section. It uses a two-dimensional finite element mesh to represent a cross section through the beam and cyclic axial symmetry conditions to prescribe the displacement field perpendicular to the mesh. Mukdadi et al. [55] used a similar semi-analytical approach (with FEM elements in the

cross-section and an analytical representation along the beam axis) to compute dispersion curves in multilayered beams with rectangular cross-section. Bartoli et al. [56] extended this approach for arbitrary cross-sectional waveguides to account for viscoelastic damping.

Complications can arise in GW testing due to the dispersive nature of many classes of these waves. For example, in plate structures, at any given frequency, there are at least three GW modes. In composite structures, this is further complicated by the directional dependence of wavespeeds, due to the difference in elastic properties along different directions. Hence, a fundamental understanding of GW theory and modeling, and characterization of the nature of GWs generated and sensed by the transducers typically used are essential. This will be crucial in effectively designing transducers and algorithms for damage detection. Generation of GWs in plates and shells with conventional ultrasonic transducers used in NDE has been examined by several researchers. The work by Viktorov [57] was an early milestone in this field, covering models for excitation of Lamb and Rayleigh waves in isotropic plates by NDE transducers in various configurations. The book by Rose [58], for example, is a more recent work, which reviews various aspects of free and forced GW theory in different structural configurations for NDE. However, a majority of these works use the assumption that the structure and transducer are infinitely wide in one direction, making the problem two-dimensional. Santosa and Pao [59] solved the generic 3-D problem of GW excitation in an isotropic plate by an impulse point body force, also using the normal modes expansion technique. Wilcox [60] presented a 3-D elasticity model describing the harmonic GW field by generic surface point sources in isotropic plates, however the model was not rigorously developed, and some intuitive reasoning was used to extend 2-D model results to 3-D. Mal [61] and Lih and Mal [62] developed a theoretical formulation to solve for the problem of forced GW excitation by finite-dimensional sources using a global matrix formulation in multilayered composite plates. The 2-D Fourier spatial integrals were inverted using a numerical scheme. Viscoelastic damping was addressed, and specifically, the cases of excitation by NDT transducers and acoustic emission were solved based on the developed formulation.

GW SHM researchers can also benefit from several mode sensitivity studies conducted for various damage types by NDE researchers to decide the mode and frequency for GW testing. The choice of the GW mode and operating frequency will depend on the type of damage to be detected. GWs are multimodal with each mode having unique through-plate-thickness stress profiles. This makes it possible to concentrate power close to the anticipated location of the specific damage of interest through the plate thickness. For example, by exciting a mode with a through thickness stress profile such that the maximum power is transmitted close to a particular interface in a composite plate, the plate can be scanned for damage along that interface, as suggested by Rose et al. [63]. They predicted through analysis of displacement and power profiles across the structural thickness, that in metallic plates, the S_0 mode would be more sensitive to detect big cracks or cracks localized in the middle of the plate. On the other hand, the S_1 mode would be better suited for finding smaller cracks or cracks closer to the surface. This idea was also proved experimentally. Kundu et al. [64] proposed the idea that often, the presence of a specific defect type at a certain location through the plate thickness reduces the ability of the plate to support a specific component of stress at that thickness location. In such cases, the GW mode with maximum level of that stress component at that through thickness location should be most sensitive to that defect. This concept can be used, for instance, to scan for broken fibers in a composite, since that reduces the normal stress carrying capacity along the fiber direction. Similarly, Guo and Cawley [65] proved that in composite plates, delaminations located at ply interfaces where the shear stress for a particular guided mode falls to zero could not be detected by that mode. Alleyne and Cawley [66] used similar ideas to propose procedures for notch characterization in steel plates. In applications where the structure is in a non-gaseous environment (e.g., fuel tanks), the mode selection depends on the level of GW attenuation due to leakage into the surrounding media [67]. There have also been several studies to investigate scattering and mode conversion of GWs from various defects (see for example [68]-[72]), which would be useful in identifying the defect type using GW signals.

I.4.B Models for SHM Transducers

While the body of literature in NDE/NDT is significant, relatively few studies have addressed the issue of GW excitation for SHM. There is a crucial difference between GW excitation/sensing in SHM applications and in NDE applications: as mentioned in section I.3, SHM transducers are typically permanently mounted on the structure unlike in NDE. Therefore, it would be desirable to use coupled models involving dynamics of both the transducer and the underlying structure for excitation models in SHM. Such models, however, can be very complex and possibly intractable for analytical solution if no simplifying assumptions are employed. This is because no generic 3-D elasticity/piezoelectricity standing wave solutions for solids bounded in all dimensions (in this case, the actuator) exist. The majority of efforts have been initiated to examine GW excitation using SHM transducers address piezos bonded on plates. These efforts can be classified as semi-analytical/numerical and analytical approaches.

i) Numerical and semi-analytical approaches

Lee and Staszewski [74] have provided a good review of several numerical approaches to GW modeling. The examined methods were the finite element method (FEM), the finite difference method (FDM), the boundary element method (BEM), the finite strip element method (FSM), the spectral element method (SEM), and the mass spring lattice method (MSLM). The merits and demerits of each are discussed. It is pointed out that conventional approaches can be computationally intensive and are unsuitable for media with boundaries or discontinuities between different media, such as multi-ply composites. In response to these, a simulation and visualization tool, Local Interaction Simulation Approach (LISA), was developed and implemented to model GW propagation for damage detection applications in metallic structures. However, in that work, coupled models were not addressed, and it is assumed that the actuator causes uniform normal traction over its surface. Wilcox [35] developed a modeling software tool to predict the acoustic fields excited in isotropic plates by PVDF IDTs. Each electrode finger of the IDT was modeled as causing normal traction over its area. By using an axisymmetric 3-D elasticity solution for a single point normal traction force and superimposition of the individual solutions due to the point sources over the IDT, the

software then finds the GW field due to the IDT by numerically integrating over all sources.

Some researchers have worked around the intractability of coupled models by using semi-analytical approaches. In those works, a non-analytical model is used for the actuator dynamics in conjunction with an analytical model for the dynamics of the underlying structure. Liu et al. [75] developed an analytical-numerical approach based on dynamic piezoelectricity theory, a discrete layer thin plate theory and a multiple integral transform method to evaluate the input impedance characteristics of an IDT and the surface velocity response of the composite plate onto which the IDT is surface-bonded. Moulin et al. [76] used a plane-strain coupled finite element-normal modes expansion method to determine the amplitudes of the GW modes excited in a composite plate with surface-bonded/embedded piezos. FEM was used in the area of the plate near the piezo, enabling the computation of the mechanical excitation field caused by the transducer, which was then introduced as a forcing function into the normal modes equations. This technique, initially developed for harmonic excitation in non-lossy materials was extended to describe transient excitation in viscoelastic materials by Duquenne et al. [77]. Glushkov et al. [78] also examined the coupled 2-D problem of Lamb waves excited in an isotropic plate by piezoelectric actuators (wherein variations were neglected along one direction normal to the direction of wave propagation). A theory of elasticity solution for the isotropic plate was coupled with a reduced order model for the actuator (incorporating the piezoelectric effect). The resulting system of integral and differential equations were tackled by reducing the problem to an algebraic system and then solving it numerically. Veidt et al. [79], [80] used a hybrid theoretical-experimental approach for solving the excitation field due to surface-bonded rectangular and circular actuators. In the theoretical development, the piezo-actuator was modeled as causing normal surface stresses, and Mindlin plate theory was used for the underlying structure. The magnitude of the normal stress exerted for a certain frequency was estimated experimentally using a laser Doppler vibrometer, which was used to characterize the electromechanical transfer properties of the piezos. This hybrid approach was used to predict experimental surface out-of-plane velocity signals with limited success.

ii) Analytical approaches

If the SHM transducer is compliant enough compared to the substrate structure (for example, if the transducer's thickness and elastic modulus are small compared to the host structure), it might be reasonable to assume uncoupled dynamics between the transducer and substrate. This allows the possibility of purely analytical solutions. This approach has been explored by some researchers using reduced structural theories or 3-D elasticity models to model excitation and sensing by piezoelectric wafer transducers. Lin and Yuan [81] modeled the transient GWs in an infinite isotropic plate generated by a pair of surface-bonded circular actuators (on either free surface at the same surface location) excited out-of-phase with respect to each other. Mindlin plate theory incorporating transverse shear and rotary inertia effects was used and the actuators were modeled as causing bending moments along their edge. A simplified equation to describe the sensor response of a surface-bonded piezo-sensor was derived, also using an uncoupled dynamics model. This assumed that the sensor was small enough so that it could be assumed a single point. Some experimental verification for the model was provided. Rose and Wang [82] conducted a systematic theoretical study of source solutions in isotropic plates using Mindlin plate theory, deriving expressions for the response to a point moment, point vertical force and various doublet combinations. These solutions were used to generate equations describing the displacement field patterns for circular and narrow rectangular piezo actuators, which were modeled as causing bending moments and moment doublets, respectively, along their edges. However, the disadvantage of using Mindlin plate theory is that it can only approximately model the lowest antisymmetric (A_0) Lamb-mode and it can only be used when the excitation frequency-plate thickness product is low enough so that higher antisymmetric modes are not excited. In addition, it cannot model symmetric GW modes. Giurgiutiu [83] studied the harmonic excitation of Lamb-waves in an isotropic plate to model the case of plane waves excited by infinitely wide surface-bonded piezos. These were treated as causing shear forces along their edges. The Fourier integral transform was applied to the 3-D linear elasticity based Lamb-wave equations, after they were simplified for the 2-D nature of this problem. The only analytical work that sought to address GW excitation by piezos in laminated composite plates again used 2-D models [84]. *However, no works*

have addressed the 3-D problem of GW excitation by finite-dimensional piezos based on the theory of elasticity in isotropic or composite structures. This is crucial to capture the true multimodal nature of GWs, capture the GW attenuation due to radiation from finite transducers and examine directivity patterns of different piezo shapes. Such models would also aid in effective transducer design for GW SHM.

It should be noted that in modeling the effect of surface-bonded piezo actuators, there has been a difference of opinion among researchers. A few works have suggested that these act similar to NDE/NDT transducers and operate by “tapping” the structure, i.e., causing uniform normal traction over their contact area. However, the majority of the works reviewed suggest that piezos are more effectively modeled as “pinching” the structure, or causing shear traction at the edge of the actuator, normal to it. This idea was inspired by the work of Crawley and de Luis [85], who proposed such a model for quasi-static induced strain actuation of piezo-actuators surface-bonded onto beams. For reduced structural models, this is equivalent to uniform bending moments along the actuator edge.

I.5 Signal Processing and Pattern Recognition

Signal processing is a crucial aspect in any GW-based SHM algorithm. The objective of this step is to extract information from the sensed signal to decide if damage has developed in the structure. Information about damage type and severity is also desirable from the signal for further prognosis. Therefore, a signal processing technique should be able to isolate from the sensed signal the time and frequency centers associated with scattered waves from the damage and identify their modes. The signal processing approach should also be robust to noise in the GW signals. One can borrow from work done on signal processing for GW based NDE testing and from other SHM algorithms, since many elements and goals of signal processing remain the same for most avenues of damage detection. There are however, a couple of differences between GW signal processing for NDE and for SHM. In the latter, the algorithm should be capable of running in near-real time or at frequent intervals, possibly during operation of the structure. Therefore, firstly, technician involvement should be minimal, and the process

should be automated. Secondly, it would be highly desirable to have a computationally efficient algorithm for SHM. Staszewski and Worden [86] have reviewed various signal processing approaches that can be exploited for damage detection algorithms. Signal processing approaches that have been used for GW testing can be grouped into data cleansing, feature extraction and selection, pattern recognition, and optimal excitation signal construction.

I.5.A Data Cleansing

Preprocessing or data cleansing may be needed to clean the signals, since any sensor, in general, is susceptible to noise from a variety of sources. This is particularly needed if the feature extraction mechanism (which is discussed next) is not robust to noise. This group includes normalization procedures, detrending, global averaging and outlier reduction, which are all standard statistical techniques. Yu et al. [87] used the techniques of statistical averaging to reduce global noise and discrete wavelet denoising using Daubechies wavelet to remove local high frequency disturbances. Rizzo and di Scalea [88] achieved denoising and compression of GW sensor signals by using a combined discrete wavelet transform and filtering process, wherein only a few wavelet coefficients representative of the signal were retained and the signal reconstructed with low-pass and high-pass frequency filters (see Fig. 6). Kercel et al. [89] used the Donoho principle to cleanse GW signals obtained from laser ultrasonics, wherein the biggest wavelet coefficients on decomposing with Daubechies wavelets (that contained 90% of the total signal energy) were retained and the rest of the coefficients were assumed as noise. A review of the various low pass filters available for data smoothing is presented in the work by Hamming [90].

I.5.B Feature Extraction and Selection

Features are any parameters extracted from signal processing. Feature extraction and selection is necessary for improved damage characterization. Feature extraction can

be defined as the process of finding the best parameters representing different structural state conditions and feature selection is the process of selecting the inputs for damage identification by pattern recognition [91]. In GW testing, the features of interest are typically time-of-flight, frequency centers, energies, time-frequency spread, and modes of individual scattered waves. The different approaches to feature extraction can be further classified into time-frequency analysis approaches and sensor array-based approaches.

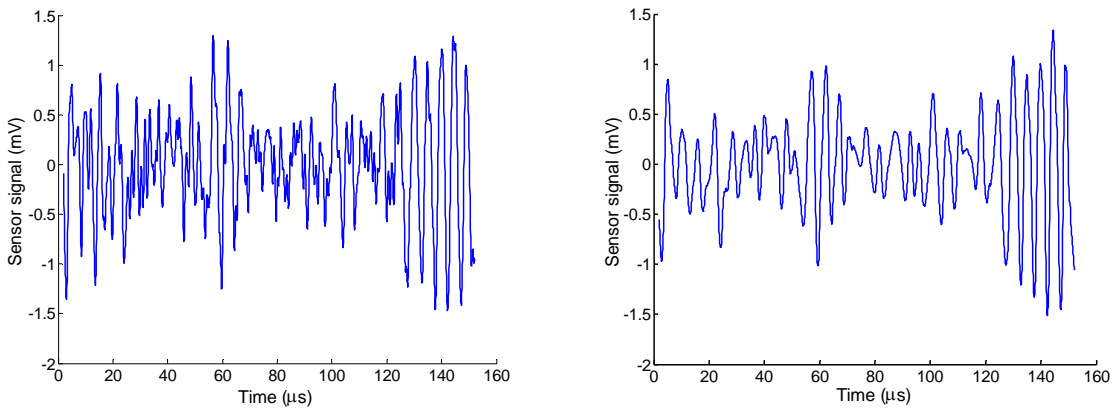


Fig. 6: Denoising using discrete wavelet transform: Raw GW signal reflected from a dent in a metallic plate averaged over 64 samples (left) and signal denoised using Daubechies wavelet

i) Time-frequency and wavelet analysis

In this group of signal processing, a number of techniques using time-frequency representations (TFRs) have been explored for GW signal analysis. While Fourier analysis gives a picture of the frequency spectrum of a signal, it does not provide visualization about what frequency component arrives at what instant of time in the signal. TFRs are designed to do exactly that, and yield an image in the time-frequency plane. They are well suited for analyzing non-stationary signals such as GW signals. Once the image is generated in the time-frequency plane, post-processing is done on these images to isolate individual reflections and identify their time-frequency centers. Their modes are identified using the time-frequency “ridges” (the loci of the frequency

centers for each time instant within each reflection). The short time Fourier transform, which is one of the easiest conventional TFRs to compute, was used by Prasad et al. [92] to extract a suitable parameter for tomographic image reconstruction mapping the structural defects. It was also used by Ihn and Chang [93] to process GW signals obtained from a network of piezoelectric wafer transducers mounted on a structure. Prosser et al. [94] used a pseudo Wigner Ville distribution to process GW signals for material characterization of composites. Niethammer et al. [95] reviewed four different TFRs to gauge their effectiveness in analyzing GW signals, viz., the reassigned spectrogram, the reassigned scalogram, the smoothed Wigner-Ville distribution and the Hilbert spectrum. Reassignment is a post-processing technique for improving resolution and decreasing spread in TFRs. While each technique was found to have its strengths and weaknesses, the reassigned spectrogram emerged as the best candidate for resolving multiple, closely spaced GW modes in terms of time and frequency. Furthermore, the strength of TFRs to facilitate the identification of arrival times of different modes was established. Kuttig et al. [96] and Hong et al. [97] used new TFRs based on different versions of the chirplet transform which has additional degrees of freedom (time shear and frequency shear) compared to the STFT. It enables superior resolution compared to conventional TFRs, but this comes at the cost of greater computational complexity. The above works were all mainly concerned with material characterization or offline NDT. Among works that have used TFRs for GW SHM, Oseguda et al. [98], Quek et al. [99] and Salvino et al. [100] used the Hilbert-Huang transform to process GW signals in plate structures. This technique allows for the separation of the GW signal into intrinsic mode functions (not to be confused with the GW modes) and a residue. This is followed by the Hilbert transform to determine the energy time signal of each mode, enabling the easy location and characterization of the notch. Kerckel et al. [101] used Bayesian parameter estimates to separate the multiple modes in GW signals obtained from laser ultrasonics on a workpiece manufacturing assembly line. Once the dominant modes were separated by this method, the signals from flaws were isolated and could be easily characterized.

The wavelet transform has emerged as a very important signal processing technique for denoising, feature extraction and feature selection in the last two decades. The wavelet technique decomposes a signal in terms of “waveform packets” directly

related to the basis used in the wavelet decomposition. The two types of wavelet transforms are the continuous and the discrete wavelet transforms. Staszewski [102] presented a summary of recent developments in wavelet-based data analysis, which provides for not only effective data storage and transmission, but also for feature selection. As pointed out in that work, continuous wavelet transforms are useful for TFR generation while discrete wavelet transforms are better suited for decomposition, compression and feature selection [86]. While a large number of wavelet bases are available in the literature ([103]-[105]), the Morlet (also referred to as “Gabor”) and Daubechies wavelets seem to be the most commonly used bases for decomposing GW responses. Paget et al. [106] constructed a new wavelet basis from a propagating GW signal. They proposed a new damage detection technique based on wavelet coefficients from the GW decomposition using the new basis. It was implemented for impact damage detection in cross ply laminates. Lefebvre and Lasaygues [107] used a wavelet basis with a Meyer-Jaffard mother wavelet on a fractional scale for crack detection under a stainless steel coating on a steel plate, and were successfully able to distinguish between cracked and undamaged interfaces. Sohn et al. [108] used the wavelet transform on GW signals obtained from a quasi-isotropic composite plate instrumented with a network of piezos. The Morlet wavelet was used as “mother” wavelet, and the component corresponding to the excitation frequency was extracted from the transform, and correlated with the same feature for pristine condition. Subsequently, extreme value statistics was used to decide whether the structure was damaged. Similarly, Lemistre and Balageas [109] used continuous wavelet transform methods with a Morlet mother wavelet for delamination detection in composite structures, while Sun et al. [110] used a similar methodology for notch characterization in pipes. Legendre et al. [111] employed the Coifman wavelet for a wavelet transform based signal-processing scheme to analyze ultrasonic signals excited and received by EMATs in isotropic plates for defect location.

The matching pursuit approach to signal processing is a recent development introduced by Mallat and Zhang [112]. A similar algorithm was proposed independently by Qian and Chen [113]. This is a “greedy” algorithm that iteratively projects a signal onto a large and redundant dictionary of waveforms. At each step, it chooses the waveform from that dictionary that is best adapted to approximate part of the signal

analyzed. Furthermore, it is robust to noise. This can be used to advantage for GW signal processing, since unlike in conventional TFRs, no post-processing has to be done to extract the time-frequency centers of the scattered waves after they are isolated. In the original paper on matching pursuits [112], an efficient algorithm using a Gaussian-modulated time-frequency atoms (which have stationary time-frequency behavior) dictionary is described. The matching pursuit algorithm with this dictionary has been explored for GW signal analysis by Zhang et al. [114] and Hong et al. [115]. However, the implicit assumption in those works is that the signals are unimodal and non-dispersive. The atoms in the dictionary are ill-suited for analyzing dispersive signals, which have non-stationary time-frequency behavior. Furthermore, those atoms would not help in GW mode classification, since different modes with the same energy at the same time-frequency center would yield similar atoms. *Thus, there is a need for a computationally efficient algorithm amenable to automation that would ideally be able to resolve and distinguish between overlapping, multimodal GW pulses scattered by structural damage.*

ii) Sensor array-based approaches

Another distinct approach that has been adopted for processing GW signals is the use of sensor arrays in conjunction with a multi-dimensional Fourier transform along both spatial and time dimensions. Alleyne and Cawley [117] implemented a two-dimensional Fourier transform method numerically, involving both spatial and time domain transforms for multi-element sensor arrays. The method allows for identifying individual GW modes and their respective amplitudes at any propagation distance even in the most dispersive regions. The idea was experimentally implemented for SHM to detect holes drilled in a metallic plate by El Youbi et al. [118]. It used a surface-bonded 32-element piezo sensor array on an Aluminum plate to obtain the 2-D Fourier transform of the received Lamb signal and thereby decompose it into its component modes. Since different modes are sensitive to different defects, the logic is that such a sensor array would be flexible enough to monitor a variety of defects. Martinez et al. [119] used a new four-dimensional space-time/wavenumber-frequency representation for processing a two-dimensional Lamb-wave space-time signal in a one-dimensional medium to characterize

transient aspects of wave generation and propagation in both space and time dimensions. This was used to investigate the generation, transmission and reflection of GWs in a cylindrical shell using a NDE transducer.

Some researchers have proposed algorithms using linear arrays of sensors for “directional tuning.” With appropriate signal processing techniques, these can be used to extract information about the direction of the incoming wave, and thereby enable virtual “scanning” of the structure without moving the transducers. Such approaches enable power efficient coverage in structures and keep the area occupied by the transducers to a minimum. It should be noted that such approaches are distinct from the actuator arrays discussed in Section I.3.A. Lin and Yuan [120] presented an interesting approach to detect and image multiple damage sites in a plate-like structure. A migration technique (inspired by a similar technique in geophysical exploration) was adopted to interpret the backscattering wave field and to image flaws in the structure. The finite difference method was used to simulate the reflection waves and in implementing the prestack migration. This approach was proposed for a linear array of piezo-actuators/sensors. Sundararaman et al. [121] developed a signal processing technique based on beamforming of diagnostic waves for damage detection and location, also using piezo linear phased arrays. Beamforming is the process of spatio-temporal filtering of propagating waveforms, done by combining waves from various directions in a weighted and phase-shifted summation to obtain higher signal-to-noise ratios in the final signal. Damage in the form of a local perturbation in mass by the addition of a small bolt and artificial damage created by scoring the plate were successfully detected within certain confidence levels. Also, adaptive beamforming using the Frost constraint and one-mode pilot signal beamforming-based techniques using a least mean squares algorithm were implemented to produce better directivity patterns and reduce noise. Giurgiutiu and Bao [122] developed an “embedded ultrasonic structural radar” (EUSR) algorithm using a 9-piezo element linear phased array. They were able to map artificially induced cracks in an Aluminum plate specimen, even in the case where the crack was not in the direct field of view of the array (i.e., an offside crack). This was integrated with a graphical user interface. Interestingly, the developed algorithm finds its roots in a similar procedure used in biomedical imaging for human health diagnostics. Similarly, Purekar and Pines

[123] presented a surface-scanning methodology using piezo linear phased arrays for damage detection in isotropic plate structures. After individually exciting the array elements with a pre-defined phase delay (which depends on the direction in which scanning is performed), the other array elements were used to listen for echoes from defects and the boundaries. Once these signals were collected, signal processing and directional filtering were used to analyze the signals. From those results, the damage areas (simulated using C-clamps) were located within 1 inch for a 1-inch diameter contact area of the clamps. Moulin et al. [124] discussed the conditions and limitations for the applicability and performance of linear phased arrays for angular steering of Lamb-waves on a plate structure using a simple scalar diffraction model. Phased arrays were used in a pitch-catch configuration to detect impact damage in Aluminum plates with sensors located close to the edge of the plate.

I.5.C Pattern Recognition

Different conditions of the features extracted and selected represent different classes of “patterns” and indicate the state of structural health. Pattern recognition relates to the process of distinguishing between different patterns. Among pattern recognition strategies, using artificial neural networks (ANN) is the most popular technique for GW based damage detection strategies. For fundamentals of ANN see, e.g., Haykin [125]. Su and Ye [126] extracted spectrographic features from Lamb wave signals in the time-frequency domain to construct a Damage Parameters Database (DPD). The DPD was then used offline to train a multi-layer feed forward ANN under supervision of an error back propagation algorithm. The proposed methodology was validated online by identifying delaminations in quasi-isotropic composite laminates with a built-in piezo network for SHM. Challis et al. [127] applied ANNs to estimate the geometrical parameters of an adhered aluminum T-joint using ultrasonic Lamb waves. The frequency spectrum of received signals was applied as input to conventional feed-forward networks, which were trained using the delta rule with momentum. Legendre et al. [111] used a neural classifier to characterize ultrasonic Lamb wave signals to test metallic welds. This was based on a multilayered ANN, which was trained by selected feature sets chosen to

be representative signals for each weld class. Zhao et al. [128] used a new type of pattern classifier, viz., support vector machine (SVM), to classify defects such as porosity, surface notches, and subsurface cracks in metal matrix composite sheets. The SVM is a quadratic learning algorithm without overtraining problems, unlike ANNs and fuzzy logic.

I.5.D Excitation Signal Tailoring

In order to overcome the dispersive nature of GW propagation, special excitation signals have been explored. Among them, time reversal techniques have been used by some researchers. The idea here is to apply a simple toneburst excitation to one piezo transducer in pitch-catch arrangement, and record the signal at the receiving transducer. The newly recorded GW signal, which is distorted due to dispersion, is reversed in the time domain and applied to the original sensor (now acting as an actuator). The received signal at the original actuator (now acting as a sensor) will be very similar to the original simple excitation toneburst if the structure is undamaged (valid for linear homogeneous media). The presence of damage in the path between the transducers will induce changes to the signal that are non-reversible and easily identified. However, this approach does not differentiate between built-in structural features (e.g., rivets) and defects. Wang et al. [129] used this technique to achieve spatial and temporal focusing in their piezoelectric transducer network designed for GW SHM. Ing and Fink [130] used a similar strategy for a GW testing system using laser excitation and a multi-element sensor array. Sohn et al. [131] used a combination of a time reversal technique and a consecutive outlier analysis to identify delaminations in composite plates using a piezo transducer network without baseline signals (on the premise that there are no structural features such as rivets in the actuator-sensor path). Alleyne and Cawley [132] designed a signal, which, by superposition of its frequency components, recombined to form a signal with a simple shape (a pulse or tone burst) at the measurement position. Kehlenbach and Hanselka [133] used chirp signals combined with matched filtering to ease time-of-flight determination in Lamb-wave based SHM for composite plates.

I.6 GW SHM System Development

For field deployment of GW-based SHM systems, several practical issues need to be addressed. The latest developments in this direction are covered in this section and are sub-divided as packaging, integrated solutions, and robustness issues.

I.6.A Packaging

Packaging of the transducers as well as ensuring reliable mechanical and electrical connections for them is an important element of the SHM system design. The packaging design should account for the demands of harsh environments, load conditions and cycling fatigue experienced by the structure. Lin et al. [134] have developed the “SMART Layer,” which is a thin dielectric film with an embedded network of distributed piezoelectric actuators and sensors, and includes the wiring for the transducers. The layer can also incorporate other types of sensors, including fiber optic sensor networks, to monitor properties such as strain and moisture. The monitoring layer can be either surface-mounted on existing structures or integrated into composite structures during fabrication, thereby enabling GW SHM. Kessler et al. [135] have presented a list of SHM system design requirements based on a survey of aerospace corporations and government agencies. In response to these requirements, fabrication techniques and packaging strategies were developed [136] for surface-mounted piezo transducers to address electrode design, encapsulation, mounting schemes and connectors for wired transducers. Yang et al. [137] embedded rod-shaped piezo transducers in washer-like packages to use for SHM in reusable launch vehicle thermal panel bolts. These transducers were able to survive unscathed in simulated re-entry environment tests in an acoustic chamber. Piezos are also available in a variety of commercially available standard packaged forms such as Moonies [138], Rainbow [139], Crescent [140], Thunder [141], QuickPack and PowerAct [142] designed for various applications. Other packaging strategies include the AFC and MFC described in Section I.3.B. These packages improve their flexibility, reliability, resistance to harsh environments and/or mechanical and electrical connectivity

characteristics. An overview of various piezoelectric materials and architectures is provided in Niezrecki et al. [143].

I.6.B Integrated Solutions

Some researchers have looked at efficient designs of the overall GW SHM system. This includes the packaged transducers, power source, wiring (for wired systems) and data logging/processing/transmission. These works are categorized as “integrated solutions” in this chapter. Among the wired systems, Acellent Technologies Inc. [134] developed a “SMART Suitcase” which essentially integrates the different GW SHM components - a high frequency signal generator, data acquisition, amplifier and processing software into a compact suitcase, which can be used for field applications involving wired sensors. It was designed to support their developed “SMART Layer” described above. Gorinevsky et al. [144] described how a GW SHM system based on the above “SMART Suitcase” would link to a Central Maintenance Computer (CMC, developed by Honeywell Aerospace) for integrated vehicle health management (IVHM) in aircraft. Kim and Lee [145] developed a hybrid coin-sized transducer that incorporates multi-layer piezoelectric disks and fiber optic sensors. A portable microprocessor-based data logger and server are integrated with the transducer and can be used as an excitation source for the piezo-actuator. Their system, called the “diagnostic network patch,” incorporates all signal processing, analysis and interpretation in these two modules, which can be done in real-time for up to 30-sensor channels.

A desirable scenario for certain applications is a SHM system consisting of self-contained transducer patches and networked to a central processor wirelessly. Such a self-contained patch would consist of the following elements: transducer, local power source, telemetry device, and some local data processing capability. The local power source and telemetry abilities are crucial to avoid wires being used to instrument an entire structure, then reducing the complexity of the SHM system. In addition, as pointed out in [146], wires are susceptible to breakage and vandalism, and they present reliability and maintenance issues. Connecting moving/oscillating and fixed sub-systems is another case

when hard wiring is difficult or sometimes impossible. The local computing capability is essential to limit the volume of raw data that needs to be transmitted to the central processor. As pointed out by Hay and Rose [147], interfacing active sensors with wireless technology for GW SHM has lagged behind passive sensor technology due mainly to the power requirements and the electronic accessories that must be added to the active sensors in order to actuate the device. The power required for passive sensors in comparison is much less (in the milliWatt range) and standard communication electronic technology suffices to interface with these. There are several impressive achievements made in passive (or very low power) wireless sensing, such as in the “Motes” program [148]. “Motes,” also called “Smart dust,” are devices that incorporate communications, processing, sensors, and power source into a package currently about two cubic inches in size. It has been tested for passive strain and loads monitoring based SHM with encouraging results. Ihlet et al. [149] presented a trade-off study of various wireless piezoelectric sensor network concepts, including a ranking of different possibilities for power supply, frequency selection, signal modulation and basic prerequisites for embedding of the sensor pad in a carbon fiber composite structure. Kim et al. [146] fabricated a wireless active piezo sensor with fingers etched to form an interdigitated pattern using MEMS technology and incorporated the required microelectronics and conformal antennas onboard chip-sized transducers. Small amplitude GWs were excited for health monitoring, using energy from radio frequency electromagnetic waves transmitted wirelessly to the transducer, thereby eliminating the need for a local power source. The data collected can be processed locally with the onboard chip to extract feature vectors, which can then be transmitted wirelessly to a central processor. To enable flush mounting onto structures with rain and erosion protection, the MEMS transducer was covered with a thin ultra-violet curable polymer coating. Lynch et al. [150] used commercially available components to design and fabricate a low-cost wireless sensing unit for deployment as the building block of wireless SHM systems for civil structures. The unit was about 10 cm × 10 cm × 3.3 cm in dimensions, had a transmitting range of about 150 m, and a power source that lasted about 50 hours. A GW based scheme with some time-series statistical pattern recognition algorithms incorporated into the onboard computing chip was tested in a bridge structure

with encouraging results. Lynch and Loh [151] have also presented an excellent review of various works examining wireless sensors (both passive and active) for SHM. Another avenue that has been explored for local power sources is power harvesting, which is the process of acquiring the energy from the surrounding environment and converting it into usable electrical energy. This captured energy could then be used to prolong the life of the power supply or in the ideal case provide endless energy for the transducer's lifespan. Developments in this emerging technology have been reviewed by Sodano et al. [152], and as pointed out in that work, this field is not mature yet. Innovations in power storage such as the use of rechargeable batteries with piezoelectric materials must be discovered before power-harvesting technology will see widespread use.

I.6.C Robustness to Different Service Conditions

In designing a SHM system for a real-world field application, ample consideration should be given to the robustness of the SHM transducer and algorithm to variable service conditions. The SHM system should be able to distinguish between signal changes due to damage events and changes in environmental conditions. It should also be able to compensate for these condition changes by the use of appropriate signal processing methods. Furthermore, the physical SHM system components should be robust enough to these anticipated changes. Kessler et al. [135] exposed their developed packaged piezo transducers, described in Section I.6.A, to various environmental conditions to test the protective ability of the package. In separate tests, the transducer was exposed to temperatures of 180°F and saturation humidity levels (for a period of one day each), and artificial electrical noise from a brush-style electric drill. They observed that the packaging sufficiently protected the transducers against these simulated environmental effects. Schulz et al. [153] studied the performance of PZT-5A patches as free vibration sensors bonded using various adhesives on aluminum beams up to 240°C. A drop of 74% in strain response amplitude (relative to room temperature value) was observed at 150°C, and the response dropped to zero at 240°C. They also explored various piezoelectric materials for high temperature applications. Commercially available materials such as PZT-5A (a.k.a. DoD Type II) can be used to temperatures up to 175°C

(which is half of its Curie limit). There exist piezoelectric materials such as lithium niobate that retain their piezoelectric properties up to temperatures as high as 1200°C. However, their performance as piezoelectric materials is much poorer in comparison to that of more common ones (e.g., PZT-5A) at room temperature. They identified nanotubes as a potential transducer material for future high temperature applications (up to 1000°C). Lee and Staszewski [154] studied the effect of temperature variation on the Lamb-wave response of a piezoceramic sensor in a pitch-catch configuration on a metallic plate from room temperature up to 70°C. They observed that the effect of temperature variation over this range was much more pronounced than the effect of damage (artificial hole), and explored signal processing options for retaining sensitivity to damage while eliminating sensitivity to temperature change. Lu and Michaels [155] and Konstantinidis, Drinkwater and Wilcox [156] examined GW SHM under mild thermal variations from 20°C to 40°C. Both addressed modeling the varying time-of-flight in this temperature range due to changing substrate elastic modulus and thermal expansion, and good agreement with experiments in this temperature range was observed. Lu and Michaels [155] also suggested using a “bank” of baseline signals for various temperatures and picking a baseline signal which minimizes difference relative to the test signal for that particular temperature. Blaise and Chang [157] investigated the performance of piezoelectric transducers (in GW pitch-catch configuration) embedded into sandwich structures for cryogenic fuel tanks at low temperatures (up to -90°C). An empirical model (linear) was fitted to experimentally obtained data points for damage detection under varying temperature. Both the reduction in signal amplitude and time-of-flight were compensated for. Reasonable agreement between the interpolated signals from the empirical model and experimental data for intermediate temperature values was obtained. *Internal spacecraft structures, which are typically protected by thermal protection systems (TPS) from reentry temperatures, are usually designed for a maximum temperature of 150°C. Thus, these would be a potential application area for GW SHM using PZT-5A piezos. However, as discussed above, no researchers have examined GW SHM at temperatures greater than 70°C.*

Paget et al. [158] studied the performance of a piezo actuator embedded in a graphite/epoxy composite for GW SHM under static and fatigue load tests. The

embedded piezoceramic transducers revealed a large working range in the static tests at least up to 90% of the final failure and were insensitive to fatigue loading for generation of GWs. Changes only occurred after 50,000-100,000 of cycles at high stress levels (260 MPa, corresponding to 0.3% strain). For lower stress levels (130 MPa, corresponding to 0.15% strain), the piezoceramic transducer lasted more than 400,000 cycles. The changes were mainly associated with matrix cracks in the composite. Biemans et al. [159] conducted a preliminary study into the application of GW based SHM for fatigue crack monitoring in aluminum plates under static and dynamic load (6 Hz) conditions, and compared the results with the unloaded condition. Various options in signal processing were explored, and it was shown that, through appropriate choice of excitation signals and signal processing technique, satisfactory damage detection results could be obtained for all load conditions. Manson et al. [160] used the signal processing method of novelty detection to build an internal representation of the system's normal condition for Lamb-wave SHM in such a way that subsequent departures from this condition due to structural damage could be identified with confidence in a robust manner. The importance of obtaining a valid set of normal conditions, which could account for temperature and load variations, was highlighted. The effect of short-term and long-term temperature changes in a composite plate on the normal condition data was experimentally quantified, and similar tests were performed for environmental humidity changes [161]. Giurgiutiu et al. [162] and Blackshire et al. [163] studied the durability and survivability of commercially available piezos (PZT) under temperature cycling in an oven, weather exposure in outdoor environment (sun, rain, humidity, freeze-thaw, etc.), and exposure to water and maintenance fluids (hydraulic fluids and maintenance oils). The test results indicate that repeated thermal cycling and extended environmental conditions could potentially lead to piezo transducer failure. The importance of appropriate bonding agents for the sensor and protective coatings was highlighted. Doane and Giurgiutiu [164] studied the behavior of piezos under large strain and fatigue cycling. The high strain tests indicated that the piezos remain operational up to at least 3000 microstrain and fail beyond 6000 microstrain. The fatigue tests, conducted up to millions of cycles, showed that the substrate always failed before the piezo.

I.7 Application Areas

The gamut of structures where GW SHM can be employed for damage prognosis is vast and ranges from ground vehicles, ships and aerospace structures to bridges, pipelines and offshore platforms. This section presents some examples where GW SHM has been demonstrated in realistic structures.

I.7.A Aerospace Structures

Aerospace structures by themselves form a huge and very significant GW SHM application area. The Aloha Airlines fuselage separation [165] and the Columbia Space Shuttle tragedy [166] brought to the fore the critical need for effective SHM systems in aerospace structures. Derriso et al. [167] outlined the importance of SHM in military aerospace vehicles to reduce maintenance downtime and to ensure high levels of reliability and safety, while Huang [168] discussed the need for SHM in future reusable launch vehicles (RLVs) to achieve affordable and routine access to space with present day aviation-like operations. Dalton et al. [169] explored the potential of GW-based SHM for application in metallic aircraft fuselage structures. GW propagation was examined in a variety of typical structural configurations found in metallic monocoque fuselages, such as free skin, tapering skin, skin loaded with paint and sealant, stringer joints, etc. It was concluded that GW SHM is not the ideal candidate for complicated structural configurations or for skin coated with sealant due to damping. However, for the free and tapered skin configurations and lap joints, results were very promising, establishing it as an effective solution for these simpler configurations. Giurgiutiu et al. [170] examined the feasibility of using piezo-based GW SHM on realistic aircraft panel specimens with rivets and splice joints and were able to clearly distinguish between reflected signals from the structural discontinuities and simulated damage (cracks). Grondel et al. [171] instrumented a single cell box composite specimen with construction and loading similar to that found in an aircraft wing box using piezos to examine the ability of GW SHM. Their experimental results revealed a large sensitivity of GWs to disbond between the stiffener and composite skin and impact damage due to low velocity impact, major causes

of in-service damage of aircraft structures. Koh et al. [172] developed a simple algorithm based on GW power transmitted between two transducers in pitch-catch configuration to detect disbond initiation and monitor its growth in a composite repair patch for aircraft panels. Matt et al. [173] tested a piezo-based GW system for monitoring the integrity of the bond between the composite wing skin and supporting spar for unmanned aerial vehicles (UAVs). Blaise and Chang [174] demonstrated the feasibility of integrating piezo transducers within the cells of cores in honeycomb sandwich structures. The sensors were incorporated on the warmer side of the panels, which are similar to those in cryogenic fuel tank construction. The system showed good potential to detect damage in the form of disbond between the skin and the core. Yang et al. [137] and Derriso et al. [175] have worked on the use of GW SHM for RLV thermal protection panels. Damage in the form of base bracket loosening, panel loosening and impact damage could be detected. Lin et al. [176] designed and manufactured special SMART layers (see Section I.6.A) for filament-wound composite bottles and embedded them during the filament winding process. A prototype of a filament-wound composite bottle with an embedded sensor network was fabricated and preliminary data analysis tools have been developed. This system exemplifies the application of GW SHM in rocket motor cases and fuel tanks for next-generation space vehicles. Lakshmanan and Pines [177] studied the applicability of GW SHM using piezos to detect damage in rotorcraft blades in the form of transverse cracks and delaminations with encouraging results.

I.7.B Civil Structures

As observed by Chong et al. [178], the civil infrastructure in any country is among its most expensive assets (e.g., an estimated \$20 trillion in the USA). These systems are deteriorating at an alarming rate, creating the need for new tools to provide feedback on the structure's health. Significant work has been done to investigate the use of embedded fiber optic sensor or strain gage networks in civil structures for SHM by strain monitoring and vibration mode testing (see, for example [179]-[182]). In comparison, relatively few activities have been done to develop GW-based SHM in civil infrastructure using in-situ transducers for remote diagnostics. This is partly because civil

structures are in general much thicker and bigger in size in comparison to aerospace structures, implying that an in-situ actuator would have to provide orders of magnitude higher actuation stresses to cover a reasonable area. While stress wave propagation methods are popular for assessing the condition of concrete structures for NDE, the greatest success in the practical application of stress wave NDE methods for testing concrete has been using mechanical impact to generate the stress pulse. Impact results in a high-energy pulse and high penetration of the stress waves, which is suitable for large-scale civil structures such as bridge decks and building walls. However, some applications for smaller scale civil structures have been tested for GW SHM with promising results. Rizzo and di Scalea [88] investigated GW SHM for multi-wire steel strands, used as pre-stressing tendons in pre-stressed concrete and as stay-cables in cable-stayed and suspension bridges, with magnetostrictive transducers. Khazem et al. [183] tested the applicability of a similar methodology on a real bridge structure, and they were able to scan the entire length of a suspender rope (about 100m) for cable tension, cracks and corrosion damage. Wu and Chang [184] showed that an embedded pair of piezos could be used for debond detection using GWs in steel-reinforced concrete columns. However, the methodology was unsuitable for crack detection. Lovell and Pines [185] presented a simple GW propagation approach, which was capable of identifying characteristics of damage associated with loss of torque preload on a simple one-bolt lap joint. This was motivated by the idea of monitoring the dynamics of large buildings and bridges to assess the level of damage in bolted or riveted assemblies following a severe loading condition (e.g., earthquake).

I.7.C Other Areas

The capability of GW SHM has been examined in a variety of other mechanical systems as well. Lin et al. [186] have recently designed and fabricated custom SMART layers for automotive applications that conform to an automobile's complex shape. Their SMART suitcase (described in Section 0.2) was specially configured to perform in-situ GW SHM in automobiles. Proof-of-concept tests were conducted using this system by the auto manufacturer BMW in carbon fiber samples for impact damage detection [187].

Na and Kundu [188] designed a transducer holder device using commercially available NDT ultrasonic transducers for GW SHM in underwater pipelines. Encouraging laboratory demonstrations showed the potential of the transducer for on-line detection of damage in the form of dents and gouges. Some researchers have also examined the use of magnetostrictive transducers (Hegeon et al. [189], Park et al. [190]) and PVDF film transducers (Hay and Rose [191]) for GW-based pipeline condition monitoring. Wang [192] described the applications of GW-based damage detection in the petrochemical industry. Those include the testing of heater tubes, pipes, vessels, risers and heat exchanger tubing. Ghoshal et al. [193] conducted preliminary investigations into the applicability of GW SHM for wind turbine blades made of fiberglass, and were able to detect artificial damage in the form of an added mass. Jones et al. [194] illustrated the usefulness of GW SHM for crack detection and size estimation in dragline clusters used for the mining industry.

I.8 Integration with Other SHM Approaches

It is crucial to realize that while GW testing has several advantages, it may not be the best SHM solution in all scenarios. For example, in pulse-echo GW testing, a known shortcoming is the blind zone area close to the collocated actuator/sensor. This is due to the finite duration of the emitting pulse as it is being generated. During that time, all reflection signals are masked by the outgoing excitation pulse. In such scenarios, however, the same network of transducers can be used for a different SHM methodology by simply changing the data processing and/or excitation signal. Passive strain sensors such as fiber optics and foil strain gages, which can be used for GW sensing, can also be used for acoustic emission, strain and load monitoring, and for modal testing. Active transducers, such as piezos, magnetostrictive sensors and nanotubes, can be used for the above listed passive SHM approaches as well as other active SHM schemes such as electro-mechanical (E-M) impedance testing and active modal testing. This can be used to advantage, since other SHM algorithms may prove to be better solutions in certain scenarios. Thus, the overall SHM scheme could be designed to use a combination of two or more of these methods, capturing the benefits of each. For example, as proposed by

Kessler and Spearing [195], a passive system such as acoustic emission or strain monitoring could be used to monitor the structure in real-time, and if this system detects a structural anomaly, then a dormant GW system could be triggered to localize and characterize the defect. This would be beneficial to minimize the power requirements of the SHM system. Such an approach was used by Mal et al. [196], who implemented a combined vibration modal analysis method and GW-based method using a network of piezos. The idea was that the former be used for global damage detection, while the latter for localized damage characterization. Giurgiutiu et al. [197] discussed the complementary nature of the E-M impedance and GW approaches in plate-like structures. The E-M impedance method is suitable for damage detection in the near field, while the GW approach is better suited for far-field damage detection in the pulse-echo mode. Therefore, their simultaneous utilization will cover the structural area completely. The suitability of piezos for acoustic emission and impact wave detection was demonstrated by Osmond et al. [198]. The feasibility of using the same network of piezos as dual mode sensors for acoustic emission and GW SHM was also confirmed. Wait et al. [199] also used a combined E-M impedance and GW SHM strategy with a piezo wafer and MFC network in a metallic plate structure bolted to a base structure. GW testing was used to detect cracks in the plate and the E-M method, due to its high sensitivity to structural boundary conditions, was used to examine the torque level of the bolt connection to the base structure. Monnier et al. [200] proposed a combined E-M impedance and GW SHM strategy for comprehensive SHM in composites. The E-M impedance method was used for detection of degradation in the viscoelastic properties of the composite structure due to aging and the GW method was used for detecting damage such as delaminations and matrix cracks. Blanas and Das-Gupta [201] have reported on the capability of piezos for simultaneous use as GW transducers as well as load monitoring sensors for dynamic and impact loads in composite structures. The final architecture of any SHM system is determined by the type of application, structure and material combinations, and power available.

I.9 Summary and Scope of this Thesis

The latest developments in the various aspects of GW SHM were reviewed in this chapter. This emerging field has its roots in GW NDE, which is a well-established industrial technology. The transducers for GW SHM, particularly for aerospace structures, are typically smaller and more compact compared to those used in NDE. In this respect, ceramic piezoelectric wafer transducers appear to be the most popular option used by SHM researchers. In order to overcome the disadvantage of brittleness in piezoceramics, several piezocomposite transducers and some non-piezoelectric alternatives have also been explored. While the relevant GW theory for NDE is fairly developed, the SHM counterpart has lagged behind. However, there have been some efforts in this direction and modeling tools and innovative numerical and semi-analytical approaches have been examined for SHM GW problems. Some reduced structural and 2-D elasticity-based analytical models for isotropic structures in simple configurations have been developed. Several signal-processing techniques have been explored for GW testing, most of which are time-frequency representations. For pattern recognition, neural networks have emerged as the popular option. There have also been several research efforts on array configurations and the associated signal processing to allow for scanning a structure from a central location with a minimum number of transducers. Several packaged versions of piezoelectric transducers are now available commercially and some commercial entities are developing custom packaging and support electronics for GW SHM transducers (piezoelectric or hybrid). In terms of integrating the transducers with an onboard power source, computing chip and wireless telemetry, the major obstacle has been the high power requirements for exciting GWs with a reasonable scan range. In order to bring this technology closer to field deployment for commercial structures, a few works have examined the effect of environmental factors and noise on the transducers and their response characteristics. From the applications perspective, aerospace structures have been extensively examined. Their thin-walled constructions make them good candidates for this technology. However, there is no reason preventing their widespread applicability to other mechanical structures, and a lot of potential exists in this class of structures. For civil structures, the development of GW SHM has lagged, perhaps due to the higher power requirement for the actuators to excite relatively bulky structures.

Finally, while GW SHM has shown a lot of potential and has several advantages, other schemes may be more applicable in certain scenarios. Some researchers have looked at hybrid schemes involving GW testing and other methodologies for more comprehensive SHM solutions.

From this detailed survey, it is also evident that several issues remain to be addressed before this technology sees widespread field deployment. The following areas, which were highlighted in italics in the discussion in the previous sections, were judged to be critical and examined in this thesis:

- a) *Modeling*: Develop models that capture GW excitation and sensing based on the theory of elasticity for transduction using finite-dimensional piezos and 3-3 anisotropic piezocomposite transducers (APTs, such as AFCs and MFCs) in isotropic and composite structures.
- b) *Design guidelines*: Provide recommendations for transducer and excitation signal design in GW SHM systems based on the developed models.
- c) *Signal processing*: Develop an algorithm amenable to automation for GW SHM that can resolve and identify overlapping, multimodal GW pulses scattered from damage.
- d) *Effects of elevated temperature*: Understand and compensate for the effects of elevated temperature as experienced in internal spacecraft structures.

These four areas are individually addressed in the subsequent chapters of this thesis. At the end, the main contributions of this thesis are summarized and future possible directions of research are suggested.

CHAPTER II

GUIDED-WAVE TRANSDUCTION BY PIEZOS IN ISOTROPIC STRUCTURES

The motivation for the work in this chapter stems from the discussion in Section I.4.B in the introductory chapter. As mentioned there, previous attempts at analytical models to capture the GW field and transduction mechanisms by uniformly poled piezos and 3-3 APTs have used reduced structural models (such as Mindlin plate theory) or 2-D elasticity models, with limited experimental validation. The objective of this chapter is to develop 3-D elasticity-based models to capture the multimodal GW field excited and sensed by finite-dimensional piezos and APTs. The GW field excited by APTs in rectangular cross-sectional beams and hollow cylinders (for the axisymmetric case) are first examined. Both these configurations involve 2-D analysis due to the uniformity of the GW field along one of the three spatial dimensions. This is followed by an analysis for the GW field by arbitrarily shaped piezos bonded on isotropic plates. Specific expressions are presented for rectangular and ring-shaped piezos and rectangular APTs, which are most commonly used in GW SHM. Results from numerical simulations to verify the case of circular piezos are summarized. A general expression for the response of piezos used as GW sensors is derived. Experiments done to validate these models and the results from those are detailed next. Finally, the use of these models in optimizing transducer dimensions is discussed.

II.1 Actuation Mechanisms of Piezos and APTs

As mentioned in Section I.4.B, there is a small group of researchers who suggest that the actuation mechanism of surface-bonded piezos is similar to that of NDT

transducers. NDT transducers are not permanently bonded on the structure and usually some lubricant is applied to the surface of the transducer before it is pressed against the structure and operated to excite GWs. As a result, no shear forces are exerted and therefore the “tapping” (or normal traction) model works well for them. However, for surface-bonded piezos permanently on the structure, due to their one free surface parallel to the structure’s surface, the normal force transmitted to the underlying structure is minimal. Therefore, the “pinching” (or shear traction) model is expected to be a better approximation of its actuation mechanism. Therefore, in this work, the uniformly-poled piezo is modeled as causing in-plane shear traction of uniform magnitude (say τ_0 per unit length) along its perimeter, in the direction normal to the free edge on the plate surface $x_3 = +b$. In this model, the dynamics of the actuator are neglected and it is assumed that the plate dynamics are uncoupled from the actuator dynamics. This model was proposed by Crawley and de Luis [85] to describe the 2-D problem of quasi-static induced strain actuation by piezo-actuators surface-bonded onto beams. For that case, they proved that the model is a good approximation if the product of the actuator Young’s modulus and thickness is small compared to that of the substrate and the bond layer is thin and stiff. This is a practical assumption, since in the aerospace industry, plate-like structures used are typically between 2 and 5 mm thick, while piezo elements typically used are 0.2 to 0.4 mm thick. This assumption will be examined in further detail when the experimental results are discussed. Another assumption made is that the piezoelectric properties of the piezo (specifically the piezoelectric constants d_{31}/d_{33} and g_{31}/g_{33}) are constant over the frequency range of interest, which is supported by the work of González and Alemany [202]. In addition, material damping is neglected. This assumption is based on the fact that, for metals, attenuation from finite excitation sources dominates amplitude decay of the GW. A similar approach can be used to model the action of 3-3 APTs. The key difference is that the 3-3 APT, when used as an actuator, is modeled as causing shear traction at the edges of the active area (the surface area occupied by piezoelectric fibers) along the fiber direction only.

II.2 Plane Lamb-wave Excitation by 3-3 APTs in Rectangular-sectional Beams

The configuration for which a solution is sought in this section is shown in Fig. 7. The beam is infinitely long along the x_1 -direction and the other two dimensions are $2b$ and $2c$ respectively along the x_2 - and x_3 -directions. The 3-3 APT spans or nearly spans the width of the beam on one free surface. Its fibers are oriented along the beam axis (i.e., in the x_1 -direction). If the problem is defined rigorously (i.e., if traction free surface conditions are to be satisfied along all the four sides of the cross-section), in principle the solution consists of an infinite number of modes at any frequency and the problem is complex to solve analytically. More details on such an approach can be found in Kastrzhitskaya and Meleshko [53]. However, if $2c \gg 2b$, then the configuration can be approximated to be a 2-D plane wave problem along the beam axis, and the condition $\partial/\partial x_3(\cdot) = 0$ can be used to simplify the governing equations. The derivation by Giurgiutiu [83] for 2-D models describing Lamb-wave excitation by piezos is then applicable here. This simplification weakens at higher frequency-thickness products when higher GW modes are stronger, which may not be uniform across the beam width. As discussed above, the effect of the 3-3 APT is to cause shear tractions at (a, b) and $(-a, b)$ as shown. Thus, one obtains the following surface condition (for harmonic excitation at angular frequency ω):

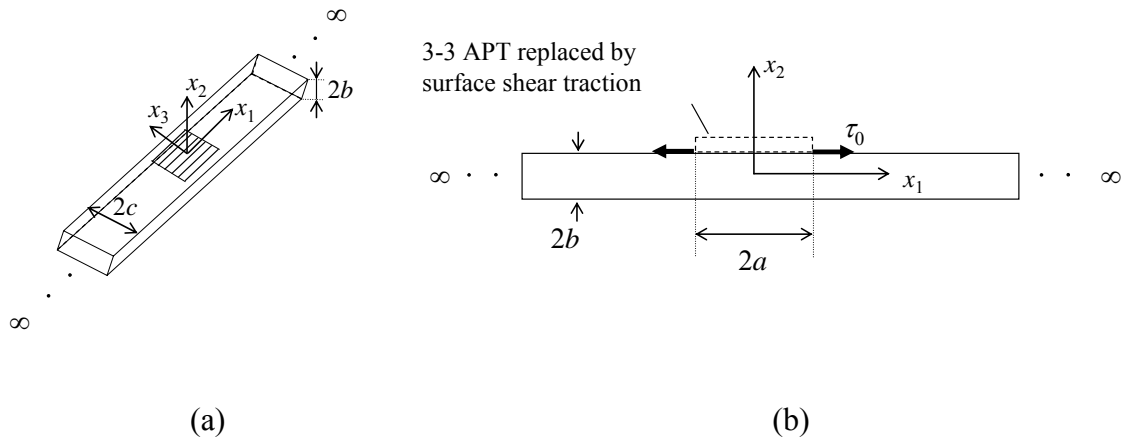


Fig. 7: (a) Configuration of 3-3 APT surface-bonded on an isotropic beam with rectangular cross-section and (b) modeled representation

$$\sigma_{21}(x_2 = b) = \tau_0[\delta(x_1 - a) - \delta(x_1 + a)]e^{-i\omega t} \quad (13)$$

where τ_0 is the magnitude of the shear traction. Here, the actual value of τ_0 is not of relevance, since the theoretical and experimental frequency response curves are both normalized relative to their respective peak values over the frequency range considered. For uniformly poled piezos operating in the 3-1 mode, it can be shown that $\tau_0 \propto d_{31}V/h_a$, where V is the actuation voltage and h_a is the actuator thickness [85]. To solve the boundary value problem, the 1-D spatial Fourier transform is applied along the x_1 -direction and the surface conditions are applied along $x_2 = b$ and $x_2 = -b$. The analysis proceeds along the lines of the harmonic analysis for free 2-D Lamb waves described in Section I.2.A, with the exception that the surfaces are not stress-free. Residue calculus from complex analysis [203] is used for the Fourier spatial inversion (this is explained in detail in the following sub-sections for other configurations). The following expression is obtained for symmetric mode displacements along the x_1 -direction:

$$u_1^S(x_1, x_2 = +b, t) = -\frac{i\tau_0}{\mu} \sum_{\xi^S} \frac{\sin \hat{\xi}^S a}{\hat{\xi}^S} \frac{N_S(\hat{\xi}^S)}{D'_S(\hat{\xi}^S)} e^{i(\hat{\xi}^S x_1 - \omega t)} \quad (14)$$

where

$$\begin{aligned} \alpha^2 &= \frac{\omega^2}{c_p^2} - \xi^2; \quad \beta^2 = \frac{\omega^2}{c_s^2} - \xi^2; \quad c_p = \sqrt{\frac{\lambda + 2\mu}{\rho}}; \quad c_s = \sqrt{\frac{\mu}{\rho}} \\ N_S(\xi) &= \xi\beta(\xi^2 + \beta^2) \cos \alpha b \cos \beta b \\ D_S(\xi) &= (\xi^2 - \beta^2)^2 \cos \alpha b \sin \beta b + 4\xi^2 \alpha\beta \sin \alpha b \cos \beta b \\ N_A(\xi) &= \xi\beta(\xi^2 + \beta^2) \sin \alpha b \sin \beta b \\ D_A(\xi) &= (\xi^2 - \beta^2)^2 \sin \alpha b \cos \beta b + 4\xi^2 \alpha\beta \cos \alpha b \sin \beta b \end{aligned} \quad (15)$$

The superscript S corresponds to the symmetric Lamb modes and the superscript A corresponds to the anti-symmetric Lamb modes. The anti-symmetric mode displacements can be obtained by replacing the superscript S by A in Eq. (14). λ and μ are Lamé's

constants for the plate material and ρ is the material density. The wavenumber $\hat{\xi}$ of a specific mode for a given ω is obtained from the solutions of the Rayleigh-Lamb equation, derived earlier. While harmonic excitation is considered here and the subsequent sections, the response to any excitation signal can be obtained by taking the inverse Fourier transform over the excited frequency range.

II.3 Axisymmetric GW Excitation by 3-3 APTs in Hollow Cylinders

In this section, the problem of axisymmetric GW excitation by 3-3 APTs in solid or hollow cylinders (with ring-like cross sections) is discussed. Consider an infinitely long, isotropic hollow cylinder of outer radius c_o and inner radius c_i (possibly zero). A 3-3 APT actuator of length $2a$ is surface-bonded on the outer free surface so that it wraps around the outer circumference. The fibers are oriented along the cylinder axis. The cylindrical coordinate system is a natural choice for solving this problem, and the origin is chosen at the center of the mid-plane of the 3-3 APT, as shown in Fig. 8. The starting point of this analysis is the governing equations of motion from 3-D elasticity:

$$(\lambda + \mu)\nabla\nabla\cdot\mathbf{u} + \mu\nabla^2\mathbf{u} + \mathbf{f} = \rho\ddot{\mathbf{u}} \quad (16)$$

where the gradient operator for cylindrical coordinates is:

$$\nabla \equiv \left(\frac{\partial}{\partial r} \hat{r} + \frac{\partial}{r\partial\theta} \hat{\theta} + \frac{\partial}{\partial z} \hat{z} \right) \quad (17)$$

In this case, the body force $\mathbf{f} = 0$. Furthermore, the equations of motion can be decomposed into the Helmholtz components using the equations:

$$\mathbf{u} = \nabla\phi + \nabla \times \mathbf{H}; \quad \nabla \cdot \mathbf{H} = 0 \quad (18)$$

It can be shown using Eq. (18), that Eq. (16) is equivalent to the equations:

$$\nabla^2\phi = \frac{\ddot{\phi}}{c_p^2}; \quad \nabla^2\mathbf{H} = \frac{\ddot{\mathbf{H}}}{c_s^2} \quad (19)$$

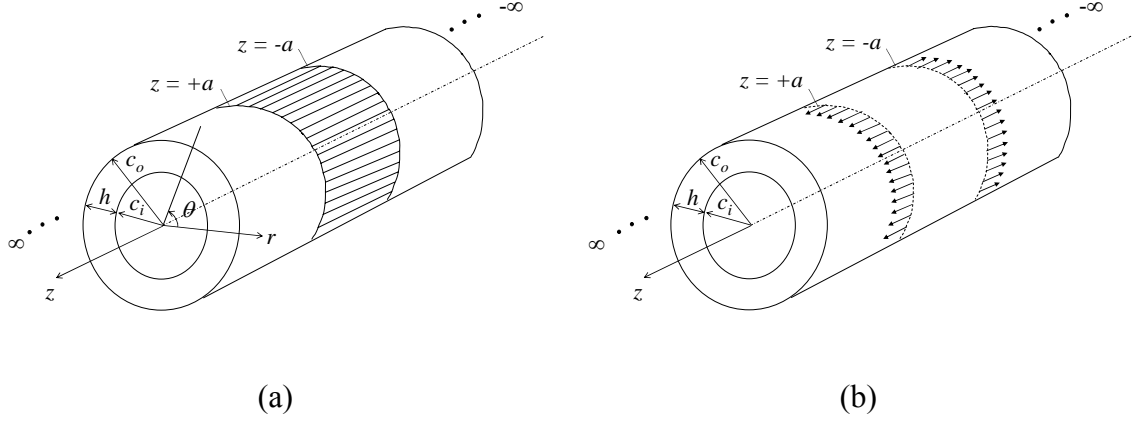


Fig. 8: (a) Configuration of 3-3 APT surface-bonded on a hollow cylinder and modeled representation (b)

In this problem, the conditions $\partial/\partial\theta = 0$ and $u_\theta = 0$ hold. The non-zero displacement components are then given by:

$$u_r = \frac{\partial\phi}{\partial r} - \frac{\partial H_\theta}{\partial z}; \quad u_z = \frac{\partial\phi}{\partial z} + \frac{1}{r} \frac{\partial(H_\theta r)}{\partial r} \quad (20)$$

Thus, only the Helmholtz components ϕ and H_θ are required. As before, the response to harmonic excitation at angular frequency ω is considered. Thus, one obtains:

$$\frac{\partial^2(\cdot)}{\partial t^2} = -\omega^2(\cdot) \quad (21)$$

Applying the spatial Fourier transform along the z -direction yields the following equations:

$$\frac{\partial^2 \tilde{\phi}}{\partial r^2} + \frac{1}{r} \frac{\partial \tilde{\phi}}{\partial r} + \alpha^2 \tilde{\phi} = 0; \quad \frac{\partial^2 \tilde{H}_\theta}{\partial r^2} + \frac{1}{r} \frac{\partial \tilde{H}_\theta}{\partial r} + \left(\beta^2 - \frac{1}{r^2} \right) \tilde{H}_\theta = 0 \quad (22)$$

where ξ is the wavenumber along the z -direction. The \sim symbol over a variable indicates the z -direction Fourier transform of that variable. The solutions to Eqs. (22) are:

$$\tilde{\phi} = (D_1 J_0(\alpha r) + D_2 Y_0(\alpha r)) e^{i\omega t}; \quad \tilde{H}_\theta = (D_3 J_1(\beta r) + D_4 Y_1(\beta r)) e^{i\omega t} \quad (23)$$

where J_0 and J_1 are the Bessel functions of the first kind and of order 0 and 1 respectively; Y_0 and Y_1 are the Bessel functions of the second kind and of order 0 and 1, respectively; and $D_1, D_2, D_3,$ and D_4 are constants to be determined using the surface conditions at $r = c_i$ and $r = c_o$. If the problem under consideration were that of a solid cylinder (i.e., $c_i = 0$), then $D_2 = D_4 = 0$ (to maintain finiteness of the solution at $r = 0$) and the other two constants could be found using the surface conditions at $r = c_o$. The stresses are related to the displacements through the equations:

$$\sigma_{rr} = (\lambda + 2\mu) \frac{\partial u_r}{\partial r} + \frac{\lambda}{r} u_r + \lambda \frac{\partial u_z}{\partial z}; \quad \sigma_{rz} = \mu \left(\frac{\partial u_r}{\partial z} + \frac{\partial u_z}{\partial r} \right) \quad (24)$$

Using, Eqs. (22) through (24) gives the stresses in terms of $D_1 - D_4$. The externally applied stresses are:

$$\begin{aligned} \sigma_{rr}(r = c_o) &= 0; & \sigma_{rz}(r = c_o) &= \tau_0 e^{i\omega t} (\delta(z - a) - \delta(z + a)) \\ \sigma_{rr}(r = c_i) &= 0; & \sigma_{rz}(r = c_i) &= 0 \end{aligned} \quad (25)$$

The Fourier transforms of the externally applied stresses are:

$$\begin{aligned} \tilde{\sigma}_{rr}(r = c_o) &= 0; & \tilde{\sigma}_{rz}(r = c_o) &= \tau_0 e^{i\omega t} 2i \sin \xi a \\ \tilde{\sigma}_{rr}(r = c_i) &= 0; & \tilde{\sigma}_{rz}(r = c_i) &= 0 \end{aligned} \quad (26)$$

From Eqs. (20), (23) and (24), the Fourier transforms of the same stress components in the cylinder are:

$$\begin{aligned} \tilde{\sigma}_{rr} &= \left[\begin{aligned} &(r(\beta^2 - \xi^2)J_0(\alpha r) - 2\alpha J_1(\alpha r))D_1 + \\ &+ (r(\beta^2 - \xi^2)Y_0(\alpha r) - 2\alpha Y_1(\alpha r))D_2 + \\ &+ (-r\beta J_0(\beta r) + J_1(\beta r))D_3 + (-r\beta Y_0(\beta r) + Y_1(\beta r))D_4 \end{aligned} \right] e^{i\omega t} \\ \tilde{\sigma}_{rz} &= \left[\begin{aligned} &2i\alpha\xi J_1(\alpha r)D_1 + 2i\alpha\xi Y_1(\alpha r)D_2 + (\xi^2 - \beta^2)J_1(\beta r)D_3 + \\ &+ (\xi^2 - \beta^2)Y_1(\beta r)D_4 \end{aligned} \right] e^{i\omega t} \end{aligned} \quad (27)$$

Equating the Fourier transforms of the externally applied stresses to the expressions in terms of $D_1 - D_4$ yields (at the inner and outer radii of the hollow cylinder):

$$\begin{bmatrix} M_{11} & M_{12} & M_{13} & M_{14} \\ M_{21} & M_{22} & M_{23} & M_{24} \\ M_{31} & M_{32} & M_{33} & M_{34} \\ M_{41} & M_{42} & M_{43} & M_{44} \end{bmatrix} \begin{bmatrix} D_1 \\ D_2 \\ D_3 \\ D_4 \end{bmatrix} = 2i\tau_0 \sin \xi a \begin{bmatrix} 0 \\ 1 \\ 0 \\ 0 \end{bmatrix} \quad (28)$$

where:

$$\begin{aligned} M_{11} &= c_o(\beta^2 - \xi^2)J_0(\alpha c_o) - 2\alpha J_1(\alpha c_o); & M_{12} &= c_o(\beta^2 - \xi^2)Y_0(\alpha c_o) - 2\alpha Y_1(\alpha c_o) \\ M_{13} &= -c_o\beta J_0(\beta c_o) + J_1(\beta c_o); & M_{14} &= -c_o\beta Y_0(\beta c_o) + Y_1(\beta c_o) \\ M_{21} &= 2i\alpha\xi J_1(\alpha c_o); & M_{22} &= 2i\alpha\xi Y_1(\alpha c_o) \\ M_{23} &= (\xi^2 - \beta^2)J_1(\beta c_o); & M_{24} &= (\xi^2 - \beta^2)Y_1(\beta c_o) \end{aligned} \quad (29)$$

and the constants M_{3i} and M_{4i} ($i = 1$ to 4) are obtained by replacing c_o by c_i in M_{1i} and M_{2i} respectively. The constants D_i ($i = 1$ to 4) can be solved for using Cramer's rule, yielding expressions of the form:

$$D_i = \frac{d_i(\xi)}{\Delta(\xi)} \quad (30)$$

where:

$$\begin{aligned} d_1(\xi) &= 2i\tau_0 \sin \xi a \det \begin{bmatrix} 0 & M_{12} & M_{13} & M_{14} \\ 1 & M_{22} & M_{23} & M_{24} \\ 0 & M_{32} & M_{33} & M_{34} \\ 0 & M_{42} & M_{43} & M_{44} \end{bmatrix}, \text{ etc} \\ \Delta(\xi) &= \det \begin{bmatrix} M_{11} & M_{12} & M_{13} & M_{14} \\ M_{21} & M_{22} & M_{23} & M_{24} \\ M_{31} & M_{32} & M_{33} & M_{34} \\ M_{41} & M_{42} & M_{43} & M_{44} \end{bmatrix} \end{aligned} \quad (31)$$

The final expressions for radial and axial displacements are of the form:

$$\begin{aligned}
u_r &= \int_{-\infty}^{\infty} \frac{1}{\Delta(\xi)} \left[-\alpha d_1(\xi) J_1(\alpha r) - \alpha d_2(\xi) Y_1(\alpha r) + \right. \\
&\quad \left. + i\xi d_3(\xi) J_1(\beta r) + i\xi d_4(\xi) Y_1(\beta r) \right] e^{-i(\xi z - \omega t)} d\xi \\
u_z &= \int_{-\infty}^{\infty} \frac{1}{\Delta(\xi)} \left[-i\xi d_1(\xi) J_0(\alpha r) - i\xi d_2(\xi) Y_0(\alpha r) + \right. \\
&\quad \left. + \beta d_3(\xi) J_0(\beta r) + \beta d_4(\xi) Y_0(\beta r) \right] e^{-i(\xi z - \omega t)} d\xi
\end{aligned} \tag{32}$$

The integral along the real ξ -axis can be found by considering a contour integral in the complex ξ -plane. The values of z will determine the shape of the contour. For example, if $z > a$ then contributions from negative wavenumbers are not allowed on physical grounds, hence the integral must only include the residues at positive wavenumbers, as shown in Fig. 9. The integrands in Eq. (32) are singular at the roots of the dispersion equation $\Delta(\xi) = 0$, designated $\hat{\xi}$. These can be obtained from the dispersion curves for the cylinder under consideration. Using the residue theorem for the first integral in Eq. (32) yields in this case:

$$\int_{-\infty}^{\infty} I d\xi + \int_C I d\xi = -\pi i \sum_{\hat{\xi}} \text{Res}(I(\hat{\xi})) \tag{33}$$

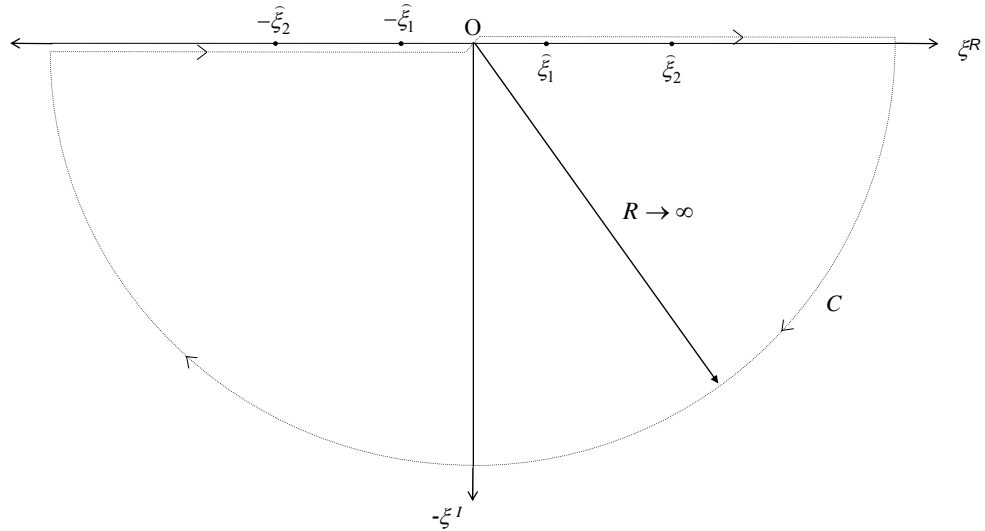


Fig. 9: Contour integral in the complex ξ -plane to invert the displacement integrals using residue theory

where:

$$I = \frac{1}{\Delta(\xi)} \left[-\alpha d_1(\xi) J_1(\alpha r) - \alpha d_2(\xi) Y_1(\alpha r) + i \xi d_3(\xi) J_1(\beta r) + i \xi d_4(\xi) Y_1(\beta r) \right] e^{-i(\xi z - \omega t)} \quad (34)$$

C is the semi-circular contour in the lower half-plane while “Res” stands for the residue of the integrand at a singularity of I . The contribution from C vanishes as the radius of the surface $R \rightarrow \infty$, as explained in Miklowitz [204] for a similar plane-wave excitation problem. Thus, the following expressions are obtained for displacement in the region $z > a$:

$$\begin{aligned} u_r &= \sum_{\hat{\xi}} \frac{-\pi i e^{-i(\hat{\xi} z - \omega t)}}{\Delta'(\hat{\xi})} \left[\begin{aligned} &-\alpha d_1(\hat{\xi}) J_1(\alpha r) - \alpha d_2(\hat{\xi}) Y_1(\alpha r) + \\ &+ i \hat{\xi} d_3(\hat{\xi}) J_1(\beta r) + i \hat{\xi} d_4(\hat{\xi}) Y_1(\beta r) \end{aligned} \right] \\ u_z &= \sum_{\hat{\xi}} \frac{-\pi i e^{-i(\hat{\xi} z - \omega t)}}{\Delta'(\hat{\xi})} \left[\begin{aligned} &-i \hat{\xi} d_1(\hat{\xi}) J_0(\alpha r) - i \hat{\xi} d_2(\hat{\xi}) Y_0(\alpha r) + \\ &+ \beta d_3(\hat{\xi}) J_0(\beta r) + \beta d_4(\hat{\xi}) Y_0(\beta r) \end{aligned} \right] \end{aligned} \quad (35)$$

II.4 3-D GW Excitation in Plates

The final configuration examined for the excited GW field is for an arbitrary shape (finite-dimensional) surface-bonded piezo actuator (or APT) on an infinite isotropic plate. This formulation is based on the 3-D elasticity equations of motion. Consider an infinite isotropic plate of thickness $2b$ with such an actuator bonded on the surface $x_3 = b$, as illustrated in Fig. 10. The origin is located midway through the plate thickness and the x_3 -axis is normal to the plate surface. The choice of in-plane location of the origin and the orientation of the x_1 and x_2 axes at this point is arbitrary, but it is constrained later. The starting point is the equations of motion in terms of the Helmholtz components (i.e., the eqs. in (19)). In this case, since the plate is infinite along two axes, the 2-D spatial Fourier transform is used to ease solution of this problem. For a generic function of two spatial coordinates φ , it is defined by:

$$\bar{\varphi}(\xi_1, \xi_2) = \int_{-\infty}^{\infty} \int_{-\infty}^{\infty} \varphi(x_1, x_2) e^{i(\xi_1 x_1 + \xi_2 x_2)} dx_1 dx_2 \quad (36)$$

and the inverse is given by:

$$\varphi(x_1, x_2) = \frac{1}{4\pi^2} \int_{-\infty}^{\infty} \int_{-\infty}^{\infty} \bar{\varphi}(\xi_1, \xi_2) e^{-i(\xi_1 x_1 + \xi_2 x_2)} d\xi_1 d\xi_2 \quad (37)$$

Applying the 2-D spatial Fourier transform on Eqs. (19) and considering harmonic excitation as before, one obtains the following equations:

$$(-\xi_1^2 - \xi_2^2)\bar{\phi} + \frac{d^2\bar{\phi}}{dx_3^2} = -\frac{\omega^2}{c_p^2}\bar{\phi} \quad (38)$$

$$(-\xi_1^2 - \xi_2^2)\bar{\mathbf{H}} + \frac{d^2\bar{\mathbf{H}}}{dx_3^2} = -\frac{\omega^2}{c_s^2}\bar{\mathbf{H}} \quad (39)$$

Let:

$$(-\xi_1^2 - \xi_2^2) + \frac{\omega^2}{c_p^2} = \alpha^2 \quad ; \quad (-\xi_1^2 - \xi_2^2) + \frac{\omega^2}{c_s^2} = \beta^2 \quad (40)$$

The solutions of Eqs. (38) and (39) are of the form:

$$\begin{aligned} \bar{\phi} &= (C_1 \sin \alpha x_3 + C_2 \cos \alpha x_3) e^{i\omega t}; & \bar{\mathbf{H}}_1 &= (C_3 \sin \beta x_3 + C_4 \cos \beta x_3) e^{i\omega t} \\ \bar{\mathbf{H}}_2 &= (C_5 \sin \beta x_3 + C_6 \cos \beta x_3) e^{i\omega t}; & \bar{\mathbf{H}}_3 &= (C_7 \sin \beta x_3 + C_8 \cos \beta x_3) e^{i\omega t} \end{aligned} \quad (41)$$

Furthermore, by examining the through-thickness displacement patterns, it can be shown that the constants C_2, C_3, C_5 , and C_8 are associated with symmetric modes and that the constants C_1, C_4, C_6 , and C_7 are associated with antisymmetric modes. For the subsequent analysis, only the symmetric modes are considered. The contributions from antisymmetric modes can be derived analogously. The linear strain-displacement relation and the constitutive equations for linear elasticity yield:

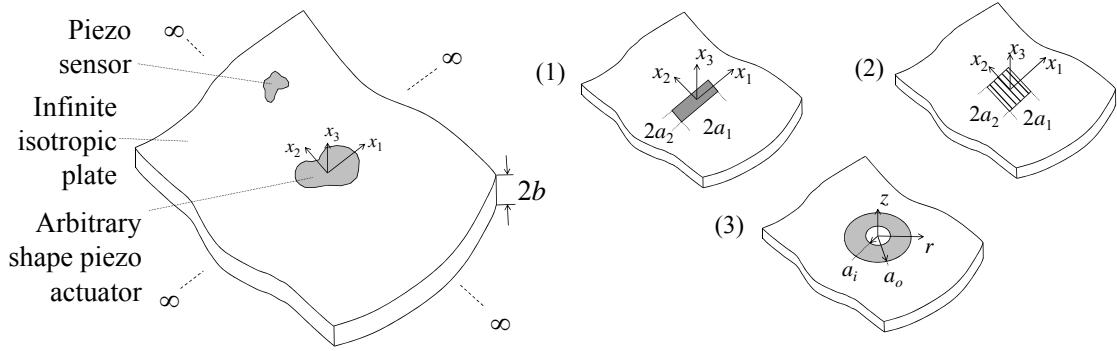


Fig. 10: Infinite isotropic plate with arbitrary shape surface-bonded piezo actuator and piezo sensor and the three specific configurations considered: (1) Rectangular piezo (2) Rectangular MFC and (3) Ring-shaped piezo

$$\varepsilon_{ij} = \frac{1}{2}(u_{i,j} + u_{j,i}); \quad \sigma_{ij} = \lambda \varepsilon_{kk} \delta_{ij} + 2\mu \varepsilon_{ij} \quad (42)$$

Using Eqs. (18), (41) and (42), it can be shown that the transformed stresses at $x_3 = b$ are:

$$\begin{aligned} \bar{\sigma}_{33} &= \mu \left[C_2(\xi_1^2 + \xi_2^2 - \beta^2) \cos \alpha b + C_3(2i\mu\xi_2\beta) \cos \beta b + C_5(-2i\xi_1\beta) \cos \beta b \right] e^{i\omega t} \\ \bar{\sigma}_{32} &= \mu \left[C_2(2i\xi_2\alpha) \sin \alpha b + C_3(\xi_2^2 - \beta^2) \sin \beta b + C_5(-\xi_1\xi_2) \sin \beta b + \right. \\ &\quad \left. + C_8(-i\xi_1\beta) \sin \beta b \right] e^{i\omega t} \\ \bar{\sigma}_{31} &= \mu \left[C_2(2i\alpha\xi_1) \sin \alpha b + C_3(\xi_1\xi_2) \sin \beta b + C_5(\beta^2 - \xi_1^2) \sin \beta b + \right. \\ &\quad \left. + C_8(i\xi_2\beta) \sin \beta b \right] e^{i\omega t} \end{aligned} \quad (43)$$

Since the piezo-actuator is modeled as causing shear traction along its edge, the externally applied traction components yield the following expressions for stresses at the free surface $x_3 = +b$ and their double spatial Fourier transforms:

$$\begin{aligned} \sigma_{33} &= 0; \quad \bar{\sigma}_{33} = 0 \\ \sigma_{32} &= \tau_0 \cdot F_2(x_1, x_2) e^{i\omega t}; \quad \bar{\sigma}_{32} = \tau_0 \cdot \bar{F}_2(\xi_1, \xi_2) e^{i\omega t} \\ \sigma_{31} &= \tau_0 \cdot F_1(x_1, x_2) e^{i\omega t}; \quad \bar{\sigma}_{31} = \tau_0 \cdot \bar{F}_1(\xi_1, \xi_2) e^{i\omega t} \end{aligned} \quad (44)$$

where F_1 and F_2 are arbitrary functions, that are zero everywhere except around the edge of the piezo actuator. It would be prudent to choose the coordinate axes x_1 and x_2 as well as the origin's in-plane location to ease the computation of \bar{F}_1 and \bar{F}_2 . Equating Eqs. (43) and (44) would give three equations in four unknowns. The fourth equation results from the divergence condition on \mathbf{H} , and consequently, $\bar{\mathbf{H}}$, given by:

$$\frac{\partial \bar{H}_1}{\partial x_1} + \frac{\partial \bar{H}_2}{\partial x_2} + \frac{\partial \bar{H}_3}{\partial x_3} = 0 \quad (45)$$

Using Eqs. (41) in (45) and evaluating at $x_3 = b$ gives:

$$C_3(-i\xi_1 \sin \beta b) + C_5(-i\xi_2 \sin \beta b) + C_8(-\beta \sin \beta b) = 0 \quad (46)$$

With four equations and four unknowns, the unknown constants C_2 , C_3 , C_5 and C_8 can be solved for from the matrix equation:

$$\begin{bmatrix} (\xi_1^2 + \xi_2^2 - \beta^2) \cos \alpha b & 2i\xi_2\beta \cos \beta b & -2i\xi_1\beta \cos \beta b & 0 \\ 2i\xi_2\alpha \sin \alpha b & (\xi_2^2 - \beta^2) \sin \beta b & -\xi_1\xi_2 \sin \beta b & -i\xi_1\beta \sin \beta b \\ 2i\xi_1\alpha \sin \alpha b & \xi_1\xi_2 \sin \beta b & (\beta^2 - \xi_1^2) \sin \beta b & i\xi_2\beta \sin \beta b \\ 0 & -i\xi_1 \sin \beta b & -i\xi_2 \sin \beta b & -\beta \sin \beta b \end{bmatrix} \begin{bmatrix} C_2 \\ C_3 \\ C_5 \\ C_8 \end{bmatrix} = \frac{\tau_0}{\mu} \begin{bmatrix} 0 \\ \bar{F}_2(\xi_1, \xi_2) \\ \bar{F}_1(\xi_1, \xi_2) \\ 0 \end{bmatrix} \quad (47)$$

Solving for the constants using Cramer's rule and applying the inverse Fourier transform ultimately yields the following expressions for the displacement components on the free surface $x_3 = b$ in the spatial domain (symmetric modes):

$$u_1^S = \frac{\tau_0}{4\mu\pi^2} \int_{-\infty}^{\infty} \int_{-\infty}^{\infty} \frac{\cos \beta b e^{-i(\xi_1 x_1 + \xi_2 x_2 - \omega t)}}{\beta \sin \beta b D_S(\xi)} \left\{ \begin{array}{l} -\bar{F}_1(\xi_1, \xi_2) \left[\begin{array}{l} ((\xi_2^2 - \beta^2)^2 + \xi_1^2(\xi_2^2 + \beta^2)) \times \\ \times \cos \alpha b \sin \beta b + \\ + 4\alpha\beta\xi_2^2 \sin \alpha b \cos \beta b \end{array} \right] + \\ +\bar{F}_2(\xi_1, \xi_2) \left[\begin{array}{l} \xi_1\xi_2(\xi^2 - 3\beta^2) \times \\ \times \cos \alpha b \sin \beta b + \\ + 4\alpha\beta\xi_1\xi_2 \sin \alpha b \cos \beta b \end{array} \right] \end{array} \right\} d\xi_1 d\xi_2 \quad (48)$$

$$u_2^S = \frac{\tau_0}{4\mu\pi^2} \int_{-\infty}^{\infty} \int_{-\infty}^{\infty} \frac{\cos \beta b e^{-i(\xi_1 x_1 + \xi_2 x_2 - \omega t)}}{\beta \sin \beta b D_S(\xi)} \left\{ \begin{array}{l} \bar{F}_1(\xi_1, \xi_2) \left[\begin{array}{l} \xi_1\xi_2(\xi^2 - 3\beta^2) \times \\ \times \cos \alpha b \sin \beta b + \\ + 4\alpha\beta\xi_1\xi_2 \sin \alpha b \cos \beta b \end{array} \right] + \\ -\bar{F}_2(\xi_1, \xi_2) \left[\begin{array}{l} ((\xi_1^2 - \beta^2)^2 + \xi_2^2(\xi_1^2 + \beta^2)) \times \\ \times \cos \alpha b \sin \beta b + \\ + 4\alpha\beta\xi_1^2 \sin \alpha b \cos \beta b \end{array} \right] \end{array} \right\} d\xi_1 d\xi_2 \quad (49)$$

$$u_3^S = \frac{\tau_0}{4\mu\pi^2} \int_{-\infty}^{\infty} \int_{-\infty}^{\infty} \frac{-i e^{-i(\xi_1 x_1 + \xi_2 x_2 - \omega t)}}{D_S(\xi)} \left[\begin{array}{l} 2\alpha\beta \sin \alpha b \cos \beta b + \\ + (\xi^2 - \beta^2) \sin \beta b \cos \alpha b \end{array} \right] \left(\begin{array}{l} \xi_1 \bar{F}_1(\xi_1, \xi_2) + \\ + \xi_2 \bar{F}_2(\xi_1, \xi_2) \end{array} \right) d\xi_1 d\xi_2 \quad (50)$$

where $\xi^2 = \xi_1^2 + \xi_2^2$ and $D_S(\xi) = (\xi^2 - \beta^2)^2 \cos \alpha b \sin \beta b + 4\xi^2 \alpha\beta \sin \alpha b \cos \beta b$. These integrals could be singular at the points corresponding to the real roots of either $D_S = 0$ or $\sin \beta b = 0$ or both (depending on which term(s) survive after substituting \bar{F}_1 and \bar{F}_2). The former correspond to the wavenumbers, ξ^S , from the solutions of the Rayleigh-Lamb equation for symmetric modes at frequency ω . The latter correspond to the wavenumbers of horizontally polarized symmetric mode shear (SH) waves, also at frequency ω . In principle, one can also include the contributions from the imaginary and complex wavenumbers satisfying these equations. However, these are usually not of

interest, since they yield evanescent or standing waves that decay very rapidly away from the source. As in Section

II.2, only symmetric modes were considered in the derivation above, but the contribution from anti-symmetric modes can be found analogously and the final solution would be a superposition of these two modal contributions. Next, the evaluation of these integrals is presented for three particular piezo shapes of interest.

II.4.A Rectangular Piezo

The configuration considered for rectangular piezos is illustrated in Fig. 10. The dimensions of the piezo are $2a_1$ and $2a_2$ along the x_1 - and x_2 - axes respectively. In this case, the functions F_1 , F_2 and their respective Fourier transforms are:

$$\begin{aligned} F_1 &= [\delta(x_1 - a_1) - \delta(x_1 + a_1)][He(x_2 + a_2) - He(x_2 - a_2)] \\ \bar{F}_1 &= -4 \sin(\xi_1 a_1) \sin(\xi_2 a_2) / i \xi_2 \\ F_2 &= [He(x_1 + a_1) - He(x_1 - a_1)][\delta(x_2 - a_2) - \delta(x_2 + a_2)] \\ \bar{F}_2 &= -4 \sin(\xi_1 a_1) \sin(\xi_2 a_2) / i \xi_1 \end{aligned} \quad (51)$$

Substituting Eqs. (51) in Eq. (48) ultimately gives the following expression for displacement along the 1-direction:

$$u_1^S(x_3 = b) = \frac{e^{i\omega t}}{4\pi^2} \int_{-\infty}^{\infty} \int_{-\infty}^{\infty} \frac{4\tau_0 \sin \xi_1 a_1 \sin \xi_2 a_2}{i\mu \xi_2 \xi} \frac{N_S(\xi)}{D_S(\xi)} e^{-i(\xi_1 x_1 + \xi_2 x_2)} d\xi_1 d\xi_2 \quad (52)$$

where $N_S(\xi) = \xi\beta(\xi^2 + \beta^2) \cos \alpha b \cos \beta b$. Observe that the $\sin \beta b$ term is absent in the denominator here, implying that only Lamb waves are excited in this case. Transforming into polar coordinates gives:

$$u_1^S(x_3 = b) = \frac{\tau_0 e^{i\omega t}}{\pi^2 i \mu} \int_0^{\infty} \int_0^{2\pi} \frac{\sin(\xi \cos \gamma a_1) \sin(\xi \sin \gamma a_2)}{\xi^2 \sin \gamma} \frac{N_S(\xi)}{D_S(\xi)} e^{-i\xi(x_1 \cos \gamma + x_2 \sin \gamma)} \xi d\gamma d\xi \quad (53)$$

Here the Cartesian wavenumbers ξ_1 and ξ_2 have been replaced by the polar wavenumber coordinates ξ and γ . They are related by the following equations:

$$\xi = \sqrt{\xi_1^2 + \xi_2^2}; \quad \gamma = \tan^{-1}(\xi_2/\xi_1) \quad (54)$$

To obtain the 2-D spatial inverse Fourier transform, residue calculus is used. For convenience, by expanding the sine functions as the difference of conjugate complex exponentials, the integral in Eq. (53) is rewritten thus:

$$u_1^S(x_3 = b) = \frac{-\tau_0}{4i\pi^2 \mu} e^{i\omega t} \int_0^\infty \int_0^{2\pi} \frac{N_S(\xi)}{\xi \cdot D_S(\xi)} \frac{(e^{i\xi a_1 \cos \gamma} - e^{-i\xi a_1 \cos \gamma})(e^{i\xi a_2 \sin \gamma} - e^{-i\xi a_2 \sin \gamma})}{\sin \gamma} \times e^{-i\xi(x_1 \cos \gamma + x_2 \sin \gamma)} d\gamma d\xi$$

$$\Rightarrow u_1^S(x_3 = b) = \frac{-\tau_0}{4i\pi^2 \mu} e^{i\omega t} \cdot \left(\int_0^\infty \int_0^{2\pi} \frac{N_S(\xi)}{\xi \cdot D_S(\xi)} \frac{e^{-i\xi^S((x_1 - a_1) \cos \gamma + (x_2 - a_2) \sin \gamma - \omega t)}}{\sin \gamma} d\gamma d\xi + \right. \quad (55)$$

$$\left. - \int_0^\infty \int_0^{2\pi} \frac{N_S(\xi)}{\xi \cdot D_S(\xi)} \frac{e^{-i\xi^S((x_1 - a_1) \cos \gamma + (x_2 + a_2) \sin \gamma - \omega t)}}{\sin \gamma} d\gamma d\xi + \right.$$

$$\left. - \int_0^\infty \int_0^{2\pi} \frac{N_S(\xi)}{\xi \cdot D_S(\xi)} \frac{e^{-i\xi^S((x_1 + a_1) \cos \gamma + (x_2 - a_2) \sin \gamma - \omega t)}}{\sin \gamma} d\gamma d\xi + \right.$$

$$\left. + \int_0^\infty \int_0^{2\pi} \frac{N_S(\xi)}{\xi \cdot D_S(\xi)} \frac{e^{-i\xi^S((x_1 + a_1) \cos \gamma + (x_2 + a_2) \sin \gamma - \omega t)}}{\sin \gamma} d\gamma d\xi \right)$$

Consider the first of the four integrals in the second line of Eq. (55), say I_1 . It is further rewritten as follows:

$$I_1 = \int_{\gamma_1 - \pi/2}^{\gamma_1 + \pi/2} \int_{-\infty}^{\infty} \frac{N_S(\xi)}{\xi \cdot D_S(\xi)} \frac{e^{-i(\xi r_1 \cos(\gamma - \gamma_1) - \omega t)}}{\sin \gamma} d\xi d\gamma \quad (56)$$

$$\text{where } \gamma_1 = \tan^{-1} \left(\frac{x_2 - a_2}{x_1 - a_1} \right) \text{ and } r_1 = \sqrt{((x_1 - a_1)^2 + (x_2 - a_2)^2)}$$

This ensures that the coefficient of ξ in the exponent remains positive over the domain of integration. The inner integral along the real ξ -axis is solved by considering a contour integral in the lower half of the complex ξ -plane, the semi-circular portion C of which

has radius $|\xi| = R \rightarrow \infty$. Using the residue theorem for the inner integral in Eq. (56) yields in this case (assuming I is the integrand in I_1):

$$\int_{-\infty}^{\infty} Id\xi + \int_C Id\xi = -\pi i \sum_{\hat{\xi}^S} \text{Res}\left(I(\hat{\xi}^S)\right) \quad (57)$$

where $\hat{\xi}^S$ are the roots of the Rayleigh-Lamb equation for symmetric modes ($D_S = 0$).

$N_S(\xi)/(\xi \cdot D_S(\xi))$ for large $|\xi|$ is of order $1/\xi$, and therefore tends to zero as $|\xi| \rightarrow \infty$.

Furthermore, along C , if $\xi = \xi^R - i\xi^I$, where $\xi^R, \xi^I > 0$, then :

$$\left| e^{-i(\xi r_1 \cos(\gamma - \gamma_1) - \omega t)} \right| = \left| e^{i\omega t} \cdot e^{-i\xi^R r_1 \cos(\gamma - \gamma_1)} \cdot e^{-\xi^I r_1 \cos(\gamma - \gamma_1)} \right| \leq \left| e^{-\xi^I r_1 \cos(\gamma - \gamma_1)} \right| \quad (58)$$

Since r_1 and $\cos(\gamma - \gamma_1)$ are both always positive or zero in the domain of integration, the term $\left| e^{-\xi^I r_1 \cos(\gamma - \gamma_1)} \right|$ is finite and is bounded by zero as $\xi^I \rightarrow \infty$. Therefore, by Jordan's lemma [203], the contribution over the semi-circular portion C of the contour vanishes, as in the derivation for hollow cylinders. Therefore:

$$\begin{aligned} \int_C Id\xi &= 0 \quad ; \quad \int_{-\infty}^{\infty} Id\xi = -\pi i \sum_{\hat{\xi}^S} \text{Res}\left(I(\hat{\xi}^S)\right) \\ I_1 &= -\pi i \sum_{\hat{\xi}^S} \int_{\gamma_1 - \pi/2}^{\gamma_1 + \pi/2} \frac{N_S(\hat{\xi}^S)}{\hat{\xi}^S \cdot D'_S(\hat{\xi}^S)} \frac{e^{-i(\hat{\xi}^S r_1 \cos(\gamma - \gamma_1) - \omega t)}}{\sin \gamma} d\gamma \end{aligned} \quad (59)$$

where ()' indicates derivative with respect to ξ . Similar analysis can be used to solve the other three integrals in Eq. (55), to finally yield the expression for u_1^S . An approximate closed form solution can be obtained for the far field using the method of stationary phase. As explained in Graff [11], for large r :

$$\int_{\psi_1}^{\psi_2} f(\psi) e^{irh(\psi)} d\psi = \sqrt{\frac{2\pi}{rh''(\psi_0)}} f(\psi_0) e^{i(rh(\psi_0) + \pi/4)} \quad (60)$$

where $h'(\psi_0) = 0$, $f(\cdot)$ is an arbitrary function, and ψ_1 and ψ_2 are arbitrary end-points of the interval of integration, which contains ψ_0 . Hence, the following asymptotic expression holds for the particle displacement along the 1-direction in the far field:

$$u_1^S(x_3 = b) = \sum_{\xi^S} \frac{-\tau_0}{\pi\mu} \frac{N_S(\xi^S)}{\xi^S D'_S(\xi^S)} \sqrt{\frac{2\pi}{\xi^S r}} \frac{\sin(\xi^S a_1 \cos \theta) \sin(\xi^S a_2 \sin \theta)}{\sin \theta} e^{-i(\xi^S r + \pi/4 - \omega t)} \quad (61)$$

where $\theta = \tan^{-1}(x_2/x_1)$ and $r = \sqrt{x_1^2 + x_2^2}$. Here it is assumed that $\gamma_k \approx \theta$ and $r_k \approx r$, $k = 1$ to 4. The corresponding far-field expressions for the other displacement components are:

$$u_2^S(x_3 = b) = \sum_{\xi^S} \frac{-\tau_0}{\pi\mu} \frac{N_S(\xi^S)}{\xi^S D'_S(\xi^S)} \sqrt{\frac{2\pi}{\xi^S r}} \frac{\sin(\xi^S a_1 \cos \theta) \sin(\xi^S a_2 \sin \theta)}{\cos \theta} e^{-i(\xi^S r + \pi/4 - \omega t)} \quad (62)$$

$$u_3^S(x_3 = b) = \sum_{\xi^S} \frac{-i\tau_0}{\pi\mu} \frac{T_S(\xi^S)}{\xi^S D'_S(\xi^S)} \sqrt{\frac{2\pi}{\xi^S r}} \frac{\sin(\xi^S a_1 \cos \theta) \sin(\xi^S a_2 \sin \theta)}{\sin \theta \cos \theta} e^{-i(\xi^S r + \pi/4 - \omega t)} \quad (63)$$

where $T_S(\xi) = \xi^2(\beta^2 - \xi^2) \cos \alpha b \sin \beta b - 2\alpha\beta\xi^2 \cos \beta b \sin \alpha b$. This indicates that the GW field tends to a spatially decaying circular crested field with angularly dependent amplitude at large distances from the actuator.

II.4.B Rectangular APT

In this case, again the dimensions of the piezo are $2a_1$ and $2a_2$ along the x_1 - and x_2 - axes respectively. The fibers of the APT are oriented along the x_2 -axis. In this case, the functions F_1 , F_2 and their respective Fourier transforms are:

$$\begin{aligned} F_1 &= 0; \quad \bar{F}_1 = 0 \\ F_2 &= [He(x_1 + a_1) - He(x_1 - a_1)][\delta(x_2 - a_2) - \delta(x_2 + a_2)] \\ \bar{F}_2 &= -4 \sin(\xi_1 a_1) \sin(\xi_2 a_2) / i\xi_1 \end{aligned} \quad (64)$$

Substituting Eqs. (64) in Eqs. (48)-(50) ultimately gives the following expression for the displacement components (symmetric modes):

$$u_1^S(x_3 = b) = \int_0^\infty \int_0^{2\pi} \frac{\tau_0}{\pi^2 i \mu} \frac{M_s(\xi^S)}{(\beta \sin \beta b D_s(\xi^S))} \sin \gamma \times \sin(\xi^S \cos \gamma a_1) \sin(\xi^S \sin \gamma a_2) e^{-i\xi^S (\cos \gamma x_1 + \sin \gamma x_2 - \omega t)} d\gamma d\xi \quad (65)$$

$$u_2^S(x_3 = b) = \int_0^\infty \int_0^{2\pi} \frac{-\tau_0}{\pi^2 i \mu} \frac{\cos \beta b}{\cos \gamma (\beta \sin \beta b D_s(\xi^S))} \times \sin(\xi^S \cos \gamma a_1) \sin(\xi^S \sin \gamma a_2) L_s(\xi^S, \gamma) e^{-i\xi^S (x_1 \cos \gamma + x_2 \sin \gamma - \omega t)} d\gamma d\xi \quad (66)$$

$$u_3^S(x_3 = b) = \int_0^\infty \int_0^{2\pi} \frac{-\tau_0}{\pi^2 \mu} \frac{T_s(\xi^S)}{\xi D_s(\xi^S)} \times \tan \gamma \sin(\xi^S \cos \gamma a_1) \sin(\xi^S \sin \gamma a_2) e^{-i\xi^S (\cos \gamma x_1 + \sin \gamma x_2 - \omega t)} d\gamma d\xi \quad (67)$$

where

$$\begin{aligned} M_s(\xi) &= \xi^2 \cos \beta b \left[(\xi^2 - 3\beta^2) \cos \alpha b \sin \beta b + 4\alpha\beta \sin \alpha b \cos \beta b \right] \\ L_s(\xi, \gamma) &= \left[\begin{aligned} &(\xi^2 \cos^2 \gamma - \beta^2)^2 + \\ &+ \xi^2 \sin^2 \gamma (\xi^2 \cos^2 \gamma + \beta^2) \end{aligned} \right] \cos \alpha b \sin \beta b + 4\alpha\beta \xi^2 \cos^2 \gamma \sin \alpha b \cos \beta b \quad (68) \\ T_s(\xi) &= \xi^2 (\beta^2 - \xi^2) \cos \alpha b \sin \beta b - 2\alpha\beta \xi^2 \cos \beta b \sin \alpha b \end{aligned}$$

These inverse Fourier integrals are evaluated along similar lines as in the previous section. In this case, SH-waves are also excited along with Lamb waves. It is interesting to note that the integrands in the Fourier inversion integrals for u_1 and u_2 are singular at the roots of both the symmetric Rayleigh-Lamb equation as well as the equation for symmetric SH-waves ($\sin \beta b = 0$), whereas that for u_3 is singular only at the roots of the Rayleigh-Lamb equation. This is logical in hindsight, since SH-waves do not cause out-of-plane displacements.

II.4.C Ring-shaped Piezo

In this case, the functions F_1 , F_2 and their respective Fourier transforms are:

$$\begin{aligned} F_1 &= [\delta(r - a_o) - \delta(r - a_i)] \cos \theta; & \bar{F}_1 &= -i(a_o J_1(\xi a_o) - a_i J_1(\xi a_i)) \xi_1 / \xi \\ F_2 &= [\delta(r - a_o) - \delta(r - a_i)] \sin \theta; & \bar{F}_2 &= -i(a_o J_1(\xi a_o) - a_i J_1(\xi a_i)) \xi_2 / \xi \end{aligned} \quad (69)$$

Using Eqs. (48) and (69), one can show that:

$$u_1^S(x_3 = b) = \frac{-i\tau_0}{4\pi^2\mu} e^{i\omega t} \int_{-\infty}^{\infty} \int_{-\infty}^{\infty} \xi_1 (a_o J_1(\xi a_o) - a_i J_1(\xi a_i)) \frac{N_S(\xi)}{\xi^2 D_S(\xi)} e^{-i(\xi_1 x_1 + \xi_2 x_2)} d\xi_1 d\xi_2 \quad (70)$$

where $N_S(\xi^S)$ is as defined before. Observe that in this case too, only Lamb-waves are excited. As before, only the symmetric modes are being considered here. Transforming into polar coordinates yields:

$$\begin{aligned} u_1^S(x_3 = b) &= \frac{-i\tau_0}{4\pi^2\mu} e^{i\omega t} \int_0^{\infty} \int_0^{2\pi} (a_o J_1(\xi a_o) - a_i J_1(\xi a_i)) \frac{N_S(\xi)}{D_S(\xi)} e^{-i\xi(x_1 \cos \gamma + x_2 \sin \gamma)} \cos \gamma d\gamma d\xi \\ &= \frac{-i\tau_0}{4\pi^2\mu} e^{i\omega t} \int_{-\infty}^{\infty} \int_0^{\pi} (a_o J_1(\xi a_o) - a_i J_1(\xi a_i)) \frac{N_S(\xi)}{D_S(\xi)} e^{-i\xi(x_1 \cos \gamma + x_2 \sin \gamma)} \cos \gamma d\gamma d\xi \end{aligned} \quad (71)$$

Without loss of generality due to axisymmetry, consider the point $x_1 = r$, $x_2 = 0$. The following formula for the Bessel function can then be used:

$$J_1(z) = \frac{-1}{\pi i} \int_0^{\pi} e^{-iz \cos \gamma} \cos \gamma d\gamma \quad (72)$$

Using Eq. (72) in Eq. (71) yields:

$$\begin{aligned} u_1^S(x_3 = b) &= \frac{\tau_0}{4\pi\mu} e^{i\omega t} \int_{-\infty}^{\infty} (a_o J_1(\xi a_o) - a_i J_1(\xi a_i)) \frac{N_S(\xi)}{D_S(\xi)} J_1(\xi r) d\xi \\ \therefore u_1^S(x_3 = b) &= \frac{\tau_0}{8\pi\mu} e^{i\omega t} \int_{-\infty}^{\infty} (a_o J_1(\xi a_o) - a_i J_1(\xi a_i)) \frac{N_S(\xi)}{D_S(\xi)} (H_1^{(2)}(\xi r) + H_1^{(1)}(\xi r)) d\xi \end{aligned} \quad (73)$$

where $H_1^{(2)}(\cdot)$ and $H_1^{(1)}(\cdot)$ are the complex Hankel functions of order 1 and the first and second types respectively, defined by:

$$\begin{aligned}
H_1^{(2)}(\xi r) &= J_1(\xi r) - iY_1(\xi r) \\
H_1^{(1)}(\xi r) &= J_1(\xi r) + iY_1(\xi r)
\end{aligned} \tag{74}$$

The following asymptotic expressions hold for the complex Hankel functions:

$$\begin{aligned}
\lim_{\xi r \rightarrow \infty} H_1^{(2)}(\xi r) &= -\sqrt{\frac{1}{\pi \xi r}} (1+i) e^{-i\xi r} \\
\lim_{\xi r \rightarrow \infty} H_1^{(1)}(\xi r) &= -\sqrt{\frac{1}{\pi \xi r}} (1+i) e^{i\xi r}
\end{aligned} \tag{75}$$

From the far-field expressions, one can infer that the Hankel function of the first type corresponds to the inward propagating wave (assuming only the positive roots are retained in the contour for residue evaluation) while the Hankel function of the second type corresponds to the outward propagating wave. Therefore, on physical grounds, only the latter is retained. The integration contour in the complex ξ -plane used is also similar to the one in Fig. 9. The final expression for displacement along the 1-direction then becomes:

$$u_1^S(x_3 = b) = \frac{-i\tau_0}{8\mu} e^{i\omega t} \sum_{\xi^S} (a_o J_1(\xi a_o) - a_i J_1(\xi a_i)) \frac{N_s(\xi)}{D_s'(\xi)} H_1^{(2)}(\xi r) \tag{76}$$

And since the point $(r, 0)$ is generic, by axisymmetry, Eq. (76) also represents the radial displacement u_r at a point at distance r from the center. The expressions for the other displacement components are:

$$u_2^S(x_1 = r, x_2 = 0) = 0 \tag{77}$$

$$u_3^S(x_1 = r, x_2 = 0) = \frac{\tau_0}{8\mu} e^{i\omega t} \sum_{\xi^S} (a_o J_1(\xi^S a_o) - a_i J_1(\xi^S a_i)) \cdot \frac{T_s(\xi^S)}{D_s'(\xi^S)} H_0^{(2)}(\xi^S r) \tag{78}$$

Thus, the angular displacement is zero at all points. The solution for a circular actuator can be recovered simply by letting $a_i = 0$ in the above equations. In practice, the Hankel function is very close to its asymptotic expression after the first four or five spatial wavelengths. Thus, the solution for a circular-crested Lamb-wave field tends to that of a spatially decaying plane Lamb-wave field after a few spatial oscillations.

The harmonic out-of-plane displacement patterns due to excitation of the A_0 Lamb mode at 100 kHz in a 1-mm Aluminum plate by rectangular, circular actuators are shown in Fig. 11. Fig. 11a illustrates how the GW field due to a rectangular actuator tends to a circular crested GW field with angularly dependent amplitude at some distance from the actuator. In the far-field, it looks similar to the GW field due to a circular actuator shown in Fig. 11 (b). In addition, one can appreciate the directionally focused nature of the GW field from 3-3 APTs in Fig. 11 (c). The waves propagate in a roughly collimated beam in a limited sector centered about the fiber direction. This directionality is expected to be refined even more if the electrode pattern of the transducer is designed in a comb-transducer like fashion, as shown in Fig. 11 (d). This can be achieved by designing the clusters of electrode fingers spaced at intervals equal to half the wavelength corresponding to the center frequency of the excited GW. Such a comb transducer also has much better modal selectivity being more tuned to excite a particular wavelength chosen by design.

While in this analysis it was assumed that a single angular frequency ω was excited, it can be used to find the response to any frequency bandwidth-limited signal. This can be accomplished by taking the inverse Fourier transform of the integral of the product of the harmonic response multiplied by the Fourier transform of the excitation signal over the bandwidth. In practice in GW testing, a limited cycle sinusoidal toneburst is used, typically modulated by a Hanning window. If modulated by a Hanning window, the excitation signal is of the form:

$$V_e(t) = \frac{1}{2} \left(1 - \cos \frac{2\pi t}{T}\right) \sin 2\pi f_0 t \quad (79)$$

where $T = n/(2f_0)$ is the duration of the toneburst, which is in practice an integral multiple n of the half-period $1/(2f_0)$. The magnitude of the Fourier transform of this signal, which gives the frequency content of the signal, is:

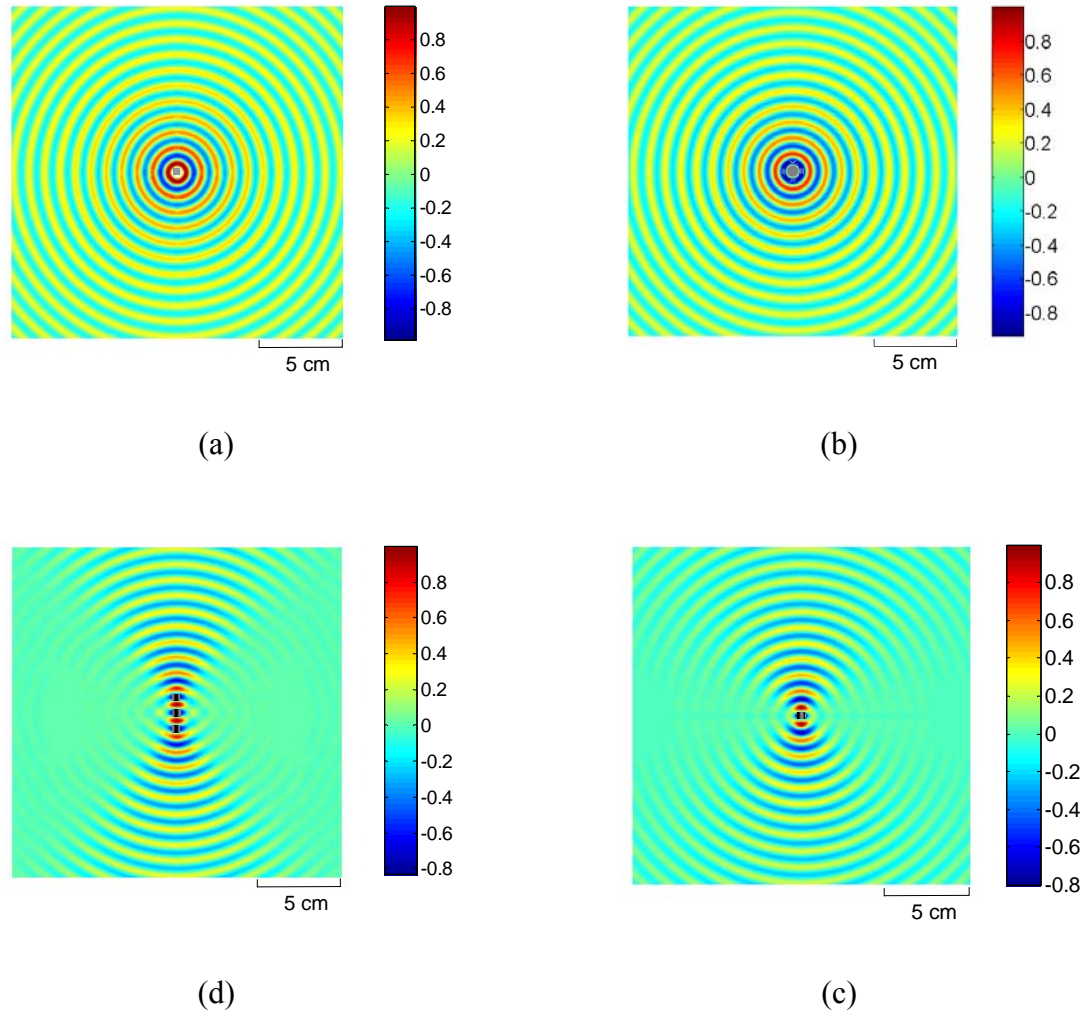


Fig. 11: Harmonic radiation field (normalized scales) for out-of-plane surface displacement (u_3) in a 1-mm thick aluminum alloy ($E = 70$ GPa, $\nu = 0.33$, $\rho = 2700$ kg/m³) plate at 100 kHz, A_0 mode, by a pair of (a) 0.5-cm \times 0.5-cm square piezos (uniformly poled, in gray, center); (b) 0.5-cm diameter circular actuators (in gray, center); (c) 0.5 cm \times 0.5 cm square 3-3 APT (in grey stripes) with the fibers along the vertical direction and (d) 3-element comb array of 0.5 cm \times 0.5 cm square 3-3 APT (in grey stripes) with the fibers along the vertical direction, excited in phase

$$\begin{aligned}
|\bar{V}_e(f)| = \frac{n}{4f_0} & \left| \operatorname{sinc}\left(\frac{\pi n}{f_0}(f - f_0)\right) + (-1)^{n+1} \operatorname{sinc}\left(\frac{\pi n}{f_0}(f + f_0)\right) + \right. \\
& + \frac{1}{2} \left\{ \operatorname{sinc}\left(\frac{\pi n}{f_0}\left(f - \frac{n-1}{n}f_0\right)\right) + (-1)^{n+1} \operatorname{sinc}\left(\frac{\pi n}{f_0}\left(f + \frac{n-1}{n}f_0\right)\right) \right\} + \\
& \left. + \frac{1}{2} \left\{ \operatorname{sinc}\left(\frac{\pi n}{f_0}\left(f - \frac{n+1}{n}f_0\right)\right) + (-1)^{n+1} \operatorname{sinc}\left(\frac{\pi n}{f_0}\left(f + \frac{n+1}{n}f_0\right)\right) \right\} \right| \quad (80)
\end{aligned}$$

where $\operatorname{sinc}(x) \equiv \sin(x)/x$. The first two terms on the right-hand side in (80) correspond to the contribution of the unmodulated sinusoidal toneburst and the last four terms are due to the Hann window. The contribution of the first two terms alone and the contribution of all the terms together on the right-hand side of Eq. (80) are plotted in Fig. 12. The effect of the Hann window modulation is to double the width of the principal lobe while significantly decreasing the side lobes and thus reducing the spread of the frequency spectrum of the toneburst, as shown in Fig. 12. As it can be seen, the peak value is $n/(4f_0)$, while the width of the principal lobe in the frequency domain of the modulated toneburst is $4f_0/n$. These relations can be used to control the frequency bandwidth of the excitation signal in order to reduce signal distortion due to dispersion¹. This will depend on what point on the group-velocity dispersion curve one is operating, which is a function of the product of f_0 and the half-plate thickness b . The response of any system to a finite frequency bandwidth signal can be obtained by taking the inverse Fourier transform of the system harmonic response to a forcing function of unit magnitude, $R_h(f)$, multiplied by the Fourier transform of the excitation signal $\bar{V}_e(f)$ over the frequency bandwidth. For the Hann window modulated sinusoidal toneburst, the frequency spectrum is concentrated mainly in the principal lobe, as seen in Fig. 12. This frequency bandwidth is denoted as Δf . Thus:

$$R(f_0) = \int_{f_0 - \frac{\Delta f}{2}}^{f_0 + \frac{\Delta f}{2}} R_h(f) \bar{V}_e(f) e^{i2\pi ft} df \quad (81)$$

¹ Dispersion is a phenomenon wherein the original signal is distorted as it travels in a medium due to the different wavespeeds of its component frequencies.

This relation is used to find the theoretical magnitude of the response to a modulated sinusoidal toneburst excitation signal employing the developed formulations for the harmonic response.

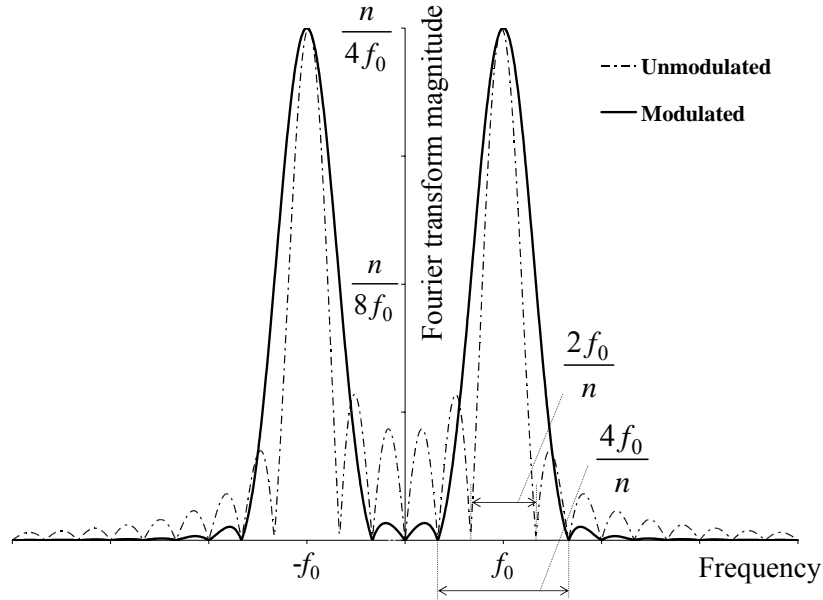


Fig. 12: Frequency content of unmodulated and modulated (Hann window) sinusoidal tonebursts

II.5 Numerical Verification for Circular Piezos on Plates

In order to verify the result of the formulation proposed for isotropic plates, FEM simulations were conducted using ABAQUS [205]. An infinite isotropic (aluminum alloy) plate with a 0.9-cm radius piezo-actuator placed at the origin of the coordinate system was modeled using a mesh of axisymmetric 4-noded continuum finite elements up to a boundary at the radial position $r = 15$ cm. These were radially followed by infinite axisymmetric elements placed at the boundary, which are used to minimize the reflected waves returning from the boundary towards the origin. The FEM model represented only half the plate thickness, and then a through-thickness symmetry or anti-symmetry condition was applied to the mid-thickness nodes to model symmetric or anti-symmetric modes, respectively. The actuator was modeled as causing a surface radial shear force at

= 0.9 cm, just as in the proposed formulation. A 3.5-cycle Hanning window modulated sinusoidal toneburst excitation signal applied to the actuator was modeled by specifying the corresponding waveform for the time variation of the shear force applied at $r = 0.9$ cm in the input file. The amplitude of radial displacement at $r = 5$ cm was recorded for a range of values of the toneburst center frequency-plate thickness product. The mesh density and the time step were chosen to be sufficiently small to resolve the smallest wavelength and capture the highest frequency response, respectively (about 20 spatial points per wavelength in the FEM mesh and 20 time steps per inverse frequency). Two sets of simulations were performed: for symmetric and for anti-symmetric modes. These were compared with the analytical predictions by the proposed formulation in Section II.4.C (while considering the frequency bandwidth excited). The results are shown in Fig. 13. The FEM results compare very well with the theoretical predictions for both the S_0 and A_0 modes, providing verification for the proposed analytical formulation.

II.6 Piezo-sensor Response Derivation

In this section, the response of a uniformly poled surface-bonded piezo-sensor operating in the 3-1 mode on a plate in a GW field and connected to a measuring device such as an oscilloscope is derived. The relation between the electric field E_i , displacement D_i and internal stress in the piezoelectric element is [206]:

$$E_i = -g_{ikl}\sigma_{kl} + \beta_{ik}^\sigma D_k \quad (82)$$

where g_{ikl} is a matrix of piezoelectric constants for the piezoelectric material, and β_{ik}^σ are the impermeability constants at constant stress of the piezoelectric material. Since the impedance of the oscilloscope is usually very high ($\sim 1 \text{ M}\Omega$), it can be assumed that there is no electric current flowing between the sensor and the measurement device. Therefore, $D_3 = 0$. Furthermore, if the sensor is thin enough, $\sigma_{33} \approx 0$. Thus, one obtains:

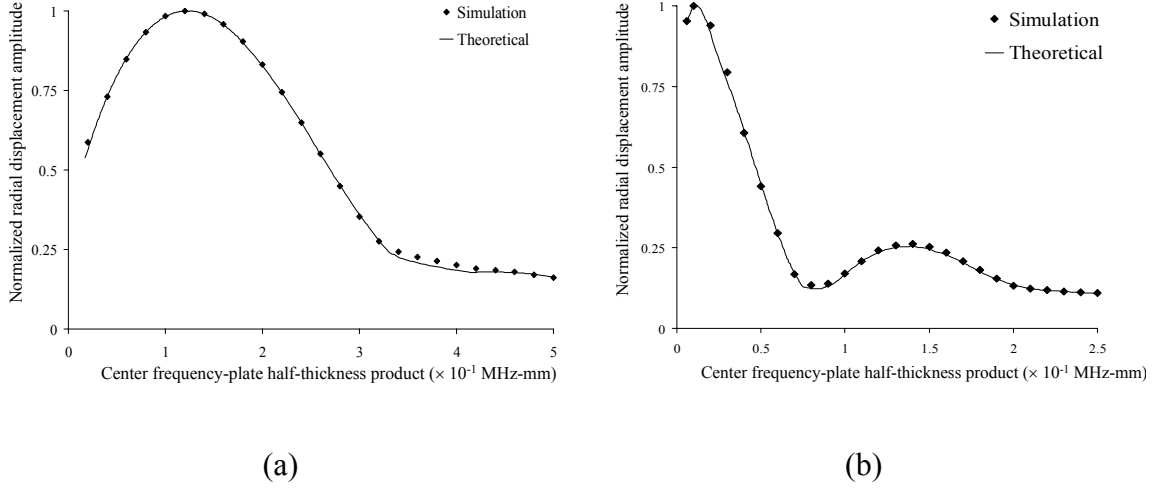


Fig. 13: Comparison of theoretical and FEM simulation results for the normalized radial displacement at $r = 5$ cm at various frequencies for: (a) S_0 mode and (b) A_0 mode

$$E_3 = -g_{31}(\sigma_{ii}) = \frac{-g_{31}Y_c^{11}}{1-\nu_c}(\varepsilon_{ii}) \quad (83)$$

where Y_c^{11} is the in-plane Young's modulus of the sensor material, ν_c is the Poisson ratio of the piezoelectric material, and ε_{ii} is the sum of the in-plane extensional surface strains. Note that the contracted notation has been used for the g -constant indices from Eq. (83) onwards. Here it is assumed that the twisting shear stresses are negligible. The voltage response of the piezo-sensor therefore is:

$$V_c = \frac{1}{S_c} \int_{S_c} -E_3 \cdot h_c dS = \frac{Y_c^{11} g_{31} h_c}{S_c (1-\nu_c)} \int_{S_c} \varepsilon_{ii} dS \quad (84)$$

where S_c is the surface area of the sensor and h_c is the sensor thickness. This assumes the electric field is uniform through the sensor thickness (satisfied for small thickness piezos). An important assumption made here is that the sensor is infinitely compliant and does not disturb the GW field. This is reasonably satisfied if the product of the sensor's thickness and Young's modulus is small compared to that of the plate onto which it is surface-bonded and it is of small size. For APTs used as sensors, a similar analysis holds,

except that they are only sensitive to extensional stress along their fiber direction. If the Poisson effect is ignored, they are consequently insensitive to strains normal to the fiber direction.

II.6.A Piezo-sensor Response in GW Fields due to Circular Piezos

Consider the response to harmonic excitation of a uniformly poled rectangular piezo-sensor of width $2s_\theta$ in a GW field (excited by a circular piezo with $a_i = 0$ and $a_o = a$) surface-bonded between $r = r_c$ and $r = r_c + 2s_r$. In this case, Eq. (84) becomes:

$$V_c = \frac{Y_c^{11} h_c g_{31}}{S_c (1 - \nu_c)} \iint_{S_c} (\varepsilon_{rr} + \varepsilon_{\theta\theta}) r dr d\theta = \frac{Y_c^{11} h_c g_{31}}{S_c (1 - \nu_c)} \iint_{S_c} \left(\frac{du_r}{dr} + \frac{u_r}{r} \right) r dr d\theta \quad (85)$$

Suppose that the length of the piezo-sensor $2s_r$ is small enough so that $\int_\theta r d\theta \approx 2s_\theta$ over the radial length of the sensor. Using this and Eqs. (76) and (85), one obtains (for symmetric modes):

$$V_c = \frac{\tau_0 a}{8\mu} \frac{Y_c^{11} h_c g_{31}}{2s_r (1 - \nu_c)} e^{i\omega t} \sum_{\xi^S} J_1(\xi^S a) \frac{N_S(\xi^S)}{D'_S(\xi^S)} \int_{r_c}^{r_c + 2s_r} \xi^S H_0^{(2)}(\xi^S r) dr \quad (86)$$

II.6.B Piezo-sensor Response in GW Fields due to Rectangular Piezos

Next, consider the response to harmonic excitation of a uniformly poled rectangular piezo-sensor placed between the coordinates $(x_c - s_1, y_c - s_2)$ and $(x_c + s_1, y_c + s_2)$ with its edges along the x_1 - and x_2 - axes in the GW field due to a rectangular piezo-actuator described in Section II.4.A. In this case, Eq. (84) becomes:

$$V_c = \frac{Y_c^{11} h_c g_{31}}{4s_1 s_2 (1 - \nu_c)} \iint_{S_c} (\varepsilon_{11} + \varepsilon_{22}) dS_c = \frac{Y_c^{11} h_c g_{31}}{4s_1 s_2 (1 - \nu_c)} \int_{x_c - s_1}^{x_c + s_1} \int_{y_c - s_2}^{y_c + s_2} \left(\frac{du_1}{dx_1} + \frac{du_2}{dx_2} \right) dx_1 dx_2 \quad (87)$$

Using the asymptotic displacement expressions (from the method of stationary phase), this leads to the following expression for sensor response in the far-field:

$$V_c^S = \sum_{\xi^S} \left(\frac{-i\tau_0 Y_c^{11} h_c g_{31}}{\mu s_1 s_2 (1-\nu_c)} \frac{N_s(\xi^S) e^{i\omega t}}{(\xi^S)^2 D'_s(\xi^S)} \sqrt{\frac{2\pi}{\xi^S r}} \times \frac{\sin(\xi^S a_1 \cos \theta) \sin(\xi^S a_2 \sin \theta) \sin(\xi^S s_1 \cos \theta) \sin(\xi^S s_2 \sin \theta)}{\sin^2 2\theta} e^{-i\xi^S r + \pi/4} \right) \quad (88)$$

This expression can be evaluated for $\theta = 0$ using L'Hospital's rule to give:

$$V_c^S(\theta = 0) = \sum_{\xi^S} \frac{-i\tau_0 Y_c^{11} h_c g_{31}}{\mu s_1 (1-\nu_c)} \frac{N_s(\xi^S)}{D'_s(\xi^S)} \sqrt{\frac{2\pi}{\xi^S r}} \frac{a_2 \sin(\xi^S a_1) \sin(\xi^S s_1)}{4} e^{-i(\xi^S r - \omega t) + \pi/4} \quad (89)$$

II.7 Setups for Experimental Validation and Results

To examine the validity of the theoretical expressions for the formulations developed above, a series of experiments were done. Each of these involved aluminum alloy specimens with three surface-bonded transducers. Two of these were at the center on each surface of the structure and used as actuators while the third was at some distance from the center and used as a GW sensor. Experiments were conducted to examine the correlation between theoretical and experimental frequency response functions. The first transmitted pulse sensed by a surface-bonded MFC sensor at some distance from the center was monitored. Two sets of readings were taken. In the first set, the actuators were excited in phase to excite symmetric modes while in the second they were excited out of phase in order to excite the anti-symmetric modes. These actuators were powered with a 3.5-cycle Hanning-windowed sinusoidal toneburst over a range of center frequencies. The highest excitation frequency was well below the cut-off frequency of the first symmetric Lamb mode in the first set. In the second set, it was well below the cut-off frequency of the first anti-symmetric Lamb mode and the first anti-symmetric SH-mode. Thus, the S_0 mode was predominantly excited in the first set while the A_0 mode was predominantly excited in the second set. Due to the piezo-actuator's capacitive behavior,

its impedance varies with frequency, and so the actual voltage drop across it varies with frequency. To account for this, the voltage amplitude across the actuator terminals was also recorded for each reading and the sensor response amplitude and error estimate were compensated accordingly. To obtain the theoretical sensor response to a Hanning-windowed toneburst at a given frequency, one needs to evaluate the inverse time domain Fourier transform over the excited frequency spectrum. The theoretical and experimental signal amplitudes, normalized by the peak amplitude over the tested frequency range, are compared over a range of frequencies for the S_0 and A_0 modes.

II.7.A Beam Experiment for Frequency Response Function of MFCs

A 1-mm thick aluminum alloy (Young's modulus $Y_{Al} = 70$ GPa, Poisson's ratio $\nu = 0.33$, density $\rho = 2700$ kg/m³) strip clamped at both ends was instrumented with three MFCs, each 0.2 mm thick, as illustrated in Fig. 14. The actuators were excited with a 5 V peak-to-peak signal and the average amplitude of the sensor response over 16 samples was noted to reduce the noise levels. To predict the theoretical sensor response trend versus frequency, one needs to use the value $2a = 3.2$ cm (which is the length of the active area of the MFC) in the expressions for beams. Only the contributions from the S_0 mode were included for the first set. Similarly, only contributions of the A_0 mode were considered for the second set. The harmonic sensor response, found using Eq. (84) should also be integrated over the frequency bandwidth of excitation for calculating the response to a 3.5-cycle sinusoidal toneburst signal. The theoretical (also referred to as analytical) and experimental results are compared in Fig. 15. Both curves are normalized to the peak response amplitude over the considered frequency range.

II.7.B Plate Experiments for Frequency Response Functions of Piezos and MFCs

A 600 mm \times 600 mm \times 3.1 mm thick aluminum alloy plate (Young's modulus $Y_{Al} = 70.28$ GPa, Poisson's ratio $\nu = 0.33$, density $\rho = 2684$ kg/m³) was instrumented with a pair of 6.5-mm radius, 0.23-mm thick PZT-5H circular piezo actuators at the center of the

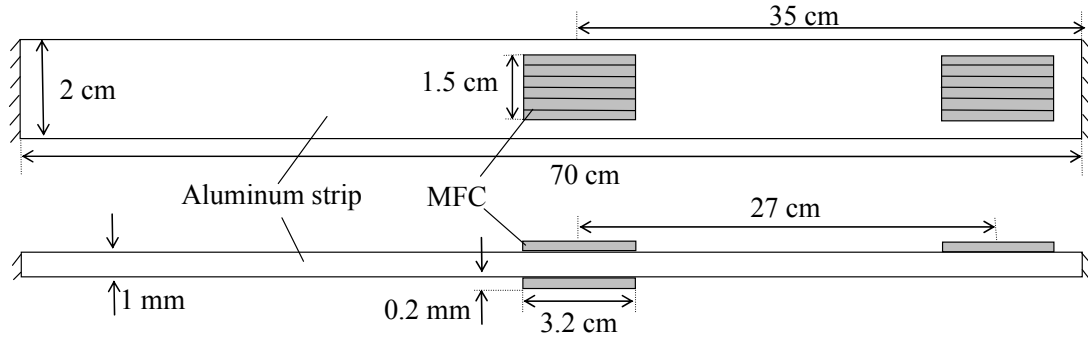


Fig. 14: Illustration of thin aluminum strip instrumented with MFCs

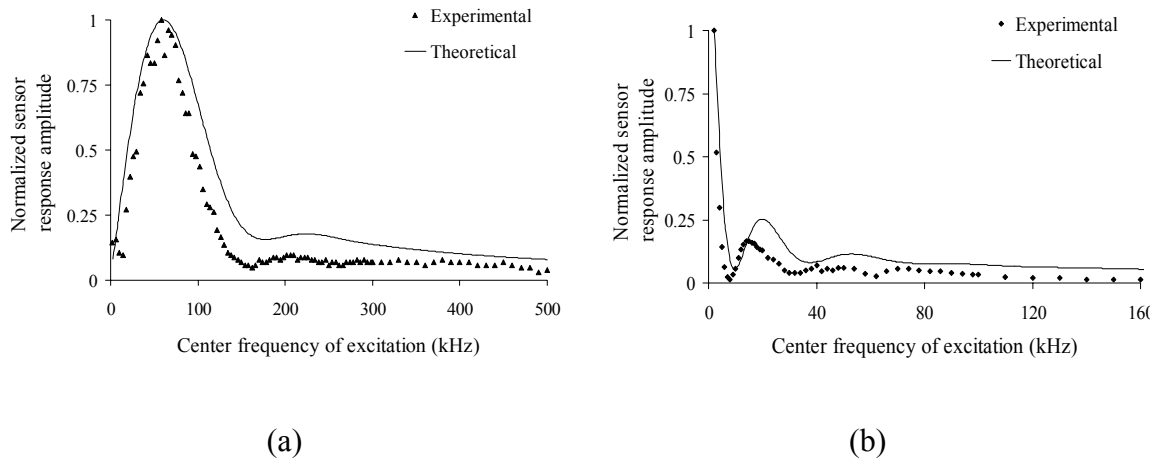


Fig. 15: Theoretical and experimental normalized sensor response over various frequencies in the beam experiment for: (a) S_0 mode and (b) A_0 mode

plate on both free surfaces. A 10 mm (radial length) \times 5 mm (width) \times 0.3 mm (thickness) PZT-5A rectangular piezo-sensor was surface-bonded at a radial distance $r_c = 50$ mm from the center of the plate, as illustrated in Fig. 16 (a). Similar specimens were built with surface-bonded rectangular piezos (Fig. 16 (b)) and MFCs (Fig. 17). The setup was designed such that reflections from the boundaries would not interfere with the first transmitted pulse received by the sensor over the frequency range tested, i.e., the infinite plate assumption holds. As before, separate tests were done for symmetric and anti-symmetric modes. These actuators were fed with a 3.5-cycle 9 V (peak-to-peak) Hanning windowed toneburst. For each reading, the excitation signal was repeated at a frequency

of 1 Hz (this was small enough so that there was no interference between successive repetitions) and the averaged signal over 64 samples was used to reduce the noise levels in the signal. The theoretical and experimental signal amplitudes, normalized by the peak amplitude over the tested frequency range, are compared over a range of frequencies for the S_0 and A_0 modes in Fig. 18. The error bars based on the standard deviation of the amplitudes over the 64 samples (capturing 99.73% of the data points), and normalized by the peak amplitude are also shown in Fig. 18. The time-domain experimental and theoretical signals, also normalized to their respective peak amplitudes over the frequency range, are compared in Fig. 19 for center frequency each in the S_0 and A_0 modes. The normalized theoretical and experimental amplitudes along with their associated error bars are compared for the rectangular actuator experiment in Fig. 20 while the comparison of the normalized time domain signals is shown in Fig. 21 for one center frequency in each mode. The corresponding frequency response curves for the rectangular MFC experiment are shown in Fig. 22 and two time domain signals from this experiment are shown in Fig. 23. The peak-to-peak excitation voltage for the MFC experiment was amplified using a Krohn-Hite 7500 amplifier to 60 V, since the sensor response was barely above the noise floor without using it, possibly due to the very small actuator sizes.

II.7.C Laser Vibrometer Experiment

To test the theoretically-predicted focusing capability of the MFC along its fiber direction in plate structures, an experiment was conducted using a Polytec scanning laser vibrometer system that employed a Polytec OFV-303 sensor head and OFV-3001-S controller. A 1-mm thick aluminum plate specimen with a pair of MFC actuators at the center (of dimensions $2a_1 = 1.5$ cm, $2a_2 = 2.8$ cm) was used. The actuators were excited with a 18 V peak-to-peak 3.5-cycle Hanning windowed sinusoidal toneburst signal. However, for this experiment, the center frequency was kept fixed at 30 kHz and the actuators were excited out-of-phase to excite the A_0 mode predominantly. The laser vibrometer measured out-of-plane surface velocity signals at a chosen point, and was equipped with a computer-controlled scanning head (Polytec OFV-040) so that the scan point could be swept with precision over the plate area. Signals were recorded over a grid

spanning a quarter section of the plate surface up to 20 cm from each symmetry axis, since the field is expected to be symmetrical about the two axes in the plane of the plate. The grid spacing was 0.6 cm along the fiber direction (which is a third of the A_0 mode wavelength at 30 kHz). Along the other direction in the plane of the plate near the

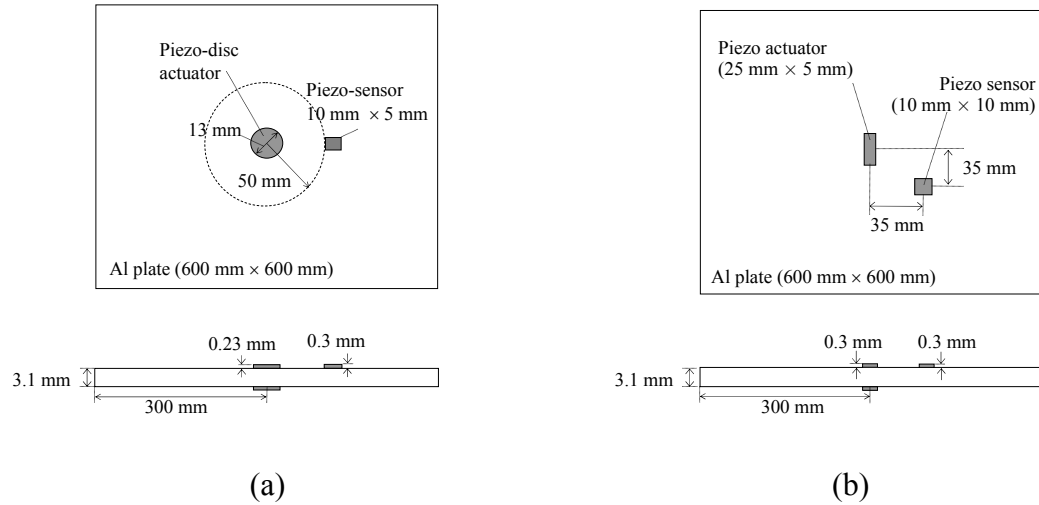


Fig. 16: Experimental setups for frequency response validation of: (a) circular actuator model and (b) rectangular actuator model

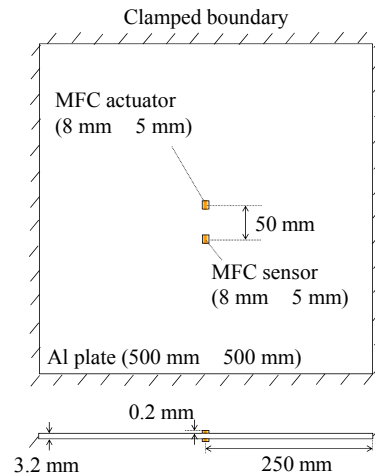


Fig. 17: Experimental setup for frequency response validation of model for surface-bonded APTs on plates

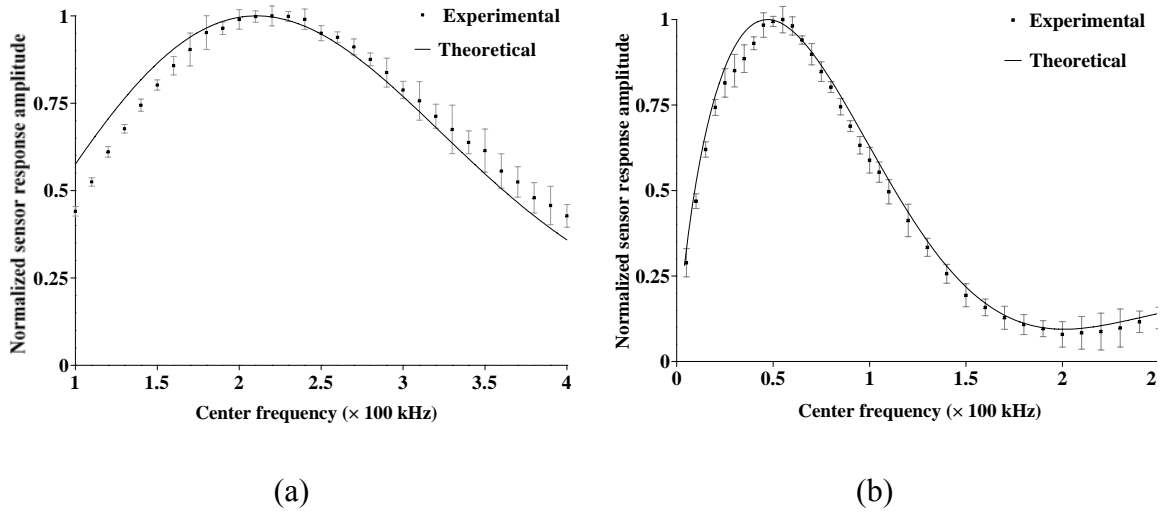


Fig. 18: Comparison between experimental and theoretical sensor response amplitudes in the circular actuator experiment at different center frequencies for: (a) S_0 mode and (b) A_0 mode

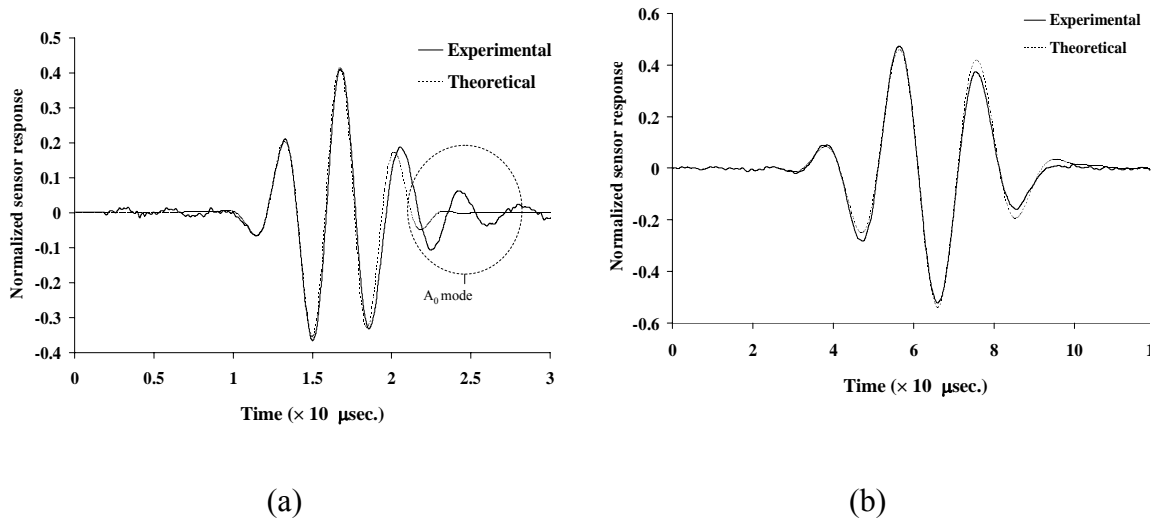
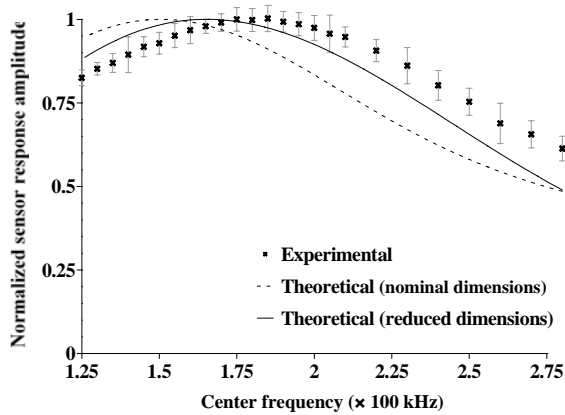
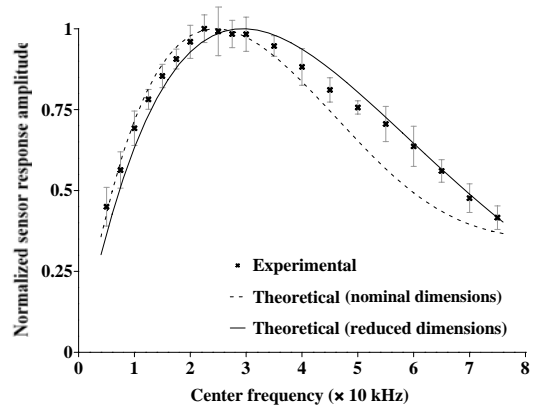


Fig. 19: Comparison between experimental and theoretical sensor response time domain signals for the circular actuator experiment: (a) S_0 mode for center frequency 300 kHz and (b) A_0 mode for center frequency 50 kHz

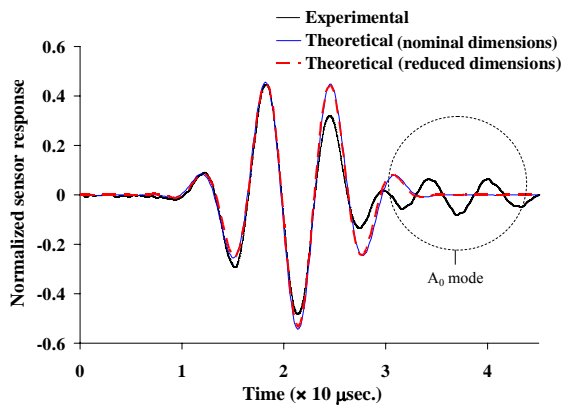


(a)

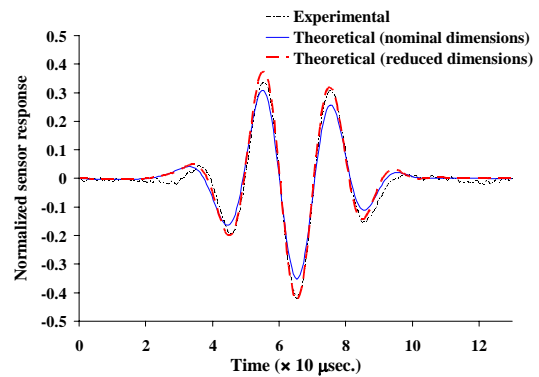


(b)

Fig. 20: Comparison between experimental and theoretical sensor response amplitudes in the rectangular actuator experiment at different center frequencies for: (a) S_0 mode and (b) A_0 mode

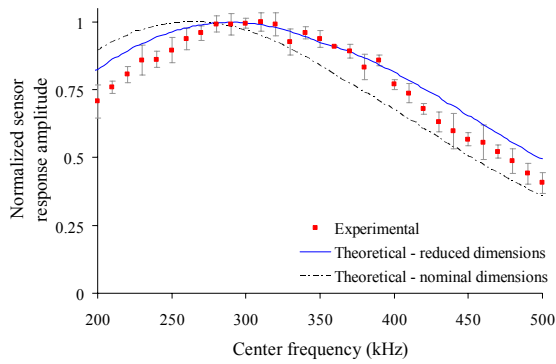


(a)

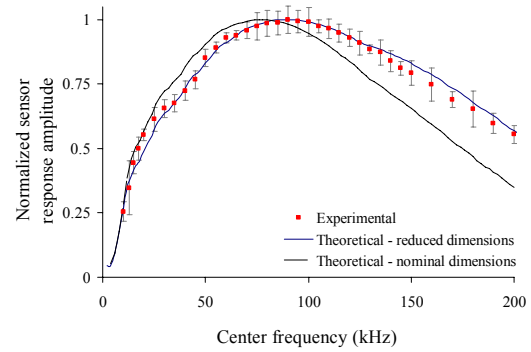


(b)

Fig. 21: Comparison between experimental and theoretical sensor response time domain signals for the circular actuator experiment: (a) S_0 mode for center frequency 150 kHz and (b) A_0 mode for center frequency 50 kHz

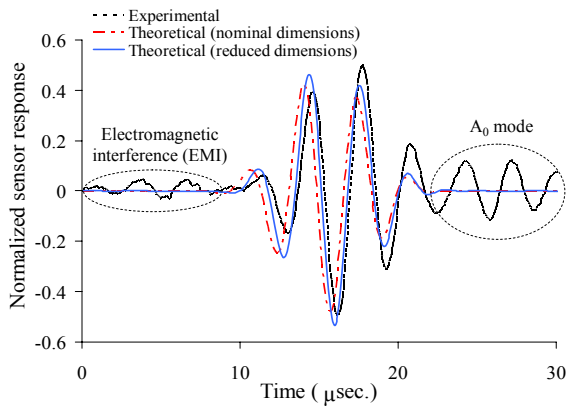


(a)

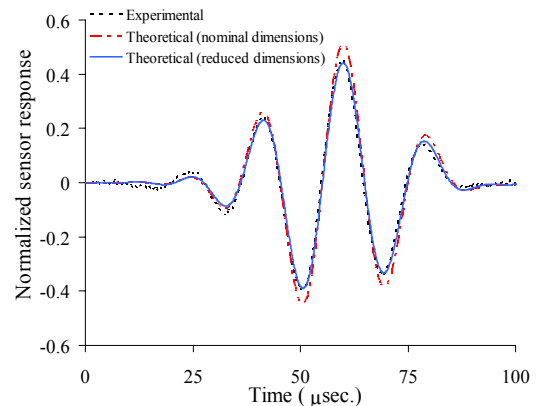


(b)

Fig. 22: Comparison between experimental and theoretical sensor response amplitudes in the rectangular MFC experiment at different center frequencies for: (a) S_0 mode and (b) A_0 mode



(a)



(b)

Fig. 23: Comparison between experimental and theoretical sensor response time domain signals for the frequency response experiment with rectangular MFCs: (a) S_0 mode for center frequency 300 kHz and (b) A_0 mode for center frequency 50 kHz

actuator, the spacing was 0.5 cm for the first four columns of the grid starting from the symmetry axis. Beyond this region, the spacing was 1 cm. In addition, as in the previous section, the excitation signal was repeated 64 times for each point at a frequency of 1 Hz and the averaged signal was recorded. Furthermore, wavelet denoising using the discrete

Meyer wavelet was employed to cleanse the signals. The experimentally obtained surface plots at three particular time instants over the quarter section of the plate are shown in Fig. 24 (normalized to the peak value of surface velocity over the plate in the time span up to 200 μ s). The surface plots for the same GW fields obtained using the theoretical model developed in this thesis are shown adjacent to these in Fig. 24. These are also normalized to the theoretically predicted peak velocity over the plate area in the same time span. These plots were generated assuming pure A_0 mode excitation. SH-modes were not considered since they do not cause out-of-plane displacements.

II.8 Discussion and Sources of Error

II.8.A Frequency Response Function Experiments

In the beam experiment, for the symmetric mode, the peak response frequency is well captured by the model. In addition, the qualitative trend of the sensor response with varying frequency is also captured. Similar conclusions hold for the anti-symmetric mode. In this case, however, the peak response frequency is the lowest frequency of testing. The qualitative prediction of the trend of the response is good, albeit with some marginal quantitative error in the location and relative magnitude of peaks. The frequency at which the second peak occurs is slightly over-estimated for both modes. This error is possibly attributable to the use of uncoupled transducer-substrate dynamics models in this thesis. Due to the relatively larger transducer to substrate thickness ratio (in this case 0.2 mm to 1 mm), in order to obtain better accuracy in theoretical predictions, models that account for the coupled dynamics will be needed. Some incipient efforts in this direction can be found in Refs. [76] and [79].

In the plate frequency response experiment, there is qualitative agreement in the trend between the theoretical and experimental results. There is some error observed in the prediction of the peak frequency for the theoretical results in the experiments, and they are particularly evident in the results for the rectangular piezo and MFC (for the nominal transducer dimensions). However, the experimental results are in good agreement with the theoretical curve for reduced transducer dimensions (by 20% for the

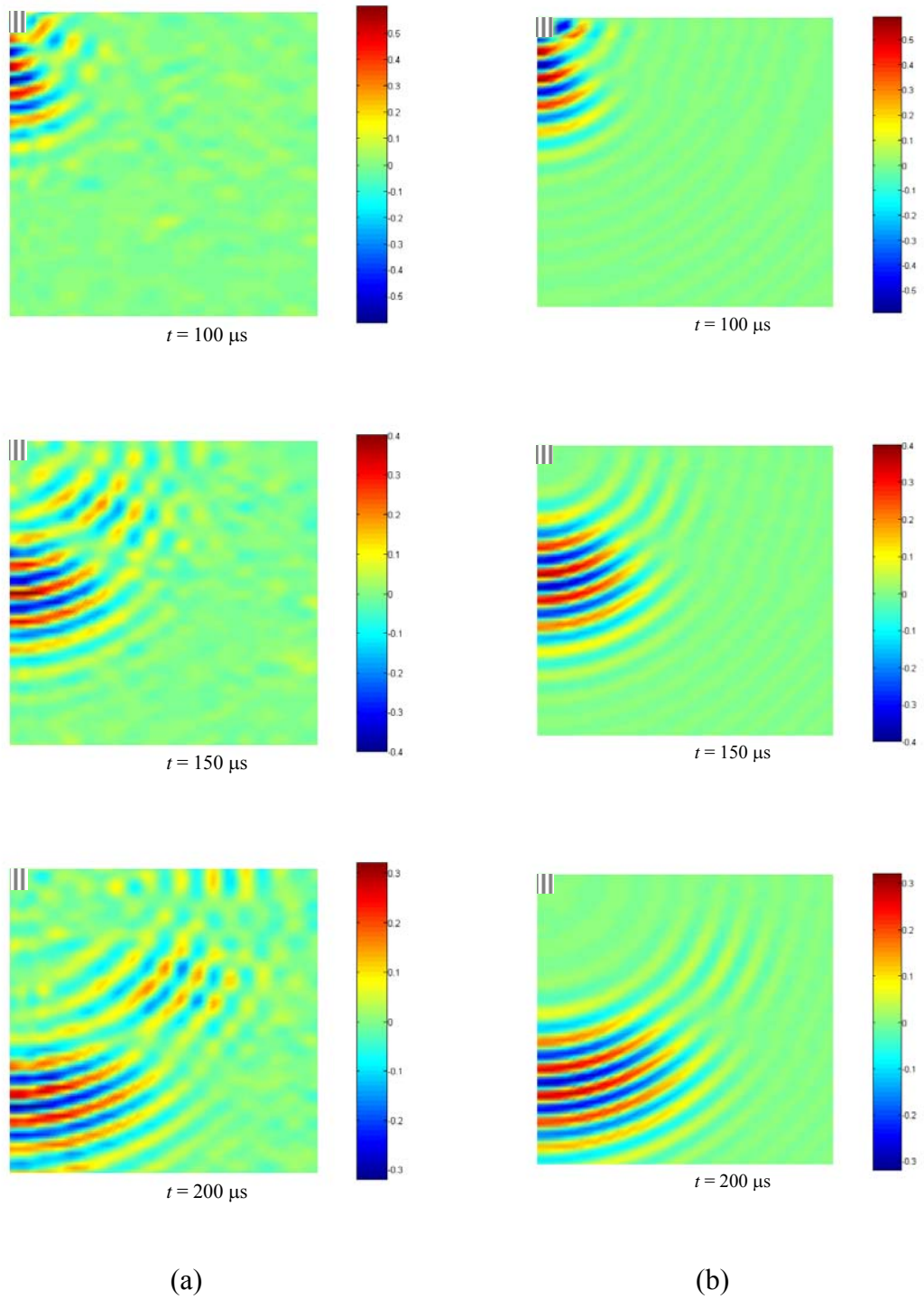


Fig. 24: Normalized surface plots showing out-of-plane velocity signals over a quarter section of the plate spanning $20 \text{ cm} \times 20 \text{ cm}$. The MFC is at the upper left corner (the striped rectangle), and its fibers along the vertical: (a) Experimental plots obtained using laser vibrometry and (b) theoretical plots obtained using the developed model for APTs

rectangular piezo and 13% along the fiber direction for the MFCs). This shift can be attributed to the shear lag phenomenon, which relates to the assumption made in the derivation pertaining to force transfer only along the free edges of the piezo. As mentioned earlier, this “pin-force” model was proposed by Crawley and de Luis [85] for the case of a pair of piezo-actuators surface bonded on opposite beam surfaces and actuated quasi-statically. Due to the finite stiffness of the actuator relative to the plate and imperfect bonding between the actuator and plate, the force transfer between the piezo and the plate occurs over a finite length close to the edge of the piezo. Therefore, the effective dimension in the models derived may be smaller than the actual physical dimension. The circular piezo was thinner (0.23 mm) and more flexible ($E = 59$ GPa) compared to the rectangular piezo (0.3 mm and 63 GPa), which possibly explains why this effect was less noticeable in the former experiment. While the MFC was even thinner (0.2 mm) and more flexible ($E = 30.34$ GPa), it is suspected that the presence of the kapton electrode layer may have caused the shear lag effect to be greater than expected. In addition, in the MFC experiment beyond about 375 kHz, the amplifier caused some noticeable signal distortion in the amplified excitation signal which may have caused some of the inconsistency at higher frequencies in the comparison between the theoretical and experimental results for that set of results.

Another source of error comes from the impossibility of exciting a pure mode. While there were two actuators bonded on either free surface at the center of the plate, there would always be some mismatch in their piezoelectric properties due to manufacturing imperfections. In addition, due to the finite thickness of the sensor, when the wave packet is incident on it a small portion of the incident GW mode is converted to other modes due to scattering. Because of this, it was verified that some excitation of antisymmetric modes existed in the symmetric mode experiments and vice versa. An effort was made to ensure that the time window over which the peak was recorded (using the theoretical time-domain waveforms) was for the relevant mode of interest. In spite of this, the results were significantly affected by the overlapping of the two modes over certain frequency ranges, which were avoided.

The theoretical models all assume infinite substrates. This is accounted for in the experiments by only examining the first transmitted pulse received by the sensor and ignoring boundary reflections. In the beam experiment, due to the proximity of the sensor to the boundary, some of the low frequency data for the first transmitted pulse is slightly compromised by reflections from the boundary. At lower frequencies, due to the larger time-spread of the excitation signal, the reflection tends to overlap with the first transmitted pulse. This is more significant for the S_0 mode due to the higher wavespeeds at low frequency. These effects were significantly reduced in the plate experiments by bonding the sensor closer to the actuators.

II.8.B Laser Vibrometer Experiment

The experimental surface out-of-plane velocity images obtained for the plate in Fig. 24 (a) are also in good agreement with their theoretical counterparts. The theoretically predicted focused nature of the GW field along the MFC fiber direction is well captured in the experiment. There is also qualitative agreement in the patterns of the weak radiation along the other directions. However, the amplitude for those is slightly stronger in the experimental plots. In addition, the tendency of the GW field towards a directionally dependent circular crested field in the far field, which was also predicted theoretically, is evident in the experiment. There is some noise in the experimental plots, despite the use of wavelet denoising. This is because the plate, in spite of lightly sanding its surface, was a poor diffuse reflector in some areas when the laser was incident at an angle. At such points, this was partially compensated by adjusting the focus of the laser's lens. Another minor source of error in correlation is the presence of a MFC sensor of size $0.9 \times 0.5 \text{ cm}^2$, 5 cm from the center. This may have caused weak scattering of the GW field due to the slight change in local stiffness and mass induced by it.

Despite these sources of error, overall there is good correlation between the experimental and theoretical results, thus providing validation for the derived models describing GW excitation as well as the sensor response equation for surface-bonded piezo-sensors.

II.9 Optimal Transducer Dimensions

This section discusses the use of the above analytical models for optimizing transducer dimensions in various configurations.

II.9.A Circular Piezo-actuators on Plates

To optimize the actuator size for maximum sensor response to harmonic excitation, everything in Eq. (86) is kept fixed except a . Then:

$$|V_c| \propto |aJ_1(\xi a)| \quad (90)$$

The right-hand side of Eq. (90) is an oscillating function of a with a monotonically increasing amplitude envelope as seen in Fig. 25. The local maxima of $|V_c|$ are attained at the corresponding local extrema of $J_1(\xi a)$. Thus, there is no optimum value for maximizing sensor response as such, and by choosing higher values of a that yield local extrema, one can in principle keep increasing the magnitude of sensor response to harmonic excitation. Notice that between any two successive peaks of the response function there is a value for the actuator radius for which the response to harmonic excitation is zero. This corresponds to a zero of the Bessel function. Although these zero “nodes” caused by certain actuator radii are presented for simple harmonic excitation, they have also a direct impact on a toneburst signal. One may take a toneburst center frequency as responsible for most of the energy being delivered by the actuator. If the product of the actuator radius and the toneburst center frequency coincides with a node as shown in Fig. 25, then most of the signal will be attenuated.

Since the piezo-actuator has some capacitance, the harmonic reactive power circulated every cycle P_a^r is:

$$P_a^r = 2\pi f C_a V^2 = \frac{2\pi f k_a \varepsilon_0 \pi a^2 V_a^2}{h_a} \propto a^2 \quad (91)$$

where V_a is the actuation voltage supplied to the piezo-actuator, f is the frequency of harmonic excitation and the rest of the notation is analogous to that used for the piezo-sensor. That is, the power circulation increases as the square of the actuator radius if all other parameters are constant. Note that the dependence of the capacitance on driving frequency and actuation voltage magnitude has not been considered (see [207], for example). However these only tend to further increase the capacitance, and thereby the reactive power circulation. This power being reactive is not dissipated, but is merely used for charging the piezo in the positive half-cycle and is gained back when the capacitor is discharged in the negative half-cycle. The power supply to drive the actuators will define how much of this energy can be recycled.

In addition to this, the power source must supply the energy that is converted into acoustic energy in the excited GW field. This is given by the expression:

$$P_a^d = \int_{S_o} \hat{n}_i (u_i \sigma_{ij}) dS \quad (92)$$

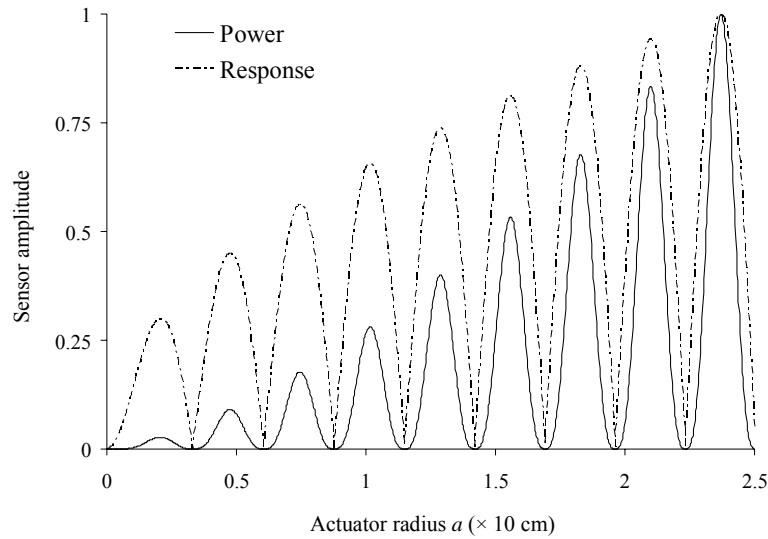


Fig. 25: Amplitude variation of sensor response and power drawn to excite the GW field due to change in actuator radius for a 1-mm thick Aluminum plate driven harmonically in the S_0 mode at 100 kHz

where S_0 is the cylindrical surface of thickness $2b$ and radius a centered at the origin, i.e., that encapsulates the region of the plate under the actuator. On substituting the expressions for plate displacement and stress and evaluating the integral, an intricate expression is obtained involving the plate material properties, plate thickness, the actuator radius, and the excitation frequency/wavenumber. Intuitively, however, one expects that this expression will also follow an oscillating trend with monotonically increasing amplitude envelope as a function of actuator radius. This is confirmed in Fig. 25, where the peaks of the expression coincide with the peaks of the sensor response curve. Evidently, the increased sensor response by actuator size tailoring is at the cost of increased power consumption by the actuator.

In summary, the choice of actuator length for the largest local maximum is limited by the power available to drive the actuator. Moreover, the area occupied by the actuator on the structure as well as the desired area covered by the actuator-sensor pair signal might be concerns that ultimately decide the actuator size.

II.9.B Rectangular Actuators

In the case of a surface-bonded rectangular piezo-actuator on a plate, due to the highly direction-dependent GW field, this will depend on the angular location of the piezo-sensor/region of interest for GW SHM on the plate relative to the piezo-actuator. For example, consider the case $\theta = 0$. If all parameters except a_1 and a_2 are kept constant in Eq. (89), one obtains:

$$|V_c^s| \propto |a_2 \sin(\xi^s a_1)| \quad (93)$$

Thus, to maximize the harmonic sensor response of a piezo-sensor in the direction $\theta = 0$, a_2 should be as large as possible. For a_1 , any of the lengths given by the relation:

$$2a_1 = (n + \frac{1}{2}) \frac{2\pi}{\xi^s}, \quad n = 0, 1, 2, 3, \dots \quad (94)$$

are equally optimal values in order to maximize sensor response. By an analysis similar to the one in Section

II.9.A, it can be shown that the power requirement increases for larger actuator dimensions. Thus, in order to minimize power consumption and the area occupied by the actuator on the structure, the value of a_1 is defined by Eq. (94) with $n = 0$. The choice of a_2 will also be limited by similar concerns. A similar analysis holds for rectangular APTs bonded on beams and plates.

II.9.C Piezo-sensors

Two particular configurations are studied for optimizing piezo sensor dimensions. First, consider the Eq. (86) for the harmonic sensor response of a piezo in the GW field due to a circular piezo-actuator. Assuming all parameters (except the sensor length $2s_r$) to be constant:

$$|V_c| \propto \left| \int_{r_c}^{r_c+2s_r} \frac{H_o^{(2)}(\xi r)}{2s_r} dr \right| \leq \int_{r_c}^{r_c+2s_r} \left| \frac{H_0^{(2)}(\xi r)}{2s_r} \right| dr \quad (95)$$

This inequality holds due to the oscillatory nature of the Hankel function. Since $|H_0^{(2)}(\xi r)|$ is a monotonically decreasing function of r :

$$|H_0^{(2)}(\xi(r_c + 2s_r))| \leq \int_{r_c}^{r_c+2s_r} \left| \frac{H_0^{(2)}(\xi r)}{2s_r} \right| dr \leq |H_0^{(2)}(\xi r_c)| \quad (96)$$

where the equality holds only at the limit of $2s_r \rightarrow 0$. Thus, the maximum sensor response is attained for $2s_r = 0$, and it decreases with increasing s_r . This implies that the sensor should be as small as possible to maximize $|V_c|$ in the case of a circular-crested GW field. A smaller sensor size would also interfere less with the GW field and is favorable from the point of view of SHM system design, since the transducers should ideally occupy minimum structural area. To validate this idea, the same setup as described in Section II.7.B was used. However this time, a 20 mm (radial length) \times 5 mm (width) \times 0.3 mm (thickness) sensor was surface-bonded at a distance of radius 50 mm from the plate center so that $r_c = 50$ mm, as before. The sensor's radial length $2s_r$ was reduced in steps of 0.5 cm by cutting the sensor on the plate with a diamond-point knife and examining the response of its remaining part. For each length, an experiment along the lines of the

earlier ones was conducted for the S_0 mode, i.e., the sensor response amplitudes were measured over 64 samples for each center frequency over a range of center frequencies. The comparison between the theoretical and experimental results is shown in Fig. 26 (both data sets are normalized to the peak value for the curve at $2s_r = 2$ cm). The theoretical curves were derived assuming uniform bond strength over all of the original piezo sensor's area. As predicted by the theoretical model, the sensor response amplitude increases with decreasing sensor length. The comparison between the theory and experimental results is good again, although the experimental curve is slightly shifted ahead of the theoretical curve along the center frequency axis due to shear lag. The comparison between the relative amplitudes is quite accurate with the exception of the last set for $2s_r = 0.5$ cm, which can be possibly attributed to weaker bond strength closer to the edge of the piezo-sensor.

Now consider Eq. (88) for the far-field harmonic sensor response of a piezo in the GW field due to a rectangular piezo-actuator. If all parameters except s_1 and s_2 are kept constant:

$$|V_c^s| \propto \left| \frac{\sin(\xi^s s_1 \cos \gamma)}{(\xi^s s_1 \cos \gamma)} \cdot \frac{\sin(\xi^s s_2 \sin \gamma)}{(\xi^s s_2 \sin \gamma)} \right| \quad (97)$$

Since the function $\frac{\sin t}{t}$ is maximum at $t = 0$, and its subsequent peaks after $t = 0$ rapidly decay, one concludes that for maximum sensor response amplitude ($|V_c|$) in the far-field, the sensor dimensions, i.e., $2s_1$ and $2s_2$, should be as small as possible, preferably much smaller than the half-wavelength of the traveling wave.

Similar analysis can be done for piezos/APTs bonded on beams/plates in the far GW field excited/scattered by an arbitrary source to conclude that the smaller the sensor size, the stronger its response. This is essentially due to the piezo-sensor's mechanism to be sensitive to the average strain over its surface area. When sensing a spatially oscillating GW, this leads to a stronger response if the area over which the averaging is done is smaller. How small the piezo can be made will be limited by shear lag, as observed in the experiment above. Depending on the strength of the bonding mechanism,

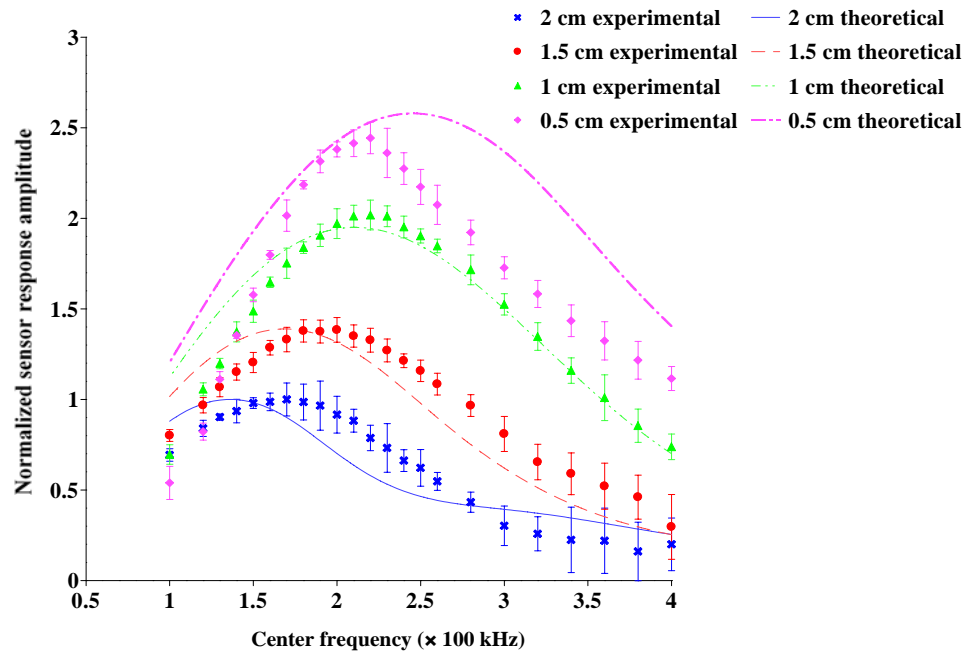


Fig. 26: Comparison between experimental and theoretical sensor response amplitudes in the variable sensor length experiment

beyond a point reducing sensor size will cause the GW signal to be completely lost in the bond layer. Another situation where this sensing mechanism can be exploited is when the sensed signal is multimodal and immunity to one of the GW modes is desired. In that case, if the sensor size is designed to be equal to the wavelength of that mode corresponding to the expected center frequency of the signal, the contribution from that mode will be negligible due to the sensor's averaging mechanism. This can be exploited to reduce the demands on the signal processing algorithm, as explored in Chapter IV.

Thus, in summary, in this chapter, 3-D elasticity models were developed for GW transduction by piezos and these were validated by FEM and experiments. Some analysis was also presented for tailoring transducer dimensions to maximize GW field strength when used as actuators and also to maximize response amplitude as sensors. The next chapter uses these models along with other concepts to provide a set of design guidelines for transducers and the excitation signal in GW SHM systems.

CHAPTER III

DESIGN GUIDELINES FOR THE EXCITATION SIGNAL AND PIEZO- TRANSDUCERS IN ISOTROPIC STRUCTURES

In this chapter, the models developed in the previous chapter along with other ideas are exploited to furnish a set of design guidelines for GW SHM systems, specifically for the excitation signal and the transducers in isotropic structures. Fig. 27 shows a tree-diagram which lists the various parameters that need to be chosen for the excitation signal and transducers in GW SHM systems. The next two sub-sections prescribe the specific guidelines for excitation signal and transducer design. Each sub-section in these begins with the guideline in italics, followed by the reasoning behind it.

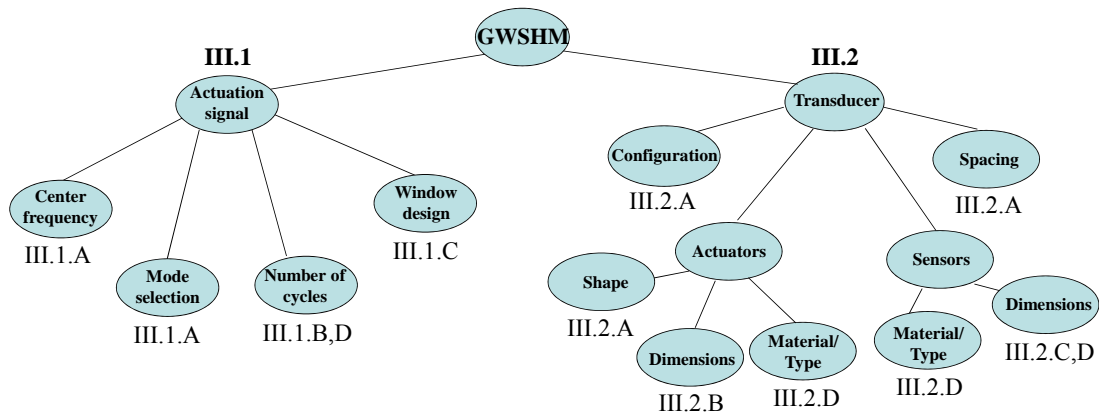


Fig. 27: Tree diagram of parameters in GW SHM (numbers above/below the boxes indicate section numbers for the corresponding parameter)

III.1 Excitation Signal

In GW SHM, the excitation signal is typically a high-frequency pulse signal. This feature distinguishes this approach from other vibration-based SHM schemes. If the excitation signal is too long in the time-domain, the response of the structure might be masked by multiple boundary reflections. Most commonly, a modulated sinusoidal toneburst signal spanning a few cycles is used. The following guidelines should aid in choosing the specifics of this signal.

III.1.A Center Frequency/GW mode

The center frequency and GW mode should be decided based on the damage types(s) of interest, using relevant information of GW sensitivity studies for each damage type.

The center frequency of the excitation signal is a crucial parameter. Along with the GW mode, it decides the wavelength, which in turns defines the minimum size of the least sensitive of the different damage types which are hoped to be detected using the GW SHM system. The wavelengths of the GWs are found from the dispersion curves. Mode sensitivity to a damage can be found using FEM-based damage sensitivity studies or from theoretical models that describe the GW-scattered field from the damage as discussed in Section I.4.A. For example, by exciting a mode with a through-thickness stress profile such that the maximum power is transmitted close to a particular interface through the plate thickness, the plate can be scanned for damage along that interface. Rose et al. [63] predicted through analysis of displacement and power profiles across the structural thickness that in metallic plates the S_0 mode would be more sensitive to detect large cracks or cracks localized in the middle of the plate. On the other hand, the S_1 mode would be better suited for finding smaller cracks or cracks closer to the surface. Alleyne and Cawley [66] found from FEM-based sensitivity studies that notches of depth of the order of $1/40$ times the wavelength could be detected by Lamb waves in a plate. They also found that the sensitivity was independent of the size of the notch in the plane of the plate, as long as the was small compared to the wavelength. Furthermore, it might be useful to test at more than one frequency, since defects of some particular dimensions can be insensitive to a given wavelength (see, e.g., Fromme et al. [73]).

The following types of structural damage/defects have been detected using GWs in the literature: delaminations in composites [65], notches [66], impact damage (usually in the form of an indentation or hole [73], structural cracks (which could be fatigue-induced, e.g., [72], loss of material due to corrosion [208], cracks in welds [209], bolt torsion in clamps/fasteners supporting structures [175], disbonds between skin and the honeycomb core in sandwich structures [157], and disbonds at adhesive joints [173].

III.1.B Number of Cycles

Decide on the number of cycles in the toneburst based on a tradeoff study between blind-zone area and dispersiveness.

There is always a small blind-zone area surrounding the transducers used in GW SHM, where damage cannot be detected. The blind-zone area results because small amplitude scattered GWs from damage sites going to the sensor cannot be easily separated from the large amplitude first transmitted GW pulse from the actuator (or the excitation signal if the actuator itself is being used as sensor) or from the GW reflections from the boundary (which are also usually significantly larger compared to reflections from damage sites). Therefore, from this standpoint, a smaller number of cycles will decrease the blind zone area. On the other hand, a larger number of cycles will reduce the frequency bandwidth, and thereby, decreases “dispersion.” Dispersion is a phenomenon wherein the original signal is distorted as it travels in a medium due to the different wavespeeds of its component frequencies. Therefore, the number of sinusoidal cycles in the excitation signal has to compromise between these two factors. The former is proportional to the square of the number of cycles for a given excitation frequency while the latter reduces with increasing number of cycles due to the reduction of the main lobe width in the frequency spectrum. Thus, if one is operating in a relatively non-dispersive region of the dispersion curve, one could afford to use a fewer number of cycles.

III.1.C Modulation Window

Choose a Kaiser window for modulating the excitation signal.

To minimize the problem of dispersion created by using a finite time-duration signal, it should be modulated by a window which minimizes the spread of the signal in

the frequency domain. The effect of truncating a harmonic signal is to smear its signal energy in the frequency domain in a main lobe centered about the original frequency, along with weaker side lobes. Modulation typically widens the main lobe and makes the side lobes smaller. The *Kaiser window* approximates the prolate spheroidal window, for which the ratio of the main-lobe energy to the side-lobe energy is maximized in the frequency domain (Papoulis [210]). It is given by the expression:

$$k(t) = \frac{I_0\left(\beta\sqrt{1-\frac{4t^2}{\tau^2}}\right)}{I_0(\beta)} \quad (98)$$

where $I_0(\cdot)$ is the modified Bessel function of the first kind of order 0, τ is the duration of the window (fixed by the number of cycles) and β is a parameter that controls the main lobe width in the frequency domain. Let Δ_{ml} be the chosen main lobe width defined by the distance between the central zero-crossings in the plot of the magnitude of the Fourier transform (see Fig. 28). Then the amplitude attenuation factor in dB of the main lobe to the largest side lobe is:

$$A_{sl} = \frac{155\Delta_{ml}\tau - 1}{24\pi} - 12 \quad (99)$$

The window parameter β is chosen to be:

$$\beta = \begin{cases} 0 & A_{sl} \leq 13.26 \\ 0.76609(A_{sl} - 13.26)^{0.4} + 0.09834(A_{sl} - 13.26) & 13.26 < A_{sl} < 60 \\ 0.12438(A_{sl} + 6.3) & 60 \leq A_{sl} < 120 \end{cases} \quad (100)$$

That is, for $A_{sl} \leq 13.26$, the Kaiser window reduces to the rectangular window.

III.1.D Consideration for Comb Array Configurations

When using a comb transducer, ensure that the main lobe in the frequency spectrum is narrow enough so that higher harmonics of the primary wavenumber of interest are not excited.

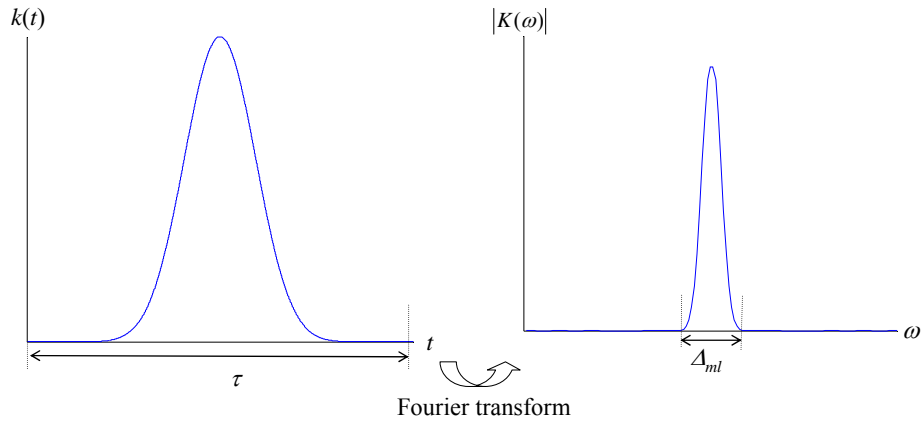


Fig. 28: The Kaiser window and its Fourier transform

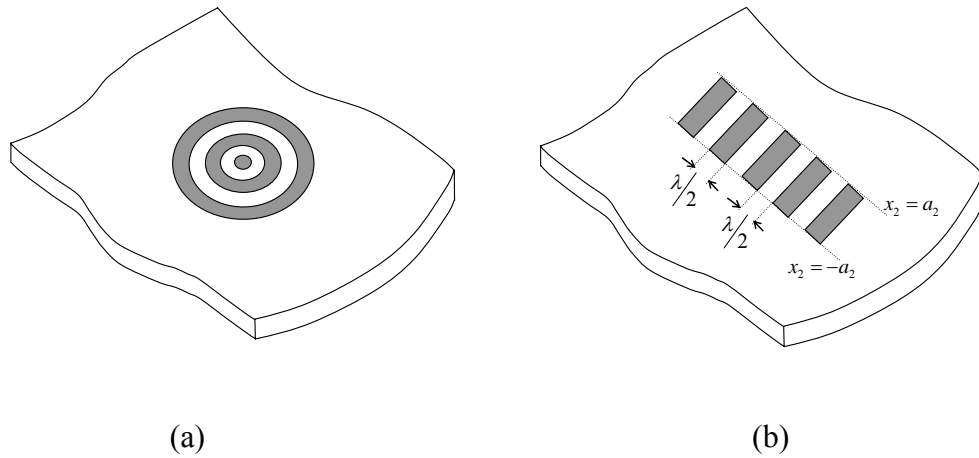


Fig. 29: Illustration of comb configurations: (a) using ring elements and (b) using rectangular elements

A comb configuration (Fig. 29) is an array of transducers that is equally spaced to a particular wavelength of interest and its integer multiples (illustrated in Fig. 30). Therefore, when using such a configuration, ensure that the excitation signal is such that its frequency bandwidth does not include any higher harmonics of the wavelength of interest. A more detailed description of comb transducers can be found in Section III.2.

III.2 Piezo-Transducers

III.2.A Configuration/Shape Selection

Choose the configuration of the transducer(s) and the individual transducer shape(s)/type(s) to suit the application:

- For large area scanning from a central point on the structure, use multi-element arrays.
- For small area scanning, use a few elements in pulse-echo or pitch-catch mode.
- For uniform radiation in all directions, use circular actuators.
- For focused radiation, use an appropriately designed rectangular piezo actuator.
- For unidirectional sensing, use an anisotropic piezocomposite transducer.
- For modal selectivity, use comb configurations.

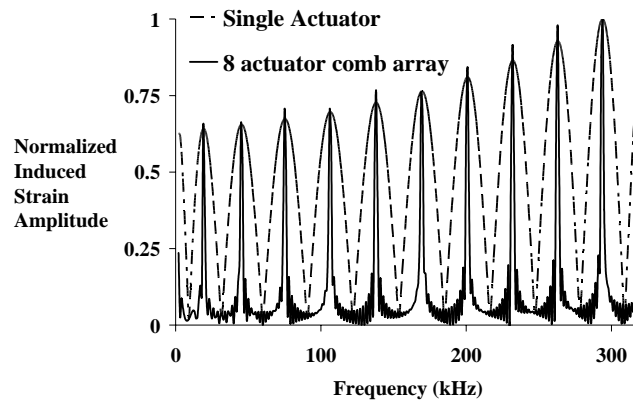


Fig. 30: Comparison of harmonic induced strain in A_0 mode between an 8-array piezo comb transducer and that of a single piezo-actuator (power is kept constant).

The configuration and shape are highly dependent on the application area. For example, if large area scanning from a central point of a structure without structural obstacles (such as a reinforcement or joint) is desired, a linear phased or circular array may be preferable. Phased arrays operate by scanning individual sector angles by applying appropriate delays and scaling factors to the excitation signals to the individual array transducer elements (see e.g., Purekar and Pines [123]). If however, a smaller area is to be monitored, a simpler solution is to use a few transducers operating in the pulse-

echo configuration. A minimum of three transducers are needed for triangulation in a plate or shell-like structure (this is further discussed in a subsequent chapter on signal processing in this thesis). The pitch-catch configuration requires a denser network of transducers in order to allow for triangulation. For beam-like structures, two transducers in the pulse-echo configuration suffice to locate the damage. Note that the notion of “small” and “large” areas depends on the material damping characteristics as well as the power available per actuator. The relative spacing between sets of transducers on the structure should be based on a calibration experiment to get an estimate of the range capability of the chosen actuator/sensor configuration for the structure of interest and actuation voltage levels.

The radiation patterns of a particular actuator depend on its shape. To ensure uniform radiation in all directions in the plane of the plate, use circular actuators. This is crucial in linear phased arrays, for example. If it is desired to monitor one or more particular area(s) of the structure selectively, focused actuator shapes such as rectangular ones are preferable. An APT may also be useful in this regard due to its preferential direction of radiation along its fibers. However, care should be taken in their design since these also excite horizontally polarized shear (SH-) modes along with Lamb modes, as seen in the previous chapter. They are also advantageous to use in certain applications due to their unidirectional sensing capability along the fiber direction. To achieve modal selectivity and thereby easier signal interpretation, a comb configuration would be much preferable.

III.2.B Actuator Size

Determine the optimal size of the actuator based on the theoretical model corresponding to the particular chosen shape.

The formulas in this sub-section are based on theoretical models in the previous chapter and assume the circulation power formula for harmonic excitation with capacitive loads (in this case, the piezo-actuators), i.e., $P = 2\pi fCV^2$. In practice, for modulated sinusoidal tonebursts, the peak power drawn is close to this value. For more accuracy, a correction factor can be used depending on the modulation window. It should be noted that, since capacitive loads are reactive, this power is used in the positive half-cycle for

charging the capacitance and is gained back in the negative half-cycle when the capacitance is discharged. The power dissipated in exciting the GW field in the structure is neglected, since that is typically orders of magnitude smaller than the reactive power. In addition, the nonlinear dependence of the capacitance of piezoelectric elements on driving voltage and frequency is neglected (see e.g., Jordan et al. [207]). This should be accounted for at high driving voltages (> 30 V). Sizing guidelines for circular and rectangular uniformly poled piezos, rectangular APTs and ring-shaped/rectangular comb actuators are presented in this sub-section. The objective of the design process here is to maximize the GW field strength while remaining within the power, voltage and maximum actuator size constraints of the system. The different parameters needed in the formulas below are:

System constraints:

V_{\max} = Maximum actuation voltage that can be applied by the power source

P = Maximum power that can be supplied by the power source

a_{\max} = Maximum allowable actuator dimension

Actuator properties:

k = Dielectric ratio of the actuator material

h_a = Thickness of actuator along the direction of polarization

Structural (substrate) properties:

E = Young's modulus of the isotropic plate structure

ν = Poisson's ratio of the isotropic plate structure

ρ = Material density of the isotropic plate structure

$2b$ = Thickness of the plate structure

Other constants/parameters:

ϵ_0 = Permittivity of free space

f = Center frequency of excitation

ξ = Wavenumber of the chosen GW mode at the operating center frequency

i) Circular actuator uniformly poled through thickness:

Let a be the variable corresponding to the radius of the circular actuator. Also, consider the parameter a_0 such that:

$$a_0 = \frac{1}{\pi V_{\max}} \sqrt{\frac{Ph_a}{2k\varepsilon_0 f}} \quad (10)$$

Fig. 31 illustrates the design space and the geometric locations of a_0 and other parameters that will be discussed for the circular actuator. Thus, a_0 is the value of a at the intersection of the power constraint curve and the line $V = V_{\max}$. If $a_0 < a_{\max}$, which is the maximum radius of an actuator permissible by the designer, then:

1. If $a = a_0$ corresponds to an extremum of $|J_1(\xi a)|$, then choose this value as actuator radius.
2. If $a = a_0$ does not correspond to an extremum of $|J_1(\xi a)|$, let a_2 correspond to the first extremum of $|J_1(\xi a)|$, such that $a_0 < a_2 \leq a_{\max}$, if it exists (else choose $a_2 = a_{\max}$) and let a_1 correspond to the maximum value of $|a.J_1(\xi a)|$ for $0 < a \leq a_0$. If:

$$a_1.J_1(\xi a_1).V_{\max} > J_1(\xi a_2).\sqrt{\frac{Ph_a}{2\pi^2 k\varepsilon_0 f}} \quad (10)$$

then choose $a = a_1$. Otherwise, choose $a = a_2$. If $a_0 > a_{\max}$, then choose the largest maxima of $|a.J_1(\xi a)|$ with $0 < a \leq a_{\max}$, if such a maximum exists, else choose a to be a_{\max} .

The suggestions for circular actuator sizing are derived from the relation between the GW strain or displacement field and actuator size/actuation voltage. As shown in the previous chapter, if one is within the limits of the power supply, the GW strain field strength for circular actuators is linearly proportional to $Va.J_1(\xi a)$ (the linear proportionality to V results from the linear dependence of τ_0 on the actuation voltage V). However, along the power constraint curve (defined by $Va = \sqrt{2\pi^2 fk\varepsilon_0 / (h_a.P)}$), since Va is fixed, the field strength for circular actuators is linearly proportional to $J_1(\xi a)$.

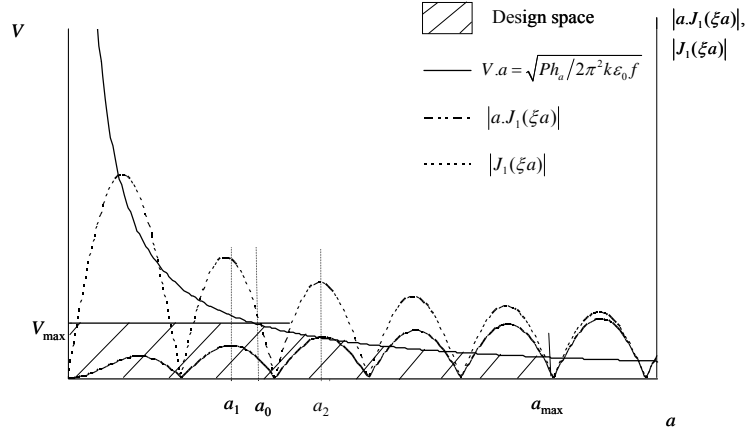


Fig. 31: Parameters and design space for circular actuator dimension optimization

ii) Rectangular actuator uniformly poled through thickness

In this case, the dimensions depend on the direction(s) in the plane of the structure where radiation is to be maximized. If, for example, it is desired to maximize radiation along a particular direction while minimizing radiation perpendicular to it, then the rectangular actuator should be oriented such that one of its two axes of symmetry is along the direction of interest, say the x_1 -axis. Let the dimensions of the actuator be $2a_1$ along x_1 and $2a_2$ perpendicular to it, with $a_1 < a_2$. Again, the formulas for the far-field GW strain field are used in conjunction with the constraints to derive these recommendations.

Consider $2a_{\max}$ to be the maximum allowable actuator dimension. As shown in Fig. 33, choose a_{2o} (the optimal value for a_2) to be the largest zero of $\sin \xi a_2$ such that $0 < a_2 \leq a_{\max}$, if it exists. If no such zero exists then choose $a_2 = a_{\max}$.

Let:

$$a_0 \equiv \frac{Ph_a}{8\pi a_2 k \epsilon_0 f V_{\max}^2} \quad (10)$$

If this value of a_0 is larger than or equal to a_{\max} , reset a_0 to be a_{\max} . If there exists \tilde{a} corresponding to an extremum of $|\sin \xi a_1|$ such that $0 < \tilde{a} \leq a_0$, then choose the smallest value of \tilde{a} for a_1 . If such an extremum does not exist, and a_0 was reset to a_{\max} , then choose $a_1 = a_{\max}$.

If such an extremum does not exist, and $a_0 < a_{\max}$, then let a_t be the first extremum of $\left|(\sin \xi a_1)/\sqrt{a_1}\right|$ such that $a_0 < a_t \leq a_{\max}$. If such a_t does not exist, choose $a_t = a_{\max}$. If:

$$\sin(\xi a_0) V_{\max} > \sin(\xi a_t) \sqrt{\frac{Ph_a}{8\pi a_t a_2 k \varepsilon_0 f}} \quad (104)$$

then the optimal value of a_1 is $a_{1o} = a_0$, else choose $a_{1o} = a_t$. The locations of these parameters in the design space are shown in Fig. 34.

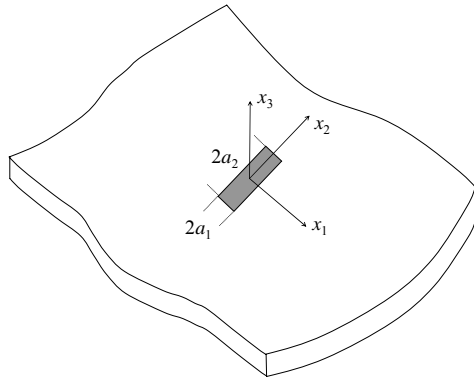


Fig. 32: Parameters and coordinate axes for rectangular actuator

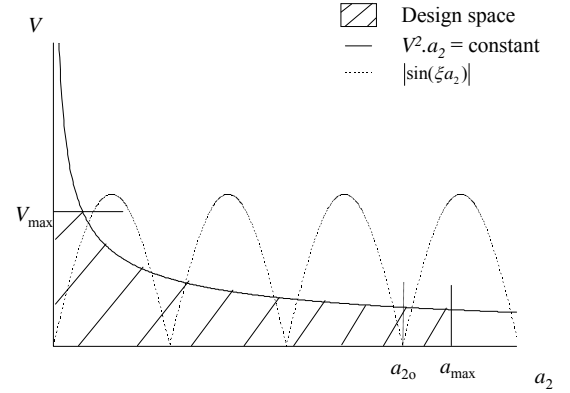


Fig. 33: Choice of a_2 for rectangular actuator

iii) Ring-shaped comb actuator uniformly poled through thickness

The possibility of using this configuration arises only if a_{\max} , which is the maximum allowable actuator radius, is larger than the value of a corresponding to the second extremum of $|a.J_1(\xi a)|$. A comb configuration can be achieved by using individual ring-shaped actuators or by using a large circular actuator with the necessary electrode pattern etched on it. A comb configuration is much more preferable compared to a circular actuator for axisymmetric GW excitation due to its modal selectivity. In designing this, the maximum number of ring shaped actuators that can be used is $n-1$, where n is the number of extrema of $|a.J_1(\xi a)|$ for $a \leq a_{\max}$. If n is odd and greater than 1, there can be one circular actuator and $n-2$ ring-shaped actuators. If $n=1$, only one

circular actuator can be used. The internal and external radii of the rings are the values of a corresponding to the extrema of $|a.J_1(\xi a)|$. In choosing the number of ring actuators n , the only issue preventing one from using the maximum possible number of elements within the allowable actuator size is the drop in amplitude due to increase in capacitance as more rings are used (which may cause reduced actuation voltage due to the finite power supply of the system). Hence, the choice of n should be made after a careful tradeoff study between tolerable dispersiveness and signal amplitude for each possible n .

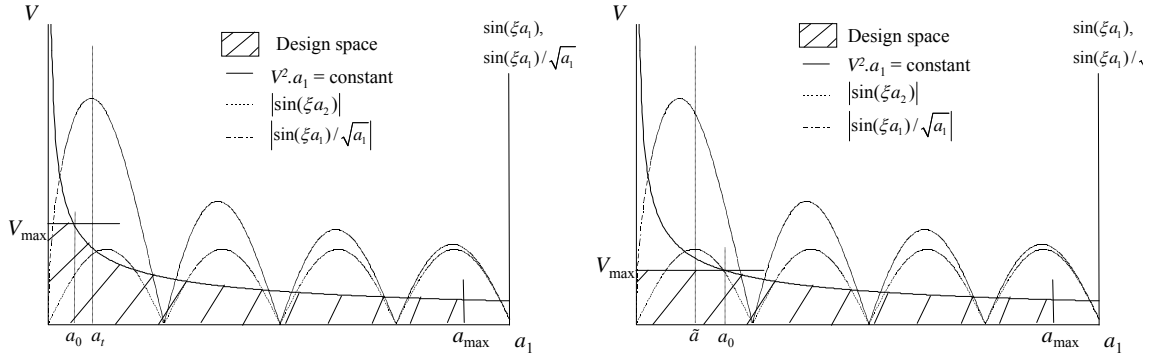


Fig. 34: Possible optimal choices of a_1 for rectangular actuator in two possible cases

iv) Comb actuator with rectangular uniformly-poled piezos

Just as for the ring-shaped comb configuration, a rectangular comb-shaped configuration (Fig. 29 (b)) is always preferable over a single rectangular actuator (if maximizing radiation along one direction is desired). The possibility of using this configuration arises if $a_{\max} \geq \frac{3\pi}{2\xi}$. The individual rectangular actuator elements can be

designed using the guideline (ii) (note that the total power is equally split among the elements of the comb array). If n is the number of extrema of $|\sin \xi a|$ in the range $-a_{\max} \leq a \leq a_{\max}$ (which is the number of half-wavelengths of the GW), then $n/2$ identical rectangular actuators need to be used and placed between the same x_2 -locations ($x_2 = a_2$ and $x_2 = -a_2$), with their edges along the x_1 -locations being the odd multiples of the half-wavelengths (see Fig. 29 (b)).

v) Rectangular APT actuators

For rectangular APTs used as actuators (which would be used for more strongly focused GW fields than the corresponding uniformly poled rectangular piezo), the design considerations are analogous to that for a rectangular uniformly poled piezo-actuator, with a_1 along the fiber direction.

III.2.C Sensor Size

Choose the sensor dimensions in the plane of the plate to be minimal, preferably much smaller than the half-wavelength of the GW. If the signal processing algorithm cannot handle multiple modes, design the sensor to be immune to the GW mode that is less sensitive to the damage type(s) of interest.

As seen in the previous chapter, the sensor response keeps increasing as the sensor dimensions in the plane of the plate are reduced, assuming the sensor is in the far-field relative to the source (a distance of five to ten wavelengths). The only constraint on decreasing sensor size is the phenomenon of shear lag wherein all the strain is taken by the bond layer and nothing is transmitted to the sensor. However, with a reliable bond layer, this limit can be stretched to a considerable extent. The exact smallest value beyond which shear lag dominates may have to be determined experimentally for a particular bonding mechanism².

However, in making the sensor dimensions small, one should take care that the signal processing algorithm in use can resolve and identify multiple GW modes. If this is not possible, then the excitation frequency can be kept low enough so that only two GW modes exist and the piezo-sensor can be designed to be immune to one of the GW modes. This is done by choosing its size to be equal to the wavelength corresponding to the center frequency for that mode. As discussed in Chapter II, due to the strain averaging mechanism of piezo-sensors, this will almost nullify the contribution of that GW mode. However, some mild contribution from that mode corresponding to the side bands of the excited frequency bandwidth may still be present in the signal.

²In the author's experience, using a two-part overnight setting epoxy (Epotek-301 from Epoxy Technology) with piezos of thickness 0.3 mm on a 3.2-mm aluminum plate, beyond an in-plane size of 0.5 cm, sensor size reduction does not yield any advantage.

Thus, it is evident that the optimal dimensions for sensors and actuators are quite different. This implies that ideally separate actuators and sensors should be used for improved signal performance. However, the final decision should be made in view of the system architecture under consideration.

III.2.D Transducer Material

Choose the actuator material with the highest value for the product of in-plane Young's modulus and piezoelectric constant (the relevant d -constant) divided by the dielectric constant. Use a sensor material with the highest value for the piezoelectric constant (the relevant g -constant) and minimum material density.

The actuation authority of the piezo increases linearly with increasing values of piezoelectric constant (d_{31} or d_{33} depending on whether a piezo with isotropic poling or an APT is used) and in-plane Young's modulus (Y_a^{11} or Y_a^{33}). The reactive circulation power increases linearly with increasing dielectric constant k . Thus to maximize the actuation capability per unit power drawn, the material with maximum value for the ratio $Y_a^{11}d_{31}/k$ (or $Y_a^{33}d_{33}/k$, as appropriate) should be chosen.

The sensor response strength is directly proportional to the product of the in-plane Young's modulus, the piezoelectric constant and sensor thickness. However, it is not advisable to increase sensor thickness or Young's modulus beyond a point. This may cause the sensor to significantly disturb the guided wave field being sensed, and the measured output will not be representative of the incident GW field. This is directly related to the relative thickness and relative Young's modulus of the sensor to the substrate. Thus, for minimum interference with the GW field, PVDF sensor elements would be more suitable due to their finer thickness and low in-plane Young's modulus, however their response strength is usually weak and often piezoceramics are preferred. This relates to the classical problem of the science of measurements, wherein one has to compromise between sensor readability and fidelity. However, an increase in the g -constant does not perturb the field and at the same time increases sensor response. The higher the material density, the greater the mass of the sensor, thereby perturbing the GW

field without any increase in the sensor response. Hence, the sensor material with minimum material density is preferable.

The actuation signal and transducers, for which detailed recommendations were provided in this chapter, are just two of the many pieces in GW SHM systems. There are several other critical design issues involved in an effective GW SHM system. For example, the bond layer should be thin, stiff (at the frequency of interest), uniform, and robust to environmental conditions to ensure good transmission of strain between the transducer and substrate. There are decisions concerning the electrical architecture, such as whether wireless connections are needed. If wires are used, the connections should be able to withstand electromagnetic interference and electrical noise (e.g., by using co-axial cables). Several other such issues exist in other areas of GW SHM such as signal processing, pattern recognition, actuation hardware, system reliability, transducer diagnostics, etc. In many of these, because GW SHM is still evolving, it might not be possible to obtain clear-cut design guidelines at this point. Some insights and recommendations for the signal processing algorithm and the effects of elevated temperature are presented in the following chapters.

CHAPTER IV

A NOVEL SIGNAL PROCESSING ALGORITHM USING CHIRPLET MATCHING PURSUITS AND MODE IDENTIFICATION

As alluded to in the introductory chapter, the objective of signal processing in GW SHM is to extract information from the sensed signal to decide if damage has developed in the structure, and if so, characterize it in terms of location. Information about damage type and severity is also desirable from the signal for further prognosis. However, classifying and quantifying damage usually requires some pattern recognition algorithm which uses the output from the signal processing. This chapter addresses signal processing by suggesting a new algorithm using chirplet matching pursuits and mode identification. Problems associated with conventional approaches are described and the potential to overcome those and automatically resolve and identify multimodal, overlapping reflections is discussed. The algorithm, designed for pulse-echo based methodologies, is tested using FEM simulations and experiments. Finally, the issue of in-plane triangulation in isotropic plates is discussed.

IV.1 Issues in GW Signal Processing

To assess the issues involved in signal processing for GW SHM, results from a couple of illustrative FEM simulations are presented. Consider a 2-D aluminum plate structure, modeled using a finite element mesh of 2-D plane strain elements as shown in Fig. 35(a) (the structure is infinitely wide normal to the plane of the paper). In the first simulation, a notch is present. It is 0.5 mm deep and 0.25 mm across, at a distance of 7.5 cm from the plate center. There are surface-bonded thin piezoelectric wafer actuators on

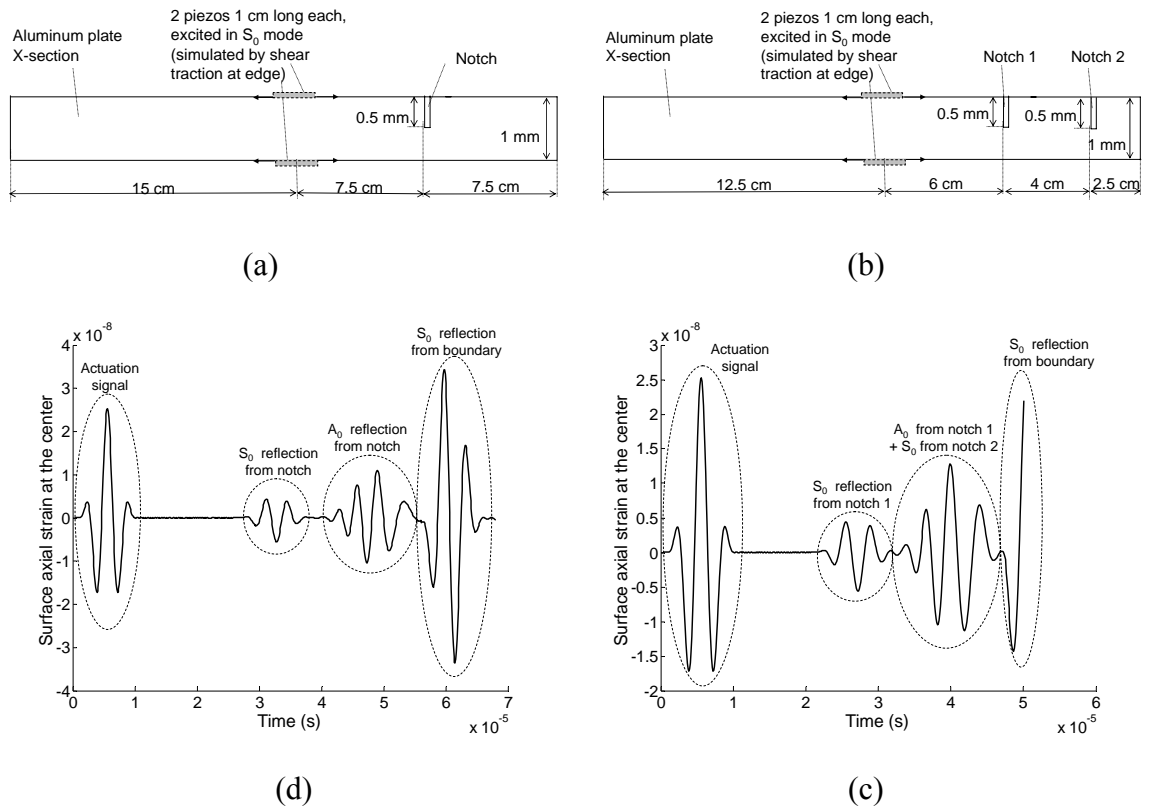


Fig. 35: From top-left, clockwise: (a) 2-D plate structure with one notch; (b) 2-D plate structure with two notches; (c) surface axial strain waveform at the center for structure in (b) and (d) surface axial strain at the center for structure in (a)

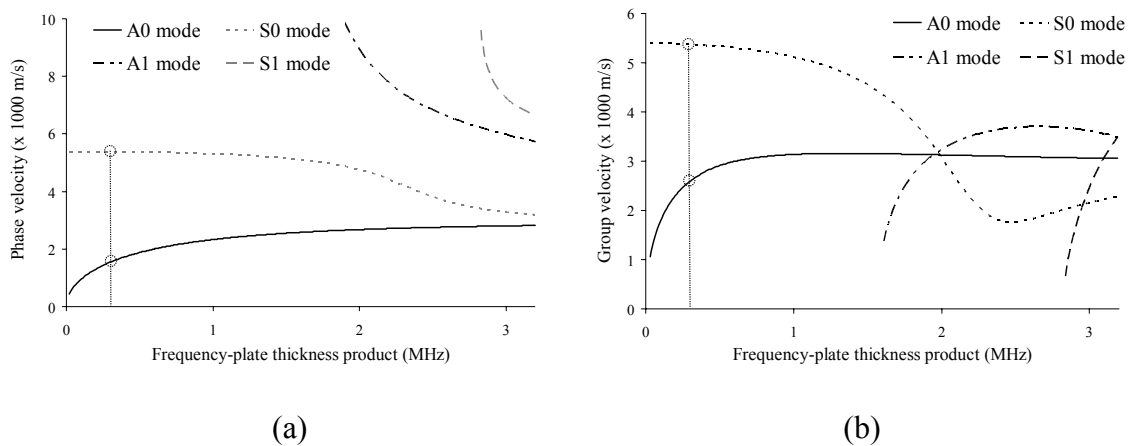


Fig. 36: The Lamb-wave dispersion curves with circles marking the excitation center frequency for the FEM simulations: (a) phase velocity and (b) group velocity

each free surface at the center. The piezo-actuators are modeled as causing shear traction along their free edges, which was shown to be effective in Chapter II. The actuators are excited symmetrically with a 2.5-cycle Hanning-windowed sinusoidal toneburst with center frequency of 275 kHz. This frequency is highlighted in Fig. 36. Even though only the S_0 mode is excited in this case, when it interacts with “damage,” all possible modes are scattered. At 275 kHz, three GW modes (the Lamb modes highlighted in Fig. 36 and the SH-modes) are possible in a 1-mm thick Aluminum plate. Due to the 2-D nature of the simulation, SH-modes are not possible, and are therefore not considered. Thus, the two possible modes that can be reflected and transmitted from the notches are the A_0 and S_0 Lamb modes. The surface axial strain wave at the center of the plate from the FEM analysis, done using ABAQUS [205], is shown in Fig. 35(d). The first wave packet is the actuation pulse, which is followed by the S_0 mode reflection from the notch. Subsequently, the slower A_0 mode reflection from the notch is received and finally the S_0 reflection from the boundary reaches the center of the structure. In this case, the presence and location of the notch was known beforehand, but in SHM, one has to estimate this information given the signal. The signal-processing algorithm must decide what mode each reflected wave packet corresponds to, what the center frequency of the packet is (though the center frequency of excitation is known, the damage site may be sensitive to higher or lower frequencies and therefore the center frequency of the reflection can change), and what the precise time-of-arrival is. Once the mode and the time-frequency center of the wave packet are known, the location of the damage site can be estimated, knowing the group velocity for that mode. Now consider a similar structure as before, shown in Fig. 35(b), with the main difference being that there are two notches. In this case, as before, in the surface strain waveform at the center, shown in Fig. 35(c), one can see the actuation pulse, followed by the S_0 mode reflection from the notch closer to the center, and the S_0 mode boundary reflection. However, in this case, the A_0 mode reflection from the notch closer to the center overlaps with the S_0 mode reflection from the notch closer to the free end. Therefore, the signal-processing algorithm should also be able to separate overlapping multimodal reflections. In addition, for SHM, since the signals are to be processed continuously in near real-time, it is desirable to have a computationally efficient algorithm. Finally, the algorithm must be robust to noise.

Before the proposed algorithm is discussed, conventional solutions to the problem of GW signal processing for SHM are first described and their shortcomings are highlighted.

IV.2 Conventional Approaches to GW Signal Processing

Conventional solutions to the problem of GW signal processing adapted from NDT are usually in the form of some time-frequency representation (TFR). Unlike the well-known Fourier transform, which provides “global” information about the frequency content and is thereby suited for signals with stationary frequency content (meaning their frequency content does not change with time), TFRs yield the “local” frequency content and are better suited for non-stationary-frequency signals. The simplest example of a TFR is the short time Fourier transform (STFT), in which the signal is divided into a number of small overlapping pieces in the time domain, each piece is multiplied in time using a fixed modulation window and the Fourier transform is used on the resulting signal. Thus, the STFT, $S(t, \omega)$, of a signal, $s(t)$, and the corresponding time-frequency energy distribution, $E(t, \omega)$, obtained from it (called the spectrogram) are [211]:

$$S(t, \omega) = \frac{1}{2\pi} \int_{-\infty}^{\infty} s(\tau)h(\tau - t)e^{-i\omega\tau} d\tau \quad E(t, \omega) = |S(t, \omega)|^2 \quad (105)$$

where $h(t)$ is the modulation window. Thus, an image is obtained for each point of the time-frequency plane (t, ω) . This TFR can be implemented quickly using the fast Fourier transform (FFT) for digital signals. Another important TFR is the Wigner-Ville distribution (WVD), which is defined as [211]:

$$W(t, \omega) = \frac{1}{2\pi} \int_{-\infty}^{\infty} s\left(t + \frac{\tau}{2}\right)s^*\left(t - \frac{\tau}{2}\right)e^{-i\omega\tau} d\tau \quad (106)$$

where * indicates the complex conjugate. An advantage of the WVD is that it can exactly localize sinusoids, Dirac impulses and linear chirps. However, for other signals it always has additional interference terms. Fig. 37 illustrates this point using the WVD of a signal composed of two Gaussian modulated linear chirps. The interference terms can be

reduced by using a smoothing filter $f(t, \omega)$ in the time-frequency plane. This yields the generic smoothed WVD [211]:

$$SW(t, \omega) = \int_{-\infty}^{\infty} \int_{-\infty}^{\infty} f(t - \tau, \omega - \varpi) W(\tau, \varpi) d\tau d\varpi \quad (107)$$

In fact, it can be shown that the spectrogram and energy distribution from all commonly used TFRs such as the scalogram (which derives from the wavelet transform), the Hilbert Huang spectrum, and others can be represented in the form of Eq. (107). The disadvantage of smoothed WVDs is that they no longer can exactly localize linear chirps, sinusoids and Dirac impulses. One always compromises between the interference terms and time-frequency resolution. Further discussion on TFRs can be found in the books by Cohen [211] and Mallat [212]. For GW signal processing, researchers typically use some smoothed WVD followed by post-processing on the images. This isolates GW packets and locates their time-frequency centers, spread in the time-frequency plane and total energy. Finally, their modes are classified using the time-frequency “ridges” of the reflections (these are the loci of the frequency centers for each time instant within each reflection). Attempts by various researchers have tried this approach are reviewed in Section I.5.B of Chapter I.

As an illustrative example, the spectrogram for the signal in Fig. 35b over the excited bandwidth is shown in Fig. 38 (the modulation window used was identical to that for the excitation signal). The spectrogram is plotted on a decibel scale (logarithmic) with the peak value over the image as reference. For this simple example, the spectrogram seems capable of isolating the individual reflections, identifying their time-frequency centers and classifying their modes using the time-frequency ridges, which are highlighted with white lines in each reflection. However, as it is shown in Section IV.5, these are, in general, incapable of resolving overlapping multimodal reflections. Superior TFRs that might be capable of resolving such overlapped signals typically have a high computational cost associated with them. Another drawback of smoothed WVDs is difficult automated post-processing. In addition, these are more suited for broadband signals while in GW SHM, usually narrow-band signals are used, in order to minimize signal spreading due to dispersion.

Another approach that has been tried for GW signal processing is the use of multi-element sensor arrays. Some of these works are also reviewed in section I.5.B. In this approach, the information about the spatial variation of the data over the sensing area of the array is used to decide the mode of each reflection. That is, a multi-dimensional Fourier transform is applied to the signals involving both time and spatial transformations. However, a large number of closely spaced transducers to avoid aliasing and sophisticated multi-channel data capture and processing hardware are needed to implement this approach for GW SHM.

IV.3 Chirplet Matching Pursuits

The matching pursuits approach has already been introduced in section I.5.B. To understand this algorithm, consider a complex valued signal $f_1(t)$ that belongs to the Hilbert space $L^2(R)$, where R is the set of real numbers. Suppose this space is an inner product space with the inner product $\langle \cdot, \cdot \rangle$. Then, the following hold:

$$\|f_1\| = \int_{-\infty}^{\infty} |f_1(t)|^2 dt < \infty \quad \langle f_1, f_2 \rangle = \int_{-\infty}^{\infty} f_1(t) f_2^*(t) dt \quad (108)$$

where $f_2(t)$ also belongs to $L^2(R)$. The property of finiteness of the 2-norm, defined by the first expression in Eq. (108), also holds for $f_2(t)$. A dictionary D of all possible expected wave structures, or “atoms,” is used, i.e., $D = \{k_i\}$, where $k_i \in L^2(R)$ and $\|k_i\| = 1$. The 2-norm is also used as a metric of signal energy in this work. Then, the matching pursuit algorithm decomposes a signal $f(t) \in L^2(R)$ into m atoms in the following iterative way (with $R^0 f = f$):

(a) Choose the best atom in D :

$$k_{i_m} = \arg \max_{k_i \in D} \left| \langle R^{m-1} f, k_i \rangle \right| \quad (109)$$

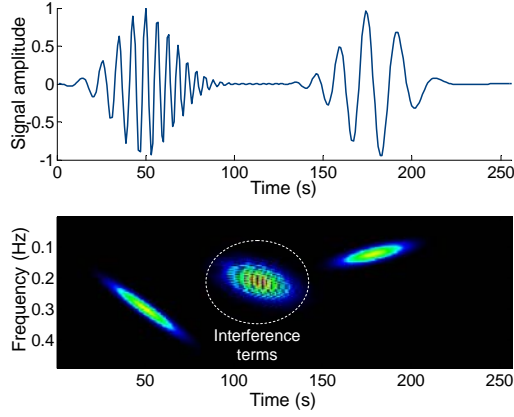


Fig. 37: WVD of two linear modulated chirps

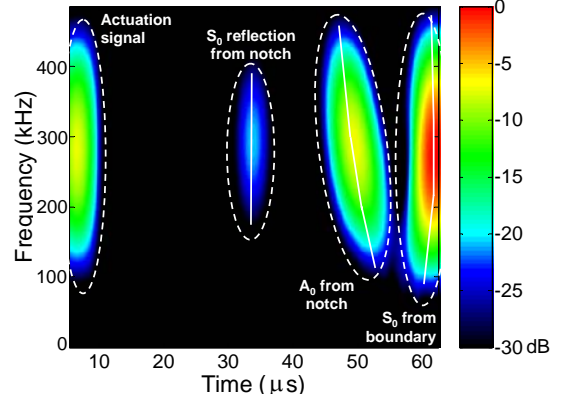


Fig. 38: Spectrogram of the signal in Fig. 35 (d)

- (b) Compute the new residual after subtracting the component along the best atom chosen in (a):

$$R^m f = R^{m-1} f - \langle R^{m-1} f, k_{i_m} \rangle k_{i_m} \quad (110)$$

Thus, it decomposes the signal into a linear expansion of waveforms chosen to match best the signal structure. Noise, in general, is uniformly distributed over the time-frequency plane. Since the matching pursuit algorithm looks for concentrated energy chunks in the time-frequency plane, it is inherently robust to noise. Due to this approach, which is distinct from conventional TFRs, the time-frequency centers, the spread in the time-frequency plane and the energy of the individual reflections are readily known, and no post-processing needs to be done on the output. It becomes much easier to automate this process in comparison to algorithms using conventional time-frequency representations. In those solutions, to automate the process, image processing algorithms would have to be used subsequent to the generation of the time-frequency plot to isolate the individual reflections.

In the original paper on matching pursuits [112], an efficient algorithm using a Gaussian modulated time-frequency atoms dictionary is described. This dictionary consists of the atoms:

$$k_{(l,u,\omega)}(t) = \frac{1}{\sqrt{l}} g\left(\frac{t-u}{l}\right) \exp(i\omega(t-u)) \quad \text{with} \quad g(t) = 2^{1/4} \exp(-\pi t^2) \quad (111)$$

where u is the time center of the atom and ω is the angular frequency center of the atom. Also, l is the scale of the atom, which is a metric representing the dilation along the time axis of the Gaussian window $g(t)$. It is indicative of the atom's time-frequency spread. These have *stationary* time-frequency behavior, i.e. the frequency at which the peak energy occurs for each time instant does not change with time, as would be seen in a WVD plot (see Fig. 39). Once the decomposition is done, it is possible to construct a time-frequency plot of the constituent atoms without the interference terms obtained using the conventional WVD. Thus, the resolution possible from such an approach is always superior to that from conventional smoothed WVDs. In addition, the use of Gaussian windows ensures that the atoms are optimal in terms of having minimal product for the root-mean squared (RMS) pulse time-width and RMS frequency bandwidth [213]. The matching pursuit algorithm with this dictionary has been explored by some researchers for GW signal analysis [114], [115]. However, the implicit assumption in these works is that the signals are unimodal and non-dispersive. The atoms in this dictionary are ill-suited for analyzing dispersive signals, which have non-stationary time-frequency behavior. Furthermore, these atoms would not help in GW mode classification, since different modes with the same energy at the same-time frequency center would yield similar atoms.

Gribonval [116] proposed an algorithm for matching pursuits using a dictionary consisting of Gaussian modulated *chirplet* atoms. That is, the dictionary comprises of atoms of the form:

$$k_{(l,u,\omega,c)}(t) = \frac{1}{\sqrt{l}} g\left(\frac{t-u}{l}\right) \exp\left[i\left(\omega(t-u) + \frac{c}{2}(t-u)^2\right)\right] \quad (112)$$

where c is the chirp-rate of the atom. These have *linear* time-frequency behavior (see Fig. 40). Once the GW signal is decomposed into chirplets, the additional parameter, i.e., the chirp-rate, can be used to identify the modes of the individual reflections. This algorithm is even more computationally efficient than the spectrogram. The computational time to

decompose an N -point signal into M atoms is $O(MN)$, whereas the complexity involved in generating the signal's spectrogram, not including post-processing, is $O(N^2 \log_2 N)$. Thus, the chirplet matching pursuit seems an attractive option for GW signal processing. In the next section, a detailed outline of the overall algorithm proposed using the chirplet matching pursuits approach is presented.

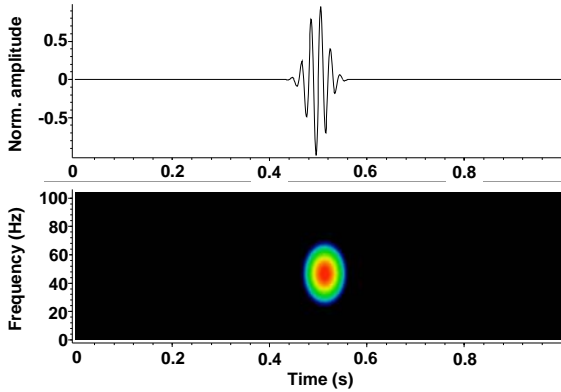


Fig. 39: A stationary Gaussian atom and its WVD

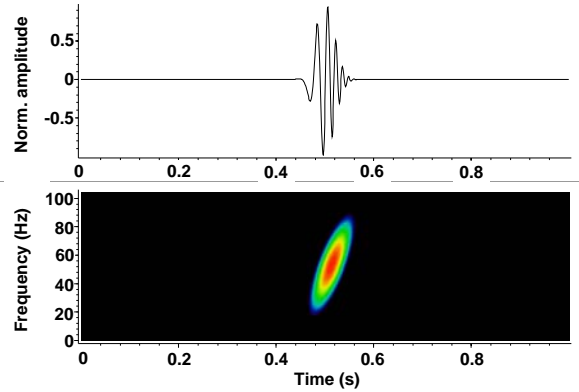


Fig. 40: A Gaussian chirplet and its WVD

IV.4 Proposed Algorithm for Isotropic Plate Structures

IV.4.A Database Creation

This algorithm is designed for GW SHM in isotropic plate structures using the pulse-echo method. That is, the structure has a central actuator excited with a high frequency pulse and a collocated sensor receiving the GW echo pulses from the damage sites, if any, and the boundaries. This presumes that a set of baseline signals is available corresponding to the pristine condition for the structure. For this algorithm, initially a database of the chirplet chirp-rates for the possible modes over the range of feasible time-frequency centers must be generated. The frequency centers are limited to the bandwidth excited in the structure, while the time centers are limited to the period between the end of the excitation signal and the time taken for the slowest mode from the boundary to reach the sensor. For this, it suffices to calculate these values for each mode at discrete

points in the feasible region of the time-frequency plane. Then, use bilinear interpolation if values for other points are needed. It should be mentioned that in this work the scale l of the chirplet atoms in the dictionary was kept fixed. The chosen value of l , say l_0 , was such that the spread of the atom in the time-domain was slightly larger than that of the excitation signal (20-30% larger by rule of thumb; however, for very dispersive signals, this might need to be further increased). To generate the database, waveforms for each mode at the discrete time-frequency points are generated assuming the defect is a point-scatterer emitting circular-crested waves. These waveforms represent the expected response of the piezoelectric wafer sensor collocated with the actuator. As discussed in Chapter II, the response of a surface-bonded piezoelectric wafer is proportional to the average in-plane extensional strain over its surface area (this assumes that the sensor is thin and compliant enough to not affect the GW incident on it). For the FEM simulations, the waveforms represent the surface displacement along the plate thickness direction at the center of the plate. To do this, for each mode, the radial distance of the damage site needs to be calculated. The phase velocity and group velocity curves for the isotropic plate structure are assumed known. Suppose the S_0 mode was excited predominantly (or purely) and the excitation frequency is low enough so that the higher Lamb modes are not possible. Since a narrow bandwidth pulse is used, the group velocity can be used as the speed of pulse propagation to get damage site location estimates. Therefore, the radial distance estimates for the possible modes at the time-angular frequency center (t_0, ω_0) are:

$$r_{S_0} = \frac{(t_0 - t_e / 2) \cdot c_{g_{S_0}}(\omega_0)}{2}; \quad r_{A_0} = \frac{(t_0 - t_e / 2) \cdot c_{g_{S_0}}(\omega_0) \cdot c_{g_{A_0}}(\omega_0)}{\left(c_{g_{S_0}}(\omega_0) + c_{g_{A_0}}(\omega_0)\right)} \quad (113)$$

where t_e is the time-span of the excitation signal and $c_g(\omega_0)$ is the group velocity of a particular mode at angular frequency ω_0 . Furthermore, a minor correction term equal to half the actuator size along the direction of propagation is added to these estimates. This is because, as seen in Chapter II, for surface-bonded piezoelectric actuators, the GWs originate from the edge of the transducer, and not its center. Next, the wavenumbers for each mode are calculated over the excited angular frequency range:

$$\xi_{S_0}(\omega) = \frac{\omega}{c_{ph_{S_0}}(\omega)}; \quad \xi_{A_0}(\omega) = \frac{\omega}{c_{ph_{A_0}}(\omega)} \quad (114)$$

It is assumed that after the GW excited by the actuator hits the damage site, it becomes a point-source emitting circular crested waves axisymmetrically. The spatial variation of the piezoelectric sensor response is therefore described by the Hankel function of order zero (as seen for circular actuators in Chapter II). Since this wave is reflected from the damage site back towards the collocated actuator/sensor, it is an incoming wave. Therefore, if time dependence is of the form $e^{i\omega t}$, then the Hankel function of the first kind represents the incoming wave. For the case of symmetric mode reflection, the entire distance $2r_{S_0}$ is traversed as symmetric mode (since it was assumed that the S_0 mode was predominantly excited). For the case of anti-symmetric mode reflection, half the total distance $2r_{A_0}$ (from the actuator to the damage site) was traveled as S_0 mode, whereas the second half was traveled as the A_0 mode. Therefore, the harmonic surface strain response waveforms $Y(\omega)$ for the two cases are (ignoring constants of proportionality, since only the shape is of interest):

$$Y_{S_0}(\omega) = H_0^{(1)}(\xi_{S_0}r_{S_0}).H_0^{(1)}(\xi_{S_0}r_{S_0}); \quad Y_{A_0}(\omega) = H_0^{(1)}(\xi_{S_0}r_{A_0}).H_0^{(1)}(\xi_{A_0}r_{A_0}) \quad (115)$$

Here the effect of the piezo sensor response being proportional to the average strain over its surface area is neglected for simplicity. For the 2-D FEM simulations, the incoming wave is given by the complex exponential function with positive exponent:

$$Y_{S_0} = e^{i\xi_{S_0}r_{S_0}}.e^{i\xi_{S_0}r_{S_0}} = e^{i(\xi_{S_0}2r_{S_0})}; \quad Y_{A_0} = e^{i(\xi_{S_0}r_{A_0} + \xi_{A_0}r_{A_0})} \quad (116)$$

The chirplet matching pursuit scheme uses a database of Gaussian atoms. Therefore, to recover the time domain waveform $y(t)$ for a band-limited burst considering the frequency bandwidth and Gaussian modulation, the following equations are used:

$$y_{S_0}(t) = \int_{\omega_0 - \Delta\omega/2}^{\omega_0 + \Delta\omega/2} g(l_0(\omega - \omega_0)).(H_0^{(1)}(\xi_{S_0}r_{S_0}))^2 e^{i\omega t} d\omega \quad (117)$$

$$y_{A_0}(t) = \int_{\omega_0 - \Delta\omega/2}^{\omega_0 + \Delta\omega/2} g(l_0(\omega - \omega_0)) \cdot H_0^{(1)}(\xi_{S0} r_{A0}) \cdot H_0^{(1)}(\xi_{A0} r_{A0}) e^{i\omega t} d\omega \quad (118)$$

where $\Delta\omega$ is the angular frequency bandwidth and $g(\cdot)$ is the Gaussian window vector centered at angular frequency ω and with the chosen scale l_0 . A similar equation holds for the 2-D FEM simulations. Of course, in practice, this is implemented in the discrete (digital) domain. The inverse fast Fourier transform can be used for efficient computation.

It should be noted that in this work, SH-modes were not considered for the following reasons:

- a) In the FEM simulations, the elements were 2-D, i.e., out-of-plane displacements are not possible by design. Thus, SH-modes are not possible.
- b) In the performed experiments, surface-bonded piezoelectric wafer transducers are used as sensors, which are almost entirely insensitive to shear waves. This is because they only sense the average in-plane surface extensional strain and not shear strain, as mentioned before.

Once these waveforms are generated, the chirplet matching algorithm is applied to them (restricting the scale of the dictionary chirplets to l_0) and the chirp-rates corresponding to each mode at each point of the time-frequency grid are obtained. The chirplet matching pursuit was implemented using *LastWave* 2.0 [215], which is freeware. Thus, one has the database required to use the proposed algorithm for GW signal processing, which is described next.

IV.4.B Processing the Signal for Damage Detection and Characterization

The signal-processing procedure consists of the following steps:

- i) The chirplet matching pursuit algorithm is applied to the difference between the test signal and the signal for the undamaged state. A dictionary of chirplets with fixed

scale l_0 as discussed in Section IV.4.A is used. Thus, the dictionary consists of signals of the form:

$$k_{(u,\omega,c)}(t) = \frac{1}{\sqrt{l_0}} g\left(\frac{t-u}{l_0}\right) \exp\left[i\left(\omega(t-u) + \frac{c}{2}(t-u)^2\right)\right] \quad (119)$$

where the time center u is between the end of the first transmitted pulse received by the sensor collocated with the actuator and the start of the boundary reflection while the angular frequency center ω is within the excited angular frequency bandwidth. This yields the time-frequency centers (t_0, f_0) , the chirp-rates (c_0) and the signal energies of the constituent atoms (note that $\omega_0 = 2\pi f_0$).

- ii) The algorithm is run until the last atom extracted has energy above a certain percentage of the first and most energetic extracted atom. In this work, this percentage was chosen to be 10%. In the author's experience, atoms below this threshold tend to correspond to approximation errors.
- iii) The most energetic atom in the time-span not corresponding to the excitation signal or boundary reflections is examined. If it has energy above a certain threshold, the structure is judged damaged. There is no hard and fast rule to decide the value of this threshold, which is a critical parameter. The decision is dependent on the energy in the signal difference corresponding to the excitation time interval. In practice, no signal generator will be able to reproduce an excitation signal with 100% accuracy, and there is always some difference in the excitation signal as seen by the collocated sensor³. In this work, the threshold was set to be 50% of the energy in the excitation signal difference. This might need to be lowered for structures with stronger damping characteristics. In addition, for the final SHM system, this threshold must also take into account false positive/false negative probabilities and risk assessment, which are highly application dependent.
- iv) Next, mode identification is done using the atom's chirp-rate. It is compared with that of the possible modes for the same time-frequency center in the database. The

³ Due to the impossibility of perfect reproduction of the excitation signal, there is a small blind zone in the vicinity of the collocated actuator-sensor pair. This is associated with the sensor being unable to distinguish the small amplitude GW reflections from damage sites that might be very close to the actuator from the strong first transmitted pulse from the actuator.

mode is identified as the one that minimizes the absolute value of the difference between the atom's chirp-rate and the chirp-rate for each mode at the same time-frequency center.

- v) Knowing the mode and time-frequency center of each atom, the damage site's radial location relative to the transducer is known. Although damage-type classification was not addressed in this work, the damage can then be characterized by using the frequency center, the energy in the reflection from the damage site, and the relative modal contributions from the damage site. This information can be used to infer what the damage type is in conjunction with an artificial neural network trained using prior experimental data or some modeling studies.

The proposed algorithm is summarized in the flowchart depicted in Fig. 41.

IV.5 Demonstration of the Algorithm's Capabilities

IV.5.A FEM Simulations

In Section IV.2, it was seen that the spectrogram was capable of isolating the individual reflections and identifying their modes for the simple case of the GW signal in Fig. 35 (d). Now consider the more complex signal in Fig. 35 (c), with overlapping multimodal reflections. The portion of the signal between the end of the excitation signal and the start of the boundary reflection, after artificial corruption with white Gaussian noise (of amplitude 5% of the peak value in the signal), is shown in Fig. 42 (a). The spectrogram for this signal (again, using a modulation window identical to that in the excitation signal) is shown in Fig. 42 (b), on a decibel scale relative to the peak value in the image. The spectrogram cannot separate the overlapping multimodal reflections from the two notches, which are smeared together in the spectrogram. The time-frequency plot from the chirplet decomposition using the matching pursuit algorithm is shown in Fig. 42 (c), also on a decibel scale. The power of this approach is evident from this figure, where clearly the individual overlapping reflections from the two notches are resolved. In addition, as highlighted in Table 1, the modes of the individual reflections are correctly identified and the axial locations of the notches are identified with a maximum deviation

of 0.6 cm, or 6% of the distance from the transducer. For the two reflections that the spectrogram could isolate, the errors for radial estimates are greater than that from the proposed algorithm. Thus, the proposed algorithm shows superior resolution compared to the spectrogram.

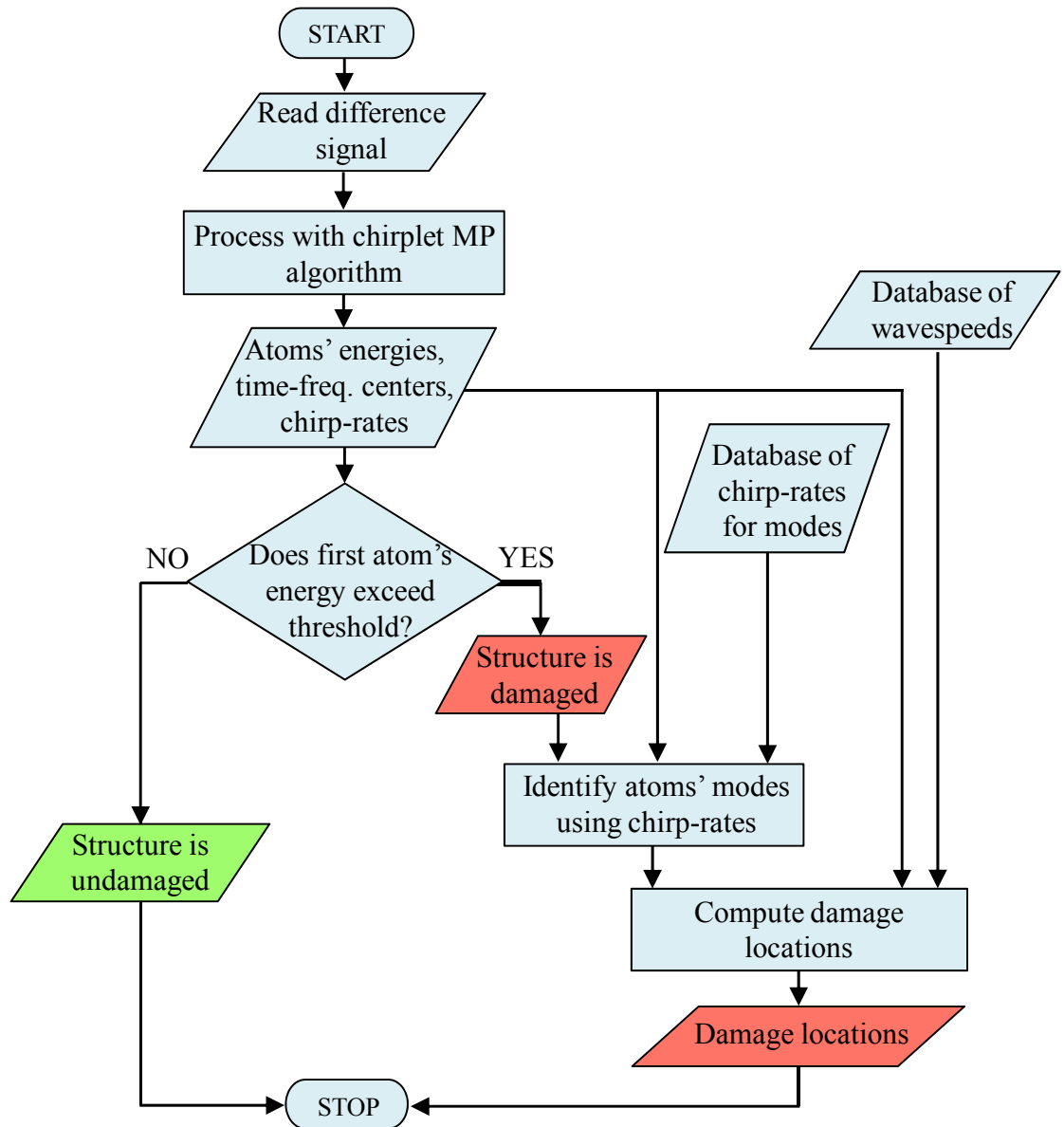
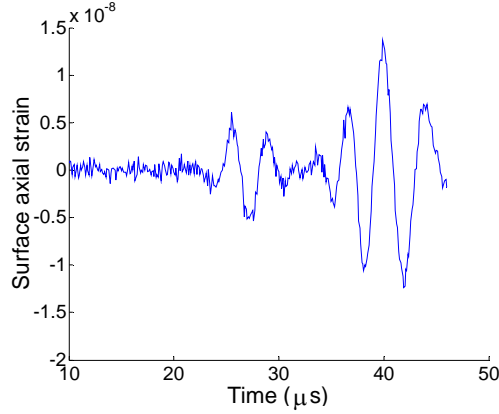
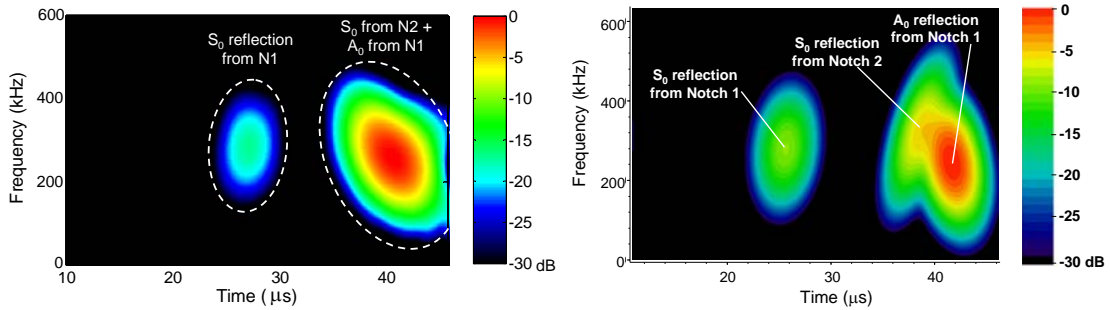


Fig. 41: Flowchart of proposed signal processing algorithm



(a)



(b)

(c)

Fig. 42: (a) Portion of signal in Fig. 35 (c) with overlapping multimodal reflections and corrupted with artificial noise; (b) Spectrogram of the signal in (a); (c) Interference-free WVD of constituent chirplet atoms for the signal in (a)

IV.5.B Experimental Results

In order to verify the proposed algorithm's potential capabilities, experiments were conducted with a 1-mm thick Aluminum plate structure, the schematic of which is shown in Fig. 43 (a). The 1-mm thick aircraft-grade Aluminum alloy plate was supported on two support struts on two edges and the other two edges were free. Surface-bonded PZT-5A piezoceramic transducers were used. The actuators were excited symmetrically with a 2.5-cycle Hanning-windowed sinusoidal toneburst of center frequency 175 kHz,

thereby predominantly exciting the S_0 mode. After baseline signals were recorded for the pristine condition, artificial “damage” sites in the form of C-clamps were introduced, seen in Fig. 43 (b). The C-clamps act as local scatterers of GWs incident on it over their contact area, causing incident GWs to be scattered from them. Damage in the structure, such as cracks, dents or impact damage would also have a similar effect on GWs incident on it. The difference signal between the pristine and “damaged” cases is shown in Fig. 44 (a). Again, in this case, the spectrogram, shown in Fig. 44 (b), is incapable of resolving the overlapping S_0 mode reflections from the two clamps. On the other hand, the proposed algorithm showed its superior resolution in this case too. The chirplet matching pursuit step was able to resolve the overlapping S_0 mode reflections as well as the S_0 and A_0 mode reflections from the boundary, as seen in shown in Fig. 44 (c). The second step correctly identified the modes, thereby allowing accurate radial location estimates of the clamps, as seen in Table 2 (Errors in location: C1 - 0.3 cm; C2 - 0.9 cm). The spectrogram’s estimated location (for the reflection from the clamp that it could localize) has the same error as the proposed algorithm. When using the relative modal contributions to characterize the damage site, one must bear in mind that a finite-dimensional piezoceramic sensor has different sensitivities to different wavelengths of the GW sensed. As a first-order approximation, it might suffice to normalize the energy

Chi- rplet #	t_0 (μ s)	f_0 (kHz)	c (kHz / μ s)	Signal energy (2-norm)	c_{A0} (kHz / μ s)	c_{S0} (kHz / μ s)	Mode	r actual (cm)	r from new algo. (cm)	r from spect. (cm)
1	41.6	245.9	-13	1.4×10^{-14}	-12.5	0.6	A_0	6.0	6.4	6.5
2	38.4	319.6	34	3.7×10^{-15}	-10.2	0.5	S_0	10.0	9.4	-NA-
3	25.6	280.8	7.4	1.8×10^{-15}	-7.9	0.3	S_0	6.0	5.9	6.3

Table 1: Simulated notch damage in FEM simulation (Key: c_{A0} \equiv chirp-rate from database assuming A_0 mode reflection; c_{S0} \equiv chirp-rate from database assuming S_0 mode reflection; Mode \equiv identified mode; r actual \equiv actual radial location of notch; r from new algo. \equiv estimate of radial location of notch from proposed algorithm; r from spect. \equiv estimate of radial location of notch from spectrogram)

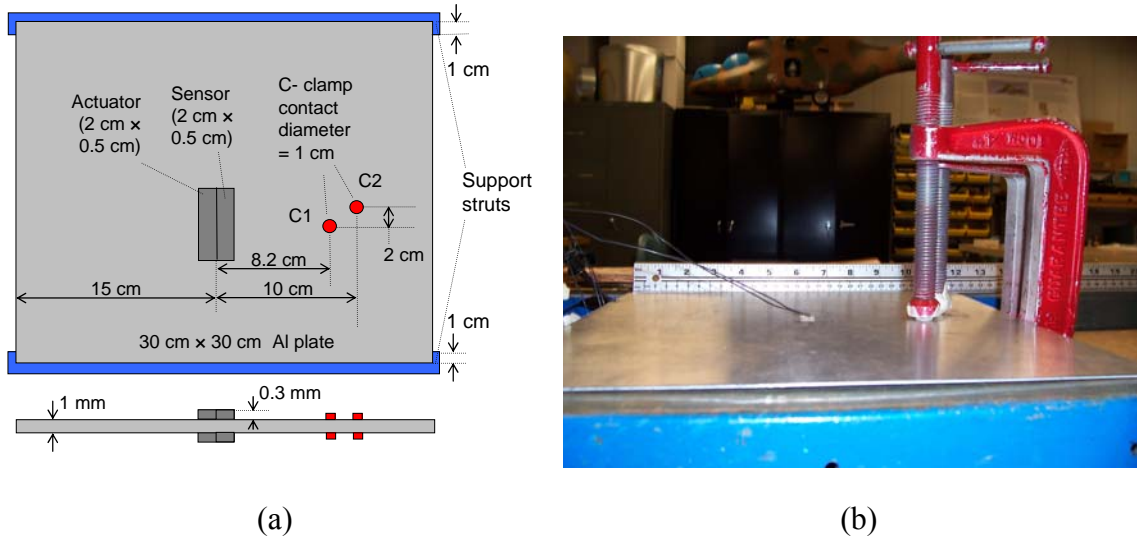


Fig. 43: (a) Schematic of experimental setup and (b) Photograph of experimental setup

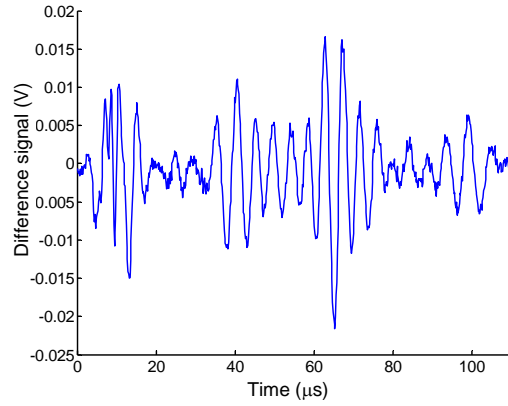
of each reflection to the sensitivity of the sensor to the wavelength corresponding to the center frequency for the GW mode of the reflection (which can be obtained using the theoretical model for piezo-sensor response in Chapter II).

It should be noted that the best accuracy in radial location estimation was in the FEM simulation with the S_0 mode reflection from N1 (error: 0.1 cm). There are two reasons for this: (i) the reflection was isolated (i.e., not overlapping with another reflection) and (ii) the notch was very thin axially (0.025 cm), and hence the “point-scatterer” damage site model was realistic. In the experiment, the clamp had a contact diameter of 1 cm, weakening this assumption, as reflected in the location errors. Furthermore, the error tends to be worse for the weaker reflection in overlapping reflections, as one would naturally expect. Another error source is the uncertainty in material properties, which affects wavespeeds. Despite these errors, which are minor, the advantages of the new algorithm over conventional approaches to GW signal processing can be clearly seen with these results. However, it should be pointed out that testing was restricted to the fundamental GW modes in this work. At higher frequencies, in the presence of higher GW modes, the use of linear chirplets may not suffice. Quadratic or higher order chirplets might need to be employed, such as in the work by Hong et al.

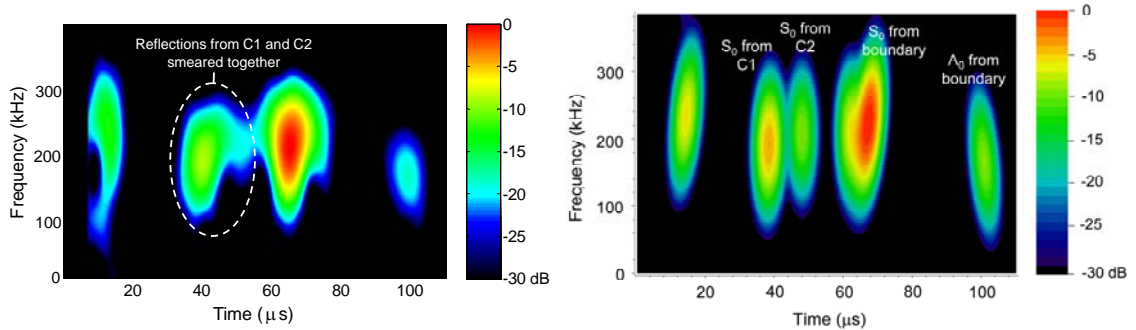
[214]. In that work, the matching pursuit approach was used with quadratic chirp functions for GW signal processing. However, in that work, sensing was restricted to one mode there (by controlling the number of coil turns in the magnetostrictive GW sensor used) and mode classification was not addressed. It should be noted that in this work, the two modes had different dispersion characteristics over the excited frequency bandwidth. If the two modes are similar to each other in terms of variation of wavespeed with frequency, the chirp-rates for the two modes may be very close to each other. The algorithm presented here may not be able to distinguish the modes. Until this point, only radial location of damage sites relative to a transducer pair has been discussed. In the next section, triangulation using multiple transducers in isotropic plates is discussed.

Chi-rplet #	t_0 (μs)	f_0 (kHz)	c (kHz/ μs)	Signal energy (2-norm)	c_{A0} (kHz/ μs)	c_{S0} (kHz/ μs)	Mode	r actual (cm)	r from new algo. (cm)	r from spect. (cm)
1	67.2	221.5	7.8	7.3×10^{-3}	-5.11	0.14	S_0	bndry	bndry	bndry
2	38.4	190.9	1.7	2.9×10^{-3}	-4.55	0.07	S_0	8.2	8.5	8.5
3	14.4	234.2	7.7	1.9×10^{-3}	-1.79	0.01	Exctn			
4	62.4	208.3	0.0	1.8×10^{-3}	-5.17	0.13	S_0	bndry	bndry	Bndry
5	100.8	166.1	-7.6	9.4×10^{-4}	-4.63	0.33	A_0	bndry	bndry	Bndry
6	48.0	208.3	0.0	9.2×10^{-4}	-4.76	0.09	S_0	10.2	11.1	-NA-

Table 2: Experimental results of isotropic plate with simulated damage (Key: c_{A0} \equiv chirp-rate from database assuming A_0 mode reflection; c_{S0} \equiv chirp-rate from database assuming S_0 mode reflection; Mode \equiv identified mode; r actual \equiv actual radial location of clamp; r from new algo. \equiv estimate of radial location of clamp from proposed algorithm; r from spect. \equiv estimate of radial location of clamp from spectrogram; bndry \equiv boundary reflection; Exctn \equiv difference in excitation signal)



(a)



(b)

(c)

Fig. 44: (a) Difference signal between pristine and “damaged” states; (b) Spectrogram of the signal in (a) and (c) Interference-free WVD of constituent chirplet atoms for the signal in (a)

IV.6 Triangulation in Isotropic Plate Structures

In order to pinpoint the in-plane location of a damage site in an isotropic plate structure and characterize it, one needs the radial locations of the damage site relative to at least three pairs of central collocated piezoelectric transducers. It is highly desirable to use circular or ring-shaped transducer wafers, so that there is no directional selectivity or preference. In addition, care must be taken to use as thin piezoelectric wafers as possible to minimize the extraneous reflections caused by the increased local stiffness of the

structure where the transducer is bonded. The proposed algorithm needs to be repeated for the signals obtained using each collocated actuator/sensor pair. If there are multiple mode reflections observed from the damage site, the average radial location obtained from the modes can be used. One can then draw three circles of radii equal to the radial locations thus found, about the centers of the corresponding actuator/sensor pairs. The intersection of the three circles would yield the location of the damage site. This is illustrated in Fig. 45 (a). In addition, as before, the relative modal contributions, the frequency center and individual modal energies can be as input parameters for a pattern recognition algorithm used to classify the damage and quantify its severity.

If however, one is mainly interested in locating damage and not in characterizing it, an easier approach can be adopted. Instead of using three collocated piezoelectric actuator/sensor pairs, it suffices to use three circular piezoelectric wafer transducers, and while one is excited, the others can be used as sensors. However, in this approach, one must ensure that the elements are sensitive only to one mode when used as sensors. Then, the chirplet matching pursuit step is used to find the time-of-flight from the actuator to the damage site and back to one of the sensors as well as the frequency center of the pulse. This yields the distance traveled by the pulse, say d (since only one group velocity is possible). The locus of all possible locations of the damage site is an ellipse with the actuator and the sensor as its foci and d as the major axis. By exciting each actuator in turn and using the others as sensors, three such ellipses can be drawn and the damage site is located at their intersection. This concept was proven experimentally using a 3.15-mm thick Aluminum 5052 alloy plate instrumented with three surface-bonded piezoelectric discs of diameter 1.3 cm each and thickness 0.23 mm each. The excitation signal used was a 2.5-cycle Hanning windowed sinusoidal toneburst with center frequency 210 kHz. At this frequency and in its vicinity, the A_0 mode wavelength nearly equals the transducer diameter. Therefore, as mentioned in Section II.9.C, the transducers are insensitive to A_0 modes when used as sensors, and only the S_0 mode needs to be considered. The results from this experiment are shown in Fig. 45 (b). A through-hole of diameter 5 mm was drilled into the plate as shown to check if its location could be found using this approach. While one expects the three ellipses to intersect at one point, due to experimental imperfections, they come close to intersecting each other at a single point but don't quite

do so, resulting in a triangular error box. This gives a crude estimate of the damaged area. The center of the error box was 0.5 cm away from the center of the drilled hole. It should be noted that in this simplified approach, it is crucial to restrict the sensing to one mode. If more than one mode is possible, the locus of all points of the damage site given the time-of-flight and center frequency from one transducer to another is not necessarily an ellipse. Since one cannot be sure about how much of the time was spent traveling as one mode and how much as another, the locus would, in general, be an intricate shape and this shape would need to be recalculated for different times-of-flight, thereby making the algorithm computationally intensive. This ellipse triangulation technique has been discussed in the open literature (e.g., Kehlenbach and Das [32]), but the case of multimodal signals has not received much attention.

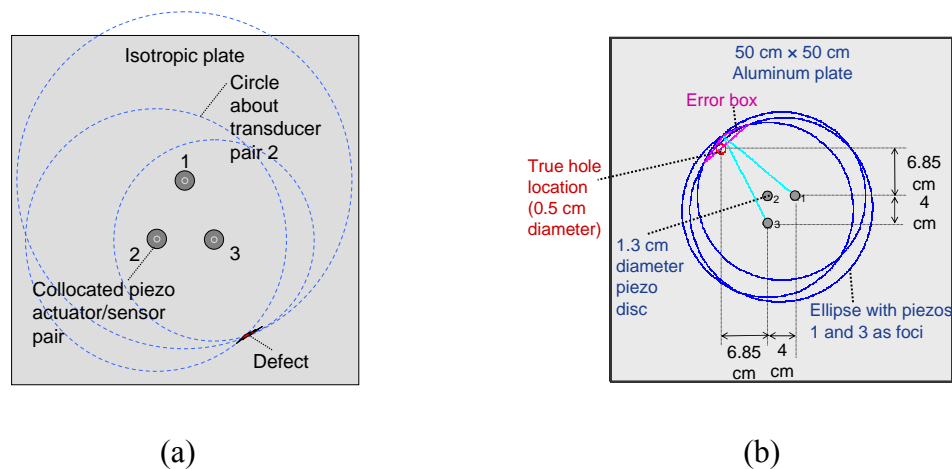


Fig. 45: (a) Approach for locating and characterizing damage sites in the plane of plate structures using multimodal signals and (b) Experimental results for in-plane damage location in plate structures using unimodal GW signals

In summary, this chapter presented a novel signal processing algorithm for GW signal processing (for pulse-echo approaches) using chirplet matching pursuits. Its theoretical advantages over conventional algorithms for GW SHM were discussed: better resolution and lack of interference terms (enables it to separate overlapping multimodal reflections), robustness to noise, and ease-to-automate post-processing as needed for

SHM. The implementation of the chirplet matching pursuit algorithm used here has computational efficiency that is better than that of spectrograms. In some initial FEM and experimental tests, the proposed algorithm was able to separate overlapping, multimodal reflections and estimate radial locations of artificially introduced damage with good accuracy. The resolution of the algorithm was shown to be superior or equal to that using a spectrogram. In tests done to examine in-plane triangulation using multiple transducers, a 0.5 cm diameter thru-hole was triangulated within 0.5 cm of its actual location (or with an error of 4% for damage located at 12.5 cm from the plate center). This damage size and location accuracy satisfy the performance metrics decided *a priori* for the project that funded this research in coordination with the collaborators and sponsors [216]. However, these tests were done at room temperature and do not necessarily simulate environmental conditions expected in field applications. For spacecraft environments in particular, as mentioned earlier, temperature changes can be significant. The next chapter explores the effects of elevated temperature on GW SHM.

CHAPTER V

EFFECTS OF ELEVATED TEMPERATURE

It is evident from the literature reviewed in Section I.6.A that the issues of compensation for and damage characterization under thermal variations expected in GW SHM for internal spacecraft structures (above room temperature) have not received much attention. This chapter aims to contribute in these aspects. First, the temperature variation in the application area where this is hoped to be applied, i.e., internal spacecraft structures is examined. Then, studies done to find a suitable bonding agent (for GW SHM using piezoceramics on aluminum plates) that does not degrade in the expected temperature range for this application are reported. With a suitable bonding agent chosen, controlled experiments are done to examine changes in GW propagation and transduction using PZT-5A piezos under quasi-statically varying temperature in the same range. All parameters changing with temperature are identified and quantified based on data from the literature. This data is used in the models developed in Chapter II to try and explain the experimental results. Finally, these results are used to explore detection and location of damage (indentations/holes) using the pulse-echo GW testing approach in the same temperature range.

V.1 Temperature Variation in Internal Spacecraft Structures

The work in this chapter is motivated by the potential application of GW SHM to NASA's spacecraft structures, specifically the planned crew exploration vehicle (CEV) for returning astronauts to the Moon and eventually to Mars. As outlined in [217], the

CEV, called “Orion,” is expected to have an aluminum alloy internal structure in the shape of a blunt body capsule protected by bulk insulation, composite skin panels, and a thermal protection system (TPS). Spacecraft structures in particular present a challenging application due to the harsh environment of outer space as well as the tremendous heat flux and high temperatures attained during re-entry into a planet’s atmosphere. The internal spacecraft structures, however, are somewhat insulated by the TPS. The TPS is typically designed to keep temperatures below 150°C in internal structures, particularly in manned missions [218]. Apart from the re-entry phase, even in the course of the flight, the temperature of spacecraft structures varies significantly, with temperatures up to 70°C (Larson and Wertz [219]) depending on whether they face towards or away from the Sun. For solar arrays, this fluctuation is even greater (up to 100°C, see [219]). Another source of temperature variation in internal spacecraft structures is the heat radiated by cabin electronics, which is difficult to reject into space, and is therefore controlled by active cooling. Commercial piezos are functional without loss in properties up to half their Curie temperature. For PZT-5A, one of the more commonly used piezoceramics, half the Curie limit is about 175°C. Thus, internal spacecraft structures become a potential application area for GW SHM using PZT-5A piezos. However, the GW SHM algorithm must account for temperature changes to minimize false damage indications and reduce errors in damage characterization. This chapter explores this issue in the temperature range 20°C to 150°C.

V.2 Bonding Agent Selection

After an initial pre-screening, three different two-part epoxies were evaluated for the temperature range of interest. These were 10-3004 (from Epoxies, Etc. [220]), and Epotek 301 and 353ND (from Epoxy Technology [221]). Epotek 301 and 353ND, both low-viscosity agents, are rated for continuous operation up to 200°C and 250°C, respectively. 10-3004 is relatively viscous, and is rated for continuous operation up to 125°C, although the manufacturer clarified that it should work up to 150°C for short-term use (hours). In addition, it was confirmed from the manufacturers that each epoxy would be suitable for surface-bonding piezoceramics (with metallic electrodes) on aluminum

plates. While 10-3004 and 301 can be cured overnight at room temperature, 353ND needs to be cured in an oven at 80°C for 25 minutes. Standard surface preparation procedures were followed with each, i.e., the plate surface was made rough by light sanding and both the plate and piezos were cleaned thoroughly using acetone to get rid of grease and dust. After uniformly applying a thin-layer film of epoxy to both surfaces and cleaning the excess, light pressure was applied using 2 lb. weights to the interface to help the bond set.

The first aluminum alloy (5005) plate specimen (shown in Fig. 46) tested had four PZT-5A piezos (0.3 mm thick) that were surface-bonded using Epotek 301. Two piezos were used as actuators (at the center, on either surface), and two as sensors. One of the sensors (sensor 1) was collocated with the actuator, and the other (sensor 2) was 10 cm away from the plate center. This specimen was thermally cycled from 20°C to 150°C in an industrial oven and then cooled back to room temperature over three cycles. A Labview-based automated thermal test setup was developed for these experiments. After turning the oven on, at every 10°C intervals (read by a type-K thermocouple with $\pm 1^\circ\text{C}$ accuracy attached to one side of the plate specimen), the Labview program triggered an Agilent 33220A function generator to send a 3.5-cycle Hanning-windowed toneburst, with center frequency 210 kHz to the actuators (excited symmetrically), 16 times each at 1-second intervals. A Hewlett Packard 54831B Infiniium oscilloscope recorded the sensor response signals, which were sampled at 10 MHz and averaged over the 16 readings at each temperature. In these tests, it was observed that the sensor response signal of sensor 2 decreased monotonically in peak-to-peak amplitude with increasing temperature (Fig. 47). The error bars shown are based on the standard deviation over the 16 readings at each temperature. Furthermore, sensor 2's response signal amplitude at room temperature decreased at the end of each cycle, and the shape of the signal also changed significantly, as shown in Fig. 48. It should be noted that the sensor response was compensated for varying actuation signal magnitude (which dropped due to the increasing capacitance of the actuators with temperature). While some amount of irrecoverable loss in response strength is expected after the first few cycles, due to thermal pre-stabilization of piezos [222], the signal shape is not expected to change. Despite the actuators being excited symmetrically, and thereby only supposedly exciting

the S_0 mode, experimental imperfections cause weak A_0 mode excitation. To counter this, the sensor was originally designed to be very weakly sensitive to the A_0 mode (as discussed in Chapter II, the sensor size equaled the A_0 mode wavelength at 210 kHz). However, after each cycle, the strength of the slower A_0 mode contribution in the sensor 2 signal increased. This suggested that the sensor's effective area kept decreasing after each cycle. Based on these factors, it was concluded that the Epotek 301 bond line was indeed degrading as a result of the thermal cycling. An analogous test was done with PZT-5A transducers bonded using 10-3004 on an Aluminum alloy (5005) plate. In this case, the results were even more drastic and the sensor response dropped gradually to the noise floor at 100°C while heating in the very first cycle, and never recovered (Fig. 49).

Finally, tests were done with Epotek 353ND. The specimen tested was similar to the ones tested above. The schematic of this is shown in Fig. 50. The specimen was thermally cycled in the same temperature range seven times in the oven. In this case, the sensor response amplitude and shape did not change (within negligible error margins, see Fig. 51) when the signals before and after each thermal cycle are compared. The very first cycle was an exception, being the thermal pre-stabilization cycle discussed before,

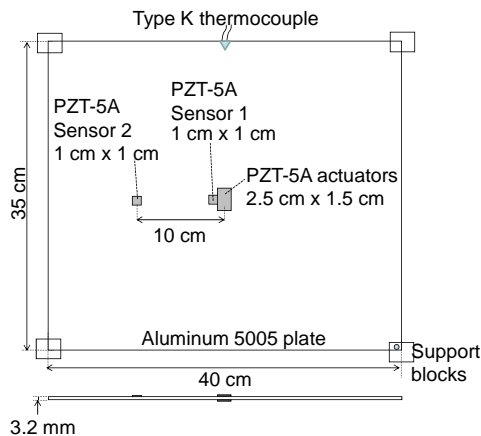


Fig. 46: Schematic of specimen for tests with Epotek 301

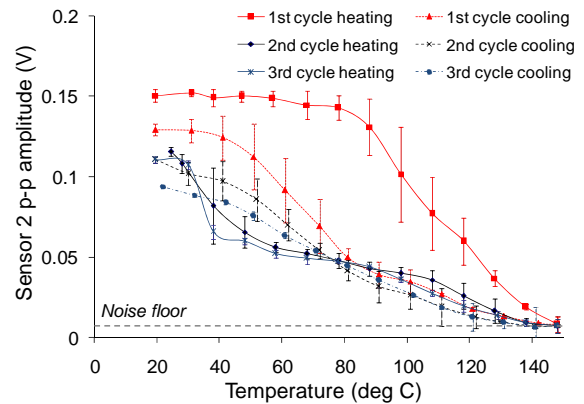


Fig. 47: Variation of sensor 2 response amplitude (peak-to-peak) and associated error bars with temperature over three thermal cycles (for tests with Epotek 301)

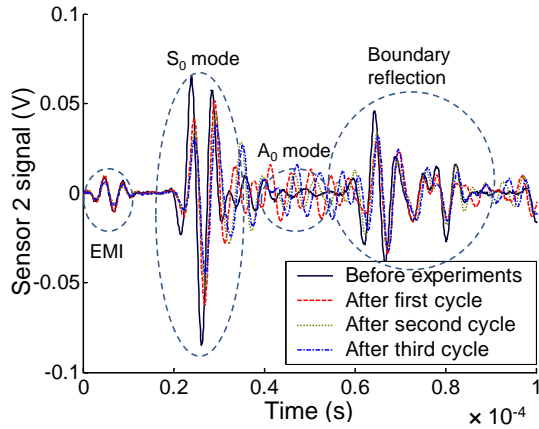


Fig. 48: Sensor 2 signal at room temperature before and after each of the three thermal cycles (for tests with Epotek 301; EMI \equiv electromagnetic interference from the actuation)

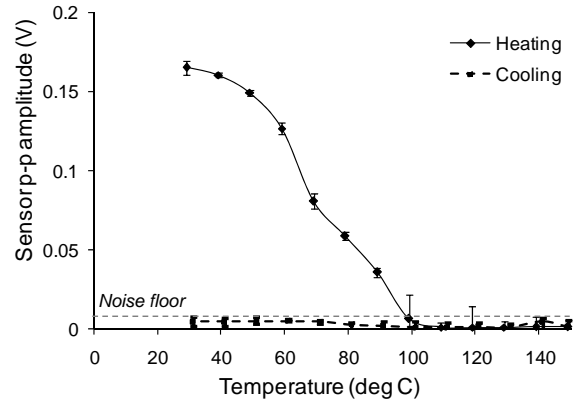


Fig. 49: Variation of sensor response amplitude (peak-to-peak) with temperature for tests with epoxy 10-3004 – the curve hits the noise floor at 100°C while heating and does not recover

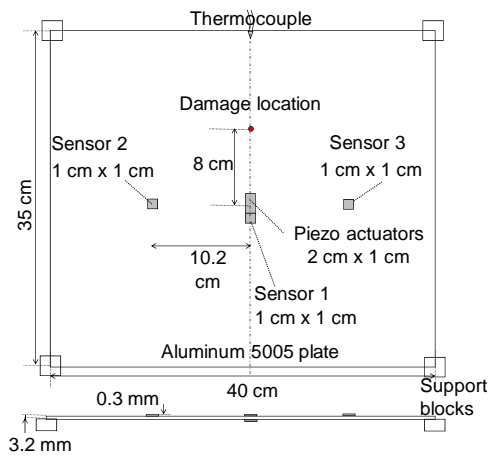


Fig. 50: Schematic of specimen for tests with Epotek 353ND (Damage introduced later and discussed in Section).

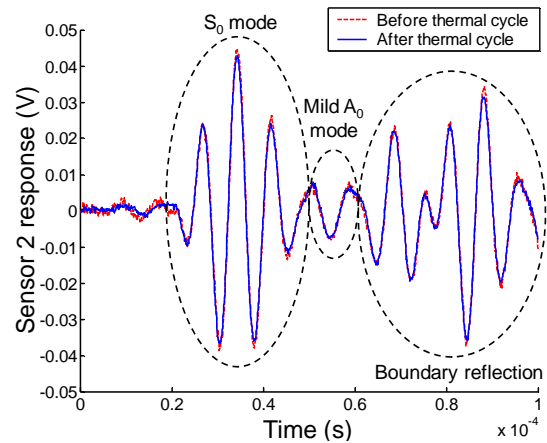


Fig. 51: GW signal sensed by sensor 2 (bonded using Epotek 353ND) before and after a thermal cycle

which caused a 17% drop in sensor 2 and 3 response amplitude. Thus, this epoxy proved to be suitable for the purposes of this study. Thereafter, more controlled tests were conducted with this same specimen to study signal changes and to explore damage characterization at different temperatures, which is discussed in the following sections.

V.3 Modeling the Effects of Temperature Change

In designing the specimen for tests with Epotek 353ND, sensor 1 was collocated with the actuators with the intention of using it for damage detection using pulse-echo tests. Sensors 2 and 3 were for tracking changes in the GW transmitted signal with temperature (in undamaged state). In addition, sensors 2 and 3 also act as mild GW scatterers, due to the increased local stiffness and mass caused by their presence. This simulates the effect of some structural features (e.g., rivets) which could act as GW scatterers in more complex structures. While the specimen was tested in the industrial oven initially to check for bond degradation, the oven's heating/cooling rate could not be tightly controlled, and was very rapid (up to 10°C/minute) at times. This fast heating rate led to non-repeatable signals for sensor 1, which could potentially be interpreted as false positives. This is discussed in the next section. More controlled tests were subsequently done in a computer-controlled autoclave (Fig. 52), where both the heating and cooling rates were set to 1°C/minute. A five-minute dwell period at 150°C was also included in the thermal cycle between the heating and cooling phases (Fig. 53). The data at 90°C and 100°C while cooling was not used, since in this temperature range, the autoclave switches from exclusively air cooling to a combination of air and water cooling, leading to oscillations in the cooling rate over this range. For these tests, the center frequency was reduced to 120 kHz. This was to minimize actuation signal distortion effects at higher frequencies caused by increasing actuator capacitance at higher temperatures. While a Krohn-Hite 7500 wideband amplifier was tried for a couple of thermal cycles in the oven, it was unable to amplify without significant signal distortion and ripple at higher temperatures. Therefore, no amplifier was used for the controlled tests in the autoclave. The actuation signal was still a 3.5-cycle Hanning windowed toneburst of 18 V peak-to-peak amplitude at 20°C, with the two actuators on either surface excited symmetrically. Samples were averaged over 30 points at all temperatures to reduce noise further. Data was collected for two thermal cycles for the pristine, undamaged condition. As mentioned before, there is a drop in actuation amplitude from 18 V to around 13 V (but negligible shape distortion) as temperature increases due to increasing actuator capacitance. All data presented for higher temperatures in this chapter have been scaled for 18-V actuation level. Fig. 54 and Fig. 55 show the GW signal read by sensor 2 at various temperatures

while heating and cooling respectively. Evidently, there is a decrease in GW speed of the first transmitted GW pulse as temperature increases. In addition, the signal amplitude seems to increase with increasing temperature up to a certain point (around 90°C) and then decreases with increasing temperature. Hysteresis effects are negligible here, unlike in the oven tests, where significant hysteresis was observed between the heating and cooling phases due to very different temperature change rates in the two phases.

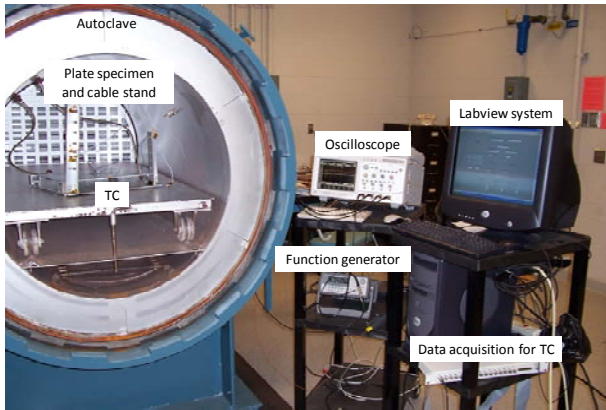


Fig. 52: Labeled photograph of setup and autoclave for controlled thermal experiments (TC \equiv thermocouple).

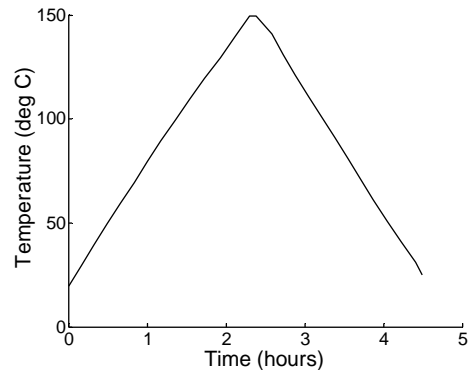


Fig. 53: Typical time-temperature curve for experiments done in the computer-controlled autoclave

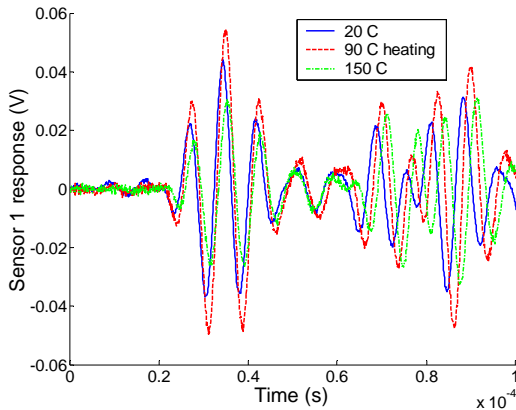


Fig. 54: GW signals recorded by sensor 2 (averaged over 30 samples) while heating

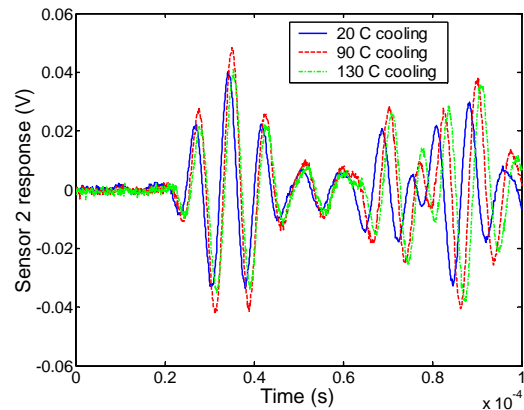


Fig. 55: GW signals recorded by sensor 2 (averaged over 30 samples) while cooling

In order to explain these effects, an effort was made to identify all parameters in the experiment that change with temperature. The following list was compiled and data for their thermal variation was found from various sources in the literature:

- a) Young's moduli of structural substrate and PZT-5A: The substrate elastic modulus is a very important parameter in modeling the effect of temperature for GW SHM. There is a significant decrease in the elastic modulus of aluminum with increasing temperature. This causes a reduction in GW speeds, as reflected in the change in dispersion curves. Furthermore, in quantifying thermal variations of elastic modulus, two different data sets were found: one, for the variation in *static* elastic modulus [223], and the other for *dynamic* elastic modulus (Lord and Orkney [224]). This data is shown in Fig. 58. The former was obtained from standard stress-strain tests conducted under varying temperature for aluminum alloy 7075, while the latter was found from measuring changes in natural frequency of aluminum beam (alloy 5052) flexural vibrations with temperature. No data was found for aluminum 5005, the material used in the tests here. However it is similar in composition to the two alloys for which data was found. The variation in elastic modulus of PZT-5A is relatively small [225]. No data was obtained for dynamic elastic modulus variation of PZT-5A.
- b) Piezoelectric properties of PZT-5A: It is well-known that the piezoelectric constants (d_{31} and g_{31}) vary significantly with temperature (Berlincourt, Krueger and Near, [222]). For GW SHM, the variation in the product $d_{31} \cdot g_{31}$ is of relevance (the d_{31} constant is associated with actuation shear stress induced, while the g_{31} constant is associated with the piezo-sensor sensitivity), and this can vary by as much as 7%, as shown in Fig. 59. In addition, the dielectric constant of PZT-5A increases linearly with temperature, which causes the load seen by the function generator to increase. This however, does not affect sensor response by itself.
- c) Thermal expansion: This is a relatively mild effect, and causes the plate thickness, piezo dimensions and distances travelled by the GWs in the plate to increase and density to decrease. Since the thermal expansion coefficients of aluminum and PZT-5A are known (average values over 20°C to 150°C are $\alpha = 25.5 \mu\text{m}/\text{m}^\circ\text{C}$ for aluminum obtained from Matweb [226]; $\alpha_1 = 2.5 \mu\text{m}/\text{m}^\circ\text{C}$ for PZT-5A, see Williams, Inman and Wilkie, [225]), these effects can be accounted for. The effect of

changing (static) elastic modulus, plate thickness and density were used to compute Lamb-wave phase velocity dispersion curves at different temperatures (Fig. 58).

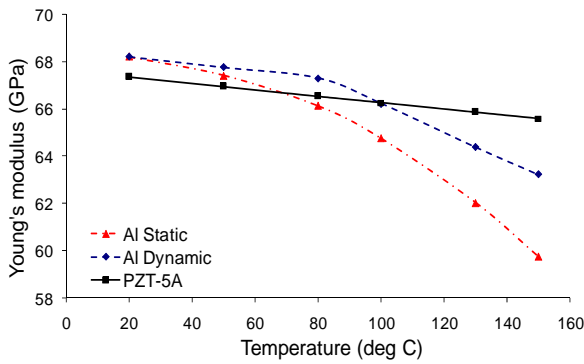


Fig. 56: Variation of Young's moduli ([223]-[225])

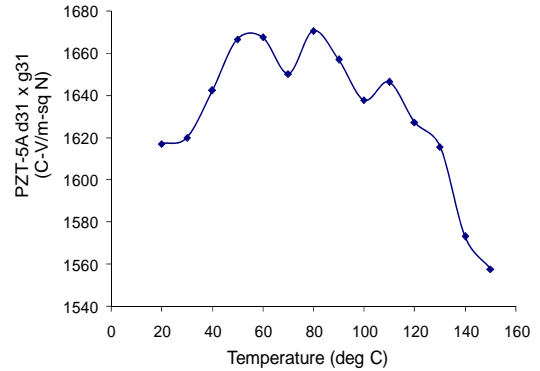


Fig. 57: Variation of $d_{31} \times g_{31}$ of PZT-5A [222]

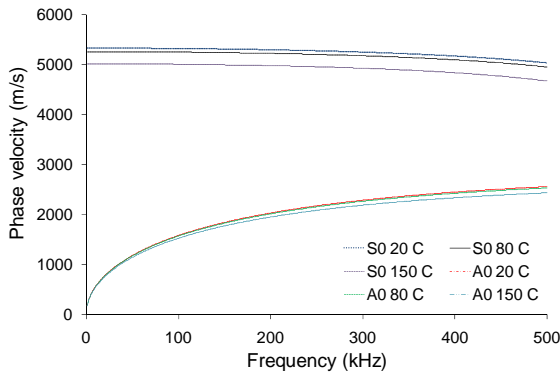


Fig. 58: Combined effect of changing aluminum elastic modulus (static) and thermal expansion on phase velocity

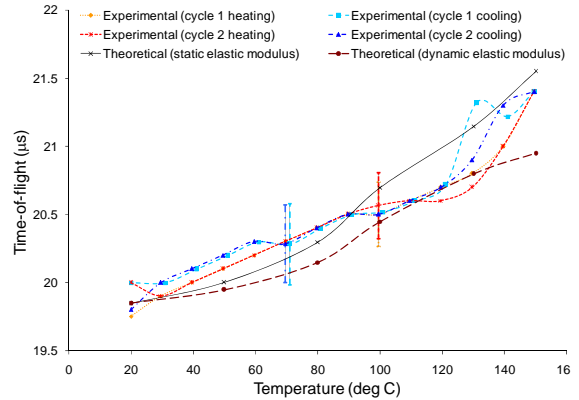


Fig. 59: Variation in time-of-flight of first transmitted S_0 mode received by sensor 2

d) Damping and pyroelectric effects (not considered): Another parameter that changes with increasing temperature is damping in the structural substrate. The best reference found in this regard (Hilton and Vail [227]) estimated an increase by a factor of 4 in the loss modulus (representative of damping) at 100 Hz in aluminum alloy 2024. This

still ensures that the loss modulus is orders of magnitude lower than the elastic modulus. The effect of damping can then be effectively ignored, as seen in the comparison of the theoretical model (without damping considered) and experimental results at room temperature described in Chapter II. Therefore, damping was ignored at higher temperatures too. Finally, due to the pyroelectric effect, temperature changes cause a static voltage to appear across a piezo's electrodes. Since the experimental signals were acquired with a 2 Hz high-pass filter built into the oscilloscope, this effect was not considered either.

Effects (a)-(c) were incorporated into the theoretical models developed in Chapter II. With that, it was examined whether the experimentally observed increase in time-of-flight (calculated by peak extraction from spectrograms) of the GW S_0 mode wave-packet received by sensor 2 and the change in sensor response amplitude could be captured. Reduced transducer dimensions (20% less than nominal values) were used to generate the theoretical plots. This is to account for shear lag, as explained in Chapter II. In addition, variations in the traction magnitude exerted by the piezo due to changing elastic moduli and dimensions were accounted for using the equation for static actuation by piezos in Chaudhry and Rogers [228]. The comparison between theory and experiment is shown in Fig. 59 for time-of-flight and in Fig. 60 for sensor response amplitude (peak-to-peak). To get an estimate of the error in time-of-flight, the raw un-averaged 30 signals were collected for two points per cycle (100°C while heating and 70°C while cooling). The data from sensor 3 is very similar. The theoretical estimates for time-of-flight are in agreement with the experimental data (within error margins) and the agreement seems better for the theoretical data set generated assuming static elastic modulus variation. The center frequency of the sensed S_0 mode pulse remained constant at 133 kHz (calculated with a resolution of 3 kHz) for both the theoretical and experimental data-sets at different temperatures. For the sensor amplitude prediction, there is clearly a significant gap between the theoretical estimate and experimental data. The experimentally observed increase of up to 33% while heating to 90°C in the response amplitude of sensor 2 is not captured by the theoretical model, but the decrease of 18% at 150°C is predicted within the error margin. One possible explanation for this is changing bond layer properties with temperature (the model used here assumed perfect bonding). Data was unavailable for

variation of bond layer elastic modulus with temperature and therefore it could not be quantified. However, the static modulus variation and thermal expansion data can give a good approximation to account for the slowing down of wave-speeds with increasing temperature, and is used in the subsequent section to generate damage location estimates. An empirical compensation approach is used for varying response amplitude.

From these experiments, it is clear that temperature can cause significant changes in the amplitude and time-of-flight for the first transmitted pulse received by the sensor. Even with the instantaneous temperature known, this causes greater error margins in the amplitude and time-of-flight measurement under slightly varying temperature. In the pitch-catch approach, changes in these very features are used to conclude whether damage is present in the actuator-sensor path or not. Therefore, the pitch-catch method is inherently more sensitive to false positives in damage detection under varying temperature. On the other hand, the pulse-echo approach relies on the absence or presence of reflections between the actuation pulse and the boundary reflection. If damage is present, regardless of temperature increase, there will always be some GW reflection towards the actuator, and a collocated sensor should be able to pick this up (assuming the damage is sensitive to the mode and frequency of the incident GW). Therefore, in principle, the only modification to make for GW pulse-echo based damage characterization under varying temperature would be to account for varying GW speeds and scale the reflection amplitude according to the changed sensor sensitivity at that particular temperature. However, a complication arises for pulse-echo methods in structures with features such as rivets in trying to detect and locate “mild” damage which is roughly at the same distance (within a few cm) from the actuator as the rivet. In this context, damage is called “mild” if the amplitude of the reflected GW by it is comparable to that of the reflection from the rivet/structural discontinuity. This is explored experimentally in the next section.

V.4 Damage Characterization at Elevated Temperatures

As mentioned in the previous section, before any damage was introduced two data-sets were obtained for the baseline, pristine condition of the specimen (which had

transducers bonded with Epotek 353ND). This was to get a sense of the repeatability of the baseline condition at different temperatures. The baseline signal read by sensor 1 (collocated with the actuator) is shown in Fig. 61. There is some non-zero signal between the actuation pulse and the boundary reflection due to mild A_0 mode excitation and some reflection from sensors 2 and 3. At 20°C, the A_0 mode reflection from sensors 2 and 3 is discernible, while the S_0 mode reflection is negligible. However, at higher temperatures, the S_0 mode reflection from sensors 2 and 3 becomes stronger (e.g., see Fig. 61). Furthermore, there is some error in the amplitudes of these mild reflections received at sensor 1 when data from the two cycles are compared. Fig. 62 shows one of the worse scenarios in this regard, while Fig. 63 is an example of better repeatability observed among the readings. This error in repeatability arises from the variation in time-of-flight and sensor response amplitude under changing temperature. With large temperature-change rates, this problem is further exacerbated. This explains why poor signal repeatability was observed in the initial experiments in the oven. The variation between the two baseline cycles defines the threshold values for the subsequent damage detection experiments. In practice it would be advisable to get some more data for the variability in baseline condition at various temperatures, particularly in less homogeneous structural layouts with rivets, stiffeners, etc. In addition, while data was collected here at 10°C intervals, it can also be used for baseline interpolation at intermediate temperatures. This can be done by simple weighted averaging of the two signals taken at the multiples of 10°C within which the intermediate temperature lies.

Thus, in implementing GW SHM with compensation for temperature, a processor will need to store a database of baseline signals for different temperatures. Subsequently, during operation, depending on the temperature (read using thermocouple(s) attached to the structure) at which the test signal was obtained, the baseline signal for the relevant temperature should be used. If the baseline signal for that temperature is not stored in the database, the processor needs to interpolate this baseline signal from the other available signals.

Once the baselines were obtained and threshold levels were defined, damage was introduced artificially in the plate by drilling. As alluded to at the end of Section V.3, the

case of “mild” damage was first explored. To ensure that the reflections were not too strong, damage was introduced along the axis of weaker actuation of the rectangular actuators. Theoretical models developed in Chapter II predicted a 30% weaker GW strain field along this direction. Experiments were first done for a triangular cross-sectional indentation of maximum diameter 5 mm and depth 1.7 mm, shown in Fig. 64 (a). The damage center is 8 cm away from the plate center and its location is shown in Fig. 50. The signal obtained from sensor 1 at room temperature after introducing this damage is shown in Fig. 65 (a), along with the pristine condition signal and the difference between the two. There is a clear signal above the threshold defined for 20°C. The two distinct reflections in the signal are the S_0 - and A_0 - mode reflections from the indentation. As explained in Chapter IV, even though the S_0 mode is predominantly excited, mode conversion is possible at a damage site. From their time-of-flight and using the group velocities at 20°C, the radial location estimates of the indentation are 7.2 cm and 8.2 cm from the plate center based on the S_0 and A_0 mode reflections respectively. The analysis in this chapter was done using spectrograms by manually tracking the reflections. In principle, the chirplet matching pursuit algorithm used in Chapter IV should allow automated tracking and better resolution for real-time processing. However, its implementation in LastWave 2.0 [215] makes approximations to reduce computational cost which do not capture the increase in time-of-flight with temperature in Fig. 59.

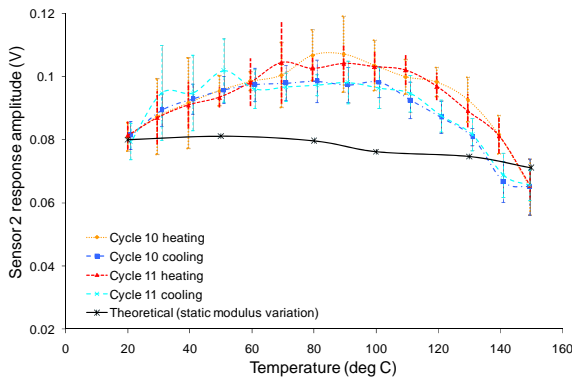


Fig. 60: Variation in response amplitude (peak-to-peak) of first transmitted S_0 mode received by sensor 2

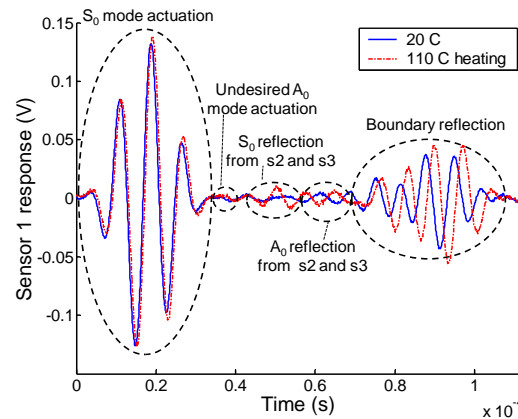


Fig. 61: Signal read by sensor 1 at 20°C and 110°C (cycle 1) for pristine condition

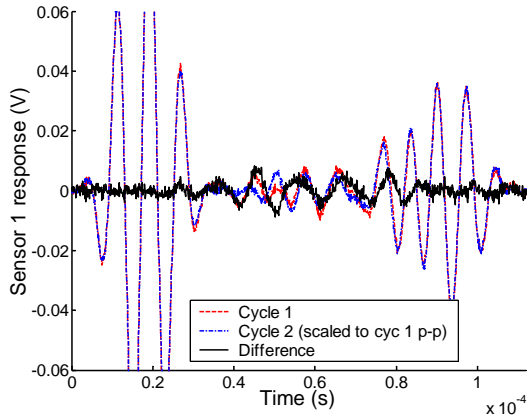


Fig. 62: Sensor 1 response during cycles 1 and 2 for pristine condition at 120°C (heating)

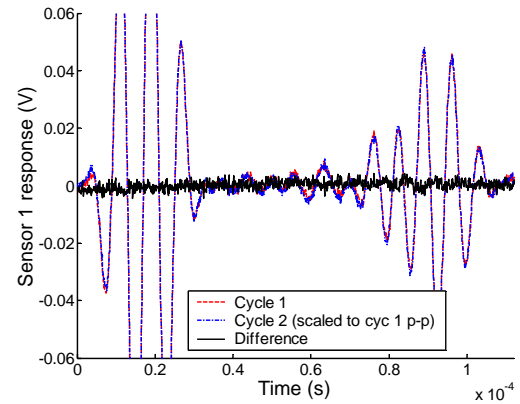
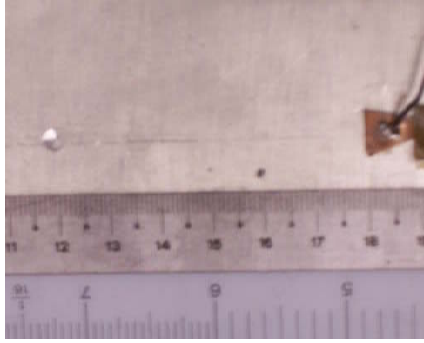
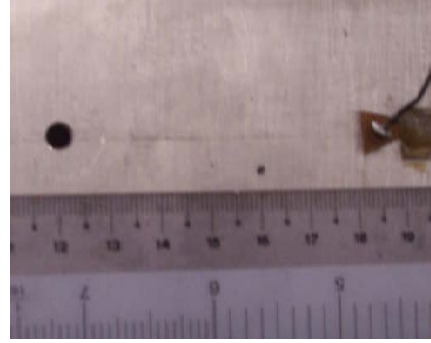


Fig. 63: Sensor 1 response during cycles 1 and 2 for pristine condition at 60°C (cooling)

The indented specimen was thermally cycled in the autoclave to check whether the signal difference remained above the pre-defined threshold level at each temperature point. Some of the signals read by sensor 1 during this experiment are shown in Fig. 65 (a)-(d). The results are also summarized in Table 3. The A_0 and S_0 mode reflections from the indentation had peak energy (from the spectrogram, in the excited frequency band) well above the threshold up to 80°C while heating. Some of the S_0 mode reflections (from 50°-80°C) mixed with the excitation signal difference, due to which the S_0 mode reflection underestimated the damage location, as shown in Fig. 65 (b). Beyond 80°C, the A_0 mode reflection was still above the threshold, but had peak energy that was comparable to the threshold. The weaker S_0 mode reflection had peak energy lower than the threshold at some points after 90°C while heating. In addition, as illustrated in Fig. 65 (c), at some points over 100°C, there is a reflection that arrives approximately where the S_0 mode was seen at lower temperatures, but can be wrongly identified as A_0 mode by its time-frequency characteristics. Subsequently, while cooling below 80°C, again both reflections were well above the threshold, and gave reasonable location estimates.

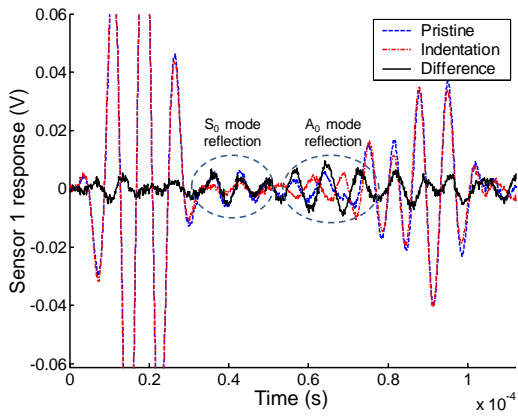


(a)

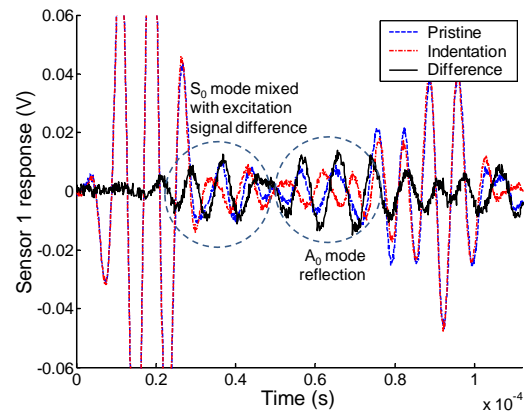


(b)

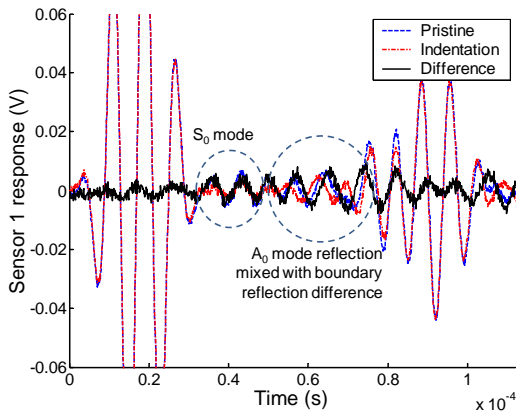
Fig. 64: Photographs of damage introduced: (a) indentation and (b) through-hole.



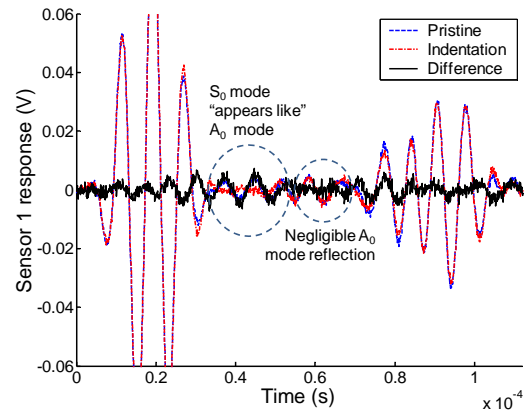
(a)



(b)



(d)



(c)

Fig. 65: Sensor 1 response for pristine and indented specimens, along with the signal difference at: (a) 20°C (before thermal cycle) ; (b) 60°C while heating; (c) 140°C while heating and (d) 40°C while cooling

Following this, a through hole of diameter 7.5 mm was drilled at the same location, seen in Fig. 64 (b). The response of sensor 1 recorded after drilling through at 20°C is shown in Fig. 66 (a). The S_0 mode reflection is now much stronger, while the A_0 mode reflection appears much weaker (but still well above the threshold at 20°C). The radial location estimates are 8.6 cm and 8.3 cm based on the S_0 and A_0 mode reflections respectively at 20°C. The results from thermally cycling the specimen with the through-hole are shown in Fig. 66 (a)-(d), and tabulated in Table 4. In this case, the S_0 mode reflection is reasonably above the threshold at all temperatures. There is an error of 1.9 cm in the estimate (based on the S_0 mode) at 150°C, where the signal is the weakest. At a couple of points, the radial location of the damage is overestimated by more than 1 cm (100°C while heating and 50°C while cooling), which is possibly due to the mixing of the S_0 mode with the difference in the reflection from sensors 2 and 3. At other temperatures, the radial location estimates based on the S_0 mode are within 1 cm. The A_0 mode reflection, which was weak at 20°C to begin with, is discernible up to 70°C while heating, but beyond that is indistinguishable from the difference in boundary reflection until the specimen cools back to room temperature.

Thus, for “mild” damage up to 80°C, detection was not problematic, but there was a slightly increased error in location as temperature increased. However, beyond that temperature, there is a definite decrease in sensitivity, as reflected in the poorer detection/characterization capability in the indentation experiment. This can be attributed to the higher sensitivity of the substrate elastic modulus to temperature at higher temperatures (Fig. 56), causing greater variation in the mild reflections from sensors 2 and 3, and consequently, poorer repeatability of the baseline signals. In addition, the sensor sensitivity (in terms of signal amplitude) drops below the value at 20°C beyond 130°C. For the thru-hole, which can be termed “moderate” damage, detection was clearly possible at all temperatures, but at a few points (3 of a total of 29 cases), there was inaccuracy in the location estimate (by up to 2.2 cm for damage located at 8 cm), partly due to interference with the difference in reflection from sensors 2 and 3 (simulating structural features in field applications). One way to reduce the error in location is to use higher center frequencies and/or fewer number of cycles (which increases frequency bandwidth) in the actuation signal. However, that was not feasible in the present setup

(which did not use amplifiers), since significant distortion was observed for such actuation signals at higher temperatures due to increasing actuator capacitance. In addition, in the present experimental setup, the scaling of the signals to compensate for changing actuation level increased the signal-to-noise ratio at higher temperatures. This indicates the need for reliable actuation signal amplification for GW SHM at elevated temperatures.

<i>Temp.</i> (°C)	<i>S₀</i> <i>ToF</i> (μs)	<i>S₀</i> <i>energy</i> (V ²)	<i>Thres.</i> <i>energy</i> (V ²)	<i>S₀</i> <i>over</i> <i>thres.?</i>	<i>S₀</i> <i>loc.</i> (cm)	<i>A₀</i> <i>ToF</i> (μs)	<i>A₀</i> <i>energy</i> (V ²)	<i>A₀</i> <i>over</i> <i>thres.?</i>	<i>A₀</i> <i>loc.</i> (cm)
20 (h)	28.10	0.0631	0.0142	Yes	7.2	50.65	0.2883	Yes	8.2
40 (h)	28.00	0.1229	0.0025	Yes	7.2	51.20	0.3695	Yes	8.6
70 (h)	18.60	0.0739	0.0154	Yes	4.7	54.60	0.5895	Yes	9.1
110 (h)	31.20	0.1808	0.1850	NO	7.9	56.00	0.1959	Yes	9.2
130 (h)	18.60	0.066	0.0517	Yes	4.5	34.10	0.0886	Yes	4.9
150	–	–	0.0275	–	–	25.50	0.0839	Yes	4.0
120 (c)	–	–	0.0375	–	–	28.60	0.1363	Yes	4.1
80 (c)	25.50	0.2688	0.0525	Yes	6.5	56.80	0.1502	Yes	9.5
50 (c)	27.50	0.0681	0.0033	Yes	7.1	55.82	0.2240	Yes	9.4
20 (c)	30.35	0.0483	0.0023	Yes	7.8	53.95	0.4228	Yes	8.8

Table 3: Summary of results showing trends in thermal experiment for damage characterization with indented specimen (Key: Temp. ≡ Temperature; (h) ≡ heating phase; (c) ≡ cooling phase ; *S₀* ToF ≡ time-of-flight for *S₀* mode reflection from indentation; Thres. ≡ Threshold; *S₀* loc. ≡ radial location estimate (relative to plate center) of damage based on *S₀* mode reflection).

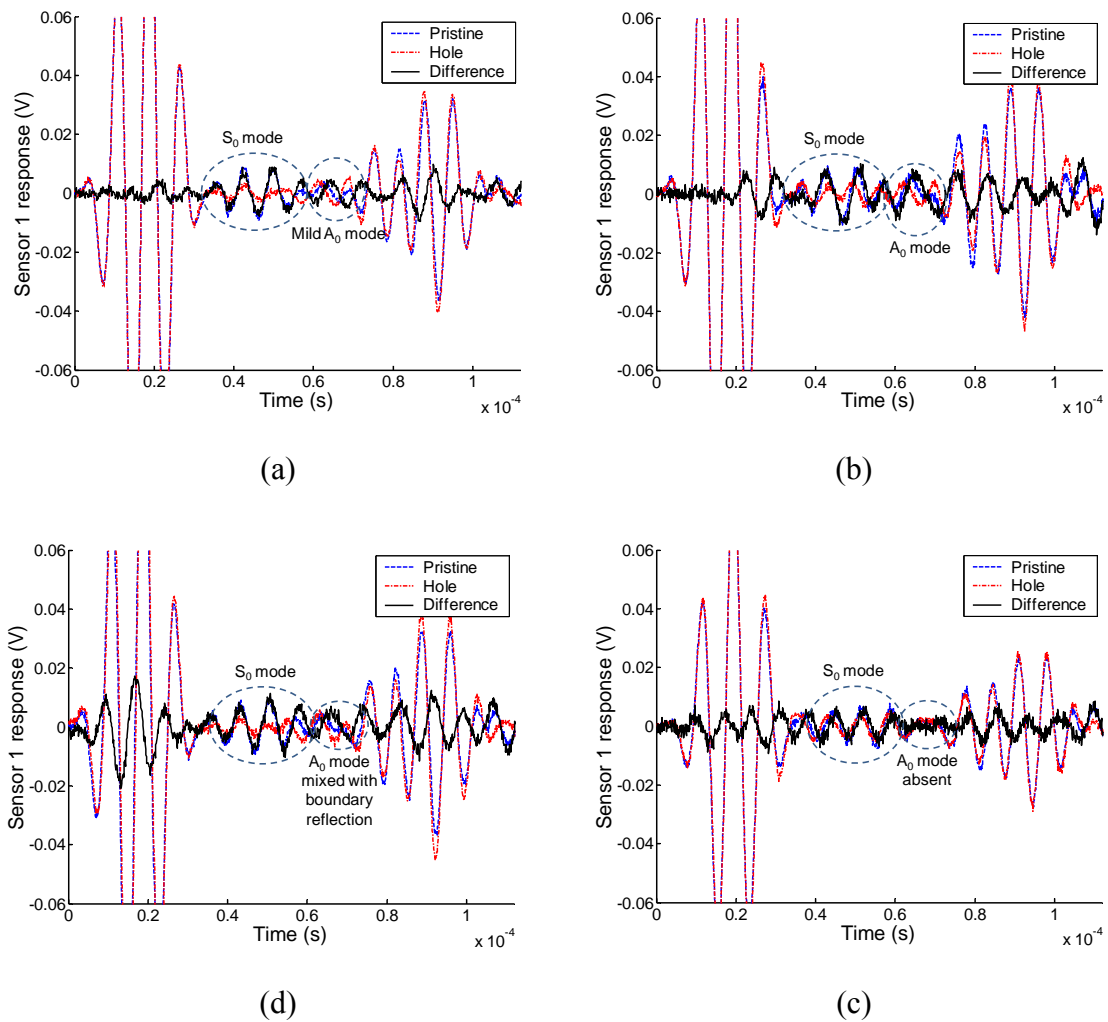


Fig. 66: Sensor 1 response for pristine and thru-hole specimens, along with the signal difference at: (a) 20°C (before thermal cycle) ; (b) 70°C while heating; (c) 150°C while heating and (d) 50°C while cooling

To conclude, this chapter examined the issue of GW SHM using piezos under elevated temperature conditions as expected in spacecraft internal structures. Experiments were done to determine a bonding agent (for piezos on aluminum plates) that did not degrade at temperatures from 20°C to 150°C. Using this bonding agent (Epotek 353ND), results from controlled experiments done to examine changes in GW propagation and transduction using PZT-5A piezos under quasi-statically varying temperature (also from 20°C to 150°C) were presented. Thermally sensitive variables in the experiments were

<i>Temp.</i> (°C)	<i>S₀</i> <i>ToF</i> (μs)	<i>S₀</i> <i>energy</i> (V ²)	<i>Thres.</i> <i>energy</i> (V ²)	<i>S₀</i> <i>over</i> <i>thres.?</i>	<i>S₀</i> <i>loc.</i> (cm)	<i>A₀</i> <i>ToF</i> (μs)	<i>A₀</i> <i>energy</i> (V ²)	<i>A₀</i> <i>over</i> <i>thres.?</i>	<i>A₀</i> <i>loc.</i> (cm)
20 (h)	33.45	0.2198	0.0142	Yes	8.6	49.75	0.0763	Yes	8.3
40 (h)	34.30	0.2972	0.0025	Yes	8.8	55.20	0.1119	Yes	9.0
70 (h)	32.50	0.2463	0.0154	Yes	8.3	56.70	0.2128	Yes	9.0
110 (h)	40.60	0.2578	0.1850	Yes	10.2	Bndry	–	–	–
130 (h)	33.40	0.3105	0.0517	Yes	8.2	Bndry	–	–	–
150	25.60	0.1073	0.0275	Yes	6.1	Bndry	–	–	–
120 (c)	31.00	0.1997	0.0375	Yes	7.6	Bndry	–	–	–
80 (c)	28.00	0.2985	0.0525	Yes	7.0	Bndry	–	–	–
50 (c)	36.20	0.3393	0.0033	Yes	9.3	Bndry	–	–	–
20 (c)	33.80	0.2018	0.0023	Yes	8.7	53.60	0.0623	Yes	8.8

Table 4: Summary of results showing trends in thermal experiment for damage characterization using specimen with thru-hole (Key: Temp. ≡ Temperature; (h) ≡ heating phase; (c) ≡ cooling phase; *S₀* ToF ≡ time-of-flight for *S₀* mode reflection from thru-hole; Thres. ≡ Threshold; *S₀* loc. ≡ radial location estimate (relative to plate center) of damage based on *S₀* mode reflection; Bndry ≡ *A₀* mode reflection peak within boundary reflection).

identified and quantified to model the experimentally observed changes under temperature variation. The increase in time-of-flight of GW pulses with increasing temperature was captured by the model (within the error margins). However, there was a significant gap in the prediction of the large increase in sensor response amplitude up to 100°C. The stronger vulnerability of pitch-catch approaches to false positives under changing temperature was then explained. Finally, detection and location of damage (by drilling) using the pulse-echo approach in the presence of mild structural GW scatterers (to simulate rivets) was explored in the same temperature range. Damage characterization

of a half-plate thickness indentation at 8 cm from the actuators was not significantly affected up to 80°C, but beyond that temperature, detection/characterization was difficult. The problems beyond 80°C can be traced to increased sensitivity of substrate elastic modulus to temperature and weaker sensor sensitivity beyond 130°C. For a through-hole, damage detection and characterization was possible at all temperatures and except at a few temperatures (3 out of 29), damage was located within 1 cm for a nominal location of 8 cm and hole diameter 0.75 cm. Suggested approaches for improving sensitivity at higher temperatures include testing at higher frequencies and/or with shorter time-span excitation pulses, with reliable actuation amplifiers.

CHAPTER VI

GUIDED-WAVE EXCITATION BY PIEZOS IN COMPOSITE LAMINATED PLATES

The studies till this point in the thesis have focused on isotropic structures. With composite materials becoming increasingly common in aerospace structures as explained in Section I.1, there is a need to extend that work to composite structures as well. The present chapter seeks to extend the modeling work in Chapter II for GW excitation by finite-dimensional piezos to multilayered, laminated fiber-reinforced composite plates. Details of the implementation of the formulation and verification of the models using numerical simulations are also presented.

VI.1 Theoretical Formulation

As in Chapter II, first a general expression for the GW field excited by an arbitrary shape piezo-actuator surface-bonded on a multilayered composite plate is derived. Consider an infinite N -layered composite plate of total thickness H , with such an actuator bonded on one free surface, as illustrated in Fig. 67. The origin is located on the free surface with the actuator and the X_3 -axis is normal to the plate surface. The individual layers are assumed to have unidirectional fibers in a matrix and are modeled as being transversely isotropic with uniform density. This is a reasonable assumption if the GW wavelength is large compared to the inter-fiber spacing and the fiber diameter [62]. The solution procedure consists of the following four components (illustrated in Fig. 68):

- (a) First, one sets up the 3-D governing equations of motion for the bulk composite medium. The 2-D Fourier transform is applied (or equivalently, plane waves propagating at a given angle in the plane of the fibers are assumed). This yields the free-wave solution in terms of the eigenvectors and possible wavenumbers through the thickness of the fibers.
- (b) Then, one imposes the free-surface conditions of the plate along with the continuity conditions across interfaces (using the global matrix formulation). This also gives the allowable in-plane wavenumbers for the possible GW modes.
- (c) Next, the forcing function due to the presence of the surface-bonded piezo-actuators is imposed (assuming they exert shear traction along their free edges as explained in Chapter II). This gives the solution in terms of a 2-D Fourier integral in the wavenumber domain.
- (d) Finally, the 2-D wavenumber-domain Fourier integral is inverted (semi-analytically) to yield the GW field due to harmonic excitation by the piezo-actuator. The response to an arbitrary excitation waveform can then be obtained by integrating the individual harmonic components of the time-domain signal (i.e., inverting the frequency-domain Fourier integral).

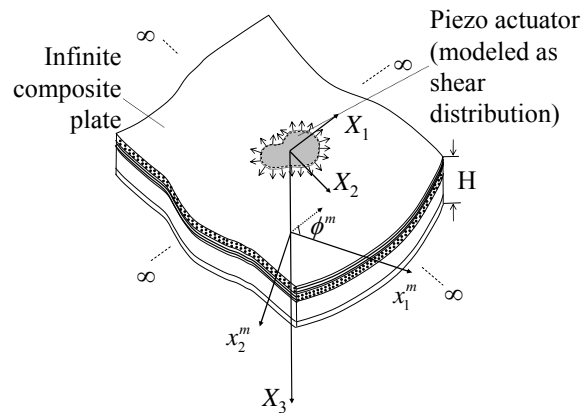


Fig. 67: Infinite multilayered composite plate with arbitrary shape surface-bonded piezo actuator

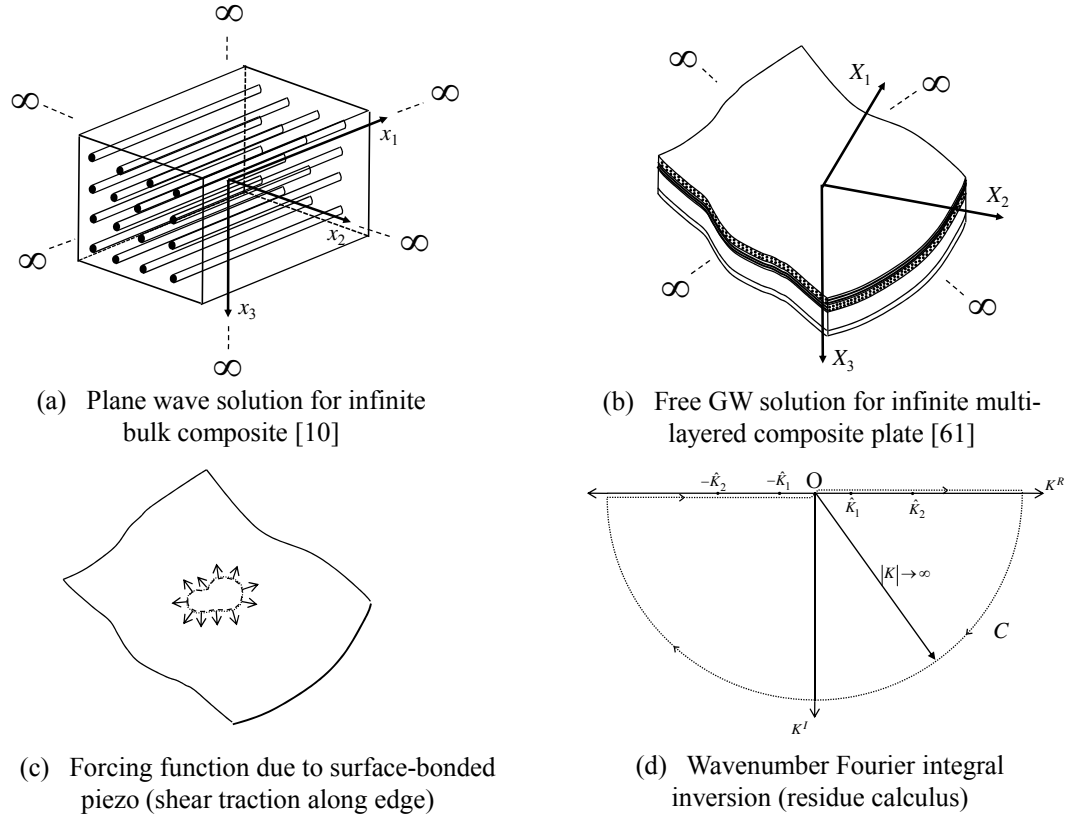


Fig. 68: Illustration of solution procedure

Among these, parts (a) and (b) are adapted from Auld [10] and Lih and Mal [62]. Parts (c) and (d) are based on the work in Chapter II. The details of the solution procedure are explained in the following sub-sections.

VI. 1.A Bulk Waves in Fiber-reinforced Composites

First, consider the general solution for bulk waves in a transversely isotropic medium. The equations of motion for the bulk medium in each layer are:

$$\nabla \mathbf{c} \nabla^T \bar{\mathbf{u}} = \rho \ddot{\bar{\mathbf{u}}} \quad (120)$$

where $\bar{\mathbf{u}}$ is the “local” displacement vector (later the “global” displacement vector \mathbf{u} will be introduced for the laminate), \mathbf{c} is the stiffness matrix, the \cdot over a variable indicates derivative with respect to time, ρ is the material density, and the operator ∇ is defined as:

$$\nabla = \begin{bmatrix} \frac{\partial}{\partial x_1} & 0 & 0 & 0 & \frac{\partial}{\partial x_3} & \frac{\partial}{\partial x_2} \\ 0 & \frac{\partial}{\partial x_2} & 0 & \frac{\partial}{\partial x_3} & 0 & \frac{\partial}{\partial x_1} \\ 0 & 0 & \frac{\partial}{\partial x_3} & \frac{\partial}{\partial x_2} & \frac{\partial}{\partial x_1} & 0 \end{bmatrix} \quad (121)$$

If the fibers are oriented along the 1-direction in the local coordinate system (x_1, x_2, x_3) of the material, the stress-strain relation and the stiffness matrix \mathbf{c} for a transversely isotropic material are:

$$\begin{bmatrix} \bar{\sigma}_{11} \\ \bar{\sigma}_{22} \\ \bar{\sigma}_{33} \\ \bar{\sigma}_{23} \\ \bar{\sigma}_{31} \\ \bar{\sigma}_{12} \end{bmatrix} = \mathbf{c} \begin{bmatrix} \bar{u}_{1,1} \\ \bar{u}_{2,2} \\ \bar{u}_{3,3} \\ \bar{u}_{2,3} + \bar{u}_{3,2} \\ \bar{u}_{1,3} + \bar{u}_{3,1} \\ \bar{u}_{2,1} + \bar{u}_{1,2} \end{bmatrix}; \quad \mathbf{c} = \begin{bmatrix} c_{11} & c_{12} & c_{12} & 0 & 0 & 0 \\ c_{12} & c_{22} & c_{23} & 0 & 0 & 0 \\ c_{12} & c_{23} & c_{22} & 0 & 0 & 0 \\ 0 & 0 & 0 & c_{44} & 0 & 0 \\ 0 & 0 & 0 & 0 & c_{55} & 0 \\ 0 & 0 & 0 & 0 & 0 & c_{55} \end{bmatrix}, \quad \text{with } c_{44} = \frac{c_{22} - c_{23}}{2} \quad (122)$$

Here $\bar{\sigma}_{ij}$, with i and j taking integer values from 1 to 3, are the local stress components.

Next, constants are introduced that correspond to the squares of the bulk wave speeds along the principal directions:

$$\begin{aligned} a_1 &= c_{22} / \rho \quad (\text{dilatational wave normal to the fiber direction}) \\ a_2 &= c_{11} / \rho \quad (\text{dilatational wave along the fiber direction}) \\ a_3 &= (c_{12} + c_{55}) / \rho \quad (\text{shear wave in the plane of isotropy}) \\ a_4 &= (c_{22} - c_{23}) / 2\rho = c_{44} / \rho \quad (\text{shear wave along the fiber direction}) \\ a_5 &= c_{55} / \rho \quad (\text{shear wave in the plane of isotropy}) \end{aligned} \quad (123)$$

Viscoelastic damping can be modeled by the use of complex stiffness constants. Suppose the wavenumber components are ξ_1 , ξ_2 and ζ along the 1-, 2- and 3- local directions, respectively. Furthermore, without loss of generality, consider harmonic excitation at angular frequency ω . Then the wave field is of the form:

$$\bar{\mathbf{u}} = \bar{\mathbf{\Omega}} e^{-i(\xi_1 x_1 + \xi_2 x_2 + \zeta x_3 - \omega t)} \quad (124)$$

where the vector $\bar{\Omega}$ is a linear superposition of the possible eigenvectors. To solve for these eigenvectors, from Eqs. (120)-(124), one obtains the Christoffel equation:

$$\begin{bmatrix} c_{11}\xi_1^2 + c_{55}(\xi_2^2 + \zeta^2) & (c_{12} + c_{55})\xi_1\xi_2 & (c_{12} + c_{55})\xi_1\zeta \\ (c_{12} + c_{55})\xi_1\xi_2 & c_{55}\xi_1^2 + c_{22}\xi_2^2 + c_{44}\zeta^2 & (c_{23} + c_{44})\xi_2\zeta \\ (c_{12} + c_{55})\xi_1\zeta & (c_{23} + c_{44})\xi_2\zeta & c_{55}\xi_1^2 + c_{44}\xi_2^2 + c_{22}\zeta^2 \end{bmatrix} \begin{bmatrix} \bar{\Omega}_1 \\ \bar{\Omega}_2 \\ \bar{\Omega}_3 \end{bmatrix} = \rho\omega^2 \begin{bmatrix} \bar{\Omega}_1 \\ \bar{\Omega}_2 \\ \bar{\Omega}_3 \end{bmatrix} \quad (125)$$

For fixed values of ξ_1 , ξ_2 , and ω , there are six possible roots $\pm\zeta_i$, $i = 1$ to 3, of this equation. The first two pairs of roots correspond to pairs of quasi-longitudinal waves (characterized by displacements dominantly along the wave propagation direction but with small components normal to it) and quasi-shear waves (characterized by displacements dominantly normal to the wave propagation direction but with small components along it, see [10]). The wavenumbers in the thickness direction for these four roots are, respectively [62]:

$$\begin{aligned} \zeta_1^2 &= -\xi_2^2 + b_1; \quad \zeta_2^2 = -\xi_2^2 + b_2 \\ b_1 &= -\left(\frac{\beta}{2\alpha}\right) - \sqrt{\left(\frac{\beta}{2\alpha}\right)^2 - \frac{\gamma}{\alpha}}; \quad b_2 = -\left(\frac{\beta}{2\alpha}\right) + \sqrt{\left(\frac{\beta}{2\alpha}\right)^2 - \frac{\gamma}{\alpha}} \\ \alpha &= a_1a_5; \quad \beta = (a_1a_2 + a_5^2 - a_3^2)\xi_1^2 - \omega^2(a_1 + a_5); \quad \gamma = (a_2\xi_1^2 - \omega^2)(a_5\xi_1^2 - \omega^2) \end{aligned} \quad (126)$$

The third pair of roots corresponds to quasi-shear waves and their through-thickness wavenumbers are given by:

$$\zeta_3^2 = -\xi_2^2 + (\omega^2 - a_5\xi_1^2)/a_4 \quad (127)$$

The displacement eigenvectors resulting from Eq. (125) corresponding to these roots are:

$$\begin{aligned} \mathbf{e}_1 &= [i\xi_1q_{11} \quad i\xi_2q_{21} \quad i\xi_1q_{21}]^T \\ \mathbf{e}_2 &= [i\xi_1q_{12} \quad i\xi_2q_{22} \quad i\xi_2q_{22}]^T \\ \mathbf{e}_3 &= [0 \quad i\xi_3 \quad -i\xi_2]^T \end{aligned} \quad (128)$$

where:

$$\begin{aligned} q_{11} &= a_3b_1; \quad q_{21} = \omega^2 - a_2\xi_1^2 - a_5b_1 \\ q_{21} &= a_3b_2; \quad q_{22} = \omega^2 - a_2\xi_1^2 - a_5b_2 \end{aligned} \quad (129)$$

and the other three eigenvectors \mathbf{e}_4 , \mathbf{e}_5 and \mathbf{e}_6 are obtained by replacing ζ_i by $-\zeta_i$. The general solution for the displacement vector is then given by:

$$\begin{aligned}\bar{\mathbf{u}} &= \begin{pmatrix} C_{1+}\mathbf{e}_1 e^{i\zeta_1 x_3} + C_{2+}\mathbf{e}_2 e^{i\zeta_2 x_3} + C_{3+}\mathbf{e}_3 e^{i\zeta_3 x_3} + \\ + C_{1-}\mathbf{e}_4 e^{-i\zeta_1 x_3} + C_{2-}\mathbf{e}_5 e^{-i\zeta_2 x_3} + C_{3-}\mathbf{e}_6 e^{-i\zeta_3 x_3} \end{pmatrix} e^{-i(\xi_1 x_1 + \xi_2 x_2 - \omega t)} \\ &= [\mathbf{Q}_{11} \quad \mathbf{Q}_{12}] \begin{bmatrix} \bar{\mathbf{E}}_+(x_3) & 0 \\ 0 & \bar{\mathbf{E}}_-(x_3) \end{bmatrix} \begin{bmatrix} \mathbf{C}_+ \\ \mathbf{C}_- \end{bmatrix} e^{-i(\xi_1 x_1 + \xi_2 x_2 - \omega t)}\end{aligned}\quad (130)$$

where $C_{i\pm}$, $i = 1$ to 3 , are free constants and:

$$\begin{aligned}\mathbf{Q}_{11} &= [\mathbf{e}_1 \quad \mathbf{e}_2 \quad \mathbf{e}_3]; \quad \mathbf{Q}_{12} = [\mathbf{e}_4 \quad \mathbf{e}_5 \quad \mathbf{e}_6] \\ \bar{\mathbf{E}}_+(x_3) &= \text{Diag}[e^{i\zeta_1 x_3}, e^{i\zeta_2 x_3}, e^{i\zeta_3 x_3}] \\ \bar{\mathbf{E}}_-(x_3) &= \text{Diag}[e^{i\zeta_1 x_3}, e^{i\zeta_2 x_3}, e^{i\zeta_3 x_3}]\end{aligned}\quad (131)$$

VI. 1.B Assembling the Laminate Global Matrix from the Individual Layer Matrices

With the general solution for the bulk medium in place, one can then seek the particular solution for the problem at hand. As mentioned earlier, the equations in this particular sub-section are adapted from Lih and Mal [62].

Due to the different orientations of the fibers in the different layers, it is useful to work with a global coordinate system (X_1, X_2, X_3) distinct from the local coordinate system, for which the x_1^m -axis is aligned with the fiber direction (with the superscript m indicating the layer number between 1 and N). However, the X_3 - and x_3^m -axes are coincident and the two coordinate systems differ only in the plane of the plate. One can relate the displacement vector \mathbf{u} in the global system and $\bar{\mathbf{u}}$ in the local system using the transformation matrix \mathbf{L}^m (defining ϕ^m to be the angle between the X_1 - and x_1^m -axes):

$$\mathbf{u} = \mathbf{L}^m \bar{\mathbf{u}}^m; \quad \text{where } \mathbf{L}^m = \begin{bmatrix} \cos \phi^m & -\sin \phi^m & 0 \\ \sin \phi^m & \cos \phi^m & 0 \\ 0 & 0 & 1 \end{bmatrix}\quad (132)$$

The surface traction conditions for this problem are:

$$\begin{aligned}\sigma_{i3}^1(X_1, X_2, 0) &= f_i(X_1, X_2, 0) \\ \sigma_{i3}^N(X_1, X_2, H) &= 0; \quad i = 1, 2, 3\end{aligned}\quad (133)$$

where the functions f_1 and f_2 depend on the shape of the actuator and $f_3 = 0$. In addition, traction and displacement continuity must be maintained across the interfaces between the different layers. As in Chapter II, the 2-D spatial Fourier transform is used to ease solution of this problem. However, it should be noted that this transform uses the “global” wavenumbers K_1 and K_2 along the X_1 and X_2 directions respectively, which are related to the local wavenumbers ξ_1 and ξ_2 in each layer by the formula:

$$\begin{bmatrix} \xi_1 \\ \xi_2 \end{bmatrix} = \begin{bmatrix} \cos(\phi^m) & \sin(\phi^m) \\ -\sin(\phi^m) & \cos(\phi^m) \end{bmatrix} \begin{bmatrix} K_1 \\ K_2 \end{bmatrix}\quad (134)$$

Let \mathbf{U} , $\mathbf{\Sigma}$ and \mathbf{F} denote the 2-D spatial Fourier transform of the variables \mathbf{u} , $\boldsymbol{\sigma}$ and \mathbf{f} , respectively. Furthermore, as for the bulk medium solution, without loss of generality, harmonic excitation at angular frequency ω is considered (the $e^{i\omega t}$ factor is suppressed for convenience and is brought back at the end). Since continuity of both traction and displacement has to be ensured across all interfaces, it is convenient to work with a “displacement-stress vector” \mathbf{S}^m in the transformed domain defined as:

$$\mathbf{S}^m(X_3) = \{\mathbf{U}^m(X_3) \quad \boldsymbol{\Sigma}_{i3}^m(X_3)\}^T\quad (135)$$

Then, from Eqs. (122), (130), and (132):

$$\mathbf{S}^m(X_3) = \begin{bmatrix} \mathbf{L}^m & \mathbf{0} \\ \mathbf{0} & \mathbf{L}^m \end{bmatrix} \begin{bmatrix} \mathbf{Q}_{11}^m & \mathbf{Q}_{12}^m \\ \mathbf{Q}_{21}^m & \mathbf{Q}_{22}^m \end{bmatrix} \begin{bmatrix} \mathbf{E}_+^m(X_3) & \mathbf{0} \\ \mathbf{0} & \mathbf{E}_-^m(X_3) \end{bmatrix} \begin{Bmatrix} \mathbf{C}_+^m \\ \mathbf{C}_-^m \end{Bmatrix} \equiv \mathbf{Q}^m(X_3) \mathbf{C}^m\quad (136)$$

where:

$$\mathbf{Q}_{21}^m = \begin{bmatrix} -\rho a_5 \xi_1 \zeta_1 (q_{11} + q_{21}) & -\rho a_5 \xi_1 \zeta_2 (q_{11} + q_{22}) & \rho a_5 \xi_1 \xi_2 \\ -2\rho a_4 \xi_2 \zeta_1 q_{21} & -2\rho a_4 \xi_2 \zeta_2 q_{22} & \rho a_4 (\xi_2^2 - \zeta_3^2) \\ \mu_1 & \mu_2 & 2\rho a_4 \xi_2 \zeta_3 \end{bmatrix}\quad (137)$$

$$\begin{aligned}
\mathbf{Q}_{22}^m &= \begin{bmatrix} \rho a_5 \xi_1 \zeta_1 (q_{11} + q_{21}) & \rho a_5 \xi_1 \zeta_2 (q_{11} + q_{22}) & \rho a_5 \xi_1 \xi_2 \\ 2\rho a_4 \xi_2 \zeta_1 q_{21} & 2\rho a_4 \xi_2 \zeta_2 q_{22} & \rho a_4 (\xi_2^2 - \zeta_3^2) \\ \mu_1 & \mu_2 & -2\rho a_4 \xi_2 \zeta_3 \end{bmatrix} \\
\mathbf{C}^m &= [\mathbf{C}_+^m \quad \mathbf{C}_-^m]^T \\
\mu_1 &= \rho [(a_5 - a_3) \xi_1^2 q_{11} - (a_1 - 2a_4) \xi_2^2 q_{21} - a_1 \zeta_1^2 q_{21}] \\
\mu_2 &= \rho [(a_5 - a_3) \xi_1^2 q_{12} - (a_1 - 2a_4) \xi_2^2 q_{22} - a_1 \zeta_1^2 q_{22}] \\
\mathbf{E}_+^m(X_3) &= \text{Diag} [e^{i\zeta_1(X_3 - X_3^{m-1})}, e^{i\zeta_2(X_3 - X_3^{m-1})}, e^{i\zeta_3(X_3 - X_3^{m-1})}] \\
\mathbf{E}_-^m(X_3) &= \text{Diag} [e^{i\zeta_1(X_3^m - X_3)}, e^{i\zeta_2(X_3^m - X_3)}, e^{i\zeta_3(X_3^m - X_3)}]
\end{aligned} \tag{138}$$

with X_3^m being the X_3 -coordinate of the interface between layers m and $(m-1)$. Here \mathbf{Q}_{21}^m and \mathbf{Q}_{22}^m are matrices whose columns are the stress eigenvectors for the m^{th} layer corresponding to wavenumbers along the 3-axis, ζ_i and $-\zeta_i$, respectively. These are obtained from the displacement eigenvectors using Eq. (121). The interface continuity conditions can then be expressed as:

$$\begin{aligned}
\mathbf{Q}_+^m \mathbf{C}^m &= -\mathbf{Q}_-^{m+1} \mathbf{C}^{m+1} \\
\text{where} \quad \mathbf{Q}_+^m &\equiv \mathbf{Q}^m(X_3^{m+1}); \quad \mathbf{Q}_-^{m+1} \equiv \mathbf{Q}^{m+1}(X_3^{m+1})
\end{aligned} \tag{139}$$

These equations ensure continuity of all displacement and traction components at the interface across two layers. The surface traction conditions can be expressed as:

$$\begin{aligned}
\hat{\mathbf{Q}}_-^1 \mathbf{C}_-^1 &= \mathbf{F}; \quad \hat{\mathbf{Q}}_+^N \mathbf{C}_+^N = \mathbf{0} \\
\text{where} \quad \hat{\mathbf{Q}}_-^1 &= [-L^1 \mathbf{Q}_{21}^1 \quad -L^1 \mathbf{Q}_{22}^1 \mathbf{E}^1]; \quad \hat{\mathbf{Q}}_+^N = [L^N \mathbf{Q}_{21}^N \mathbf{E}^N \quad L^N \mathbf{Q}_{22}^N]
\end{aligned} \tag{140}$$

Here the matrices $\hat{\mathbf{Q}}$ correspond to the lower-half of \mathbf{Q} relating to stress. The system of equations is then solved by assembling Eqs. (139) and (140) together into a $6N \times 6N$ banded matrix (called the global matrix, say \mathbf{G}):

$$\begin{bmatrix} \hat{Q}_-^1 & \mathbf{0} & \dots & & & & & & & \\ Q_+^1 & Q_-^2 & \mathbf{0} & \dots & & & & & & \\ & \vdots & & & & & & & & \\ \dots & \mathbf{0} & Q_+^{m-1} & Q_-^m & \mathbf{0} & \dots & & & & \\ & \dots & \mathbf{0} & Q_+^m & Q_-^{m+1} & \mathbf{0} & \dots & & & \\ & & & & & & \vdots & & & \\ & & & & \dots & \mathbf{0} & Q_+^{N-1} & Q_-^N & & \\ & & & & \dots & \mathbf{0} & \hat{Q}_+^N & & & \end{bmatrix} \begin{bmatrix} C^1 \\ C^2 \\ \vdots \\ C^N \end{bmatrix} = \begin{bmatrix} F \\ \mathbf{0} \\ \vdots \\ \mathbf{0} \end{bmatrix} \quad (141)$$

Alternatively, if the layup is symmetric about the mid-plane of the plate, then the system can be solved for the symmetric and anti-symmetric modes separately, thereby saving some computational time. The surface condition must also be split into its “symmetric” and “anti-symmetric” components. Then, the relevant surface condition on the top layer is enforced along with the continuity conditions up to the interface between layers $N/2$ and $N/2 - 1$ along with conditions of symmetry (u_3 , σ_{32} and σ_{31} being zero at the mid-plane) or anti-symmetry (u_1 , u_2 and σ_{33} being zero at the mid-plane). The problem is thus reduced to two systems, each of complexity $3N \times 3N$. With the problem constraints now enforced, if the forcing function is also known, this equation can be solved to find the constants, C^m .

VI. 1.C Forcing Function due to Piezo-actuator

The piezo actuator is modeled as causing in-plane shear traction of uniform magnitude (say τ_0 per unit length) along its perimeter, in the direction normal to the free edge on the plate surface $X_3 = 0$ (see Fig. 68), as was done in Chapter II. While the above formulation is generic enough to capture GW excitation by an arbitrary shape piezo, for brevity only the rectangular piezo shape is analyzed here. For the rectangular uniformly poled piezo-actuator of dimensions $2A_1 \times 2A_2$ (along the X_1 - and X_2 -axes respectively), which is located at the center of the coordinate system:

$$u_1(X_3 = 0) = \int_0^{2\pi} \int_0^\infty \left(\frac{-\tau_0}{i\pi^2} \sin(KA_1 \cos \Gamma) \sin(KA_2 \sin \Gamma) \right) \left(\times \frac{N(K, \Gamma)}{\Delta(K, \Gamma)} e^{-i(K(X_1 \cos \Gamma + X_2 \sin \Gamma) - \omega t)} \right) K dK d\Gamma \quad (145)$$

The procedure for inversion of this integral is analogous to that in Section II.4. The integrand is singular at the roots $\hat{K}(\Gamma)$ of $\Delta(K, \Gamma) = 0$, which is the dispersion equation for the multilayered composite plate. These roots are the allowable in-plane radial wavenumbers for the multilayered composite plate at angular frequency ω . $\Delta(K, \Gamma)$ is symmetric about the K -axis. The final expression for u_1 that would be obtained is:

$$\begin{aligned} u_1(X_3 = 0) = & \sum_{\hat{K}} \int_{\tilde{\Theta}_1 - \pi/2}^{\tilde{\Theta}_1 + \pi/2} \frac{-\tau_0}{4\pi} \cdot \frac{N(\hat{K}, \Gamma)}{\Delta'(\hat{K}, \Gamma)} e^{-i(\hat{K}\tilde{R}_1 \cos(\Gamma - \tilde{\Theta}_1) - \omega t)} d\Gamma + \\ & + \sum_{\hat{K}} \int_{\tilde{\Theta}_2 - \pi/2}^{\tilde{\Theta}_2 + \pi/2} \frac{\tau_0}{4\pi} \cdot \frac{N(\hat{K}, \Gamma)}{\Delta'(\hat{K}, \Gamma)} e^{-i(\hat{K}\tilde{R}_2 \cos(\Gamma - \tilde{\Theta}_2) - \omega t)} d\Gamma + \\ & + \sum_{\hat{K}} \int_{\tilde{\Theta}_3 - \pi/2}^{\tilde{\Theta}_3 + \pi/2} \frac{\tau_0}{4\pi} \cdot \frac{N(\hat{K}, \Gamma)}{\Delta'(\hat{K}, \Gamma)} e^{-i(\hat{K}\tilde{R}_3 \cos(\Gamma - \tilde{\Theta}_3) - \omega t)} d\Gamma + \sum_{\hat{K}} \int_{\tilde{\Theta}_4 - \pi/2}^{\tilde{\Theta}_4 + \pi/2} \frac{-\tau_0}{4\pi} \cdot \frac{N(\hat{K}, \Gamma)}{\Delta'(\hat{K}, \Gamma)} e^{-i(\hat{K}\tilde{R}_4 \cos(\Gamma - \tilde{\Theta}_4) - \omega t)} d\Gamma \end{aligned} \quad (146)$$

where:

$$\tilde{\Theta}_1 = \tan^{-1} \left(\frac{X_2 - A_2}{X_1 - A_1} \right); \quad \tilde{R}_1 = \sqrt{(X_1 - A_1)^2 + (X_2 - A_2)^2}, \text{ etc.} \quad (147)$$

Again, this notation is analogous to that in Section II.4. Furthermore, an approximate closed form solution can be obtained for the far field using the method of stationary phase. This is assuming damping is not modeled and that the integrand is real-valued. If damping is modeled, then a similar approximation can be done using the method of steepest descent [11]. Thus, for large values of R (which leads to large values of \tilde{R}_k , $k = 1$ to 4):

$$\begin{aligned}
u_1(X_3 = 0) = & \sum_{\hat{K}} \sqrt{\frac{2\pi}{\tilde{R}_1 \cdot \left. \frac{d^2(\hat{K} \cos(\Gamma - \tilde{\Theta}_1))}{d\Gamma^2} \right|_{\Gamma=\bar{\Gamma}_1}}} \frac{-\tau_0 N(\hat{K}, \bar{\Gamma}_1)}{4\pi\Delta'(\hat{K}, \bar{\Gamma}_1)} e^{-i(\hat{K}\tilde{R}_1 \cos(\bar{\Gamma}_1 - \tilde{\Theta}_1) - \omega t + \pi/4)} + \\
& + \sum_{\hat{K}} \sqrt{\frac{2\pi}{\tilde{R}_2 \cdot \left. \frac{d^2(\hat{K} \cos(\Gamma - \tilde{\Theta}_2))}{d\Gamma^2} \right|_{\Gamma=\bar{\Gamma}_2}}} \frac{\tau_0 N(\hat{K}, \bar{\Gamma}_2)}{4\pi\Delta'(\hat{K}, \bar{\Gamma}_2)} e^{-i(\hat{K}\tilde{R}_2 \cos(\bar{\Gamma}_2 - \tilde{\Theta}_2) - \omega t + \pi/4)} + \\
& + \sum_{\hat{K}} \sqrt{\frac{2\pi}{\tilde{R}_3 \cdot \left. \frac{d^2(\hat{K} \cos(\Gamma - \tilde{\Theta}_3))}{d\Gamma^2} \right|_{\Gamma=\bar{\Gamma}_3}}} \frac{\tau_0 N(\hat{K}, \bar{\Gamma}_3)}{4\pi\Delta'(\hat{K}, \bar{\Gamma}_3)} e^{-i(\hat{K}\tilde{R}_3 \cos(\bar{\Gamma}_3 - \tilde{\Theta}_3) - \omega t + \pi/4)} + \\
& + \sum_{\hat{K}} \sqrt{\frac{2\pi}{\tilde{R}_4 \cdot \left. \frac{d^2(\hat{K} \cos(\Gamma - \tilde{\Theta}_4))}{d\Gamma^2} \right|_{\Gamma=\bar{\Gamma}_4}}} \frac{-\tau_0 N(\hat{K}, \bar{\Gamma}_4)}{4\pi\Delta'(\hat{K}, \bar{\Gamma}_4)} e^{-i(\hat{K}\tilde{R}_4 \cos(\bar{\Gamma}_4 - \tilde{\Theta}_4) - \omega t + \pi/4)} +
\end{aligned} \tag{148}$$

where $\tan(\bar{\Gamma}_k - \tilde{\Theta}_k) = \frac{1}{\hat{K}} \frac{d\hat{K}}{d\Gamma}$. Thus, $(\bar{\Gamma}_k - \tilde{\Theta}_k)$ is the angle between the phase velocity and group velocity vectors [10], as shown in Fig. 69 (a). For composites, the group velocity is along the normal to the “slowness curve,” which is the polar plot of the reciprocal of the phase velocity versus propagation direction. This implies that the contributions from $\bar{\Gamma}_k$ dominate the integrals over Γ at large distances from the source. This reiterates a well-known fact about wave propagation in anisotropic media, i.e., the wave travels at a “steering angle,” which may be different from the angle that it was launched along by its source [10], as shown in Fig. 69 (b).

VI. 2 Implementation of the Formulation and Slowness Curve Computation

The theoretical formulation described above was implemented in Fortran 90. The linear algebra package LAPACK [229] for Fortran 90 was employed to evaluate the determinants of large banded matrices. The roots of the dispersion equation $\Delta(K, \Gamma) = 0$ were simply computed by the “zero-crossing” approach, i.e., by evaluating the determinant of the matrix over a fine grid in the (K, Γ) plane and looking for sign changes

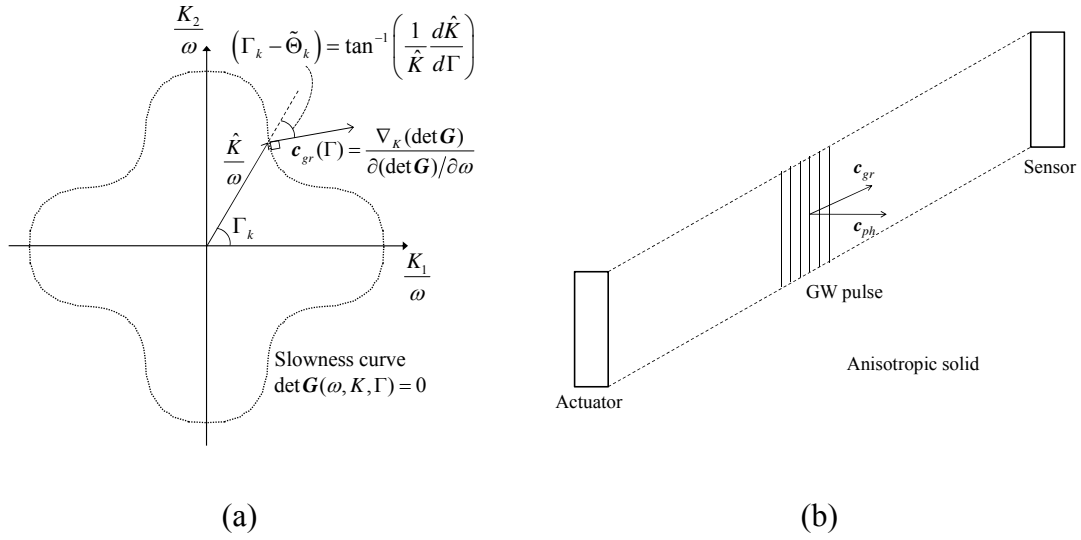


Fig. 69: (a) Relation between group velocity and slowness curve and (b) “Steering” in anisotropic media

in the value of the determinant. In doing so, one has to avoid the bulk wave velocities of the composite material, which are also roots of the dispersion equation. One also has to take care to use double-precision variables and compute the roots with high precision since with the very large matrices involved, small errors in the values of the roots cause large errors in the response solution. Furthermore, in tracking zero-crossings on a grid of (K, Γ) , due to the large variations in order of magnitude, it is convenient to plot determinant values on a logarithmic scale. The derivatives w.r.t. K were evaluated analytically. The code implemented in Fortran 90 to evaluate the determinant values (for zero-crossings) and integrand values (for the kernel of the integral) was computationally efficient, with each run being completed in a few minutes on a standard desktop computer (1.2 GHz Pentium IV with 256 MB RAM). The integrals over Γ were evaluated numerically (by summing the integrand’s values taken at intervals of 1°).

Some results for the slowness curves obtained are presented here. Graphite-epoxy composite plates (material properties: $\rho = 1578 \text{ kg/m}^3$; $c_{11} = 160.73 \text{ GPa}$, $c_{12} = 6.44 \text{ GPa}$, $c_{22} = 13.92 \text{ GPa}$, $c_{23} = 6.92 \text{ GPa}$, $c_{55} = 7.07 \text{ GPa}$; this is the same material used in [62]) were analyzed. Damping was not considered for these analyses. The slowness surfaces

(plots of inverse of phase velocity versus propagation direction) for the A_0 and S_0 modes in a 1-mm thick unidirectional plate at 500 kHz are shown in Fig. 70 (a). As seen there, the wavespeeds along the fiber direction (0°) are much faster than those along the normal direction. The corresponding plots for a quasi-isotropic laminate at 200 kHz of layup $[0/45/-45/90]_s$, with each ply being 0.11 mm thick, is shown in Fig. 70 (b). The S_0 mode for this laminate is approximately isotropic, with the differences in wavespeeds along different directions being invisible to the naked eye. However, the A_0 mode for the same laminate has significant directional dependence.

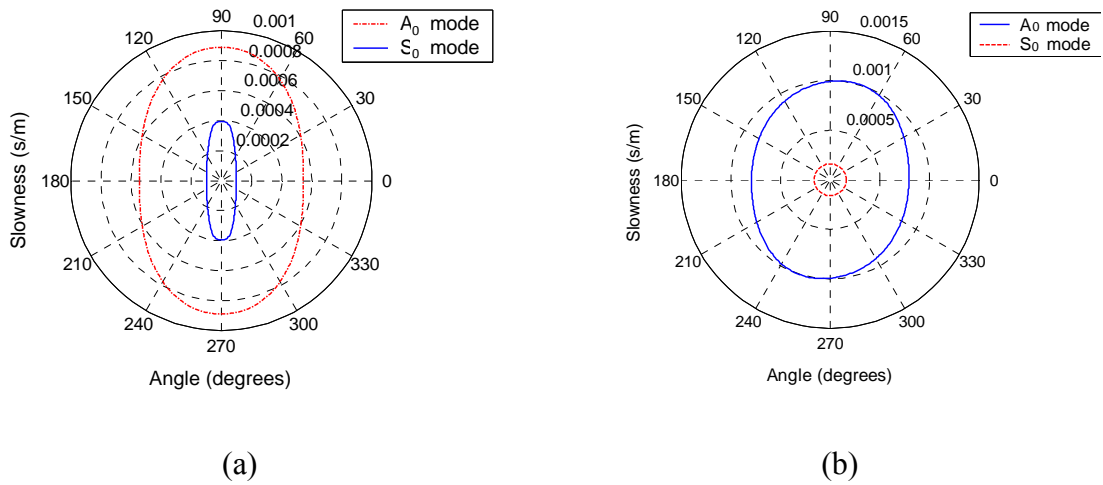


Fig. 70: Slowness curves for (a) 1-mm unidirectional plate at 500 kHz and (b) quasi-isotropic laminate at 200 kHz of layup $[0/45/-45/90]_s$, each ply being 0.11-mm thick

VI. 3 Results and Comparison with Numerical Simulations

Results were generated for a couple of test cases to compare with FEM simulations using ABAQUS [205] and examine the correlation between the two in terms of angular dependence of GW radiation patterns. The cases examined were for the unidirectional (in antisymmetric mode) and quasi-isotropic composite plates (in symmetric mode) described above, for which slowness curves were generated. In the case of the unidirectional plate, due to symmetry about three axes, a $1/8^{\text{th}}$ plate section of size

3 cm × 3 cm × 0.5 mm was modeled. For the quasi-isotropic plate, since it is symmetric about only one axis, a half-plate section of the modeled area was 20 cm × 20 cm × 0.44 mm (illustrated in Fig. 76). The quasi-isotropic plate also has “periodic” symmetry in the plane of the plate, i.e., the half-section from 0° to 180° can be rotated about an axis going through the plate center normal to its plane by 180° to obtain the other half. However, this cannot be used to reduce problem complexity in ABAQUS. A uniform mesh of 3-D 8-noded brick elements was used and the elements were small enough ($0.375 \times 0.375 \times 0.125 \text{ mm}^3$ for the unidirectional plate and $1.3 \times 1.3 \times 0.11 \text{ mm}^3$ for the quasi-isotropic laminate) to resolve the smallest wavelength excited over the frequency bandwidth. The element edges were all parallel to any of the three coordinate axes shown. Infinite elements could not be used to suppress reflections in these simulations, since they are not available in ABAQUS for use with anisotropic materials. Therefore, the simulation results were only used till the first excited GW pulse hit the plate boundary. Transversely isotropic material properties (identical to the values in Section VI. 2) were specified for the individual finite elements. For the transversely isotropic composite plate, four separate layers were modeled using one layer of finite elements each, and different material orientations were specified to model the $[0/45/-45/90]_s$ layup. Symmetry conditions were imposed along two edges along the in-plane axes for the unidirectional composite. Since antisymmetric modes were of interest for the unidirectional composite, thru-thickness antisymmetry conditions were applied to the nodes on the lower plate surface. Similarly, thru-thickness symmetric conditions were applied to the nodes on the lower plate surface of the quasi-isotropic laminate. On the upper plate surface of the unidirectional composite, to simulate the action of a square piezo exciting GWs at the center, a quarter section of the piezo was modeled. The complete piezo was modeled for the quasi-isotropic laminate. Shear forces were applied at nodes along the piezo’s edges.

In both cases, a 3.5-cycle Hanning window-modulated sinusoidal toneburst with center frequency 200 kHz was applied as excitation signal by specifying this waveform for the time variation of the shear force applied at the piezo’s edges. Again, the time step was chosen to be small enough to accurately capture the highest excited frequency. The out-of-plane displacements over the plate’s top surface (which has the surface-bonded

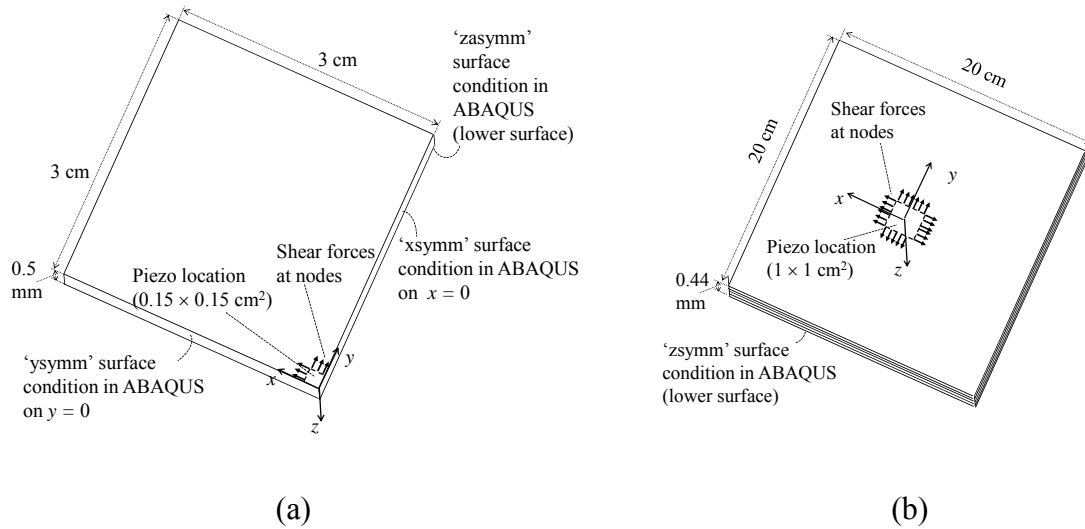


Fig. 71: Geometry of FEM models for: (a) 1-mm unidirectional plate and (b) quasi-isotropic plate of layup $[0/45/-45/90]_s$, each ply being 0.11 mm thick.

piezo on it) were recorded at various time steps. The corresponding values from the semi-analytical model were also generated. The results are shown in Fig. 72 and Fig. 73 for the unidirectional composite and quasi-isotropic laminate respectively, both normalized to the respective peak value of out-of-plane displacement over all time steps. Only results from half the plate-section of the quasi-isotropic plate are shown, due to its periodic symmetry. The row of nodes immediately adjacent to the piezo was not considered for the normalization to avoid errors due to the local numerical noise caused by the discrete nodal shear forces.

To generate the antisymmetric mode surface plots from the semi-analytical model for the unidirectional composite, only the A_0 mode was considered, since the highest frequency in the excited bandwidth is below the cutoff frequency for the A_1 mode. Similarly, to generate the symmetric mode surface plots for the quasi-isotropic plate, only the S_0 mode was considered. While the SH_0 mode also exists for the symmetric mode analysis at all frequencies, being approximately isotropic, it can be considered to be a “pure” mode [10]. Thus, the displacements in this case are for all practical purposes

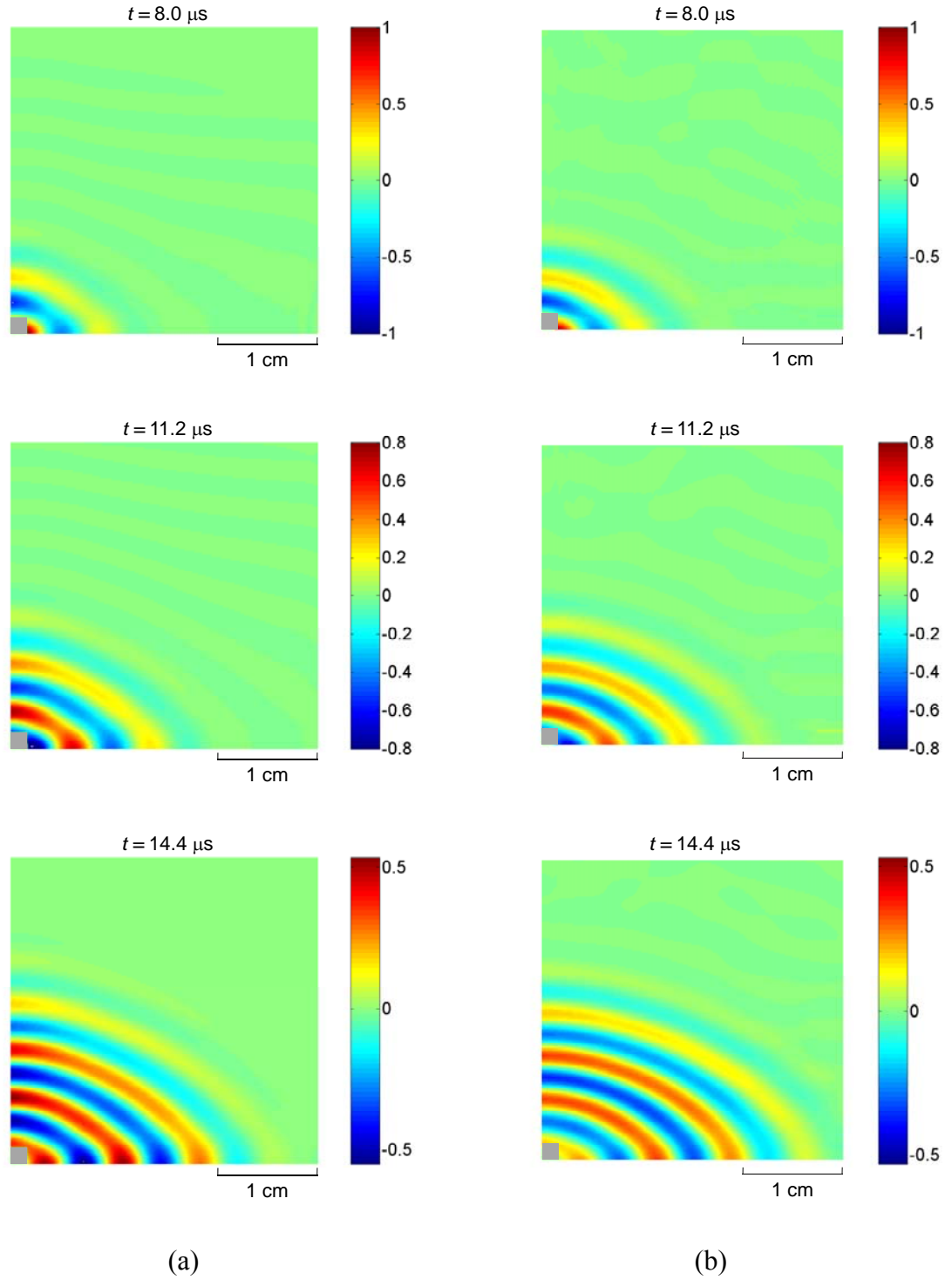


Fig. 72: Surface out-of-plane displacements at different time instants for the unidirectional composite excited in the antisymmetric mode (by the piezo, in gray) with a 3.5-cycle Hanning windowed toneburst at 200 kHz obtained using: (a) FEM (b) the developed model.

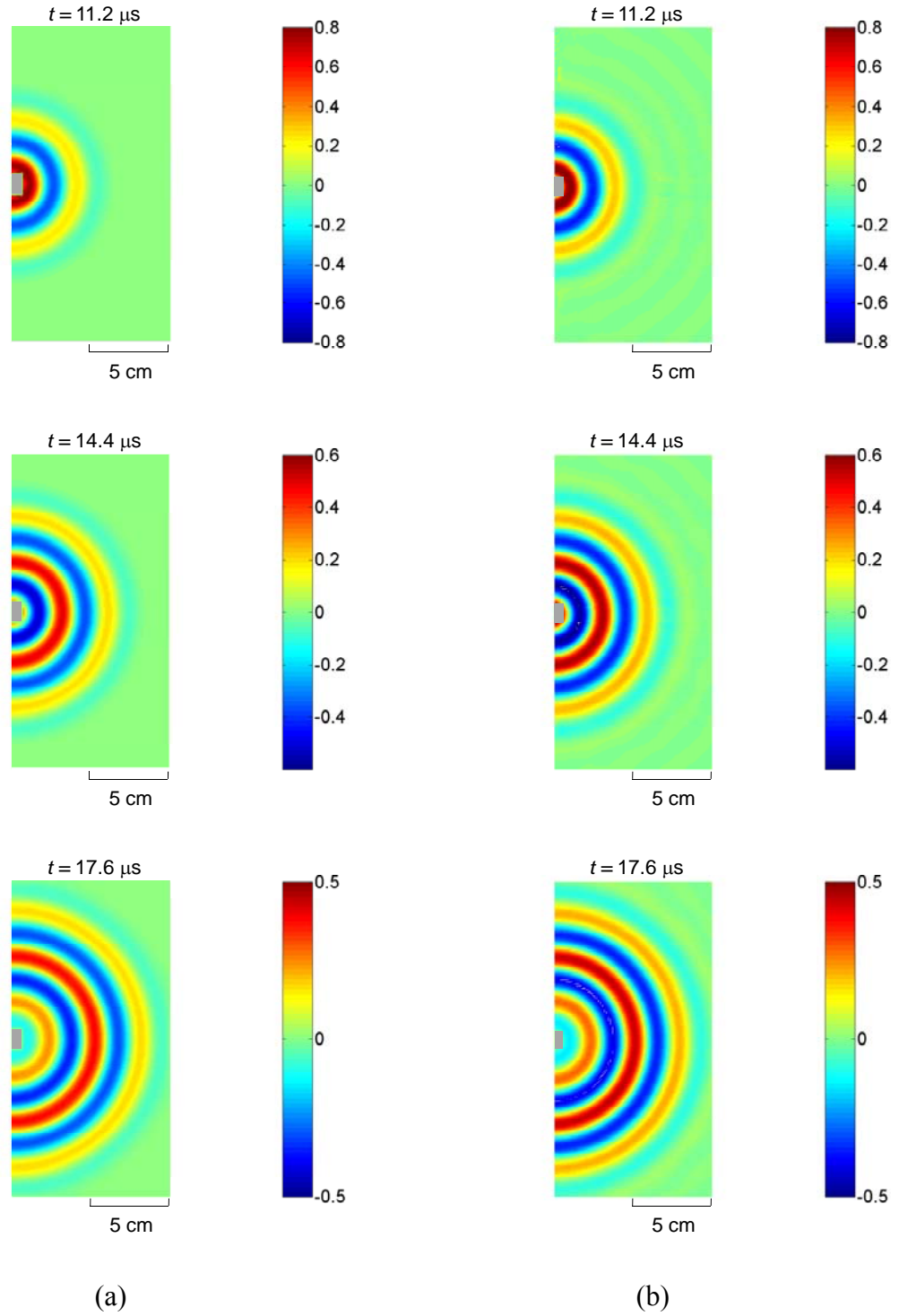


Fig. 73: Surface out-of-plane displacements at different time instants for the quasi-isotropic composite excited symmetrically (by the piezo, in gray) with a 3.5-cycle Hanning windowed toneburst at 200 kHz obtained using: (a) FEM (b) the developed model.

within the plane of the plate. Therefore, as in the analysis for isotropic plates, it does not cause out-of-plane displacements. However, the SH_0 mode would contribute to *symmetric* mode simulations for the *unidirectional* composite plate. This is because in that case, it is significantly dependent on direction and is therefore a “quasi-” SH_0 mode. Consequently, the displacement patterns in this mode are not entirely in the plane of the plate for directions not along or normal to the fiber direction.

The results from the FEM simulations are in agreement with that obtained from the semi-analytical model, thus verifying the accuracy of the model within the assumptions made. There are mild discrepancies in relative amplitudes between the two results. However, these are minor and can be ascribed to the limitations of the discrete mesh used in FEM and the application of the shear force at discrete nodal points along the piezo’s edge versus a continuous solid and uniform magnitude over the piezo edge modeled in the theoretical model. These models also need to be validated by experiment to ensure that the assumptions made here are sufficient before these models can be exploited for GW SHM system design in composite structures.

CHAPTER VII

CONCLUDING REMARKS, KEY CONTRIBUTIONS AND PATH FORWARD

This thesis examined a broad range of research issues in guided-wave structural health monitoring (GW SHM), an emerging area of structural mechanics with potential for application in a wide spectrum of aerospace, civil and mechanical structures. It started with an introduction to the topic including motivational drivers and basic concepts. As explained there, GW SHM essentially involves exciting structures using an onboard network of transducers with high frequency tonebursts and examining their response to get information about damage in them, if present. Work done by various researchers was reviewed and divided into different categories, viz., transducer technology, developments in theory and modeling, signal processing and pattern recognition, and GW SHM system development. Examples of application areas where GW SHM has been tested were then presented. Limitations of GW SHM in terms of blind zone areas in the vicinity of the transducers were identified and the use of piezos to implement alternative SHM approaches was discussed.

Based on this detailed survey, some important areas where further work was required and those that were chosen to be addressed herein were highlighted. Those included modeling of GW transduction by piezoelectric wafer transducers or *piezos* (both uniformly poled wafers and anisotropic piezocomposites), furnishing guidelines for choosing various parameters in GW SHM, developing improved signal processing algorithms and understanding the effects of elevated temperature. The rest of this chapter summarizes the key contributions of this thesis and suggests some future directions for research and desirable developments to bring this technology closer to field deployment.

VII. 1 Key Contributions

- a) Reliable models for GW transduction by piezos in isotropic structures were developed. This work was original in that 3-D elasticity was used for modeling the GW field excited by arbitrary shape, finite-dimensional piezos with a semi-analytical formulation to capture the GW radiation patterns by various piezo shapes. The 3-D nature of these models ensures that they can capture the true multimodal nature as well as the attenuation and modified frequency response characteristics of GW fields due to excitation of GW fields in infinite plates by finite-dimensional piezos. This also enables the design of rectangular uniformly poled piezos and APTs for spatial focusing of GW fields in plates. Furthermore, these models were extensively validated with numerical and experimental results.
- b) The models developed above were used to optimize actuator and sensor dimensions for maximizing GW strain field and response strength. This was the first work to suggest the idea that the optimal dimensions for piezo-actuators and sensors are very different. It was found that larger sizes are preferable for actuators (if one avoids the nodal points) while sensors should ideally have as small dimensions as allowed by the shear lag limit of the bonding mechanism. The idea of designing sensors to be immune to one GW mode and thereby reducing demands on the signal processing algorithm was also discussed.
- c) A set of guidelines were furnished for the design of excitation signal and piezo transducers in GW SHM, backed by the theoretical reasoning for each. The recommendations for transducer selection were based on the models developed in this thesis and took into consideration practical system constraints. This was a unique effort to standardize selection of these test parameters in GW SHM.
- d) A novel signal processing was proposed for GW SHM using chirplet matching pursuits and mode identification. The algorithm's potential advantages in terms of improved resolution, robustness to noise and ease of automated post-processing were highlighted. Results with this algorithm in initial numerical and experimental tests were very promising, where overlapping, multimodal GW reflections were successfully resolved and identified.

- e) The effects of elevated temperature on GW propagation and transduction by piezos were also addressed. While earlier efforts to examine effects of temperature on GW SHM only went up to 70°C, the temperature range up to 150°C was examined in this thesis. This was motivated by the potential application of GW SHM in internal spacecraft structures. A suitable bonding agent was identified to withstand degradation in the face of this elevated temperature range (Epotek 353ND). The variation of thermally sensitive parameters was quantified based on data available in the literature. This data was used in conjunction with the theoretical models for GW transduction using piezos in isotropic plates developed earlier in this thesis to model the effects of elevated temperature. The increase in time-of-flight in a pitch-catch experiment with increasing temperature was captured within the error margins of the experiment. This can therefore be exploited to compensate for the effect of temperature on group velocity to improve damage triangulation at elevated temperatures.
- f) The feasibility of damage characterization at elevated temperatures in the presence of structural features which may add complications was also investigated. It was found that the sensitivity of GW SHM in aluminum plates suffered beyond 80°C. The cause of this was attributed to the sharper rate of decrease in the elastic modulus of aluminum with increasing temperature beyond 80°C. “Mild” damage in the form of an indentation could be detected and located with reasonable accuracy till 80°C. “Moderate” damage in the form of a through-hole could be detected at all temperatures and located with good accuracy at the vast majority of temperature points. Suggestions for improving these results were also given.
- g) The semi-analytical models for isotropic plates were also extended to address GW excitation by finite dimensional piezos in multilayered, laminated plates built using unidirectional fibrous composite materials. These composites are gaining popularity as the structural material of choice in the aerospace industry. The developed models’ accuracy was verified by numerical simulations (within the assumptions made).
- h) Efforts by other researchers in various facets of this multidisciplinary field were brought together and thoroughly reviewed and the state-of-the-art in this area was

presented. This will be very useful not just as a starting point for any new researcher venturing into GW SHM but also for others engaged in research in this area to get a global perspective.

VII. 2 Path Forward

There are still several issues worthy of consideration to further advance the field of GW SHM. Transducers represent one crucial area where progress is needed. As discussed earlier, the majority of reviewed works and this thesis have employed piezoceramic wafer transducers. This is natural, since as pointed out in Niezrecki et al. [143], for high frequency actuation applications, piezoelectric transducers are most efficient and have high power density. There are two aspects in which these fall short: first, being brittle, they might be unsuitable for field application. In SHM, it is crucial that the transducers be able to survive events such as impact or collisions, so that they are in a position to decide the extent of damage to the structure from such events. Second, these have a limited temperature range of operation (e.g., PZT-5A is rated for up to 175°C), and their performance degrades significantly as the temperature crosses roughly half their Curie temperatures. Furthermore, while the piezoelectric effect works at temperatures down to zero degrees Kelvin, the strength of the effect weakens at lower temperatures. To overcome the mechanical issue, piezocomposite transducers are a good start. These include the active/macro fiber composites (AFCs/MFCs) which were modeled in this thesis. These have been originally developed for low-frequency structural actuation and efforts should be invested into tailoring these for high frequency GW transduction. Simultaneously, more detailed studies into other non-conventional transducer options such as those discussed in Section I.3 are desirable. Those might turn out to be superior to piezoelectric transducers. To address the second concern, high performance active materials that do not significantly degrade at high or low temperatures need to be developed. The current piezoelectric materials developed for extremely high temperatures (such as lithium niobate) are much weaker in terms of response compared to conventional piezoceramics at room temperature. Nanotechnology may provide new candidates in this regard. While some activities have been initiated into examining the non-obtrusiveness

and robustness of GW SHM system packaging to environmental extremes, further efforts in this direction are also needed. Suggestions for improving the performance of GW SHM systems under elevated temperature environments were provided in Section V.4. The effect of other harsh environmental conditions such as shock loads, humidity, etc. on packaging and the development of signal processing algorithms to overcome these effects should be pursued. In addition, more research into reliable electrical and mechanical connections is desirable including access to embedded transducers in composite structures. These may allow GW SHM to be used in extreme environment applications such as in long-duration mission spacecraft, aircraft engines, thermal protection system structures, cryogenic tanks, etc. In addition, transducer design should consider minimizing power and incorporating an onboard energy source for independent functioning. Significant advances in energy storage and/or harvesting devices are required to enable onboard power supply for GW excitation. Emerging alternatives in this regard are micro-engines (see for example Mehra et al. [230]) and fuel cells ([231], [232]), however these are still far from commercialization. Another promising option is the wireless transmission of energy in the form of radio frequency waves, as was done in the work by Kim et al. [146].

The models for composites developed in Chapter VI need to be experimentally validated before they can be utilized for designing GW SHM systems in composite structures. In addition, the theoretical work to model GW excitation by SHM transducers should be extended to more complex structural configurations such as curved shells, built-up structural constructions and composite structures. More investigation into different array configurations is also needed – these have better potential to monitor larger structural areas from a central location on the structure. Furthermore, coupled dynamics models of the transducer and the base structure are needed and should be pursued. In many of the above scenarios, pure analytical models may not be possible and a combination of semi-analytical and numerical methodologies might be needed. The modeling work done in this thesis for piezos will need to be extended towards modeling other non-conventional transducers.

In the majority of the reviewed literature and this thesis, GW testing was restricted to the lower GW modes. This might suffice if one is purely interested in locating the damage site, and not in characterizing it. For the latter, higher modes would be very useful due to their higher selectivity and better damage sensitivity. The reluctance of researchers to use higher modes can be traced to two reasons: first, the higher power requirements associated with exciting the necessary higher frequencies, and second, and most important, the inadequacy of the current signal processing algorithms for higher mode testing. Advanced signal processing methodologies that can accommodate such testing should be explored. One possible approach to handle higher mode testing would be using the matching pursuit algorithm with a dictionary of nonlinear chirplets, such as that used in [214] (however in that work, the algorithm was only tested for one of the fundamental GW modes). These should be complemented by the development and use of damage sensitivity models for better theoretical foundations in conjunction with pattern recognition algorithms for damage type and severity estimation. While several signal-processing methodologies have been developed, most have not considered automation amenability, minimizing the computational complexity and processing power requirements. Future developments in this area should consider optimizing the local processing requirements and minimizing data to be transmitted to a central controller.

It is hoped that the design guidelines provided in Chapter III will inspire similar efforts for choosing the other parameters and set standards for GW SHM systems by researchers/structural operators with the relevant expertise and experience. These will allow for the rapid dissemination of the GW SHM research knowledgebase to technicians and managers. System reliability and transducer diagnostics form another area where significant improvements are needed. Accurate methodologies for testing transducer health online are also highly desirable to ensure confidence in the data they collect. These will be crucial to avoid frequent false alarms being raised, which might take away from the desired benefit of fitting SHM systems of not having to frequently take the structure offline for inspection.

Finally, structural designers must take a holistic view of all SHM approaches and make use of the advantages of each in attacking SHM system problems. GW methods

may certainly provide for the large-area coverage of more homogeneous structural layouts. There are several opportunities for retrofitting SHM systems in existing structures. However, it is the author's view that SHM systems will be much more effective if made an integral part of the structural design process, right from the planning stage. Much more work is needed in this area.

APPENDIX A

NOTES ON EXPERIMENTAL PROCEDURES AND SETUPS

This appendix contains descriptions of several of the common experimental procedures used for the experiments. During the course of the research for this thesis, the author has gained experience with different instruments, transducers, and other components, along with the corresponding manufacturers/vendors. What follows is a simple compilation of that to ease the learning curve for other researchers and is not intended to be comprehensive. Moreover, the author has no stake in the companies listed here and cannot guarantee anything on their behalf.

A.1 Cutting Piezoceramics and MFCs to Size

Piezoelectric transducers can be obtained from several suppliers. Over this thesis, the author has come across the following companies:

1. APC International (www.americanpiezo.com)
2. EBL Products (www.eblproducts.com)
3. Piezo Systems (www.piezo.com)
4. Projects Unlimited (www.pui.com)
5. Network Cable (www.networkcable.com)

In particular, circular PZT-5H transducers with metal backing plates can be obtained at inexpensive prices (~ \$1 apiece) from the last two manufacturers in the list above, since they are manufactured in large volumes for use as audio buzzers. The following companies supply anisotropic piezocomposite transducers:

1. Smart Material (www.smart-material.com, for MFCs)
2. Continuum Control (www.powerofmotion.com, for AFCs)

Often, the transducer dimensions desired for the experiment are different from the wafer sizes in stock. In addition, MFCs are available in big sizes which may need to be trimmed for an experiment. An Exacto knife usually suffices to cut through piezoceramics and MFCs. However, for some harder piezoceramics, a diamond point knife (one such knife was purchased from Ted Pella Inc., www.tedpella.com) may be needed. The procedure to cut a piezo to size is as follows:

- First, the required size is marked off on one surface of the piezo with a sharp pencil. For uniformly poled ceramics, it should be ensured that identifying marks are made on the surface of the individual pieces to indicate the poling direction (usually it points inwards into the surface on which the manufacturer marks a round dot).
- Three small (a few inches square or rectangular, bigger than the piezo and a few mm thick) metal pieces with reasonably accurate linearity of edge finish (e.g. steel rulers) and a table, preferably with a glass top, are required. Each of them should be washed with acetone to clean off any grease or dust.
- The ceramic is then placed on the glass/table top and taped down with paper tape, leaving the pencil lines along which a cut is desired in clear view. This will ensure that the piezo does not shift while cuts are being made with the knife.
- With a steel ruler to ensure a straight cut, the Exacto/diamond-point knife is used to score the piezo along the line where the cut is desired. This should be repeated four to five times (preferably without lifting the knife from the groove to avoid cutting a new groove) or until about a third to half the piezo thickness is penetrated. The groove should span the whole width of the wafer, regardless of whether the whole width is needed or not.
- After this, the paper tape is removed and the piezo is aligned on top of one of the metal pieces (which is placed on the glass/table top). The freshly-cut groove should be just ahead its edge, so that the smaller part of the piezo is overhung from the metal piece. Again, paper tape is used to hold the portion of the piezo on top of the metal

piece in place. Then another metal piece is placed on top of the portion of the piezo on the first metal piece, with its edge lining up with the groove. Slight pressure is applied with one hand on the second metal piece.

- Finally, the third metal piece is placed on top of the overhung portion of the piezo to snap it. This is illustrated in Fig. 74. If there is only a single groove, the effort required for snapping the piezo will be minimal. This approach usually results in the cleanest cuts.
- Alternatively, the piezo can be cut by repeatedly scoring the piezo in the same groove with the Exacto/diamond-point knife till the groove goes through the thickness. This usually results in piezos with slightly rough edges, but this approach might be necessary for cutting MFCs, which are more mechanically flexible and may not “snap.”

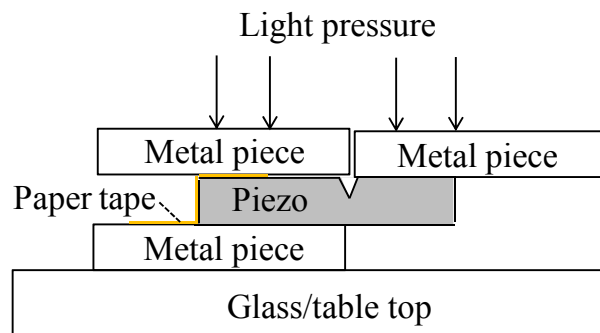


Fig. 74: Schematic of arrangement to cut piezos to size

A.2 Bonding Piezos to Plates

Epoxies were found to be the best bonding mechanism for reliably mounting the piezo to ensure effective transduction. Alternative bonding mechanisms such as electrically conductive tapes were found to be much less effective for transduction, even though those could allow for easier peeling off of the piezos. Using epoxies, it might be much more difficult to remove the piezos from the substrate, but at the same time, a strong bond and consequently efficient strain transmission is ensured. This section explains the procedure used to bond piezoceramics/macro fiber composite transducers to

aluminum plates using three different two-part epoxies, viz., Epoxies Etc. 10-3004 [220] and Epotek 301 and 353 ND [221]. The steps involved are as follows:

- First, pencil markings are made on the plate onto which the piezos will be bonded to mark the regions where the piezos will be attached.
- Next, the plate region where the piezos will be attached is made a slightly rough by light sanding (using grade 150 sandpaper). The resulting aluminum chips are dusted off, and the plate and the piezos are washed using some acetone to remove residual dust/grease.
- If the piezo is bonded onto a metallic plate, the plate itself can be used as common ground to access the lower electrode. If it bonded to a non-conducting substrate, a small copper/kapton tab can be attached to a corner of the lower surface while bonding. However, care should be taken to ensure that this has small in-plane dimensions and is thin compared to the piezo, otherwise the shear lag caused by this additional layer between the piezo and the substrate can affect transduction efficiency.
- The piezo is bonded such that the positive electrode (the side marked with a dot) faces up, and the negative one faces the plate (unless needed otherwise, e.g., for A_0 mode actuation with a pair of piezos excited out-of-phase). For a MFC, ensure that the surface with the tabs for soldering wires faces up.
- Uniform width strips (0.5 cm) of cork are cut in advance, to be of appropriate size to surround the piezo after it is placed for setting. One piece of cork strip is cut to the same size as the piezo and goes on top of the piezo (without removing the adhesive peel, so that it doesn't stick to the piezo) to apply light pressure for setting.
- Small portions of the epoxy components are mixed using an electronic scale to ensure the correct mixing ratio by weight. The epoxy is uniformly applied using wooden toothpicks/sticks to have a thin layer on both surfaces, the lower electrode of the piezo, and the plate region where the piezo will be bonded.
- The piezo is then placed on the plate and aligned to fit within the pencil markings on the plate. Light pressure is applied to the piezo to allow excess epoxy to flow out.

Then, a gauze swab is used to wipe off the excess epoxy. The bond layer should be as thin and uniform as possible to maximize transduction efficiency.

- The cork strips are subsequently glued on the plate to surround the piezo. These ensure that the piezo does not displace from its location when setting. The cork strip piece cut to the size of the piezo (with its adhesive peel strip intact) is then placed on top of the piezo with the adhesive peel layer facing the piezo.
- A gauze swab is placed on top of the cork strip pieces, and taped down using paper tape. This will keep the cork strips in place.
- Finally, weight is applied on top of the gauze swabs. Uniform weights are applied on each of the piezos. This is usually achieved by placing a thick sponge layer (or a big book) over the plate and then using small weights (~ 2 lbs.) over this layer.
- There is no requirement for minimum pressure to be applied specified by the manufacturers as long as the two surfaces to be bonded are in good contact with each other. For bonding onto curved surfaces, this might imply designing a special clamp/fixture to maintain contact between the surfaces during curing.
- The mixing ratios (part A:part B) and cure cycles for the three epoxies are:
Epotek 301: 4:1; 24 hours at room temperature.

Epoxies Etc. 10-3004: 1:1; 24 hours at room temperature.

Epotek 353ND: 10:1; 30 minutes at 80°C.

- When Epotek 353ND was used along with another epoxy on the same plate (as in the initial bonding agent evaluation tests), the piezo bonded with 353ND was cured first in the oven before the other piezos were attached for curing.
- Epotek 301 and Epoxies Etc. 10-3004 are effective only for low temperature applications (up to ~ 40°C) while Epotek 353ND is effective for elevated temperature applications (tested up to 150°C, as reported in Chapter V).

A.3 Soldering Wires to Piezos

For making electrical connections to piezos, standard multi-strand wires are the best option: single-strand wires, which can be easier to handle, break faster, due to poorer

mechanical fatigue properties and can pick electrical noise easily. BNC cables, which have excellent electrical noise robustness, on the other hand, can be cumbersome to handle for soldering on to piezos. It is advisable to use multi-strand wires up to a cable stand with connectors that provide strain relief and then use a thin BNC cable from that point to the instrument (as shown in Fig. 75). However, BNC cables can add more impedance to the circuit and consequently suppress the signal. Therefore, the length of the BNC cable should be minimal. For the thermal experiments, it should be ensured that the wires and BNC cables can withstand the temperature range of the experiment (standard wires and cables with polyvinyl chloride, i.e., PVC insulation are only good up to 70°C).

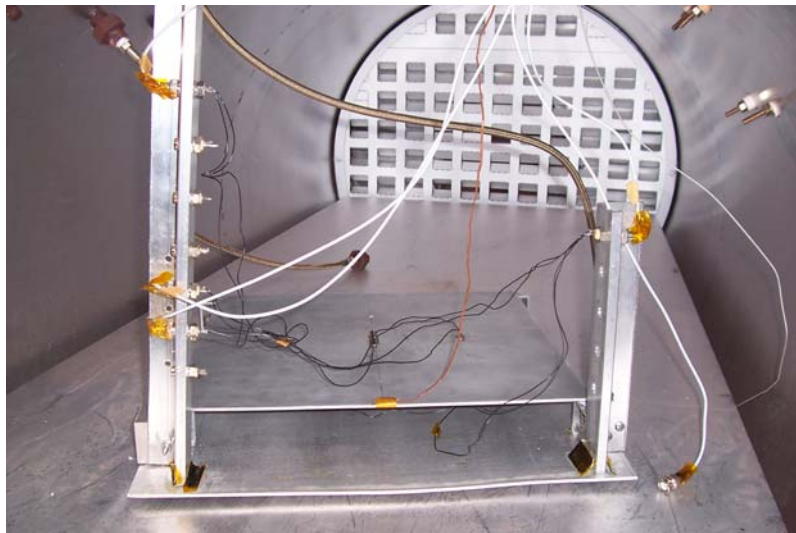


Fig. 75: Photograph of specimen with cable stand in the autoclave for thermal experiments

For soldering, again ensure that the solder is rated up to the maximum temperature of the experiment. For the thermal experiments in this thesis, tin-lead-silver alloy solder wire (HMP 570-28R Sn-Pb-Ag of diameter 0.71 mm from Vishay was used) was used, which is capable of withstanding 150°C. The soldering iron was set at 450°C (850°F) for soldering with this wire. This is above the Curie limit for PZT-5A (360°C),

however if care is taken to ensure the solder iron is not in contact with the piezo's metal electrode for more than a few seconds at a time, the piezo will not be damaged. For the room temperature experiments in Chapters II and IV, alloy Sn63/Pb37 solder wire of diameter 0.78 mm (purchased from McMaster-Carr) was used and the solder iron temperature was set at 340°C (650°F).

Before starting, the piezo electrode surface to be soldered should be cleaned with acetone. A wire stripper or knife should be used to strip off a small portion of the insulation for soldering. The portion of the wire exposed for soldering should be minimal to avoid the possibility that the exposed lead touches the metallic plate or some other lead and causes a short circuit. As recommended by Ferroperm, a manufacturer of piezoceramics (<http://www.ferroperm-piezo.com>), the wire's exposed cross-section should be in contact with and parallel to the electrode surface at the solder joint, as shown in Fig. 76, for better strength.

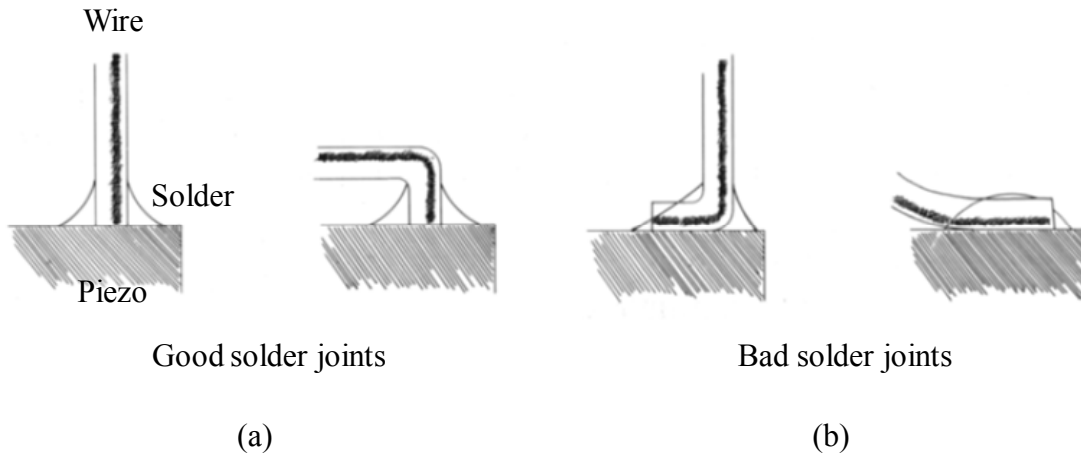


Fig. 76: Illustration of solder joints: (a) Preferable configuration for strong connections and (b) Undesirable configuration

A.4 Configuring the Function Generator

The function generator used in this thesis was Agilent's 33220A. Other manufacturers of similar function generators are Tektronix (Models AFG 3021 and AFG

3022, www.tektronix.com), Rohde and Schwarz (Model R & S AM300 and above, www.rohde-schwarz.com) BK Precision (Model 4070A and above, www.bkprecision.com). The remainder of this section describes the settings for the Agilent 33220A function generator used in most of the experiments.

A limited cycle sinusoidal tonebursts modulated by some window function was most commonly used as the excitation signal. This is not a standard signal available with the 33220A. Therefore, the signal had to be specified in the “arbitrary waveform” mode. The signal was produced in Matlab [233] and saved as a comma-separated values or .csv file (a sample code for generating such a signal is listed in the Appendix B in this thesis). It is preferable to define as many points as allowed by the instrument to minimize interpolation errors and also to allow for higher amplitude signals (the function generator tends to limit the amplitude for signals with fewer data points). Both these models come with “Agilent Intuilink,” which is special software for generating/downloading these signals from any standard desktop computer. It is menu-driven software which is fairly straightforward to use. Agilent 33220A can be connected via a local area network (LAN) cable through a router to the desktop. After identifying the instrument in Intuilink, the .csv file must be opened and downloaded to the instrument. If there is an error in downloading, the instrument usually gives an error code which can be looked up in the manual. Most commonly, errors result from improperly connected instruments.

Once the signal is downloaded, it should be stored into the permanent memory. Once this is done, the “Arb” function key should be pressed (see Fig. 77). Several menu options appear on the screen which can be accessed via the softkeys. The “Select Wform” softkey should be pressed next, followed by the “Stored Wforms” softkey and the softkey for the downloaded waveform that was stored earlier. Once the desired waveform appears on the screen, the “Select Arb” softkey should be pressed. Next, the frequency of the arbitrary waveform signal should be chosen (by hitting the “Freq” softkey and entering a value by the number keypad or turning the number dial). It should be noted that this is different from the desired center frequency of the signal. If, for example, the waveform consists of 3.5 sinusoidal cycles, the center frequency will be 3.5 times the frequency setting of the arbitrary waveform. The amplitude should be selected next. The maximum amplitude was 18.2 V when outputting a 32,000-point 3.5 cycle Hanning windowed

toneburst and this was the default value chosen. The D.C. offset should be set to 0 V using the “Offset” softkey.

With these settings, the function generator will continuously produce the arbitrary waveform. In the experiments done, tonebursts at regular intervals were required. To allow for this, the “Burst” key should be pressed which opens up a new menu on the screen. In this menu, the “# Cycles” softkey is used to set the number of cycles to “1 Cyc”. Pressing the “Trigger Setup” softkey will open up the “Source” menu, and the “Int” option should be chosen there. The “Burst Period” should be chosen to be “1.0 s,” which allows a one-second gap between subsequent bursts. This usually is enough time to allow the multiple boundary reflections from the previous excited GW burst to die out. After making these settings, hit the “Arb” function key again. Hitting “Output” after this will emit the downloaded toneburst signal at the desired frequency and amplitude at one-second intervals. A 3.5 V square wave is emitted from the “Sync” terminal for the duration of each burst. A BNC cable should be connected between this terminal and the auxiliary trigger input terminal of the oscilloscope to synchronize the start of the toneburst excitation signal and the start of sensor signal collection (the start of the burst then becomes time $t = 0$). Before the oscilloscope settings are discussed, one last point to note is that the function generator’s LAN address can be found using the “Utility” function key, followed by the “I/O,” “LAN” and “Current Config” softkeys. This will be needed as an input parameter for the thermal experiments’ Labview [234] module file (discussed later in this appendix). The “Store/Recall” function key can be used to store these settings, once they are configured, for easy retrieval later. Finally, pressing the “Output” key will enable the actuation signal being produced at the “Output” terminal.

A.5 Setting the Oscilloscope Up for Reading and Saving Signals

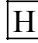

The oscilloscope used in this work was the Agilent Infiniium 54831B (shown in Fig. 78), which has four data channels and can handle signals up to 4 Gigasamples per second. Other manufacturers of similar oscilloscopes include Tektronix (THS 700 and above, www.tektronix.com), LeCroy (Waverunner-2 and above, www.lecroy.com), BK Precision (5105A and above, www.bkprecision.com). The rest of this section describes



Fig. 77: Agilent 33220A front view

the settings needed for data acquisition using the Infiniium 54831B, which has an in-built computer with a Windows 98 operating system:

- The oscilloscope should be powered on and after it boots up, the mouse icon at the top-right corner should be clicked using the mouse, which leads one to the menu-driven interface.
- It should be ensured that each of the channels which are connected to the piezos are in the “AC coupling” mode (which automatically includes an inline 3 Hz high-pass filter to remove DC offsets) and have “1 M Ω ” input coupling impedance (this ensures that negligible current flows into the oscilloscope thereby ensuring accurate measurements). These buttons are right above the respective channel on/off switch to the right of the screen.
- The channel scales should be set suitably, depending on whether the channel is reading an actuator or a sensor signal (using the menu sequence “Setup \rightarrow Channel 1” and adjusting the “Scale” in the popup). Typically, 5 V/div is a good scale for the actuation channel and 50 mV/div for the sensor channels ensures that the signal does not go out of the screen. However, these numbers may need to be tweaked depending on the center frequency, sensor sensitivity, etc.
- Next, the horizontal scale (for time) and offset needs to be adjusted so that the relevant portion of the signal is visible (typically the actuation/first transmitted signal

- and first boundary reflection). The menu sequence “Setup → Horizontal” opens a popup where these parameters can be changed (alternatively these fields are located at the bottom of the screen to the right of the symbol ). Assuming the offset is relative to a center reference (indicated by a highlight on “Center” instead of “Left” or “Right” below the offset tab), the offset value needs to be 5 times the horizontal scale so that $t = 0$ is at the extreme left of the screen. Usually, for center frequencies in the vicinity of 200 kHz, setting the scale to 5 μs and the offset to 25 μs suffices.
- To configure the trigger (assuming the BNC cable from the “Sync” terminal of the function generator is connected to the “Aux Trig In” terminal at the back of the oscilloscope), the menu sequence Setup → Trigger should be used, which opens the “Trigger Setup” popup. The following parameters should be used for the fields in the popup: Mode: “Edge”; Sweep: “Triggered”; Source: “Aux”; Level: “3 V” (with the rising icon checked next to the “Level” field). The last two fields can also be adjusted at the bottom of the screen next to the  icon.
 - The acquisition parameters can be adjusted using the menu sequence “Setup → Acquisition” to open the “Acquisition Setup” popup. The following settings should be used: Sampling Mode: Real Time, Normal; Memory Depth: Automatic (this should be set to Manual and adjusted accordingly if many signal data files have to be saved); Averaging: Enabled (64); Sampling Rate: Manual (the number here should be the value just greater than 20 times the maximum expected frequency in the signal, which is usually the upper limit of the excited signal bandwidth). Also, the “Sin(x)/x Interpolation” box should be checked. After all these adjustments are made, close the popup by clicking the “Close” tab.
 - In order to readily obtain peak-to-peak measurements from each of the sensor signal channels, click on the icon to the left of the screen that reads “Vp-p” when the mouse is moved over it. The sensor channels in use should be chosen one at a time and the following entries are displayed at the bottom of screen for each of the chosen channels: Current, Mean, Std Dev, Min, Max.
 - The “Run” button to the right of the screen should be hit to start collecting data. The “Stop” button can be used to stop data acquisition after the required number of

samples is obtained for averaging. It should be noted that the channel statistics at the bottom of the screen will be reset if the signal is shifted using the mouse or zoomed into (which can be done by creating a box around the desired portion with the mouse and right-clicking). The signal can be saved using the menu sequence “File → Save → Save Waveform”. The desired channel number should be chosen in the resulting popup and the signal should be saved as a .wfm format waveform if it is to be loaded on the screen for later viewing. If it is to be downloaded for plotting/processing externally, it should be saved as a .csv/.tsv (comma/tab-separated variable) file.

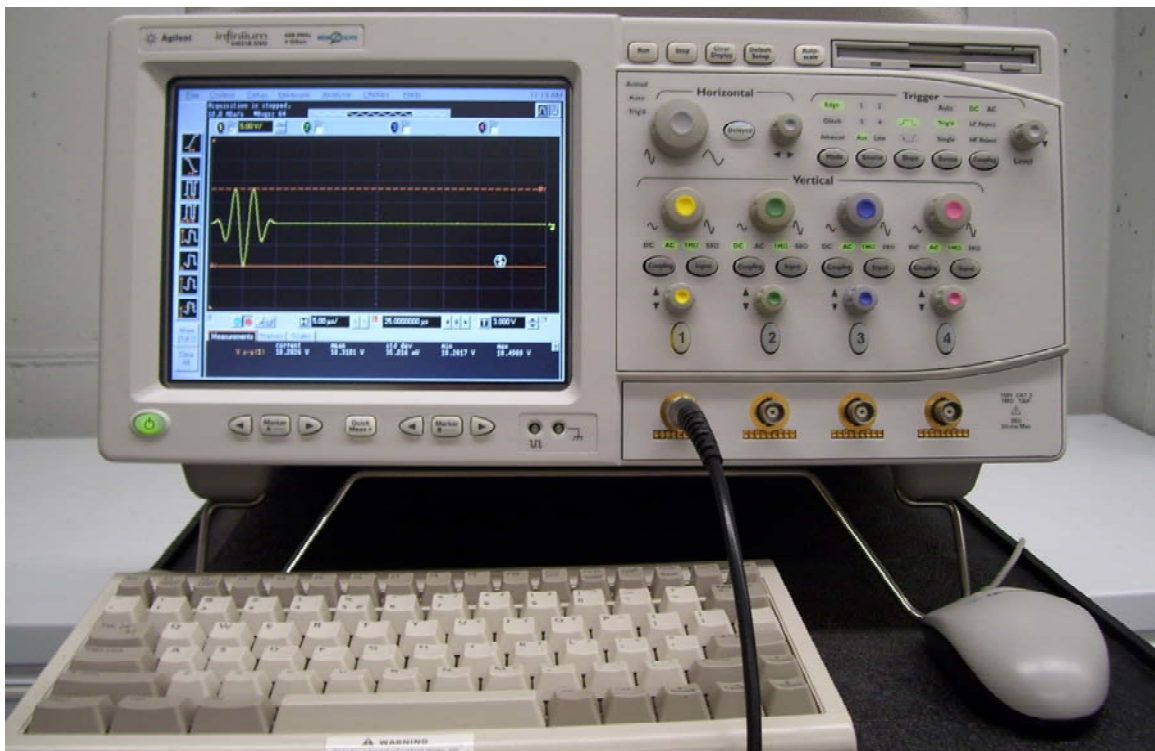


Fig. 78: Infiniium 54831B oscilloscope front view

- The oscilloscope can be connected to a computer via the LAN through a router for file sharing/downloading. A small office/home network between the desktop/laptop and the Infiniium might need to be set up from the desktop/laptop to which data needs to be downloaded. Care should be taken to not connect the oscilloscope to the internet, since the vulnerable Windows 98 system will be hacked into within no time.

After connecting it to a router, the LAN address of the oscilloscope can be obtained using the menu sequence “Utilities → GPIB Setup” which opens a popup showing the LAN address at the bottom (between the parentheses after “lan” and before “:inst0”).

A.6 Using an Oscilloscope for Electromechanical Impedance Measurements

As mentioned in Chapter I, it might be necessary to supplement the GW approach to SHM with another methodology to scan the blind zone area close to a transducer. The same piezos mounted on the structure can be used to obtain electromechanical (EM) impedance measurements. Only the excitation signal and signal acquisition/processing method need to be changed. The paper by Park et al. [235] presents an overview of this approach.

Early efforts to take EM impedance readings used expensive impedance analyzers. However, as suggested by Peairs et al. [236], an oscilloscope and function generator can be used in conjunction with a simple operational amplifier-based current measurement circuit to obtain electromechanical impedance measurements. The circuit diagram for this is shown in Fig. 79. The output voltage of the amplifier circuit, GV_o , is proportional to the current flowing through the piezo (labeled “pzt”). A separate channel is used to measure the voltage drop across the piezo (V). A sine sweep function spanning 1-2 seconds in the time domain is typically used as the excitation signal. The frequency range of the sweep has to be determined empirically for the structure and damage type of interest. Then, the impedance signal shape in the frequency domain is given by $Z(f) \propto V(f)/GV_o(f)$. The sensing resistor R_s should be around 100 Ω or so. This circuit was implemented on a breadboard using an LM741 operational amplifier chip and preliminary tests were done for bolt torque testing in an aluminum strip instrumented with piezos (Fig. 80). A gain factor of 1000 was set using $R_2 = 100 \text{ k}\Omega$; $R_1 = 100 \Omega$. To avoid strong interference from the power supply’s 50 Hz signal and other radio frequency noise, the circuit had to be enclosed in a “Faraday cage.” This is essentially a metallic box with terminals on the outside for the cables connecting to the circuit. Encouraging

results were obtained for detecting bolt torque of the clamp in this initial experiment (Fig. 81). A clear shift in the EM impedance signature is observed when one of the bolts is loosened in the clamp, and it returns close to the original signature when the bolt is retightened.

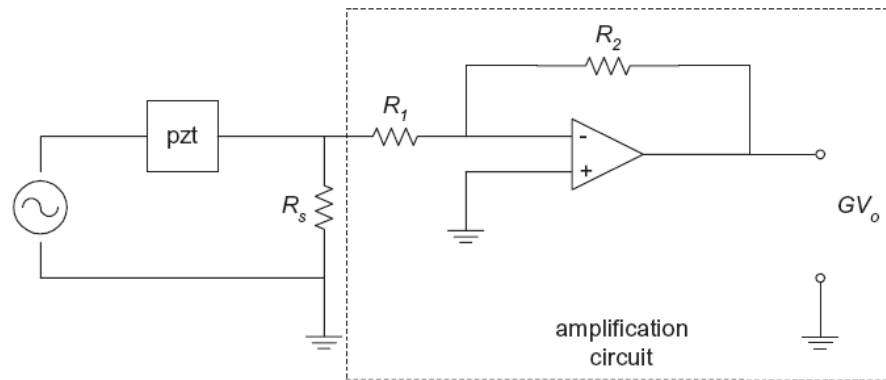


Fig. 79: Current measurement circuit using operational amplifier [236]

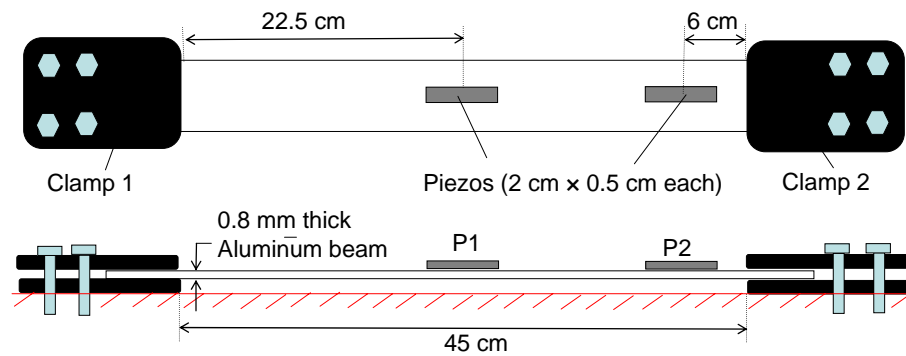


Fig. 80: Experimental setup for EM impedance measurements of bolt torque

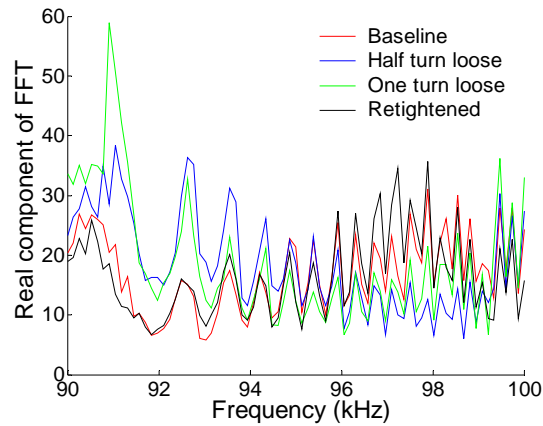


Fig. 81: Results from preliminary experiments done for bolt torque detection (FFT \equiv fast Fourier transform)

A.7 Notes on the Labview-based Setup for Automated Thermal Experiments

A fairly complex Labview [234] program was developed for taking readings automatically in the elevated temperature experiments done in Chapter V. The specimen was placed in the autoclave (which had one port opened to allow BNC cables and thermocouple wire to go through and connect the specimen to the instruments outside). The objective of the Labview program was to monitor the specimen temperature and at intervals of 10°C , it had to force the function generator to send an excitation signal to the actuators (a 3.5-cycle Hanning window toneburst with center frequency 120 kHz) 30 times at one-second intervals. The oscilloscope was simultaneously activated and recorded the averaged signal after 30 such readings for each channel along with the statistics for each channel. The specimen temperature was increased at $1^{\circ}\text{C}/\text{minute}$ from 20°C to 150°C , after which the autoclave was pre-programmed to dwell the specimen at 150°C for five minutes and then cool at the same rate to 20°C . At two pre-defined temperatures (100°C while heating and 70°C while cooling), instead of taking just the averaged signal, the 30 raw signals were recorded individually to get an estimate for error in time-of-flight (which cannot be obtained in the channel statistics). This is only done for two temperatures since doing so for all temperatures could cause the hard disk to fill up pretty quickly due to the large volumes of data.

The temperature was recorded using a K-type thermocouple, which was connected to a thermocouple module (Fluke 80TK), shown in Fig. 82 (a). This converts the K-type thermocouple signal into a voltage signal (at 1 mV/°C or 1 mV/°F depending on the switch setting). This module in turn was connected to the desktop with LABVIEW through a data acquisition (DAQ) system, shown in Fig. 82 (b) (in principle, a one-channel temperature module DAQ would also suffice). The DAQ was a PCI-DAS6070 system from Measurement Computing, which can be configured using “INSTACAL,” which is software that comes with the board. In configuring this DAQ board, it should be ensured that only the P3 connector is connected and the board is set to “16 channels (reference to ground), single-ended.” The Labview program assumes the thermocouple module is connected to “CH 0.”



(a)



(b)

Fig. 82: (a) Thermocouple module and (b) data acquisition system

The front-end for the Labview program is shown in Fig. 83. The input parameters for this program are the IP addresses for the function generator and oscilloscope, the local directory on the desktop for saving the statistics files, the prefixes for the names of the signal files, the number of averages after which to stop acquiring data and total number of temperature points (at 10°C intervals) over the heating and cooling phases. The last two

fields are 11 and 10 respectively if the starting temperature is just below 20°C and the maximum temperature is 150°C. The oscilloscope channel number is automatically prefixed to the signal files and the temperature at which it is recorded is also added at the end of the filename. The signal files are saved in the Infinium’s hard disk in the directory “C:\Scope\Data” by default while the statistics files are saved on the desktop where specified. The temperature read by the thermocouple is shown in the fields labeled “Heating temp.” and “Cooling temp.” as well as by the thermometer graphics. The “Switch to cooling cycle” switch is a feature that would be desirable that does not presently function. It would enable one to manually switch to the cooling phase readings in the unlikely event that the autoclave does not heat the specimen all the way to 150°C, since there is no interaction between the LABVIEW system and the autoclave computer.

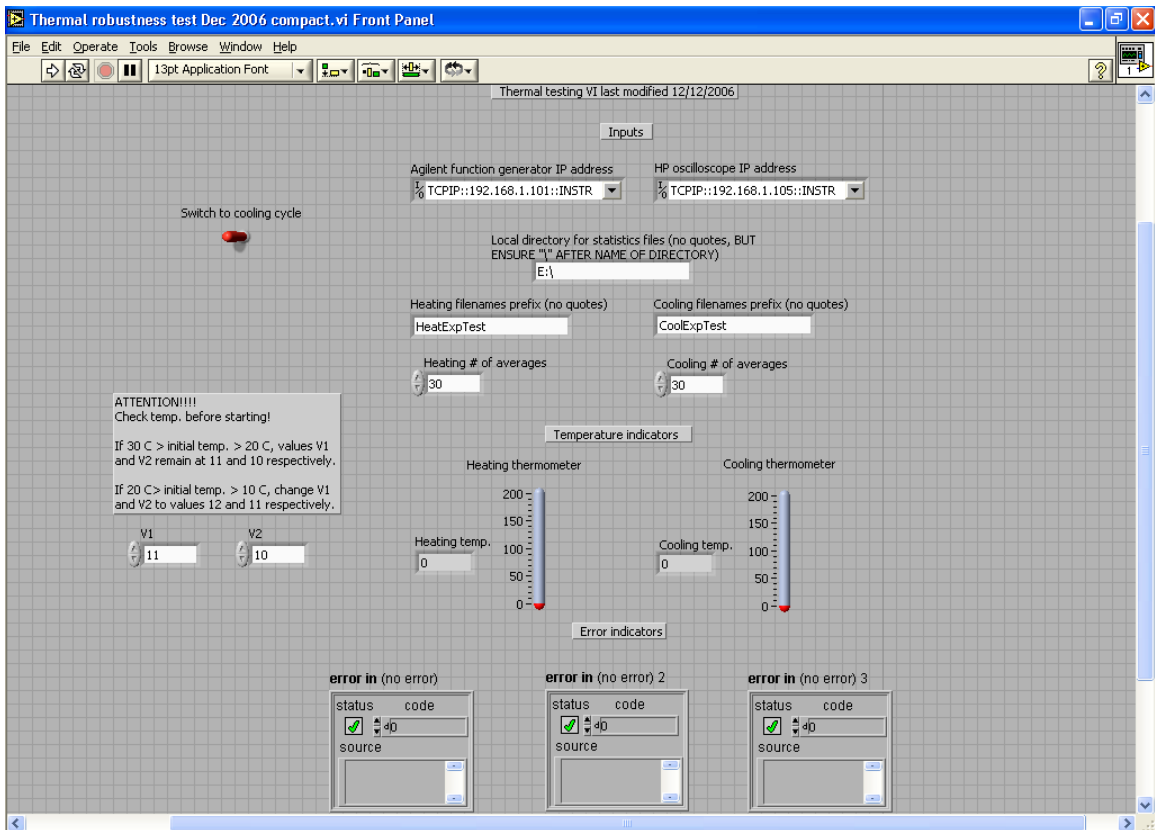


Fig. 83: Front panel showing inputs for Labview program

The basic sequence of operations done by the Labview program for each reading is shown in Fig. 84. Some of the modules for the instruments were downloaded from Agilent's website while some other minor ones had to be written borrowing the basic structure from the downloaded modules. The Labview program has two blocks, one each for the heating and cooling phases (indicated by "0" and "1" at the top of the structure). Each block executes two basic sub-blocks in a sequence, which is enclosed in a loop preprogrammed to run a finite number of times (defined as an input). The first sub-block reads the temperature through the DAQ (using the xAin module) and checks if it is within 0.5°C of one of the pre-set temperature points (in this case a multiple of 10°C). The 0.5°C tolerance is needed, since without this allowance, occasionally some temperature readings are skipped. This is because of the noise in the thermocouple reading. It would be desirable to add a low pass filter to the temperature read from the thermocouple. As soon as the temperature is within 0.5°C of a 10°C multiple (and it is not the pre-defined temperature for collecting all the raw signals in the heating phase, indicated by the True/False state on top of the second sub-block), the second sub-block in the sequence begins and the instruments are awoken for data collection. First, the oscilloscope screen is cleared and it is activated (the "Run" light glows). Then, the output of the function generator is enabled and there is a time delay of 30 seconds to allow the signals to average over 30 readings. After that, the oscilloscope stops data collection (the "Run" light stops glowing) and the statistics are downloaded to the desktop and saved in a file in the pre-defined local directory. After a minor time delay of 2 seconds (to allow for the statistics data to download), the individual averaged signals recorded by the four channels are saved into .tsv files. The modules at the bottom concatenate the pre-defined file name string with the respective channel number and the temperature reading of the thermocouple (ignoring the value after the decimal point). Finally, the function generator output is disabled and the Labview program switches back to recording the temperature. For the two temperature points at which individual signals without averaging are desired, first the averaging feature of the oscilloscope is turned off and then a similar sequence of steps is executed and the individual signal files are saved (this is not shown in Fig. 84). The averaging feature is then turned back on and the Labview program switches back to monitoring temperature. After data is collected and stored for the pre-defined number of

temperatures at 10°C intervals during the heating phase, the loop in block “0” stops and the control switches to block “1” corresponding to the cooling phase and stops after collecting signals for the pre-defined temperature points (also at 10°C intervals).

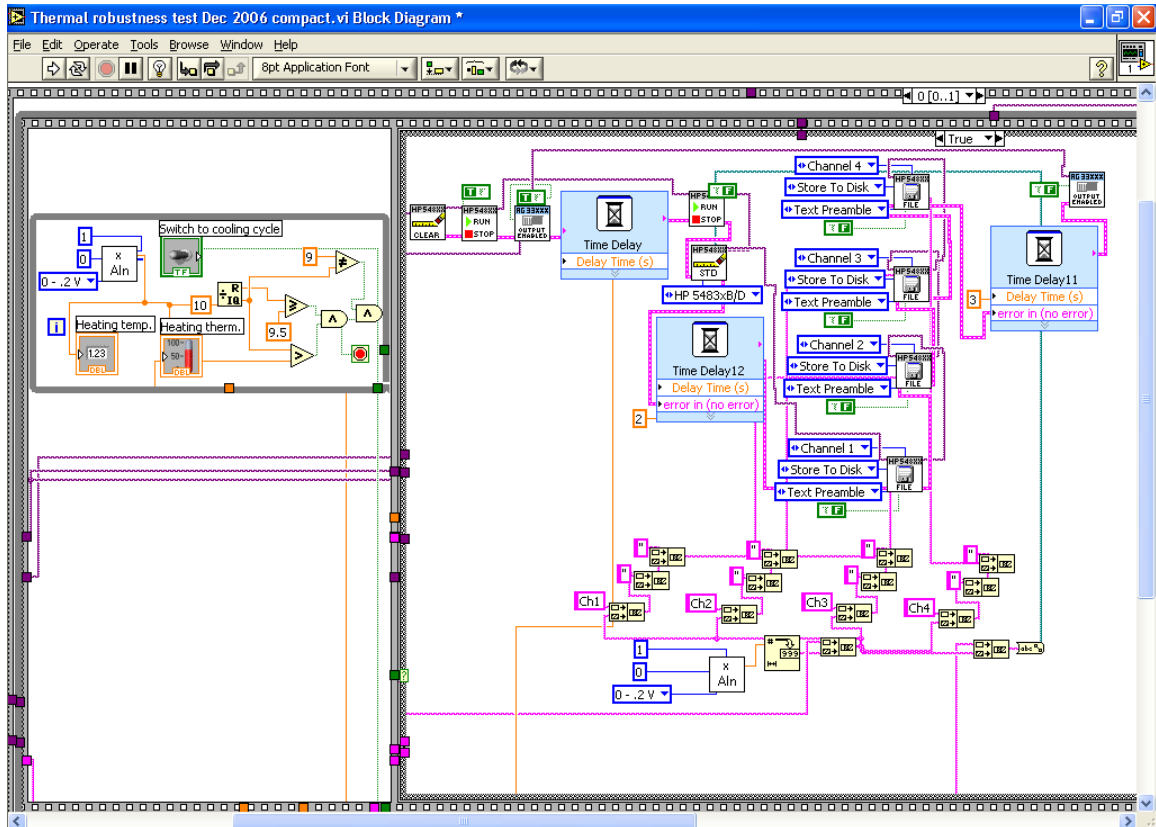


Fig. 84: Portion of the block diagram of the LABVIEW program

APPENDIX B

SOFTWARE CODE AND COMMANDS

This appendix lists some representative code files used for the FEM simulations (in Abaqus [205]), implementing the theoretical models (in Maple [237] and Fortran 90 using LAPACK [229]) and generating movies/images (in Matlab [233]). It also gives a brief tutorial on using LastWave 2.0 [215] to implement the chirplet matching pursuit. Each sub-section heading also indicates where in the thesis results from that code was used.

B.1 Abaqus Code for FEM Simulations

Some explanatory notes have been added following the “#” symbol, which is the comments symbol in Abaqus. Furthermore, the “\” symbol is used to signify line continuation.

B.1.A Circular Actuator Model Verification (Fig. 13)

*HEADING

Simulation for circular actuator on plate model, 0.9 cm radius actuator, symmetric mode

*NODE #These are the four corners of the plate cross-section and the infinite elements

1,0,0,0

601,15e-2,0,0

602,30e-2,0,0

4001,0,1e-3,0

4601,15e-2,1e-3,0

4602,30e-2,1e-3,0

*NGEN,NSET=END #This command generates intermediate nodes at equal spacing

```

602,4602,1000
*NGEN,NSET=N1
1,601,1
*NGEN,NSET=N2
4001,4601,1
*NFILL,NSET=PLATE #This command generates intermediate rows of nodes at equal
# spacing
N1,N2,4,1000
*NSET,NSET=MID,GENERATE
1,4001,1000
*NSET,NSET=PE #Actuator node
4037
*NSET,NSET=MIDPLANE,GENERATE
1,602,1
*ELEMENT,TYPE=CAX4 #This command generates a 4-noded axisymmetric element
1,1,2,1002,1001
*ELGEN,ELSET=PLATE #This command generates the remaining elements
1,600,1,1,4,1000,1000
*ELEMENT,TYPE=CINAX4 #This command generates a 4-noded infinite axisymmetric
# element
601,1601,601,602,1602
*ELGEN,ELSET=INFINITE
601,4,1000,1000
*SOLID SECTION, MATERIAL=ALM, ELSET=PLATE #This command associates
# material properties to the element sets
*SOLID SECTION, MATERIAL=ALM, ELSET=INFINITE
*MATERIAL,NAME=ALM
*ELASTIC,TYPE=ISOTROPIC
70E9,0.33 #Elastic modulus in Pa and Poisson ratio
*DENSITY
2700 #Material density in kg/m3
*BOUNDARY
MID,XYMM
*BOUNDARY
MIDPLANE,YSYMM #For symmetric modes. The corresponding option for
# antisymmetric modes is YASYMM
*AMPLITUDE,NAME=HANNING,INPUT=waveform400khz.inp,DEFINITION=TAB\
ULAR,TIME=TOTAL # Ensure that this file is in the local directory
TIME,VALUE=RELATIVE
*STEP,INC=127 #Adjust the number of steps according to the signal file
*DYNAMIC,DIRECT,NOHAF
1.59091E-06,0.000202811 #Adjust these numbers according to the signal file
*CLOAD,AMPLITUDE=HANNING
PE,1,1
*EL PRINT,FREQUENCY=0
*PRINT,FREQUENCY=127 #Adjust the number of steps according to the signal file

```

*END STEP

B.1.B 2-D Plate with Two Dents (Chapter IV)

*HEADING

2nd simulation in Chapter IV for 2-D plate with 2 dents

*NODE

1,0,0,0

501,12.5e-2,0,0

4001,0,1e-3,0

4501,12.5e-2,1e-3,0

*NGEN,NSET=N1

1,501,1

*NGEN,NSET=N2

4001,4501,1

*NFILL,NSET=PLATE

N1,N2,4,1000

*NSET,NSET=MID,GENERATE

1,4001,1000

*NSET,NSET=PE

4021,21

*ELEMENT,TYPE=CPE4 #This command generates a 4-noded plane-strain element

1,1,2,1002,1001

*ELGEN,ELSET=PLATE

1,239,1,1,4,1000,1000

*ELEMENT,TYPE=CPE4

2240,2240,2241,3241,3240

*ELEMENT,TYPE=CPE4

3240,3240,3241,4241,4240

*ELEMENT,TYPE=CPE4

241,241,242,1242,1241

*ELGEN,ELSET=PLATE2

241,159,1,1,4,1000,1000

*ELEMENT,TYPE=CPE4

2400,2400,2401,3401,3400

*ELEMENT,TYPE=CPE4

3400,3400,3401,4401,4400

*ELEMENT,TYPE=CPE4

401,401,402,1402,1401

*ELGEN,ELSET=PLATE3

401,100,1,1,4,1000,1000

*ELSET,ELSET=PLATE4

2240,3240,PLATE2,2400,3400,PLATE3

*SOLID SECTION, MATERIAL=ALM, ELSET=PLATE

*SOLID SECTION, MATERIAL=ALM, ELSET=PLATE4

*MATERIAL,NAME=ALM

*ELASTIC,TYPE=ISOTROPIC

```

70E9,0.33
*DENSITY
2700
*BOUNDARY
MID, XSYMM
*AMPLITUDE, NAME=HANNING, INPUT=waveform275khz.inp, DEFINITION=TAB\
ULAR, TIME=TOTAL
TIME, VALUE=RELATIVE
*STEP, INC=5000
*DYNAMIC, DIRECT, NOHAF
1e-8, 5e-5
*CLOAD, AMPLITUDE=HANNING
PE, 1, 1
*EL PRINT, FREQUENCY=0
*PRINT, FREQUENCY=5000
*END STEP

```

B.1.C Composite Plate Model Verification (Fig. 73, Chapter VI)

```

*HEADING
3-D quasiisotropic composite 1/2 plate S0 simulation 200 kHz; Actuator dimensions\ a1
and a2 are 0.5 cm each
*NODE
1, 0., 0., 0.
161, 20e-2, 0., 0.
160001, 0., 20e-2, 0.
160161, 20e-2, 20e-2, 0.
*NGEN, NSET=N1
1, 161, 1
*NGEN, NSET=N2
160001, 160161, 1
*NFILL, NSET=N5
N1, N2, 160, 1000
*NSET, NSET=TOP
N5
*NCOPY, CHANGE NUMBER=1000000, OLD SET=TOP, SHIFT, MULTIPLE=1, NEW\
SET=INTER
0, 0, 0.11E-3
0,,,,,
*NCOPY, CHANGE NUMBER=1000000, OLD
SET=INTER, SHIFT, MULTIPLE=1, NEW SET=INTER1
0, 0, 0.11E-3
0,,,,,
*NCOPY, CHANGE NUMBER=1000000, OLD
SET=INTER1, SHIFT, MULTIPLE=1, NEW SET=INTER2
0, 0, 0.11E-3
0,,,,,

```

```

*NCOPY,CHANGE NUMBER=1000000,OLD
SET=INTER2,SHIFT,MULTIPLE=1,NEW SET=MIDZ
0,0,0.11E-3
0,,,,,
*NSET,NSET=EDGE1,GENERATE
76077,76085,1
*NSET,NSET=EDGE2,GENERATE
76077,84077,1000
*NSET,NSET=EDGE3,GENERATE
84077,84085,1
*NSET,NSET=EDGE4,GENERATE
76085,84085,1000
*ELEMENT,TYPE=C3D8
1,1,2,1002,1001,1000001,1000002,1001002,1001001
*ELGEN,ELSET=ZERO
1,160,1,1,160,1000,1000
*ELEMENT,TYPE=C3D8
1000001,1000001,1000002,1001002,1001001,2000001,2000002,2001002,2001001
*ELGEN,ELSET=FORTYFIVE
1000001,160,1,1,160,1000,1000
*ELEMENT,TYPE=C3D8
2000001,2000001,2000002,2001002,2001001,3000001,3000002,3001002,3001001
*ELGEN,ELSET=MFORTYFIVE
2000001,160,1,1,160,1000,1000
*ELEMENT,TYPE=C3D8
3000001,3000001,3000002,3001002,3001001,4000001,4000002,4001002,4001001
*ELGEN,ELSET=NINETY
3000001,160,1,1,160,1000,1000
*SOLID\
SECTION,ELSET=ZERO,MATERIAL=GRAPHITEEPOXY,ORIENTATION=OZERO
*SOLID\
SECTION,ELSET=FORTYFIVE,MATERIAL=GRAPHITEEPOXY,ORIENTATION=
OFORTYFIVE
*SOLID\
SECTION,ELSET=MFORTYFIVE,MATERIAL=GRAPHITEEPOXY,ORIENTATION\
=OMFORTYFIVE
*SOLID\
SECTION,ELSET=NINETY,MATERIAL=GRAPHITEEPOXY,ORIENTATION=ONI\
NETY
*ORIENTATION,NAME=OZERO
1,0,0,0,1,0
*ORIENTATION,NAME=OFORTYFIVE
1,1,0,0,1,0
*ORIENTATION,NAME=OMFORTYFIVE
1,-1,0,0,1,0
*ORIENTATION,NAME=ONINETY

```



```

0,1,0,1,0,0
*MATERIAL,NAME=GRAPHITEEPOXY
*ELASTIC,TYPE=ORTHOTROPIC
160.73E9,6.44E9,13.92E9,6.44E9,6.92E9,13.92E9,3.5E9,7.07E9
7.07E9
*DENSITY
1578
*BOUNDARY
MIDZ,ZSYMM
*AMPLITUDE,NAME=HANNING,INPUT=waveform200khz.inp,DEFINITION=TAB\
ULAR,TIME=TOTAL
TIME,VALUE=RELATIVE
*STEP,INC=150
*DYNAMIC,DIRECT,NOHAF
1.6E-07,2.4E-05
*CLOAD,AMPLITUDE=HANNING
EDGE1,2,-1
EDGE2,1,-1
EDGE3,2,1
EDGE4,1,1
*NODE PRINT,FREQUENCY=300
U1,U2,U3
*EL PRINT,FREQUENCY=0
*PRINT,FREQUENCY=300
*END STEP

```

B.2 Maple Code for Theoretical Model Implementation (Isotropic Structures)

It should be noted that some explanatory notes have been added following the “#” symbol, which is the comments symbol in Maple (as in Abaqus above). Some of these can take a while to run, so it may be necessary to leave these running overnight or longer.

B.2.A Image Data for MFC Harmonic u_3 Displacement (Fig. 11 (c))

```

> restart;
> with(plots):
> xi:=658.6148; #This is the wavenumber (m-1)
> for i from 1 by 1 to 200 do x(i):=10e-2/200*i: y(i):=10e-2/200*i: end do: #Spatial grid
> fn1:=fopen("N:/sqmfcharmonicu3ap25cmp1.txt",WRITE): #Part of the data is saved to
this file

```

```

>ax1:=0.25e-2: ay1:=0.25e-2: for j from 1 by 1 to 200 do for k from 6 by 1 to 200 do
theta1:=evalf(arctan((y(k)-ay1)/(x(j)-ax1))): theta2:=evalf(arctan((y(k)+ay1)/(x(j)-ax1))):
theta3:=arctan((y(k)-ay1)/(x(j)+ax1)): theta4:=arctan((y(k)+ay1)/(x(j)+ax1)):
t1a:=evalf(theta1-Pi/2): t1b:=evalf(theta1+Pi/2): t2a:=evalf(theta2-Pi/2):
t2b:=evalf(theta2+Pi/2): t3a:=evalf(theta3-Pi/2): t3b:=evalf(theta3+Pi/2):
t4a:=evalf(theta4-Pi/2): t4b:=evalf(theta4+Pi/2): u3(j,k):=simplify(Re(-
4*int(sin(xi*cos(theta)*ax1)*sin(xi*sin(theta)*ax1)*exp(-I*xi*x(j)*cos(theta)-
I*xi*y(k)*sin(theta))*tan(theta),theta=t2a..t2b)+int(exp(-I*xi*(x(j)-ax1)*cos(theta)-
I*xi*(y(k)-ay1)*sin(theta))*tan(theta),theta=t1a..t1b)+int(exp(-I*xi*(x(j)-
ax1)*cos(theta)-I*xi*(y(k)-ay1)*sin(theta))*tan(theta),theta=t3b..t3b)-int(exp(-
I*xi*(x(j)-ax1)*cos(theta)-
I*xi*(y(k)+ay1)*sin(theta))*tan(theta),theta=t3b..t2b)+int(exp(-
I*xi*(x(j)+ax1)*cos(theta)-I*xi*(y(k)-
ay1)*sin(theta))*tan(theta),theta=t3a..t2a))+int(exp(-I*xi*(x(j)+ax1)*cos(theta)-
I*xi*(y(k)+ay1)*sin(theta))*tan(theta),theta=t4a..t4a)+int(exp(-
I*xi*(x(j)+ax1)*cos(theta)-I*xi*(y(k)+ay1)*sin(theta))*tan(theta),theta=t3b..t4b)));
writedata[APPEND](fn1,[u3(j,k)]): end do; end do; fclose(fn1):

```

```

>fn1:=fopen("N:/ sqmfcharmonicu3ap25cmp2.txt",WRITE): #The second part of the
data is saved to this file

```

```

>ax1:=0.25e-2: ay1:=0.25e-2: for j from 6 by 1 to 200 do for k from 1 by 1 to 5 do
theta1:=evalf(arctan((y(k)-ay1)/(x(j)-ax1))): theta2:=evalf(arctan((y(k)+ay1)/(x(j)-ax1))):
theta3:=arctan((y(k)-ay1)/(x(j)+ax1)): theta4:=arctan((y(k)+ay1)/(x(j)+ax1)):
t1a:=evalf(theta1-Pi/2): t1b:=evalf(theta1+Pi/2): t2a:=evalf(theta2-Pi/2):
t2b:=evalf(theta2+Pi/2): t3a:=evalf(theta3-Pi/2): t3b:=evalf(theta3+Pi/2):
t4a:=evalf(theta4-Pi/2): t4b:=evalf(theta4+Pi/2): u3(j,k):=simplify(Re(-
4*int(sin(xi*cos(theta)*ax1)*sin(xi*sin(theta)*ax1)*exp(-I*xi*x(j)*cos(theta)-
I*xi*y(k)*sin(theta))*tan(theta),theta=t2a..t2b)+int(exp(-I*xi*(x(j)-ax1)*cos(theta)-
I*xi*(y(k)-ay1)*sin(theta))*tan(theta),theta=t1a..t1a)+int(exp(-I*xi*(x(j)-
ax1)*cos(theta)-I*xi*(y(k)-ay1)*sin(theta))*tan(theta),theta=t3b..t1b)-int(exp(-
I*xi*(x(j)-ax1)*cos(theta)-
I*xi*(y(k)+ay1)*sin(theta))*tan(theta),theta=t3b..t2b)+int(exp(-
I*xi*(x(j)+ax1)*cos(theta)-I*xi*(y(k)-
ay1)*sin(theta))*tan(theta),theta=t3a..t2a))+int(exp(-I*xi*(x(j)+ax1)*cos(theta)-
I*xi*(y(k)+ay1)*sin(theta))*tan(theta),theta=t4a..t2a)+int(exp(-
I*xi*(x(j)+ax1)*cos(theta)-I*xi*(y(k)+ay1)*sin(theta))*tan(theta),theta=t3b..t4b)));
writedata[APPEND](fn1,[u3(j,k)]): end do; end do; fclose(fn1):

```

B.2.B Circular Actuator Model Results for FEM Verification (Fig. 13 (a))

```

> restart; #This analysis is for the A0 Lamb mode

```

```

> with(plots):

```

```

> f:=tan(d*sqrt(1-zeta^2))/tan(d*sqrt(xi^2-zeta^2))+(2*zeta^2-1)^2/(4*zeta^2*sqrt(1-
zeta^2)*sqrt(xi^2-zeta^2))=0:

> E:=70e9: nu:=0.33: rho:=2700: t:=0.001: #Material properties

> d:=omega*t*sqrt((2*rho*(1+nu))/E): xi:=sqrt((1-2*nu)/(2-2*nu)):

> for j from 1 by 1 to 500 do f2(j):=subs(omega=2*Pi*2000*j,f) end do:

> for j1 from 2 by 1 to 18 do zeta2(j1):=fsolve(f2(j1),zeta,0..32) end do: for j1 from 19 by
1 to 500 do zeta2(j1):=fsolve(f2(j1),zeta,0..10.1) end do:
> for j3 from 2 by 1 to 500 do c1(j3):=sqrt(E/(2*rho*(1+nu)*zeta2(j3)^2)) end do:

> for j3 from 2 by 1 to 500 do fre(j3):=2000*j3 end do:

> l1:=[[fre(n), c1(n)] $n=2..500]: plot(l1); #plots the phase velocity dispersion curve

> mu:=E/(2*(1+nu)): lambda1:=E*nu/((1-2*nu)*(1+nu)): ct:=(mu/rho)^0.5:
cl:=((lambda1+2*mu)/rho)^0.5:

> for k1 from 1 to 5 do critfre1a(k1):=k1*cl/t end do: for k2 from 1 by 2 to 7 do
critfre2a(k2):=k2*ct/(2*t) end do: for k3 from 1 by 2 to 7 do critfre1s(k3):=k3*cl/(2*t)
end do: for k4 from 1 to 5 do critfre2s(k4):=k4*ct/t end do: #These are cut-off
frequencies for higher modes

> for n1 from 3 to 499 do c1g(n1):=c1(n1)/(1-(fre(n1)*(c1(n1+1)-c1(n1-
1)))/(c1(n1)*4000)) end do: #This gives the group velocity curve in the vector c1g

> q:=sqrt(omega1^2/ct^2-xiv^2): p:=sqrt(omega1^2/cl^2-xiv^2): Da:=(xiv^2-
q^2)^2*sin(p)*cos(q)+4*xiv^2*p*q*cos(p)*sin(q): Dad:=diff(Da,xiv):
Na:=xiv*q*(xiv^2+q^2)*sin(p)*sin(q):

> a1:=0.9e-2: rs1:=5e-2: #Actuator radius and radial location of test point

> for i from 2 by 1 to 500 do
ural(i):=simplify(I*subs(omega1=fre(i)*2*Pi,xiv=Omega1(i),Na)*BesselJ(1,Omega1(i)*
a1)*a1*HankelH2(1,Omega1(i)*rs1)/(subs(omega1=fre(i)*2*Pi,xiv=Omega1(i),Dad)*m
u)) end do:

> f2p1c2:=2*Pi*(fr+fr/n1n)*(cos(2*Pi*n1n)*exp(-I*omegav*n1n/fr)-1)/(omegav^2-
4*Pi^2*(fr+fr/n1n)^2):

> f2p2c2:=2*Pi*(fr-fr/n1n)*(cos(2*Pi*n1n)*exp(-I*omegav*n1n/fr)-1)/(omegav^2-
4*Pi^2*(fr-fr/n1n)^2):

```

```

> f2c2:=2*Pi*fr*(cos(2*Pi*n1n)*exp(-I*omegav*n1n/fr)-1)/(omegav^2-4*Pi^2*fr^2)-
0.5*f2p1c2-0.5*f2p2c2:
> f2c3:=-I*n1n/(2*fr)-0.5*f2p1c2-0.5*f2p2c2:
> for i from 2 by 1 to 125 do start1(i):=floor(i-i*2/3.5): end1(i):=ceil(i+i*2/3.5): end do:
> for i from 2 by 1 to 125 do ura1td(i):=0: for j from start1(i) by 1 to end1(i) do if (j <> i)
then
ura1td(i):=ura1td(i)+simplify(ura1(j)*subs(n1n=3.5,fr=fre(i),omegav=2*Pi*fre(j),f2c2)*2
*Pi*2e3*exp(I*2*Pi*fre(j)*time)): else
ura1td(i):=ura1td(i)+simplify(ura1(j)*subs(n1n=3.5,fr=fre(i),omegav=2*Pi*fre(j),f2c3)*2
*Pi*2e3*exp(I*2*Pi*fre(j)*time)): end if: end do: end do:
> for i from 5 by 1 to 50 do for j from 1 by 1 to 1000 do
ura1tdd1(i,j):=evalf(subs(time=j*4e-7,Re(ura1td(i)))) end do:
ura1mag(i):=simplify(max(ura1tdd1(i,n) $n=1..1000)-min(ura1tdd1(i,n) $n=1..1000))
end do: for i from 51 by 1 to 101 do for j from 1 by 1 to 750 do
ura1tdd1(i,j):=evalf(subs(time=j*9.33e-8,ura1td(i))) end do:
ura1mag(i):=simplify(max(ura1tdd1(i,n) $n=1..1000)-min(ura1tdd1(i,n) $n=1..1000))
end do:
> for i from 102 by 1 to 125 do for j from 1 by 1 to 500 do
ura1tdd1(i,j):=evalf(subs(time=j*8e-8,Re(ura1td(i)))) end do:
ura1mag(i):=simplify(max(ura1tdd1(i,n) $n=1..500)-min(ura1tdd1(i,n) $n=1..500)) end
do:
> l1:=[[fre(n), ura1mag(n)] $n=5..125]: plot(l1); #plots the radial displacement
frequency response curve corrected for finite time excitation

```

B.2.C Sensor Response Plots for Circular Actuators (Fig. 18 and Fig. 19)

```

> restart; #This analysis is for S0 Lamb mode
> with(plots):
> E:=70.28e9: nu:=0.33: rho:=2684.87: t:=1.575e-3: #Material properties and plate half-
thickness, all in SI units
> d:=omega*t*sqrt((2*rho*(1+nu))/E): xi:=sqrt((1-2*nu)/(2-2*nu)):
> for j3 from 1 by 1 to 630 do fre(j3):=1000*j3 end do:
> mu:=E/(2*(1+nu)): lambda1:=E*nu/((1-2*nu)*(1+nu)):
> ct:=(mu/rho)^0.5: cl:=((lambda1+2*mu)/rho)^0.5:

```

```

> fs:=tan(d*sqrt(1-zeta^2))/tan(d*sqrt(xi^2-zeta^2))+(4*zeta^2*sqrt(1-zeta^2)*sqrt(xi^2-
zeta^2))/(2*zeta^2-1)^2=0:

> for j from 1 by 1 to 630 do f2s(j):=subs(omega=2*Pi*1000*j,fs) end do:

> for j from 1 by 1 to 630 do zeta4(j):=fsolve(f2s(j),zeta,0.5..2.0) end do:

> for j from 1 by 1 to 630 do
Omega1(j):=2*Pi*fre(j)/(sqrt(E/(2*rho*(1+nu)*zeta4(j)^2))) end do:

> q:=sqrt(omega1^2/ct^2-xiv^2): p:=sqrt(omega1^2/cl^2-xiv^2):

> Ns:=xiv*q*(xiv^2+q^2)*cos(p*t)*cos(q*t):

> Ds:=(xiv^2-q^2)^2*cos(p*t)*sin(q*t)+4*xiv^2*p*q*sin(p*t)*cos(q*t):
Dsd:=diff(Ds,xiv):

> a1:=0.65e-2: rs1:=5e-2: cb1:=0.5e-2: #Actuator radius, radial location of sensor and
sensor length respectively

> for i from 1 by 1 to 630 do snrsp(i):=simplify(-
I*subs(omega1=fre(i)*2*Pi,xiv=Omega1(i),Ns)*BesselJ(1,Omega1(i)*a1)*Omega1(i)*a
1*int(HankelH2(0,Omega1(i)*r)/cb1,r=rs1..(rs1+cb1))/subs(omega1=fre(i)*2*Pi,xiv=Om
ega1(i),Dsd) end do:

> ln6:=[[fre(n), abs(a0snrsp1(n))] $n=1..630]: #plot(ln6):

> f2p1c2:=2*Pi*(fr+fr/n1n)*(cos(2*Pi*n1n)*exp(-I*omegav*n1n/fr)-1)/(omegav^2-
4*Pi^2*(fr+fr/n1n)^2):

> f2p2c2:=2*Pi*(fr-fr/n1n)*(cos(2*Pi*n1n)*exp(-I*omegav*n1n/fr)-1)/(omegav^2-
4*Pi^2*(fr-fr/n1n)^2):

> f2c2:=2*Pi*fr*(cos(2*Pi*n1n)*exp(-I*omegav*n1n/fr)-1)/(omegav^2-4*Pi^2*fr^2)-
0.5*f2p1c2-0.5*f2p2c2:

> f2c3:=-I*n1n/(2*fr)-0.5*f2p1c2-0.5*f2p2c2:

> for i from 100 by 2 to 400 do start1(i):=floor(i-i*2/3.5): end1(i):=ceil(i+i*2/3.5): end
do:

> for i from 100 by 2 to 400 do snrsptd(i):=0: for j from start1(i) by 1 to end1(i) do if (j
<> i) then
snrsptd(i):=snrsptd(i)+simplify(snrsp(j)*subs(n1n=3.5,fr=fre(i),omegav=2*Pi*fre(j),f2c2)
*2*Pi*2e3*exp(I*2*Pi*fre(j)*time)): else
snrsptd(i):=snrsptd(i)+simplify(snrsp(j)*subs(n1n=3.5,fr=fre(i),omegav=2*Pi*fre(j),f2c3)
*2*Pi*2e3*exp(I*2*Pi*fre(j)*time)): end if: end do: end do:

```

```

> for i from 100 by 2 to 200 do for j from 1 by 1 to 500 do
snrsptdd1(i,j):=evalf(subs(time=j*1e-7,Re(snrsptd(i)))) end do:
snrspmag(i):=simplify(max(snrsptdd1(i,n) $n=1..500)-min(snrsptdd1(i,n) $n=1..500))
end do: for i from 202 by 2 to 300 do for j from 1 by 1 to 500 do
snrsptdd1(i,j):=evalf(subs(time=j*6e-8, snrsptd(i))) end do:
snrspmag(i):=simplify(max(snrsptdd1(i,n) $n=1..500)-min(snrsptdd1(i,n) $n=1..500))
end do:

```

```

> for i from 302 by 1 to 400 do for j from 1 by 1 to 250 do
snrsptdd1(i,j):=evalf(subs(time=j*1e-7,Re(snrsptd(i)))) end do:
snrspmag(i):=simplify(max(snrsptdd1(i,n) $n=1..250)-min(snrsptdd1(i,n) $n=1..250))
end do:

```

B.2.D Theoretical Images for the Laser Vibrometer Experiment (Fig. 24 (a))

```
> restart;
```

```
> with(plots):
```

```
> E:=70e9: nu:=0.33: rho:=2700: t:=0.5e-3:
```

```
> f1:=fopen("N:/Maple/1mmAlplatecpa0.txt",READ): a:=readdata(f1,float): fclose(f1);
#This text file should have the A0 mode dispersion curve for a 1-mm thick Al plate in a
single column
```

```
> mu:=E/(2*(1+nu)): lambda1:=E*nu/((1-2*nu)*(1+nu)): ct:=(mu/rho)^0.5:
cl:=((lambda1+2*mu)/rho)^0.5:
```

```
> for i from 12 by 1 to 48 do fre(i):=1000*i end do: for i from 12 by 1 to 48 do
xi1(i):=2*Pi*fre(i)/a[i] end do:
```

```
> q:=sqrt(omega1^2/ct^2-xiv^2): p:=sqrt(omega1^2/cl^2-xiv^2):
```

```
> Ta:=xiv^2*(q^2-xiv^2)*sin(p*t)*cos(q*t)-2*p*q*xiv^2*sin(q*t)*cos(p*t): Da:=(xiv^2-
q^2)^2*sin(p*t)*cos(q*t)+4*xiv^2*p*q*cos(p*t)*sin(q*t): Dad:=diff(Da,xiv):
```

```
> for j from 1 by 1 to 41 do x(j):=(j-1)*0.5e-2: end do: for j from 1 by 1 to 66 do y(j):=(j-
1)*0.3e-2+0.1e-2: end do: #These coordinates match those for which experimental
readings were taken with the laser vibrometer
```

```
> ax1:=1.45e-2/2: ay1:=1.4e-2: #These values are the half-dimensions of the MFC's
active area along the x-axis and y-axis (the latter being along the MFC fiber direction)
```

```

> fn1:=fopen("N:/mfcmovietheoRexj3to41yk1to5.txt",WRITE):
fn2:=fopen("N:/mfcmovietheoImxj3to41yk1to5.txt",WRITE): for j from 3 by 1 to 41 do
for k from 1 by 1 to 5 do for i from 12 by 1 to 48 do theta1:=evalf(arctan((y(k)-ay1)/(x(j)-
ax1))): theta2:=evalf(arctan((y(k)+ay1)/(x(j)-ax1))): theta3:=arctan((y(k)-
ay1)/(x(j)+ax1)): theta4:=arctan((y(k)+ay1)/(x(j)+ax1)): t1a:=evalf(theta1-Pi/2):
t1b:=evalf(theta1+Pi/2): t2a:=evalf(theta2-Pi/2): t2b:=evalf(theta2+Pi/2):
t3a:=evalf(theta3-Pi/2): t3b:=evalf(theta3+Pi/2): t4a:=evalf(theta4-Pi/2):
t4b:=evalf(theta4+Pi/2):
v3(i,j,k):=simplify(8*Pi*fre(i)*subs(omega1=fre(i)*2*Pi,xiv=xil(i),Ta)/(subs(omega1=fr
e(i)*2*Pi,xiv=xil(i),Dad)*xil(i))*(int(sin(xil(i)*cos(theta)*ax1)*exp(-
I*xil(i)*x(j)*cos(theta)-
I*xil(i)*(y(k)+ay1)*sin(theta))*tan(theta),theta=t2a..t4b)+int(exp(-I*xil(i)*(x(j)-
ax1)*cos(theta)-I*xil(i)*(y(k)+ay1)*sin(theta))*tan(theta),theta=t4b..t2b)/(2*I)-int(exp(-
I*xil(i)*(x(j)+ax1)*cos(theta)-
I*xil(i)*(y(k)+ay1)*sin(theta))*tan(theta),theta=t4a..t2a)/(2*I)+int(sin(xil(i)*cos(theta)*
ax1)*exp(-I*xil(i)*x(j)*cos(theta)-I*xil(i)*(y(k)-
ay1)*sin(theta))*tan(theta),theta=t3a..t1b)+int(exp(-I*xil(i)*(x(j)-ax1)*cos(theta)-
I*xil(i)*(y(k)-ay1)*sin(theta))*tan(theta),theta=t1a..t3a)/(2*I)-int(exp(-
I*xil(i)*(x(j)+ax1)*cos(theta)-I*xil(i)*(y(k)-
ay1)*sin(theta))*tan(theta),theta=t1b..t3b)/(2*I)));
writedata[APPEND](fn1,[Re(v3(i,j,k))]): writedata[APPEND](fn2,[Im(v3(i,j,k))]): end
do; end do; end do; fclose(fn1): fclose(fn2):

```

```

>fn1:=fopen("N:/mfcmovietheoRexj1to2yk6to66.txt",WRITE):
fn2:=fopen("N:/mfcmovietheoImxj1to2yk6to66.txt",WRITE): ax1:=1.45e-2/2:
ay1:=1.4e-2: for j from 1 by 1 to 2 do for k from 6 by 1 to 66 do for i from 12 by 1 to 48
do theta1:=evalf(Pi+arctan((y(k)-ay1)/(x(j)-ax1))):
theta2:=evalf(Pi+arctan((y(k)+ay1)/(x(j)-ax1))): theta3:=arctan((y(k)-ay1)/(x(j)+ax1)):
theta4:=arctan((y(k)+ay1)/(x(j)+ax1)): t1a:=evalf(theta1-Pi/2): t1b:=evalf(theta1+Pi/2):
t2a:=evalf(theta2-Pi/2): t2b:=evalf(theta2+Pi/2): t3a:=evalf(theta3-Pi/2):
t3b:=evalf(theta3+Pi/2): t4a:=evalf(theta4-Pi/2): t4b:=evalf(theta4+Pi/2):
v3(i,j,k):=simplify(-
2*Pi*fre(i)*subs(omega1=fre(i)*2*Pi,xiv=xil(i),Ta)/(subs(omega1=fre(i)*2*Pi,xiv=xil(i
),Dad)*xil(i))*(-4*int(sin(xil(i)*cos(theta)*ax1)*sin(xil(i)*sin(theta)*ay1)*exp(-
I*xil(i)*x(j)*cos(theta)-I*xil(i)*y(k)*sin(theta))*tan(theta),theta=t2a..t3b)+int(exp(-
I*xil(i)*(x(j)-ax1)*cos(theta)-I*xil(i)*(y(k)-
ay1)*sin(theta))*tan(theta),theta=t1a..t2a)+int(exp(-I*xil(i)*(x(j)-ax1)*cos(theta)-
I*xil(i)*(y(k)-ay1)*sin(theta))*tan(theta),theta=t3b..t1b)-(int(exp(-I*xil(i)*(x(j)-
ax1)*cos(theta)-I*xil(i)*(y(k)+ay1)*sin(theta))*tan(theta),theta=t3b..t2b)+int(exp(-
I*xil(i)*(x(j)+ax1)*cos(theta)-I*xil(i)*(y(k)-
ay1)*sin(theta))*tan(theta),theta=t3a..t2a))+int(exp(-I*xil(i)*(x(j)+ax1)*cos(theta)-

```

```

I*x1(i)*(y(k)+ay1)*sin(theta))*tan(theta),theta=t4a..t2a)+int(exp(-
I*x1(i)*(x(j)+ax1)*cos(theta)-
I*x1(i)*(y(k)+ay1)*sin(theta))*tan(theta),theta=t3b..t4b)))
writedata[APPEND](fn1,[Re(v3(i,j,k))]); writedata[APPEND](fn2,[Im(v3(i,j,k))]); end
do; end do; end do; fclose(fn1); fclose(fn2):

```

>#The following loop is particularly computationally intensive and it is advised that the spatial grid be split and run in parallel on 4-5 machines to save time

```

> fn1:=fopen("N:/mfcmovietheoRexj3to41yk6to66.txt",WRITE):
fn2:=fopen("N:/mfcmovietheoImxj3to41yk6to66.txt",WRITE): for j from 3 by 1 to 41
do for k from 6 by 1 to 66 do for i from 12 by 1 to 48 do theta1:=evalf(arctan((y(k)-
ay1)/(x(j)-ax1))); theta2:=evalf(arctan((y(k)+ay1)/(x(j)-ax1))); theta3:=arctan((y(k)-
ay1)/(x(j)+ax1)); theta4:=arctan((y(k)+ay1)/(x(j)+ax1)): t1a:=evalf(theta1-Pi/2):
t1b:=evalf(theta1+Pi/2): t2a:=evalf(theta2-Pi/2): t2b:=evalf(theta2+Pi/2):
t3a:=evalf(theta3-Pi/2): t3b:=evalf(theta3+Pi/2): t4a:=evalf(theta4-Pi/2):
t4b:=evalf(theta4+Pi/2): v3(i,j,k):=simplify(-
2*Pi*fre(i)*subs(omega1=fre(i)*2*Pi,xiv=xi1(i),Ta)/(subs(omega1=fre(i)*2*Pi,xiv=xi1(i)
),Dad)*xi1(i))*(-4*int(sin(xi1(i)*cos(theta)*ax1)*sin(xi1(i)*sin(theta)*ay1)*exp(-
I*x1(i)*x(j)*cos(theta)-I*x1(i)*y(k)*sin(theta))*tan(theta),theta=t2a..t3b)+int(exp(-
I*x1(i)*(x(j)-ax1)*cos(theta)-I*x1(i)*(y(k)-
ay1)*sin(theta))*tan(theta),theta=t1a..t2a)+int(exp(-I*x1(i)*(x(j)-ax1)*cos(theta)-
I*x1(i)*(y(k)-ay1)*sin(theta))*tan(theta),theta=t3b..t1b)-(int(exp(-I*x1(i)*(x(j)-
ax1)*cos(theta)-I*x1(i)*(y(k)+ay1)*sin(theta))*tan(theta),theta=t3b..t2b)+int(exp(-
I*x1(i)*(x(j)+ax1)*cos(theta)-I*x1(i)*(y(k)-
ay1)*sin(theta))*tan(theta),theta=t3a..t2a))+int(exp(-I*x1(i)*(x(j)+ax1)*cos(theta)-
I*x1(i)*(y(k)+ay1)*sin(theta))*tan(theta),theta=t4a..t2a)+int(exp(-
I*x1(i)*(x(j)+ax1)*cos(theta)-
I*x1(i)*(y(k)+ay1)*sin(theta))*tan(theta),theta=t3b..t4b)));
writedata[APPEND](fn1,[Re(v3(i,j,k))]); writedata[APPEND](fn2,[Im(v3(i,j,k))]); end
do; end do; end do; fclose(fn1); fclose(fn2):

```

```

> f2p1c2:=2*Pi*(fr+fr/n1n)*(cos(2*Pi*n1n)*exp(-I*omegav*n1n/fr)-1)/(omegav^2-
4*Pi^2*(fr+fr/n1n)^2): f2p2c2:=2*Pi*(fr-fr/n1n)*(cos(2*Pi*n1n)*exp(-
I*omegav*n1n/fr)-1)/(omegav^2-4*Pi^2*(fr-fr/n1n)^2):
f2c2:=2*Pi*fr*(cos(2*Pi*n1n)*exp(-I*omegav*n1n/fr)-1)/(omegav^2-4*Pi^2*fr^2)-
0.5*f2p1c2-0.5*f2p2c2:

```

```

> f2c3:=-I*n1n/(2*fr)-0.5*f2p1c2-0.5*f2p2c2:

```

```

> for i from 3 by 1 to 41 do for j from 1 by 1 to 5 do v3td(i,j):=0: for k from 12 by 1 to 48
do if (k <> 30) then

```



```

v3td(i,j):=v3td(i,j)+simplify(v3(k,i,j)*subs(n1n=3.499,fr=30e3,omegav=2*Pi*fre(k),f2c2
)*2*Pi*2e3*exp(I*2*Pi*fre(k)*time)): else
v3td(i,j):=v3td(i,j)+simplify(v3(k,i,j)*subs(n1n=3.499,fr=30e3,omegav=2*Pi*fre(k),f2c3
)*2*Pi*2e3*exp(I*2*Pi*fre(k)*time)): end if: end do: end do: end do:

> for i from 1 by 1 to 41 do for j from 6 by 1 to 66 do v3td(i,j):=0: for k from 12 by 1 to
48 do if (k <> 30) then
v3td(i,j):=v3td(i,j)+simplify(v3(k,i,j)*subs(n1n=3.499,fr=30e3,omegav=2*Pi*fre(k),f2c2
)*2*Pi*2e3*exp(I*2*Pi*fre(k)*time)): else
v3td(i,j):=v3td(i,j)+simplify(v3(k,i,j)*subs(n1n=3.499,fr=30e3,omegav=2*Pi*fre(k),f2c3
)*2*Pi*2e3*exp(I*2*Pi*fre(k)*time)): end if: end do: end do: end do:

> f1:=fopen("N:/mfcmoviei3to41j1to5.txt",WRITE):

> for i from 3 by 1 to 41 do for j from 1 by 1 to 5 do for k from 1 by 1 to 40 do
v3tdv(i,j,k):=evalf(subs(time=k*4e-4/40,Re(v3td(i,j)))):
writedata[APPEND](f1,[v3tdv(i,j,k)]) end do: end do: end do: fclose(f1):

> f2:=fopen("N:/mfcmoviei1to41j6to66.txt",WRITE):

> for i from 1 by 1 to 41 do for j from 6 by 1 to 66 do for k from 1 by 1 to 40 do
v3tdv(i,j,k):=evalf(subs(time=k*4e-4/40,Re(v3td(i,j)))):
writedata[APPEND](f2,[v3tdv(i,j,k)]) end do: end do: end do: fclose(f2):

```

B.3 Fortran 90 Code for Implementing GW Excitation Models in Composites

The code below is used to evaluate the out-of-plane displacement response kernel for a quasi-isotropic laminate $[0/45/-45/90]_s$ in the S_0 mode over a range of frequencies. It uses the phase velocities at 3° intervals as input. Those can be computed by tweaking this code to only evaluate the global matrix determinant over a grid of (K, Γ) and looking for zero-crossings. Of course, the code for unidirectional composites can be derived from this too.

```

program main
implicit none
! Variable type definitions
complex*16 :: F1,F2,xi
complex*16,dimension(2) ::
Qv,Qv1v,C1mv,C2mv,C3mv,C4mv,C5mv,C6mv,C1,C2,C3,C4,C5,C6,Qmvtv
integer ::
i,j,k,l,n1,C1minfo,C2minfo,C3minfo,C4minfo,C5minfo,C6minfo,Qv1info,Qmvtinfo,ierr
or,nlayer

```

```

real*8 :: ang,pi,omega,r
real*8,dimension(181) :: angle
complex*16,dimension(2340) :: cp
complex*16,dimension(24,24) ::
Qmv,Qmvd,Qmv1,Qmv2,Qv1,C1m,C2m,C3m,C4m,C5m,C6m,Qdiffv,Qm,Qmvt
integer,dimension(24) ::
C1mpvt,C2mpvt,C3mpvt,C4mpvt,C5mpvt,C6mpvt,Qv1pvt,Qmvtpvt
complex*16,dimension(6,1) :: Cst
complex*16,dimension(3,6) :: Q1pluoh1
complex*16,dimension(3,1) :: u
complex*16,dimension(91) :: u1,u2,u3

```

! The real and imaginary harmonic out-of-plane displacement components are written to these files

```

open
(unit=1,file='multiQmkernS020to800khz045m4590p11mmlayertssymmre.txt',status='new',action='write',iostat=ierror)
open
(unit=2,file='multiQmkernS020to800khz045m4590p11mmlayertssymmim.txt',status='new',action='write',iostat=ierror)

```

nlayer=4 !Half the total # of layers in the laminate - for a unidirectional composite,
nlayer=1

! The ray surfaces (plots of phase velocity v/s angle) are stored in this file
! for frequencies from 20 kHz to 800 kHz in steps of 20 kHz

```

open
(unit=1,file='S0multi045m4590p11mmlayertssymmroot20to800khzallangs.txt',status='old',action='read',iostat=ierror)
read(1,*),(cp(i),i=1,2340)
close(1)
pi=3.14159

```

```

do k=1,2340
ang=pi*(mod(k-1,60))*3/180
omega=(((k-1-mod(k-1,60))/60+2)*20e3)*2*pi
F1=(0.d0,1.d0)*cos(ang)
F2=(0.d0,1.d0)*sin(ang)
xi=omega/cp(k)
call layerprops(Q1pluoh1,Qmv,Qmvd,xi,ang,omega)

```

!This sequence of lines computes the derivative of the global matrix determinant

```

do n1=1,24
Qv1=reshape((/ (0.d0,i=1,576) /),(/ 24,24 /))
Qv1=Qmv
Qv1(n1,:)=Qmvd(n1,:)

```

```

call zgetrf(24,24,Qv1,24,Qv1pvt,Qv1info)
Qv1v(1) = ( 1.0D+00, 0.0D+00)
Qv1v(2) = ( 0.0D+00, 0.0D+00)
do i=1,24
  if (Qv1pvt(i)/=i) then
    Qv1v(1)=-Qv1v(1)
  end if
  Qv1v(1)=Qv1v(1)*Qv1(i,i)
  do while ( abs(real(Qv1v(1)))+abs(aimag(Qv1v(1))) < 1.0D+00 )
    Qv1v(1) = Qv1v(1)*(10.0D+00,0.0D+00)
    Qv1v(2) = Qv1v(2)-(1.0D+00,0.0D+00)
  end do
  do while ( 10.0D+00 <= abs(real(Qv1v(1)))+abs(aimag(Qv1v(1))) )
    Qv1v(1) = Qv1v(1)/(10.0D+00,0.0D+00)
    Qv1v(2) = Qv1v(2)+(1.0D+00,0.0D+00)
  end do
end do
if (n1==1) then
  Qv=Qv1v
else
  if (min(real(Qv1v(2)),real(Qv(2)))==real(Qv(2))) then
    do while (Qv1v(2)/=Qv(2))
      Qv1v(1) = Qv1v(1)*(10.0D+00,0.0D+00)
      Qv1v(2) = Qv1v(2)-(1.0D+00,0.0D+00)
    end do
  else
    do while (Qv1v(2)/=Qv(2))
      Qv(1) = Qv(1)*(10.0D+00,0.0D+00)
      Qv(2) = Qv(2)-(1.0D+00,0.0D+00)
    end do
  end if
  Qv(1)=Qv(1)+Qv1v(1)
  do while ( abs(real(Qv(1)))+abs(aimag(Qv(1))) < 1.0D+00 )
    Qv(1) = Qv(1)*(10.0D+00,0.0D+00)
    Qv(2) = Qv(2)-(1.0D+00,0.0D+00)
  end do
  do while ( 10.0D+00 <= abs(real(Qv(1)))+abs(aimag(Qv(1))) )
    Qv(1) = Qv(1)/(10.0D+00,0.0D+00)
    Qv(2) = Qv(2)+(1.0D+00,0.0D+00)
  end do
end if
end do

```

! This sequence of lines computes the constants C1 to C6
C1m=Qmv
C1m(1,1)=F1

```

C1m(2,1)=F2
C1m(3:24,1)=(/ (0.d0,i=1,22) /)
call zgetrf(24,24,C1m,24,C1mpvt,C1minfo)
C1mv(1) = ( 1.0D+00, 0.0D+00)
C1mv(2) = ( 0.0D+00, 0.0D+00)
do i=1,24
  if (C1mpvt(i)/=i) then
    C1mv(1)=-C1mv(1)
  end if
  C1mv(1)=C1mv(1)*C1m(i,i)
  do while ( abs(real(C1mv(1)))+abs(aimag(C1mv(1))) < 1.0D+00 )
    C1mv(1) = C1mv(1)*(10.0D+00,0.0D+00)
    C1mv(2) = C1mv(2)-(1.0D+00,0.0D+00)
  end do
  do while ( 10.0D+00 <= abs(real(C1mv(1)))+abs(aimag(C1mv(1))) )
    C1mv(1) = C1mv(1)/(10.0D+00,0.0D+00)
    C1mv(2) = C1mv(2)+(1.0D+00,0.0D+00)
  end do
end do

```

```

C2m=Qmv
C2m(1,2)=F1
C2m(2,2)=F2
C2m(3:24,2)=(/ (0.d0,i=1,22) /)
call zgetrf(24,24,C2m,24,C2mpvt,C2minfo)
C2mv(1) = ( 1.0D+00, 0.0D+00)
C2mv(2) = ( 0.0D+00, 0.0D+00)
do i=1,24
  if (C2mpvt(i)/=i) then
    C2mv(1)=-C2mv(1)
  end if
  C2mv(1)=C2mv(1)*C2m(i,i)
  do while ( abs(real(C2mv(1)))+abs(aimag(C2mv(1))) < 1.0D+00 )
    C2mv(1) = C2mv(1)*(10.0D+00,0.0D+00)
    C2mv(2) = C2mv(2)-(1.0D+00,0.0D+00)
  end do
  do while ( 10.0D+00 <= abs(real(C2mv(1)))+abs(aimag(C2mv(1))) )
    C2mv(1) = C2mv(1)/(10.0D+00,0.0D+00)
    C2mv(2) = C2mv(2)+(1.0D+00,0.0D+00)
  end do
end do

```

```

C3m=Qmv
C3m(1,3)=F1
C3m(2,3)=F2
C3m(3:24,3)=(/ (0.d0,i=1,22) /)

```

```

call zgetrf(24,24,C3m,24,C3mpvt,C3minfo)
C3mv(1) = ( 1.0D+00, 0.0D+00)
C3mv(2) = ( 0.0D+00, 0.0D+00)
do i=1,24
  if (C3mpvt(i)/=i) then
    C3mv(1)=-C3mv(1)
  end if
  C3mv(1)=C3mv(1)*C3m(i,i)
  do while ( abs(real(C3mv(1)))+abs(aimag(C3mv(1))) < 1.0D+00 )
    C3mv(1) = C3mv(1)*(10.0D+00,0.0D+00)
    C3mv(2) = C3mv(2)-(1.0D+00,0.0D+00)
  end do
  do while ( 10.0D+00 <= abs(real(C3mv(1)))+abs(aimag(C3mv(1))) )
    C3mv(1) = C3mv(1)/(10.0D+00,0.0D+00)
    C3mv(2) = C3mv(2)+(1.0D+00,0.0D+00)
  end do
end do

```

```

C4m=Qmv
C4m(1,4)=F1
C4m(2,4)=F2
C4m(3:24,4)=(/ (0.d0,i=1,22) /)
call zgetrf(24,24,C4m,24,C4mpvt,C4minfo)
C4mv(1) = ( 1.0D+00, 0.0D+00)
C4mv(2) = ( 0.0D+00, 0.0D+00)
do i=1,24
  if (C4mpvt(i)/=i) then
    C4mv(1)=-C4mv(1)
  end if
  C4mv(1)=C4mv(1)*C4m(i,i)
  do while ( abs(real(C4mv(1)))+abs(aimag(C4mv(1))) < 1.0D+00 )
    C4mv(1) = C4mv(1)*(10.0D+00,0.0D+00)
    C4mv(2) = C4mv(2)-(1.0D+00,0.0D+00)
  end do
  do while ( 10.0D+00 <= abs(real(C4mv(1)))+abs(aimag(C4mv(1))) )
    C4mv(1) = C4mv(1)/(10.0D+00,0.0D+00)
    C4mv(2) = C4mv(2)+(1.0D+00,0.0D+00)
  end do
end do

```

```

C5m=Qmv
C5m(1,5)=F1
C5m(2,5)=F2
C5m(3:24,5)=(/ (0.d0,i=1,22) /)
call zgetrf(24,24,C5m,24,C5mpvt,C5minfo)
C5mv(1) = ( 1.0D+00, 0.0D+00)

```

```

C5mv(2) = ( 0.0D+00, 0.0D+00)
do i=1,24
  if (C5mpvt(i)/=i) then
    C5mv(1)=-C5mv(1)
  end if
  C5mv(1)=C5mv(1)*C5m(i,i)
  do while ( abs(real(C5mv(1)))+abs(aimag(C5mv(1))) < 1.0D+00 )
    C5mv(1) = C5mv(1)*(10.0D+00,0.0D+00)
    C5mv(2) = C5mv(2)-(1.0D+00,0.0D+00)
  end do
  do while ( 10.0D+00 <= abs(real(C5mv(1)))+abs(aimag(C5mv(1))) )
    C5mv(1) = C5mv(1)/(10.0D+00,0.0D+00)
    C5mv(2) = C5mv(2)+(1.0D+00,0.0D+00)
  end do
end do

C6m=Qmv
C6m(1,6)=F1
C6m(2,6)=F2
C6m(3:24,6)=(/ (0.d0,i=1,22) /)
call zgetrf(24,24,C6m,24,C6mpvt,C6minfo)
C6mv(1) = ( 1.0D+00, 0.0D+00)
C6mv(2) = ( 0.0D+00, 0.0D+00)
do i=1,24
  if (C6mpvt(i)/=i) then
    C6mv(1)=-C6mv(1)
  end if
  C6mv(1)=C6mv(1)*C6m(i,i)
  do while ( abs(real(C6mv(1)))+abs(aimag(C6mv(1))) < 1.0D+00 )
    C6mv(1) = C6mv(1)*(10.0D+00,0.0D+00)
    C6mv(2) = C6mv(2)-(1.0D+00,0.0D+00)
  end do
  do while ( 10.0D+00 <= abs(real(C6mv(1)))+abs(aimag(C6mv(1))) )
    C6mv(1) = C6mv(1)/(10.0D+00,0.0D+00)
    C6mv(2) = C6mv(2)+(1.0D+00,0.0D+00)
  end do
end do
C1(1)=xi*C1mv(1)/Qv(1)
C1(2)=C1mv(2)-Qv(2)
C2(1)=xi*C2mv(1)/Qv(1)
C2(2)=C2mv(2)-Qv(2)
C3(1)=xi*C3mv(1)/Qv(1)
C3(2)=C3mv(2)-Qv(2)
C4(1)=xi*C4mv(1)/Qv(1)
C4(2)=C4mv(2)-Qv(2)
C5(1)=xi*C5mv(1)/Qv(1)

```

```

C5(2)=C5mv(2)-Qv(2)
C6(1)=xi*C6mv(1)/Qv(1)
C6(2)=C6mv(2)-Qv(2)

```

```

Cst(1,1)=C1(1)*10**C1(2)
Cst(2,1)=C2(1)*10**C2(2)
Cst(3,1)=C3(1)*10**C3(2)
Cst(4,1)=C4(1)*10**C4(2)
Cst(5,1)=C5(1)*10**C5(2)
Cst(6,1)=C6(1)*10**C6(2)

```

```

u=matmul(Q1pluh1,Cst)

```

```

write(1,*,real(u(3,1)))
write(2,*,aimag(u(3,1)))
end do

```

```

close(1)
close(2)
end program main

```

```

! This subroutine evaluates the global matrix, its determinant and the displacement
! response matrix
! Inputs: wavenumber, angular excitation frequency, propagation angle
subroutine layerprops(Q1pluh,Qm,Qmd,xi,ang,omega)
implicit none
real*8,intent(in) :: ang,omega
complex*16,intent(in) :: xi
real*8 :: theta1,theta2,theta3,theta4,rho,h1,h2,h3,h4,pi
complex*16 ::
C11,C12,C22,C23,C55,C44,A1,A2,A3,A4,A5,alpha,beta,gamma1,q11,q12
complex*16 :: q21,q22,zeta1,zeta2,xi1,xi2,delta1,delta2,zeta3,b1,b2,b1d,b2d,xi1d,xi2d
complex*16,dimension(3,3) ::
L1,L2,L3,L4,Q111,Q121,Q211,Q221,Q112,Q122,Q212,Q222,Q113
complex*16,dimension(3,3) ::
Q123,Q213,Q223,Q114,Q124,Q214,Q224,E1,E2,E3,E4,Q111d,Q121d
complex*16,dimension(3,3) ::
Q211d,Q221d,Q112d,Q122d,Q212d,Q222d,Q113d,Q123d,Q213d,Q223d
complex*16,dimension(3,3) :: Q114d,Q124d,Q214d,Q224d,E1d,E2d,E3d,E4d
complex*16,dimension(6,6) ::
Q1min,Q2min,Q3min,Q4min,Q2plu,Q3plu,Q4plu,Q1mind,Q2mind
complex*16,dimension(6,6) :: Q3mind,Q4mind,Q2plud,Q3plud,Q4plud
complex*16,dimension(3,6) :: Q1pluh,Q1pluhd
complex*16,dimension(3,6),intent(out) :: Q1pluh
complex*16,dimension(24,24),intent(out) :: Qm,Qmd
pi=3.14159

```

```

! Layer angles
theta1=0.d0
theta2=pi/4
theta3=-pi/4
theta4=pi/2
L1=reshape((/ cos(theta1),sin(theta1),0.d0,-sin(theta1),cos(theta1),0.d0,0.d0,0.d0,1.d0
/),(/ 3,3 /))
L2=reshape((/ cos(theta2),sin(theta2),0.d0,-sin(theta2),cos(theta2),0.d0,0.d0,0.d0,1.d0
/),(/ 3,3 /))
L3=reshape((/ cos(theta3),sin(theta3),0.d0,-sin(theta3),cos(theta3),0.d0,0.d0,0.d0,1.d0
/),(/ 3,3 /))
L4=reshape((/ cos(theta4),sin(theta4),0.d0,-sin(theta4),cos(theta4),0.d0,0.d0,0.d0,1.d0
/),(/ 3,3 /))
h1=0.11e-3
h2=h1
h3=h1
h4=h1
!Material properties
C11=160.73e9
C12=6.44e9
C22=13.92e9
C23=6.92e9
C55=7.07e9
rho=1.578e3

A1=C22/rho
A2=C11/rho
A3=(C12+C55)/rho
A4=(C22-C23)/(2*rho)
A5=C55/rho

!For layer 1
xi1=xi*cos(ang)
xi2=xi*sin(ang)
alpha=A1*A5
beta=(A1*A2+A5**2-A3**2)*xi1**2-omega**2*(A1+A5)
gamma1=(A2*xi1**2-omega**2)*(A5*xi1**2-omega**2)
b1=-((beta*0.5/alpha)-((beta*0.5/alpha)**2-gamma1/alpha)**0.5)
b2=-((beta*0.5/alpha)+((beta*0.5/alpha)**2-gamma1/alpha)**0.5)
b1d=-1.0*(A1*A2+A5**2-A3**2)*xi*cos(ang)**2/A1/A5-.5/(.25*((A1*A2+A5**2-
A3**2)*xi**2*cos(ang)**2-omega**2*(A1+A5))**2/A1**2/A5**2-
(A2*xi**2*cos(ang)**2-omega**2)*(A5*xi**2*cos(ang)**2-
omega**2)/A1/A5)**.5*(1.00*((A1*A2+A5**2-A3**2)*xi**2*cos(ang)**2-
omega**2*(A1+A5))/A1**2/A5**2*(A1*A2+A5**2-A3**2)*xi*cos(ang)**2-

```



```

2*A2*xi*cos(ang)**2*(A5*xi**2*cos(ang)**2-omega**2)/A1/A5-
2*(A2*xi**2*cos(ang)**2-omega**2)*xi*cos(ang)**2/A1
b2d=-1.0*(A1*A2+A5**2-A3**2)*xi*cos(ang)**2/A1/A5+.5/(.25*((A1*A2+A5**2-
A3**2)*xi**2*cos(ang)**2-omega**2*(A1+A5))**2/A1**2/A5**2-
(A2*xi**2*cos(ang)**2-omega**2)*(A5*xi**2*cos(ang)**2-
omega**2)/A1/A5)**.5*(1.00*((A1*A2+A5**2-A3**2)*xi**2*cos(ang)**2-
omega**2*(A1+A5))/A1**2/A5**2*(A1*A2+A5**2-A3**2)*xi*cos(ang)**2-
2*A2*xi*cos(ang)**2*(A5*xi**2*cos(ang)**2-omega**2)/A1/A5-
2*(A2*xi**2*cos(ang)**2-omega**2)*xi*cos(ang)**2/A1)
zeta1=(-xi2**2+b1)**0.5
if (aimag(zeta1)/=abs(aimag(zeta1))) then
zeta1=-zeta1
end if
zeta2=(-xi2**2+b2)**0.5
if (aimag(zeta2)/=abs(aimag(zeta2))) then
zeta2=-zeta2
end if
zeta3=(-xi2**2+(omega**2-A5*xi1**2)/A4)**0.5
if (aimag(zeta3)/=abs(aimag(zeta3))) then
zeta3=-zeta3
end if
q11=A3*b1
q21=(omega**2-A2*xi1**2-A5*b1)
q12=A3*b2
q22=(omega**2-A2*xi1**2-A5*b2)
delta1=rho*((A5-A3)*xi1**2*q11-(A1-2*A4)*xi2**2*q21-A1*zeta1**2*q21)
delta2=rho*((A5-A3)*xi1**2*q12-(A1-2*A4)*xi2**2*q22-A1*zeta2**2*q22)
Q111=reshape((/
(0.d0,1.d0)*xi1*q11,(0.d0,1.d0)*xi2*q21,(0.d0,1.d0)*zeta1*q21,(0.d0,1.d0)*xi1*q12,(0.
d0,1.d0)*xi2*q22,(0.d0,1.d0)*zeta2*q22,(0.d0,0.d0),(0.d0,1.d0)*zeta3,(0.d0,-1.d0)*xi2
/),(/ 3,3 /))
Q121=reshape((/ (0.d0,1.d0)*xi1*q11,(0.d0,1.d0)*xi2*q21,(0.d0,-
1.d0)*zeta1*q21,(0.d0,1.d0)*xi1*q12,(0.d0,1.d0)*xi2*q22,(0.d0,-
1.d0)*zeta2*q22,(0.d0,0.d0),(0.d0,-1.d0)*zeta3,(0.d0,-1.d0)*xi2 /),(/ 3,3 /))
Q211=reshape((/ -rho*A5*xi1*zeta1*(q11+q21),-2*rho*A4*xi2*zeta1*q21,delta1,-
rho*A5*xi1*zeta2*(q12+q22),-
2*rho*A4*xi2*zeta2*q22,delta2,rho*A5*xi1*xi2,rho*A4*(xi2**2-
zeta3**2),2*rho*A4*xi2*zeta3 /),(/ 3,3 /))
Q221=reshape((/
rho*A5*xi1*zeta1*(q11+q21),2*rho*A4*xi2*zeta1*q21,delta1,rho*A5*xi1*zeta2*(q12
+q22),2*rho*A4*xi2*zeta2*q22,delta2,rho*A5*xi1*xi2,rho*A4*(xi2**2-zeta3**2),-
2*rho*A4*xi2*zeta3 /),(/ 3,3 /))
E1=reshape((/
exp((0.d0,1.d0)*zeta1*h1),(0.d0,0.d0),(0.d0,0.d0),(0.d0,0.d0),exp((0.d0,1.d0)*zeta2*h1),
(0.d0,0.d0),(0.d0,0.d0),(0.d0,0.d0),exp((0.d0,1.d0)*zeta3*h1) /),(/ 3,3 /))

```

```

Q111d=reshape((/ (0.d0,1.d0)*(xi1*A3*b1d+cos(ang)*q11),(0.d0,1.d0)*(-
xi2*(2*A2*xi*cos(ang)**2+A5*b1d)+sin(ang)*q21),(0.d0,1.d0)*((-
2*xi*sin(ang)**2+b1d)*q21/(2*zeta1)+zeta1*(-2*A2*xi*cos(ang)**2-
A5*b1d)),(0.d0,1.d0)*(xi1*A3*b2d+cos(ang)*q12),(0.d0,1.d0)*(-
xi2*(2*A2*xi*cos(ang)**2+A5*b2d)+sin(ang)*q22),(0.d0,1.d0)*((-
2*xi*sin(ang)**2+b2d)*q22/(2*zeta2)+zeta2*(-2*A2*xi*cos(ang)**2-
A5*b2d)),(0.d0,0.d0),(0.d0,1.d0)*(-2*xi*sin(ang)**2-
2*A5/A4*xi*cos(ang)**2)/(2*zeta3),-(0.d0,1.d0)*sin(ang) /),(/ 3,3 /))
Q121d=reshape((/ (0.d0,1.d0)*(xi1*A3*b1d+cos(ang)*q11),(0.d0,1.d0)*(-
xi2*(2*A2*xi*cos(ang)**2+A5*b1d)+sin(ang)*q21),-(0.d0,1.d0)*((-
2*xi*sin(ang)**2+b1d)*q21/(2*zeta1)+zeta1*(-2*A2*xi*cos(ang)**2-
A5*b1d)),(0.d0,1.d0)*(xi1*A3*b2d+cos(ang)*q12),(0.d0,1.d0)*(-
xi2*(2*A2*xi*cos(ang)**2+A5*b2d)+sin(ang)*q22),-(0.d0,1.d0)*((-
2*xi*sin(ang)**2+b2d)*q22/(2*zeta2)+zeta2*(-2*A2*xi*cos(ang)**2-
A5*b2d)),(0.d0,0.d0),-(0.d0,1.d0)*(-2*xi*sin(ang)**2-
2*A5/A4*xi*cos(ang)**2)/(2*zeta3),-(0.d0,1.d0)*sin(ang) /),(/ 3,3 /))
Q211d(1,1)=-rho*A5*(xi1*zeta1*(A3*b1d-2*A2*xi*cos(ang)**2-
A5*b1d)+zeta1*(q11+q21)*cos(ang)+xi1*(q11+q21)*(-
2*xi*sin(ang)**2+b1d)/(2*zeta1))
Q211d(1,2)=-rho*A5*(xi1*zeta2*(A3*b2d-2*A2*xi*cos(ang)**2-
A5*b2d)+zeta2*(q12+q22)*cos(ang)+xi1*(q12+q22)*(-
2*xi*sin(ang)**2+b2d)/(2*zeta2))
Q211d(1,3)=rho*A5*(xi1*sin(ang)+xi2*cos(ang))
Q211d(2,1)=-2*rho*A4*(xi2*zeta1*(-2*A2*xi*cos(ang)**2-
A5*b1d)+zeta1*q21*sin(ang)+xi2*q21*(-2*xi*sin(ang)**2+b1d)/(2*zeta1))
Q211d(2,2)=-2*rho*A4*(xi2*zeta2*(-2*A2*xi*cos(ang)**2-
A5*b2d)+zeta2*q22*sin(ang)+xi2*q22*(-2*xi*sin(ang)**2+b2d)/(2*zeta2))
Q211d(2,3)=rho*A4*(4*xi*sin(ang)**2+2*A5*xi*cos(ang)**2/A4)
Q211d(3,1)=rho*((A5-A3)*(2*xi*cos(ang)**2*q11+xi1**2*A3*b1d)-(A1-
2*A4)*(2*xi*sin(ang)**2*q21-xi2**2*(2*A2*xi*cos(ang)**2+A5*b1d))-A1*(q21*(-
2*xi*sin(ang)**2+b1d)-zeta1**2*(2*A2*xi*cos(ang)**2+A5*b1d)))
Q211d(3,2)=rho*((A5-A3)*(2*xi*cos(ang)**2*q12+xi1**2*A3*b2d)-(A1-
2*A4)*(2*xi*sin(ang)**2*q22-xi2**2*(2*A2*xi*cos(ang)**2+A5*b2d))-A1*(q22*(-
2*xi*sin(ang)**2+b2d)-zeta2**2*(2*A2*xi*cos(ang)**2+A5*b2d)))
Q211d(3,3)=2*rho*A4*zeta3*sin(ang)-
2*rho*A4*xi2*(xi*sin(ang)**2+A5*xi*cos(ang)**2/A4)/zeta3
Q221d=Q211d
Q221d(1:2,1:2)=-Q211d(1:2,1:2)
Q221d(3,3)=-Q211d(3,3)
E1d=reshape((/ exp((0.d0,1.d0)*zeta1*h1)*(0.d0,1.d0)*h1*(-
2*xi*sin(ang)**2+b1d)/(2*zeta1),(0.d0,0.d0),(0.d0,0.d0),(0.d0,0.d0),exp((0.d0,1.d0)*zet
a2*h1)*(0.d0,1.d0)*h1*(-
2*xi*sin(ang)**2+b2d)/(2*zeta2),(0.d0,0.d0),(0.d0,0.d0),(0.d0,0.d0),exp((0.d0,1.d0)*zet
a3*h1)*(0.d0,1.d0)*h1*(-2*xi*sin(ang)**2-2*A5*xi*cos(ang)**2/A4)/(2*zeta3) /),(/ 3,3
/))

```

$Q1min(1:3,1:3)=matmul(Q111,E1)$
 $Q1min(1:3,4:6)=Q121$
 $Q1min(4:6,1:3)=matmul(Q211,E1)$
 $Q1min(4:6,4:6)=Q221$
 $Q1pluh(1:3,1:3)=-Q211$
 $Q1pluh(1:3,4:6)=-matmul(Q221,E1)$
 $Q1pluoh(1:3,1:3)=-Q111$
 $Q1pluoh(1:3,4:6)=-matmul(Q121,E1)$

$Q1mind(1:3,1:3)=matmul(Q111d,E1)+matmul(Q111,E1d)$
 $Q1mind(1:3,4:6)=Q121d$
 $Q1mind(4:6,1:3)=matmul(Q211d,E1)+matmul(Q211,E1d)$
 $Q1mind(4:6,4:6)=Q221d$
 $Q1pluhd(1:3,1:3)=-Q211d$
 $Q1pluhd(1:3,4:6)=-matmul(Q221d,E1)-matmul(Q221,E1d)$

!For layer 2

$xi1=\cos(\theta_2)*xi*\cos(\alpha)+\sin(\theta_2)*xi*\sin(\alpha)$
 $xi2=-\sin(\theta_2)*xi*\cos(\alpha)+\cos(\theta_2)*xi*\sin(\alpha)$
 $\alpha=A1*A5$
 $\beta=(A1*A2+A5**2-A3**2)*xi1**2-\omega**2*(A1+A5)$
 $\gamma1=(A2*xi1**2-\omega**2)*(A5*xi1**2-\omega**2)$
 $b1=-(\beta*0.5/\alpha)-((\beta*0.5/\alpha)**2-\gamma1/\alpha)**0.5$
 $b2=-(\beta*0.5/\alpha)+((\beta*0.5/\alpha)**2-\gamma1/\alpha)**0.5$
 $b1d=-1.0*(A1*A2+A5**2-A3**2)*(cos(\theta_2)*xi*cos(\alpha)+sin(\theta_2)*xi*sin(\alpha))*(cos(\theta_2)*cos(\alpha)+sin(\theta_2)*sin(\alpha))/A1/A5-.5/(.25*((A1*A2+A5**2-A3**2)*(cos(\theta_2)*xi*cos(\alpha)+sin(\theta_2)*xi*sin(\alpha))**2-\omega**2*(A1+A5))**2/A1**2/A5**2-(A2*(cos(\theta_2)*xi*cos(\alpha)+sin(\theta_2)*xi*sin(\alpha))**2-\omega**2*(A5*(cos(\theta_2)*xi*cos(\alpha)+sin(\theta_2)*xi*sin(\alpha))**2-\omega**2)/A1/A5)**.5*(1.00*((A1*A2+A5**2-A3**2)*(cos(\theta_2)*xi*cos(\alpha)+sin(\theta_2)*xi*sin(\alpha))**2-\omega**2*(A1+A5))/A1**2/A5**2*(A1*A2+A5**2-A3**2)*(cos(\theta_2)*xi*cos(\alpha)+sin(\theta_2)*xi*sin(\alpha))*(cos(\theta_2)*cos(\alpha)+sin(\theta_2)*sin(\alpha))-2*A2*(cos(\theta_2)*xi*cos(\alpha)+sin(\theta_2)*xi*sin(\alpha))*(cos(\theta_2)*cos(\alpha)+sin(\theta_2)*sin(\alpha))*(A5*(cos(\theta_2)*xi*cos(\alpha)+sin(\theta_2)*xi*sin(\alpha))**2-\omega**2)/A1/A5-2*(A2*(cos(\theta_2)*xi*cos(\alpha)+sin(\theta_2)*xi*sin(\alpha))**2-\omega**2)*(cos(\theta_2)*xi*cos(\alpha)+sin(\theta_2)*xi*sin(\alpha))*(cos(\theta_2)*cos(\alpha)+sin(\theta_2)*sin(\alpha))/A1)$
 $b2d=-1.0*(A1*A2+A5**2-A3**2)*(cos(\theta_2)*xi*cos(\alpha)+sin(\theta_2)*xi*sin(\alpha))*(cos(\theta_2)*cos(\alpha)+sin(\theta_2)*sin(\alpha))/A1/A5+.5/(.25*((A1*A2+A5**2-A3**2)*(cos(\theta_2)*xi*cos(\alpha)+sin(\theta_2)*xi*sin(\alpha))**2-\omega**2*(A1+A5))**2/A1**2/A5**2-$

```

(A2*(cos(theta2)*xi*cos(ang)+sin(theta2)*xi*sin(ang))**2-
omega**2)*(A5*(cos(theta2)*xi*cos(ang)+sin(theta2)*xi*sin(ang))**2-
omega**2)/A1/A5)**.5*(1.00*((A1*A2+A5**2-
A3**2)*(cos(theta2)*xi*cos(ang)+sin(theta2)*xi*sin(ang))**2-
omega**2*(A1+A5))/A1**2/A5**2*(A1*A2+A5**2-
A3**2)*(cos(theta2)*xi*cos(ang)+sin(theta2)*xi*sin(ang))*(cos(theta2)*cos(ang)+sin(theta2)*sin(ang))-
2*A2*(cos(theta2)*xi*cos(ang)+sin(theta2)*xi*sin(ang))*(cos(theta2)*cos(ang)+sin(theta2)*sin(ang))*(A5*(cos(theta2)*xi*cos(ang)+sin(theta2)*xi*sin(ang))**2-
omega**2)/A1/A5-2*(A2*(cos(theta2)*xi*cos(ang)+sin(theta2)*xi*sin(ang))**2-
omega**2)*(cos(theta2)*xi*cos(ang)+sin(theta2)*xi*sin(ang))*(cos(theta2)*cos(ang)+sin(theta2)*sin(ang))/A1)
xi1d=cos(theta2)*cos(ang)+sin(theta2)*sin(ang)
xi2d=-sin(theta2)*cos(ang)+cos(theta2)*sin(ang)
zeta1=(-xi2**2+b1)**0.5
zeta2=(-xi2**2+b2)**0.5
zeta3=(-xi2**2+(omega**2-A5*xi1**2)/A4)**0.5
q11=A3*b1
q21=(omega**2-A2*xi1**2-A5*b1)
q12=A3*b2
q22=(omega**2-A2*xi1**2-A5*b2)
delta1=rho*((A5-A3)*xi1**2*q11-(A1-2*A4)*xi2**2*q21-A1*zeta1**2*q21)
delta2=rho*((A5-A3)*xi1**2*q12-(A1-2*A4)*xi2**2*q22-A1*zeta2**2*q22)
Q112=reshape((/
(0.d0,1.d0)*xi1*q11,(0.d0,1.d0)*xi2*q21,(0.d0,1.d0)*zeta1*q21,(0.d0,1.d0)*xi1*q12,(0.
d0,1.d0)*xi2*q22,(0.d0,1.d0)*zeta2*q22,(0.d0,0.d0),(0.d0,1.d0)*zeta3,-(0.d0,1.d0)*xi2
/),(/ 3,3 /))
Q122=reshape((/ (0.d0,1.d0)*xi1*q11,(0.d0,1.d0)*xi2*q21,-
(0.d0,1.d0)*zeta1*q21,(0.d0,1.d0)*xi1*q12,(0.d0,1.d0)*xi2*q22,-
(0.d0,1.d0)*zeta2*q22,(0.d0,0.d0),-(0.d0,1.d0)*zeta3,-(0.d0,1.d0)*xi2 /),(/ 3,3 /))
Q212=reshape((/ -rho*A5*xi1*zeta1*(q11+q21),-2*rho*A4*xi2*zeta1*q21,delta1,-
rho*A5*xi1*zeta2*(q12+q22),-
2*rho*A4*xi2*zeta2*q22,delta2,rho*A5*xi1*xi2,rho*A4*(xi2**2-
zeta3**2),2*rho*A4*xi2*zeta3 /),(/ 3,3 /))
Q222=reshape((/
rho*A5*xi1*zeta1*(q11+q21),2*rho*A4*xi2*zeta1*q21,delta1,rho*A5*xi1*zeta2*(q12
+q22),2*rho*A4*xi2*zeta2*q22,delta2,rho*A5*xi1*xi2,rho*A4*(xi2**2-zeta3**2),-
2*rho*A4*xi2*zeta3 /),(/ 3,3 /))
E2=reshape((/
exp((0.d0,1.d0)*zeta1*h2),(0.d0,0.d0),(0.d0,0.d0),(0.d0,0.d0),exp((0.d0,1.d0)*zeta2*h2),
(0.d0,0.d0),(0.d0,0.d0),(0.d0,0.d0),exp((0.d0,1.d0)*zeta3*h2) /),(/ 3,3 /))
Q112d=reshape((/ (0.d0,1.d0)*(xi1*A3*b1d+xi1d*q11),(0.d0,1.d0)*(-
xi2*(2*A2*xi1*xi1d+A5*b1d)+xi2d*q21),(0.d0,1.d0)*((-
2*xi2d*xi2+b1d)*q21/(2*zeta1)+zeta1*(-2*A2*xi1*xi1d-
A5*b1d)),(0.d0,1.d0)*(xi1*A3*b2d+xi1d*q12),(0.d0,1.d0)*(-
xi2*(2*A2*xi1*xi1d+A5*b2d)+xi2d*q22),(0.d0,1.d0)*((-

```

$2 * xi2 * xi2d + b2d) * q22 / (2 * zeta2) + zeta2 * (-2 * A2 * xi1 * xi1d - A5 * b2d), (0.d0, 0.d0), (0.d0, 1.d0) * (-2 * xi2 * xi2d - 2 * A5 / A4 * xi1 * xi1d) / (2 * zeta3), - (0.d0, 1.d0) * xi2d /), (/ 3, 3 /)$
 $Q122d = reshape((/ (0.d0, 1.d0) * (xi1 * A3 * b1d + xi1d * q11), (0.d0, 1.d0) * (-xi2 * (2 * A2 * xi1 * xi1d + A5 * b1d) + xi2d * q21), - (0.d0, 1.d0) * (-2 * xi2d * xi2 + b1d) * q21 / (2 * zeta1) + zeta1 * (-2 * A2 * xi1 * xi1d - A5 * b1d)), (0.d0, 1.d0) * (xi1 * A3 * b2d + xi1d * q12), (0.d0, 1.d0) * (-xi2 * (2 * A2 * xi1 * xi1d + A5 * b2d) + xi2d * q22), - (0.d0, 1.d0) * ((-2 * xi2 * xi2d + b2d) * q22 / (2 * zeta2) + zeta2 * (-2 * A2 * xi1 * xi1d - A5 * b2d)), (0.d0, 0.d0), - (0.d0, 1.d0) * (-2 * xi2 * xi2d - 2 * A5 / A4 * xi1 * xi1d) / (2 * zeta3), - (0.d0, 1.d0) * xi2d /), (/ 3, 3 /))$
 $Q212d(1,1) = -rho * A5 * (xi1 * zeta1 * (A3 * b1d - 2 * A2 * xi1 * xi1d - A5 * b1d) + zeta1 * (q11 + q21) * xi1d + xi1 * (q11 + q21) * (-2 * xi2 * xi2d + b1d) / (2 * zeta1))$
 $Q212d(1,2) = -rho * A5 * (xi1 * zeta2 * (A3 * b2d - 2 * A2 * xi1 * xi1d - A5 * b2d) + zeta2 * (q12 + q22) * xi1d + xi1 * (q12 + q22) * (-2 * xi2 * xi2d + b2d) / (2 * zeta2))$
 $Q212d(1,3) = rho * A5 * (xi1 * xi2d + xi2 * xi1d)$
 $Q212d(2,1) = -2 * rho * A4 * (xi2 * zeta1 * (-2 * A2 * xi1 * xi1d - A5 * b1d) + zeta1 * q21 * xi2d + xi2 * q21 * (-2 * xi2 * xi2d + b1d) / (2 * zeta1))$
 $Q212d(2,2) = -2 * rho * A4 * (xi2 * zeta2 * (-2 * A2 * xi1 * xi1d - A5 * b2d) + zeta2 * q22 * xi2d + xi2 * q22 * (-2 * xi2 * xi2d + b2d) / (2 * zeta2))$
 $Q212d(2,3) = rho * A4 * (4 * xi2 * xi2d + 2 * A5 * xi1 * xi1d / A4)$
 $Q212d(3,1) = rho * ((A5 - A3) * (2 * xi1 * xi1d * q11 + xi1 ** 2 * A3 * b1d) - (A1 - 2 * A4) * (2 * xi2 * xi2d * q21 - xi2 ** 2 * (2 * A2 * xi1 * xi1d + A5 * b1d)) - A1 * (q21 * (-2 * xi2 * xi2d + b1d) - zeta1 ** 2 * (2 * A2 * xi1 * xi1d + A5 * b1d)))$
 $Q212d(3,2) = rho * ((A5 - A3) * (2 * xi1 * xi1d * q12 + xi1 ** 2 * A3 * b2d) - (A1 - 2 * A4) * (2 * xi2 * xi2d * q22 - xi2 ** 2 * (2 * A2 * xi1 * xi1d + A5 * b2d)) - A1 * (q22 * (-2 * xi2 * xi2d + b2d) - zeta2 ** 2 * (2 * A2 * xi1 * xi1d + A5 * b2d)))$
 $Q212d(3,3) = 2 * rho * A4 * zeta3 * xi2d - 2 * rho * A4 * xi2 * (xi2 * xi2d + A5 * xi1 * xi1d / A4) / zeta3$
 $Q222d = Q212d$
 $Q222d(1:2, 1:2) = -Q212d(1:2, 1:2)$
 $Q222d(3, 3) = -Q212d(3, 3)$
 $E2d = reshape((/ exp((0.d0, 1.d0) * zeta1 * h2) * (0.d0, 1.d0) * h2 * (-2 * xi2 * xi2d + b1d) / (2 * zeta1), (0.d0, 0.d0), (0.d0, 0.d0), (0.d0, 0.d0), exp((0.d0, 1.d0) * zeta2 * h2) * (0.d0, 1.d0) * h2 * (-2 * xi2 * xi2d + b2d) / (2 * zeta2), (0.d0, 0.d0), (0.d0, 0.d0), (0.d0, 0.d0), exp((0.d0, 1.d0) * zeta3 * h2) * (0.d0, 1.d0) * h2 * (-2 * xi2 * xi2d - 2 * A5 * xi1 * xi1d / A4) / (2 * zeta3) /), (/ 3, 3 /))$

$Q2min(1:3, 1:3) = matmul(L2, matmul(Q112, E2))$
 $Q2min(1:3, 4:6) = matmul(L2, Q122)$
 $Q2min(4:6, 1:3) = matmul(L2, matmul(Q212, E2))$
 $Q2min(4:6, 4:6) = matmul(L2, Q222)$
 $Q2plu(1:3, 1:3) = matmul(-L2, Q112)$
 $Q2plu(1:3, 4:6) = matmul(-L2, matmul(Q122, E2))$
 $Q2plu(4:6, 1:3) = matmul(-L2, Q212)$
 $Q2plu(4:6, 4:6) = matmul(-L2, matmul(Q222, E2))$

$Q2mind(1:3, 1:3) = matmul(L2, (matmul(Q112d, E2) + matmul(Q112, E2d)))$

$Q2mind(1:3,4:6)=matmul(L2,Q122d)$
 $Q2mind(4:6,1:3)=matmul(L2,(matmul(Q212d,E2)+matmul(Q212,E2d)))$
 $Q2mind(4:6,4:6)=matmul(L2,Q222d)$
 $Q2plud(1:3,1:3)=matmul(-L2,Q112d)$
 $Q2plud(1:3,4:6)=matmul(-L2,(matmul(Q122d,E2)+matmul(Q122,E2d)))$
 $Q2plud(4:6,1:3)=matmul(-L2,Q212d)$
 $Q2plud(4:6,4:6)=matmul(-L2,(matmul(Q222d,E2)+matmul(Q222,E2d)))$

!For layer 3

$xi1=\cos(\theta_3)*xi*\cos(\alpha)+\sin(\theta_3)*xi*\sin(\alpha)$
 $xi2=-\sin(\theta_3)*xi*\cos(\alpha)+\cos(\theta_3)*xi*\sin(\alpha)$
 $\alpha=A1*A5$
 $\beta=(A1*A2+A5^{**2}-A3^{**2})*xi1^{**2}-\omega^{**2}*(A1+A5)$
 $\gamma1=(A2*xi1^{**2}-\omega^{**2})*(A5*xi1^{**2}-\omega^{**2})$
 $b1=-(\beta*0.5/\alpha)-((\beta*0.5/\alpha)^{**2}-\gamma1/\alpha)^{**0.5}$
 $b2=-(\beta*0.5/\alpha)+((\beta*0.5/\alpha)^{**2}-\gamma1/\alpha)^{**0.5}$
 $b1d=-1.0*(A1*A2+A5^{**2}-$
 $A3^{**2})*(\cos(\theta_3)*xi*\cos(\alpha)+\sin(\theta_3)*xi*\sin(\alpha))*(\cos(\theta_3)*\cos(\alpha)+\sin(\theta_3)*\sin(\alpha))/A1/A5-.5/((.25*(A1*A2+A5^{**2}-$
 $A3^{**2})*(\cos(\theta_3)*xi*\cos(\alpha)+\sin(\theta_3)*xi*\sin(\alpha))^{**2}-$
 $\omega^{**2}*(A1+A5))^{**2}/A1^{**2}/A5^{**2}-$
 $(A2*(\cos(\theta_3)*xi*\cos(\alpha)+\sin(\theta_3)*xi*\sin(\alpha))^{**2}-$
 $\omega^{**2}*(A5*(\cos(\theta_3)*xi*\cos(\alpha)+\sin(\theta_3)*xi*\sin(\alpha))^{**2}-$
 $\omega^{**2}/A1/A5)^{**}.5*(1.00*((A1*A2+A5^{**2}-$
 $A3^{**2})*(\cos(\theta_3)*xi*\cos(\alpha)+\sin(\theta_3)*xi*\sin(\alpha))^{**2}-$
 $\omega^{**2}*(A1+A5))/A1^{**2}/A5^{**2}*(A1*A2+A5^{**2}-$
 $A3^{**2})*(\cos(\theta_3)*xi*\cos(\alpha)+\sin(\theta_3)*xi*\sin(\alpha))*(\cos(\theta_3)*\cos(\alpha)+\sin(\theta_3)*\sin(\alpha))-$
 $2*A2*(\cos(\theta_3)*xi*\cos(\alpha)+\sin(\theta_3)*xi*\sin(\alpha))*(\cos(\theta_3)*\cos(\alpha)+\sin(\theta_3)*\sin(\alpha))*(A5*(\cos(\theta_3)*xi*\cos(\alpha)+\sin(\theta_3)*xi*\sin(\alpha))^{**2}-$
 $\omega^{**2}/A1/A5-2*(A2*(\cos(\theta_3)*xi*\cos(\alpha)+\sin(\theta_3)*xi*\sin(\alpha))^{**2}-$
 $\omega^{**2}*(\cos(\theta_3)*xi*\cos(\alpha)+\sin(\theta_3)*xi*\sin(\alpha))*(\cos(\theta_3)*\cos(\alpha)+\sin(\theta_3)*\sin(\alpha))/A1)$
 $b2d=-1.0*(A1*A2+A5^{**2}-$
 $A3^{**2})*(\cos(\theta_3)*xi*\cos(\alpha)+\sin(\theta_3)*xi*\sin(\alpha))*(\cos(\theta_3)*\cos(\alpha)+\sin(\theta_3)*\sin(\alpha))/A1/A5+.5/((.25*(A1*A2+A5^{**2}-$
 $A3^{**2})*(\cos(\theta_3)*xi*\cos(\alpha)+\sin(\theta_3)*xi*\sin(\alpha))^{**2}-$
 $\omega^{**2}*(A1+A5))^{**2}/A1^{**2}/A5^{**2}-$
 $(A2*(\cos(\theta_3)*xi*\cos(\alpha)+\sin(\theta_3)*xi*\sin(\alpha))^{**2}-$
 $\omega^{**2}*(A5*(\cos(\theta_3)*xi*\cos(\alpha)+\sin(\theta_3)*xi*\sin(\alpha))^{**2}-$
 $\omega^{**2}/A1/A5)^{**}.5*(1.00*((A1*A2+A5^{**2}-$
 $A3^{**2})*(\cos(\theta_3)*xi*\cos(\alpha)+\sin(\theta_3)*xi*\sin(\alpha))^{**2}-$
 $\omega^{**2}*(A1+A5))/A1^{**2}/A5^{**2}*(A1*A2+A5^{**2}-$
 $A3^{**2})*(\cos(\theta_3)*xi*\cos(\alpha)+\sin(\theta_3)*xi*\sin(\alpha))*(\cos(\theta_3)*\cos(\alpha)+\sin(\theta_3)*\sin(\alpha))-$
 $2*A2*(\cos(\theta_3)*xi*\cos(\alpha)+\sin(\theta_3)*xi*\sin(\alpha))*(\cos(\theta_3)*\cos(\alpha)+\sin(\theta_3)*\sin(\alpha))$

```

a3)*sin(ang))*(A5*(cos(theta3)*xi*cos(ang)+sin(theta3)*xi*sin(ang))**2-
omega**2)/A1/A5-2*(A2*(cos(theta3)*xi*cos(ang)+sin(theta3)*xi*sin(ang))**2-
omega**2)*(cos(theta3)*xi*cos(ang)+sin(theta3)*xi*sin(ang))*(cos(theta3)*cos(ang)+si
n(theta3)*sin(ang))/A1)
xi1d=cos(theta3)*cos(ang)+sin(theta3)*sin(ang)
xi2d=-sin(theta3)*cos(ang)+cos(theta3)*sin(ang)
zeta1=(-xi2**2+b1)**0.5
zeta2=(-xi2**2+b2)**0.5
zeta3=(-xi2**2+(omega**2-A5*xi1**2)/A4)**0.5
q11=A3*b1
q21=(omega**2-A2*xi1**2-A5*b1)
q12=A3*b2
q22=(omega**2-A2*xi1**2-A5*b2)
delta1=rho*((A5-A3)*xi1**2*q11-(A1-2*A4)*xi2**2*q21-A1*zeta1**2*q21)
delta2=rho*((A5-A3)*xi1**2*q12-(A1-2*A4)*xi2**2*q22-A1*zeta2**2*q22)
Q113=reshape((/
(0.d0,1.d0)*xi1*q11,(0.d0,1.d0)*xi2*q21,(0.d0,1.d0)*zeta1*q21,(0.d0,1.d0)*xi1*q12,(0.
d0,1.d0)*xi2*q22,(0.d0,1.d0)*zeta2*q22,(0.d0,0.d0),(0.d0,1.d0)*zeta3,-(0.d0,1.d0)*xi2
/),(/ 3,3 /))
Q123=reshape((/ (0.d0,1.d0)*xi1*q11,(0.d0,1.d0)*xi2*q21,-
(0.d0,1.d0)*zeta1*q21,(0.d0,1.d0)*xi1*q12,(0.d0,1.d0)*xi2*q22,-
(0.d0,1.d0)*zeta2*q22,(0.d0,0.d0),-(0.d0,1.d0)*zeta3,-(0.d0,1.d0)*xi2 /),(/ 3,3 /))
Q213=reshape((/ -rho*A5*xi1*zeta1*(q11+q21),-2*rho*A4*xi2*zeta1*q21,delta1,-
rho*A5*xi1*zeta2*(q12+q22),-
2*rho*A4*xi2*zeta2*q22,delta2,rho*A5*xi1*xi2,rho*A4*(xi2**2-
zeta3**2),2*rho*A4*xi2*zeta3 /),(/ 3,3 /))
Q223=reshape((/
rho*A5*xi1*zeta1*(q11+q21),2*rho*A4*xi2*zeta1*q21,delta1,rho*A5*xi1*zeta2*(q12
+q22),2*rho*A4*xi2*zeta2*q22,delta2,rho*A5*xi1*xi2,rho*A4*(xi2**2-zeta3**2),-
2*rho*A4*xi2*zeta3 /),(/ 3,3 /))
E3=reshape((/
exp((0.d0,1.d0)*zeta1*h3),(0.d0,0.d0),(0.d0,0.d0),(0.d0,0.d0),exp((0.d0,1.d0)*zeta2*h3),
(0.d0,0.d0),(0.d0,0.d0),(0.d0,0.d0),exp((0.d0,1.d0)*zeta3*h3) /),(/ 3,3 /))
Q113d=reshape((/ (0.d0,1.d0)*(xi1*A3*b1d+xi1d*q11),(0.d0,1.d0)*(-
xi2*(2*A2*xi1*xi1d+A5*b1d)+xi2d*q21),(0.d0,1.d0)*((-
2*xi2d*xi2+b1d)*q21/(2*zeta1)+zeta1*(-2*A2*xi1*xi1d-
A5*b1d)),(0.d0,1.d0)*(xi1*A3*b2d+xi1d*q12),(0.d0,1.d0)*(-
xi2*(2*A2*xi1*xi1d+A5*b2d)+xi2d*q22),(0.d0,1.d0)*((-
2*xi2*xi2d+b2d)*q22/(2*zeta2)+zeta2*(-2*A2*xi1*xi1d-
A5*b2d)),(0.d0,0.d0),(0.d0,1.d0)*(-2*xi2*xi2d-2*A5/A4*xi1*xi1d)/(2*zeta3),-
(0.d0,1.d0)*xi2d /),(/ 3,3 /))
Q123d=reshape((/ (0.d0,1.d0)*(xi1*A3*b1d+xi1d*q11),(0.d0,1.d0)*(-
xi2*(2*A2*xi1*xi1d+A5*b1d)+xi2d*q21),-(0.d0,1.d0)*((-
2*xi2d*xi2+b1d)*q21/(2*zeta1)+zeta1*(-2*A2*xi1*xi1d-
A5*b1d)),(0.d0,1.d0)*(xi1*A3*b2d+xi1d*q12),(0.d0,1.d0)*(-
xi2*(2*A2*xi1*xi1d+A5*b2d)+xi2d*q22),-(0.d0,1.d0)*((-

```

$2 * xi2 * xi2d + b2d) * q22 / (2 * zeta2) + zeta2 * (-2 * A2 * xi1 * xi1d - A5 * b2d), (0.d0, 0.d0), -$
 $(0.d0, 1.d0) * (-2 * xi2 * xi2d - 2 * A5 / A4 * xi1 * xi1d) / (2 * zeta3), -(0.d0, 1.d0) * xi2d / (/ 3, 3 /)$
 $Q213d(1,1) = -rho * A5 * (xi1 * zeta1 * (A3 * b1d - 2 * A2 * xi1 * xi1d -$
 $A5 * b1d) + zeta1 * (q11 + q21) * xi1d + xi1 * (q11 + q21) * (-2 * xi2 * xi2d + b1d) / (2 * zeta1))$
 $Q213d(1,2) = -rho * A5 * (xi1 * zeta2 * (A3 * b2d - 2 * A2 * xi1 * xi1d -$
 $A5 * b2d) + zeta2 * (q12 + q22) * xi1d + xi1 * (q12 + q22) * (-2 * xi2 * xi2d + b2d) / (2 * zeta2))$
 $Q213d(1,3) = rho * A5 * (xi1 * xi2d + xi2 * xi1d)$
 $Q213d(2,1) = -2 * rho * A4 * (xi2 * zeta1 * (-2 * A2 * xi1 * xi1d -$
 $A5 * b1d) + zeta1 * q21 * xi2d + xi2 * q21 * (-2 * xi2 * xi2d + b1d) / (2 * zeta1))$
 $Q213d(2,2) = -2 * rho * A4 * (xi2 * zeta2 * (-2 * A2 * xi1 * xi1d -$
 $A5 * b2d) + zeta2 * q22 * xi2d + xi2 * q22 * (-2 * xi2 * xi2d + b2d) / (2 * zeta2))$
 $Q213d(2,3) = rho * A4 * (4 * xi2 * xi2d + 2 * A5 * xi1 * xi1d / A4)$
 $Q213d(3,1) = rho * ((A5 - A3) * (2 * xi1 * xi1d * q11 + xi1 ** 2 * A3 * b1d) - (A1 -$
 $2 * A4) * (2 * xi2 * xi2d * q21 - xi2 ** 2 * (2 * A2 * xi1 * xi1d + A5 * b1d)) - A1 * (q21 * (-$
 $2 * xi2 * xi2d + b1d) - zeta1 ** 2 * (2 * A2 * xi1 * xi1d + A5 * b1d)))$
 $Q213d(3,2) = rho * ((A5 - A3) * (2 * xi1 * xi1d * q12 + xi1 ** 2 * A3 * b2d) - (A1 -$
 $2 * A4) * (2 * xi2 * xi2d * q22 - xi2 ** 2 * (2 * A2 * xi1 * xi1d + A5 * b2d)) - A1 * (q22 * (-$
 $2 * xi2 * xi2d + b2d) - zeta2 ** 2 * (2 * A2 * xi1 * xi1d + A5 * b2d)))$
 $Q213d(3,3) = 2 * rho * A4 * zeta3 * xi2d - 2 * rho * A4 * xi2 * (xi2 * xi2d + A5 * xi1 * xi1d / A4) / zeta3$
 $Q223d = Q213d$
 $Q223d(1:2, 1:2) = -Q213d(1:2, 1:2)$
 $Q223d(3,3) = -Q213d(3,3)$
 $E3d = reshape(/ exp((0.d0, 1.d0) * zeta1 * h3) * (0.d0, 1.d0) * h3 * (-$
 $2 * xi2 * xi2d + b1d) / (2 * zeta1), (0.d0, 0.d0), (0.d0, 0.d0), (0.d0, 0.d0), exp((0.d0, 1.d0) * zeta2 * h3)$
 $* (0.d0, 1.d0) * h3 * (-$
 $2 * xi2 * xi2d + b2d) / (2 * zeta2), (0.d0, 0.d0), (0.d0, 0.d0), (0.d0, 0.d0), exp((0.d0, 1.d0) * zeta3 * h3)$
 $* (0.d0, 1.d0) * h3 * (-2 * xi2 * xi2d - 2 * A5 * xi1 * xi1d / A4) / (2 * zeta3) / (/ 3, 3 /)$

$Q3min(1:3, 1:3) = matmul(L3, matmul(Q113, E3))$
 $Q3min(1:3, 4:6) = matmul(L3, Q123)$
 $Q3min(4:6, 1:3) = matmul(L3, matmul(Q213, E3))$
 $Q3min(4:6, 4:6) = matmul(L3, Q223)$
 $Q3plu(1:3, 1:3) = matmul(-L3, Q113)$
 $Q3plu(1:3, 4:6) = matmul(-L3, matmul(Q123, E3))$
 $Q3plu(4:6, 1:3) = matmul(-L3, Q213)$
 $Q3plu(4:6, 4:6) = matmul(-L3, matmul(Q223, E3))$
 $Q3mind(1:3, 1:3) = matmul(L3, (matmul(Q113d, E3) + matmul(Q113, E3d)))$
 $Q3mind(1:3, 4:6) = matmul(L3, Q123d)$
 $Q3mind(4:6, 1:3) = matmul(L3, (matmul(Q213d, E3) + matmul(Q213, E3d)))$
 $Q3mind(4:6, 4:6) = matmul(L3, Q223d)$
 $Q3plud(1:3, 1:3) = matmul(-L3, Q113d)$
 $Q3plud(1:3, 4:6) = matmul(-L3, (matmul(Q123d, E3) + matmul(Q123, E3d)))$
 $Q3plud(4:6, 1:3) = matmul(-L3, Q213d)$
 $Q3plud(4:6, 4:6) = matmul(-L3, (matmul(Q223d, E3) + matmul(Q223, E3d)))$

!For layer 4

$$xi1 = \cos(\theta_4) * xi * \cos(\alpha) + \sin(\theta_4) * xi * \sin(\alpha)$$

$$xi2 = -\sin(\theta_4) * xi * \cos(\alpha) + \cos(\theta_4) * xi * \sin(\alpha)$$

$$\alpha = A1 * A5$$

$$\beta = (A1 * A2 + A5^{**2} - A3^{**2}) * xi1^{**2} - \omega^{**2} * (A1 + A5)$$

$$\gamma = (A2 * xi1^{**2} - \omega^{**2}) * (A5 * xi1^{**2} - \omega^{**2})$$

$$b1 = -(\beta * 0.5 / \alpha) - ((\beta * 0.5 / \alpha)^{**2} - \gamma / \alpha)^{**0.5}$$

$$b2 = -(\beta * 0.5 / \alpha) + ((\beta * 0.5 / \alpha)^{**2} - \gamma / \alpha)^{**0.5}$$

$$b1d = -1.0 * (A1 * A2 + A5^{**2} - A3^{**2}) * (\cos(\theta_4) * xi * \cos(\alpha) + \sin(\theta_4) * xi * \sin(\alpha)) * (\cos(\theta_4) * \cos(\alpha) + \sin(\theta_4) * \sin(\alpha)) / A1 / A5 - .5 / (.25 * ((A1 * A2 + A5^{**2} - A3^{**2}) * (\cos(\theta_4) * xi * \cos(\alpha) + \sin(\theta_4) * xi * \sin(\alpha))^{**2} - \omega^{**2} * (A1 + A5))^{**2} / A1^{**2} / A5^{**2} - (A2 * (\cos(\theta_4) * xi * \cos(\alpha) + \sin(\theta_4) * xi * \sin(\alpha))^{**2} - \omega^{**2}) * (A5 * (\cos(\theta_4) * xi * \cos(\alpha) + \sin(\theta_4) * xi * \sin(\alpha))^{**2} - \omega^{**2}) / A1 / A5)^{**2} * (1.00 * ((A1 * A2 + A5^{**2} - A3^{**2}) * (\cos(\theta_4) * xi * \cos(\alpha) + \sin(\theta_4) * xi * \sin(\alpha))^{**2} - \omega^{**2} * (A1 + A5)) / A1^{**2} / A5^{**2} * (A1 * A2 + A5^{**2} - A3^{**2}) * (\cos(\theta_4) * xi * \cos(\alpha) + \sin(\theta_4) * xi * \sin(\alpha)) * (\cos(\theta_4) * \cos(\alpha) + \sin(\theta_4) * \sin(\alpha)) - 2 * A2 * (\cos(\theta_4) * xi * \cos(\alpha) + \sin(\theta_4) * xi * \sin(\alpha)) * (\cos(\theta_4) * \cos(\alpha) + \sin(\theta_4) * \sin(\alpha)) * (A5 * (\cos(\theta_4) * xi * \cos(\alpha) + \sin(\theta_4) * xi * \sin(\alpha))^{**2} - \omega^{**2}) / A1 / A5 - 2 * (A2 * (\cos(\theta_4) * xi * \cos(\alpha) + \sin(\theta_4) * xi * \sin(\alpha))^{**2} - \omega^{**2}) * (\cos(\theta_4) * xi * \cos(\alpha) + \sin(\theta_4) * xi * \sin(\alpha)) * (\cos(\theta_4) * \cos(\alpha) + \sin(\theta_4) * \sin(\alpha)) / A1)$$

$$b2d = -1.0 * (A1 * A2 + A5^{**2} - A3^{**2}) * (\cos(\theta_4) * xi * \cos(\alpha) + \sin(\theta_4) * xi * \sin(\alpha)) * (\cos(\theta_4) * \cos(\alpha) + \sin(\theta_4) * \sin(\alpha)) / A1 / A5 + .5 / (.25 * ((A1 * A2 + A5^{**2} - A3^{**2}) * (\cos(\theta_4) * xi * \cos(\alpha) + \sin(\theta_4) * xi * \sin(\alpha))^{**2} - \omega^{**2} * (A1 + A5))^{**2} / A1^{**2} / A5^{**2} - (A2 * (\cos(\theta_4) * xi * \cos(\alpha) + \sin(\theta_4) * xi * \sin(\alpha))^{**2} - \omega^{**2}) * (A5 * (\cos(\theta_4) * xi * \cos(\alpha) + \sin(\theta_4) * xi * \sin(\alpha))^{**2} - \omega^{**2}) / A1 / A5)^{**2} * (1.00 * ((A1 * A2 + A5^{**2} - A3^{**2}) * (\cos(\theta_4) * xi * \cos(\alpha) + \sin(\theta_4) * xi * \sin(\alpha))^{**2} - \omega^{**2} * (A1 + A5)) / A1^{**2} / A5^{**2} * (A1 * A2 + A5^{**2} - A3^{**2}) * (\cos(\theta_4) * xi * \cos(\alpha) + \sin(\theta_4) * xi * \sin(\alpha)) * (\cos(\theta_4) * \cos(\alpha) + \sin(\theta_4) * \sin(\alpha)) - 2 * A2 * (\cos(\theta_4) * xi * \cos(\alpha) + \sin(\theta_4) * xi * \sin(\alpha)) * (\cos(\theta_4) * \cos(\alpha) + \sin(\theta_4) * \sin(\alpha)) * (A5 * (\cos(\theta_4) * xi * \cos(\alpha) + \sin(\theta_4) * xi * \sin(\alpha))^{**2} - \omega^{**2}) / A1 / A5 - 2 * (A2 * (\cos(\theta_4) * xi * \cos(\alpha) + \sin(\theta_4) * xi * \sin(\alpha))^{**2} - \omega^{**2}) * (\cos(\theta_4) * xi * \cos(\alpha) + \sin(\theta_4) * xi * \sin(\alpha)) * (\cos(\theta_4) * \cos(\alpha) + \sin(\theta_4) * \sin(\alpha)) / A1)$$

$$xi1d = \cos(\theta_4) * \cos(\alpha) + \sin(\theta_4) * \sin(\alpha)$$

$$xi2d = -\sin(\theta_4) * \cos(\alpha) + \cos(\theta_4) * \sin(\alpha)$$

$$zeta1 = (-xi2^{**2} + b1)^{**0.5}$$

$$zeta2 = (-xi2^{**2} + b2)^{**0.5}$$

$$zeta3 = (-xi2^{**2} + (\omega^{**2} - A5 * xi1^{**2}) / A4)^{**0.5}$$

```

q11=A3*b1
q21=(omega**2-A2*xi1**2-A5*b1)
q12=A3*b2
q22=(omega**2-A2*xi1**2-A5*b2)
delta1=rho*((A5-A3)*xi1**2*q11-(A1-2*A4)*xi2**2*q21-A1*zeta1**2*q21)
delta2=rho*((A5-A3)*xi1**2*q12-(A1-2*A4)*xi2**2*q22-A1*zeta2**2*q22)
Q114=reshape((/
(0.d0,1.d0)*xi1*q11,(0.d0,1.d0)*xi2*q21,(0.d0,1.d0)*zeta1*q21,(0.d0,1.d0)*xi1*q12,(0.
d0,1.d0)*xi2*q22,(0.d0,1.d0)*zeta2*q22,(0.d0,0.d0),(0.d0,1.d0)*zeta3,-(0.d0,1.d0)*xi2
/),(/ 3,3 /))
Q124=reshape((/ (0.d0,1.d0)*xi1*q11,(0.d0,1.d0)*xi2*q21,-
(0.d0,1.d0)*zeta1*q21,(0.d0,1.d0)*xi1*q12,(0.d0,1.d0)*xi2*q22,-
(0.d0,1.d0)*zeta2*q22,(0.d0,0.d0),-(0.d0,1.d0)*zeta3,-(0.d0,1.d0)*xi2 /),(/ 3,3 /))
Q214=reshape((/ -rho*A5*xi1*zeta1*(q11+q21),-2*rho*A4*xi2*zeta1*q21,delta1,-
rho*A5*xi1*zeta2*(q12+q22),-
2*rho*A4*xi2*zeta2*q22,delta2,rho*A5*xi1*xi2,rho*A4*(xi2**2-
zeta3**2),2*rho*A4*xi2*zeta3 /),(/ 3,3 /))
Q224=reshape((/
rho*A5*xi1*zeta1*(q11+q21),2*rho*A4*xi2*zeta1*q21,delta1,rho*A5*xi1*zeta2*(q12
+q22),2*rho*A4*xi2*zeta2*q22,delta2,rho*A5*xi1*xi2,rho*A4*(xi2**2-zeta3**2),-
2*rho*A4*xi2*zeta3 /),(/ 3,3 /))
E4=reshape((/
exp((0.d0,1.d0)*zeta1*h4),(0.d0,0.d0),(0.d0,0.d0),(0.d0,0.d0),exp((0.d0,1.d0)*zeta2*h4),
(0.d0,0.d0),(0.d0,0.d0),(0.d0,0.d0),exp((0.d0,1.d0)*zeta3*h4) /),(/ 3,3 /))
Q114d=reshape((/ (0.d0,1.d0)*(xi1*A3*b1d+xi1d*q11),(0.d0,1.d0)*(-
xi2*(2*A2*xi1*xi1d+A5*b1d)+xi2d*q21),(0.d0,1.d0)*((-
2*xi2d*xi2+b1d)*q21/(2*zeta1)+zeta1*(-2*A2*xi1*xi1d-
A5*b1d)),(0.d0,1.d0)*(xi1*A3*b2d+xi1d*q12),(0.d0,1.d0)*(-
xi2*(2*A2*xi1*xi1d+A5*b2d)+xi2d*q22),(0.d0,1.d0)*((-
2*xi2*xi2d+b2d)*q22/(2*zeta2)+zeta2*(-2*A2*xi1*xi1d-
A5*b2d)),(0.d0,0.d0),(0.d0,1.d0)*(-2*xi2*xi2d-2*A5/A4*xi1*xi1d)/(2*zeta3),-
(0.d0,1.d0)*xi2d /),(/ 3,3 /))
Q124d=reshape((/ (0.d0,1.d0)*(xi1*A3*b1d+xi1d*q11),(0.d0,1.d0)*(-
xi2*(2*A2*xi1*xi1d+A5*b1d)+xi2d*q21),-(0.d0,1.d0)*((-
2*xi2d*xi2+b1d)*q21/(2*zeta1)+zeta1*(-2*A2*xi1*xi1d-
A5*b1d)),(0.d0,1.d0)*(xi1*A3*b2d+xi1d*q12),(0.d0,1.d0)*(-
xi2*(2*A2*xi1*xi1d+A5*b2d)+xi2d*q22),-(0.d0,1.d0)*((-
2*xi2*xi2d+b2d)*q22/(2*zeta2)+zeta2*(-2*A2*xi1*xi1d-A5*b2d)),(0.d0,0.d0),-
(0.d0,1.d0)*(-2*xi2*xi2d-2*A5/A4*xi1*xi1d)/(2*zeta3),-(0.d0,1.d0)*xi2d /),(/ 3,3 /))
Q214d(1,1)=-rho*A5*(xi1*zeta1*(A3*b1d-2*A2*xi1*xi1d-
A5*b1d)+zeta1*(q11+q21)*xi1d+xi1*(q11+q21)*(-2*xi2*xi2d+b1d)/(2*zeta1))
Q214d(1,2)=-rho*A5*(xi1*zeta2*(A3*b2d-2*A2*xi1*xi1d-
A5*b2d)+zeta2*(q12+q22)*xi1d+xi1*(q12+q22)*(-2*xi2*xi2d+b2d)/(2*zeta2))
Q214d(1,3)=rho*A5*(xi1*xi2d+xi2*xi1d)
Q214d(2,1)=-2*rho*A4*(xi2*zeta1*(-2*A2*xi1*xi1d-
A5*b1d)+zeta1*q21*xi2d+xi2*q21*(-2*xi2*xi2d+b1d)/(2*zeta1))

```

$Q214d(2,2)=-2*\rho*A4*(xi2*zeta2*(-2*A2*xi1*xi1d-A5*b2d)+zeta2*q22*xi2d+xi2*q22*(-2*xi2*xi2d+b2d))/(2*zeta2)$
 $Q214d(2,3)=\rho*A4*(4*xi2*xi2d+2*A5*xi1*xi1d/A4)$
 $Q214d(3,1)=\rho*((A5-A3)*(2*xi1*xi1d*q11+xi1**2*A3*b1d)-(A1-2*A4)*(2*xi2*xi2d*q21-xi2**2*(2*A2*xi1*xi1d+A5*b1d))-A1*(q21*(-2*xi2*xi2d+b1d)-zeta1**2*(2*A2*xi1*xi1d+A5*b1d)))$
 $Q214d(3,2)=\rho*((A5-A3)*(2*xi1*xi1d*q12+xi1**2*A3*b2d)-(A1-2*A4)*(2*xi2*xi2d*q22-xi2**2*(2*A2*xi1*xi1d+A5*b2d))-A1*(q22*(-2*xi2*xi2d+b2d)-zeta2**2*(2*A2*xi1*xi1d+A5*b2d)))$
 $Q214d(3,3)=2*\rho*A4*zeta3*xi2d-2*\rho*A4*xi2*(xi2*xi2d+A5*xi1*xi1d/A4)/zeta3$
 $Q224d=Q214d$
 $Q224d(1:2,1:2)=-Q214d(1:2,1:2)$
 $Q224d(3,3)=-Q214d(3,3)$
 $E4d=reshape((/ exp((0.d0,1.d0)*zeta1*h4)*(0.d0,1.d0)*h4*(-2*xi2*xi2d+b1d)/(2*zeta1),(0.d0,0.d0),(0.d0,0.d0),(0.d0,0.d0),exp((0.d0,1.d0)*zeta2*h4)*(0.d0,1.d0)*h4*(-2*xi2*xi2d+b2d)/(2*zeta2),(0.d0,0.d0),(0.d0,0.d0),(0.d0,0.d0),exp((0.d0,1.d0)*zeta3*h4)*(0.d0,1.d0)*h4*(-2*xi2*xi2d-2*A5*xi1*xi1d/A4)/(2*zeta3) /),(/ 3,3 /))$

$Q4min(1:3,1:3)=matmul(L4,matmul(Q114,E4))$
 $Q4min(1:3,4:6)=matmul(L4,Q124)$
 $Q4min(4:6,1:3)=matmul(L4,matmul(Q214,E4))$
 $Q4min(4:6,4:6)=matmul(L4,Q224)$
 $Q4plu(1:3,1:3)=matmul(-L4,Q114)$
 $Q4plu(1:3,4:6)=matmul(-L4,matmul(Q124,E4))$
 $Q4plu(4:6,1:3)=matmul(-L4,Q214)$
 $Q4plu(4:6,4:6)=matmul(-L4,matmul(Q224,E4))$

$Q4mind(1:3,1:3)=matmul(L4,(matmul(Q114d,E4)+matmul(Q114,E4d)))$
 $Q4mind(1:3,4:6)=matmul(L4,Q124d)$
 $Q4mind(4:6,1:3)=matmul(L4,(matmul(Q214d,E4)+matmul(Q214,E4d)))$
 $Q4mind(4:6,4:6)=matmul(L4,Q224d)$
 $Q4plud(1:3,1:3)=matmul(-L4,Q114d)$
 $Q4plud(1:3,4:6)=matmul(-L4,(matmul(Q124d,E4)+matmul(Q124,E4d)))$
 $Q4plud(4:6,1:3)=matmul(-L4,Q214d)$
 $Q4plud(4:6,4:6)=matmul(-L4,(matmul(Q224d,E4)+matmul(Q224,E4d)))$
 $Qm(1:24,1:24)=0.d0$
 $Qm(1:3,1:6)=Q1pluh$
 $Qm(4:9,1:6)=Q1min$
 $Qm(4:9,7:12)=Q2plu$
 $Qm(10:15,7:12)=Q2min$
 $Qm(10:15,13:18)=Q3plu$
 $Qm(16:21,13:18)=Q3min$
 $Qm(16:21,19:24)=Q4plu$
 $!Qm(22:23,19:24)=Q4min(1:2,1:6) !For AntiSymmetric modes$
 $Qm(22:24,19:24)=Q4min(3:5,1:6) !For Symmetric modes$

```

!Qm(24,19:24)=Q4mind(6,1:6) !For Antisymm modes

Qmd(1:24,1:24)=0.d0
Qmd(1:3,1:6)=Q1pluhd
Qmd(4:9,1:6)=Q1mind
Qmd(4:9,7:12)=Q2plud
Qmd(10:15,7:12)=Q2mind
Qmd(10:15,13:18)=Q3plud
Qmd(16:21,13:18)=Q3mind
Qmd(16:21,19:24)=Q4plud
!Qmd(22:23,19:24)=Q4mind(1:2,1:6) !For AntiSymmetric modes
Qmd(22:24,19:24)=Q4mind(3:5,1:6) !For Symmetric modes
!Qmd(24,19:24)=Q4mind(6,1:6) !For Antisymm modes

end subroutine layerprops

```

B.4 Matlab Code for Generating Images/Movies and Waveform Files

Some explanatory notes have been added following the “%” symbol, which is the commenting symbol in Matlab.

B.4.A Out-of-Plane Displacement Field Image for Circular Actuator (Fig. 11 (b))

```

for i=1:1600
    x(i)=-10e-2+i*10e-2/800;
end
for i=1:1600
    for j=1:1600
        if (x(i)^2+x(j)^2 > 6.25e-6)
            uz(i,j)=BESSELJ(0,2*pi*(x(i)^2+x(j)^2)^0.5/0.9542e-2);
        else
            uz(i,j)=0;
        end
    end
end
end
uz=uz/min(min(uz));
figure; surf(x,x,uz');
shading interp; view(2)
axis off;
colorbar

```

B.4.B Waveform Generation and Storage in a File (for Agilent Intuilink/Abaqus)

```
f=275e3; % Center frequency
step=1E-08; % Time step – note that this is much finer for Intuilink. For Abaqus, it
% should only be fine enough to resolve the highest frequency ( $\sim (20f_{\max})^{-1}$ )
end1=10E-5; % Last instant of time in signal: if no zero padding is needed, this is n/f
n=2.5; % Number of cycles
t=0:step:n/f;
% The following line is for a n-cycle Hanning windowed sinusoidal toneburst
y=0.5*sin(2*pi*f*t)-0.25*(sin(2*(n+1)*pi*f*t/n)+sin(2*(n-1)*pi*f*t/n));
a=max(size(t));
b=floor(end1/step);
t(a+1:b)=(n/f+step):step:end1;
y(a+1:b)=0;
plot(t,y)
csvwrite('waveform275khz.csv',y) %Use this line only for signal generation to download
% to the function generator
% If using the file for ABAQUS, include the remaining lines and delete the above line
for i=1:b/4 %The steps of 4 data points in each line is needed for ABAQUS
    l=(4*(i-1)+1);
    ll=4*i;
    for j=1:ll
        y2(i,2*(j-4*(i-1))-1)=t(j);
        y2(i,2*(j-4*(i-1)))=y(j);
    end
end
csvwrite('waveform275khz.inp',y2)
```

B.4.C Post-Processing the Data from the Laser Vibrometer Experiment (Fig. 24 (a))

```
clear all
x(1:4)=0:0.5:1.5; x(5:23)=2:1:20;
x3=floor(x/2);
x2=round(10*(x/2-floor(x/2)));
y=-19.6:0.6:-0.4;
y1=(12.6/25*(25+y)-3.6);
y2=round(abs(100*y1))-100*floor(abs(y1));
y3=floor(abs(y1));
t=0:1.25e-7:933*1.25e-7;
f=sin(2*pi*30e3*t).*window(934,'Hanning');
j=1;
for i=1:30
    x2s=num2str(x2(j));
    x3s=num2str(x3(j));
    y2s=num2str(y2(i));
```

```

y3s=num2str(y3(i));
if y2(i)==3
    y2s='03';
end
if y2(i)==5
    y2s='05';
end
if y2(i)==8
    y2s='08';
end
if y1(i)>0
    fn=strcat('x0y',y3s,'p',y2s,'_30khza0.tsv');
else
    fn=strcat('x0ym',y3s,'p',y2s,'_30khza0.tsv');
end
[z(j,i,:),gr,cr]=wden(detrend(dlmread(fn,'t',25,1)), 'heursure','s','one',6,'dmey');
end

for j=2:23
for i=1:30
    x2s=num2str(x2(j));
    x3s=num2str(x3(j));
    if x2(j)==3
        x2s='25';
    end
    if x2(j)==8
        x2s='75';
    end
    y2s=num2str(y2(i));
    y3s=num2str(y3(i));
    if y2(i)==3
        y2s='03';
    end
    if y2(i)==5
        y2s='05';
    end
    if y2(i)==8
        y2s='08';
    end
    if y1(i)>0
        fn=strcat('x',x3s,'p',x2s,'y',y3s,'p',y2s,'_30khza0.tsv');
    else
        fn=strcat('x',x3s,'p',x2s,'ym',y3s,'p',y2s,'_30khza0.tsv');
    end
    [z(j,i,:),gr,cr]=wden(detrend(dlmread(fn,'t',25,1)), 'heursure','s','one',6,'dmey');
end
end

```

```

end
for j=4:23
for i=31:33
    x2s=num2str(x2(j));
    x3s=num2str(x3(j));
    if x2(j)==3
        x2s='25';
    end
    if x2(j)==8
        x2s='75';
    end
    y2s=num2str(y2(i));
    y3s=num2str(y3(i));
    if y2(i)==3
        y2s='03';
    end
    if y2(i)==5
        y2s='05';
    end
    if y2(i)==8
        y2s='08';
    end
    if y1(i)>0
        fn=strcat('x',x3s,'p',x2s,'y',y3s,'p',y2s,'_30khza0.tsv');
    else
        fn=strcat('x',x3s,'p',x2s,'ym',y3s,'p',y2s,'_30khza0.tsv');
    end
    [z(j,i,:),gr,cr]=wden(detrend(dlmread(fn,'\t',25,1)), 'heursure','s','one',6,'dmey');
end
end
figure;
z=-z/max(max(max(z)));
c2=[-0.8 0.8];
[xo,yo]=meshgrid(x,y);
[xi,yi]=meshgrid(0.1:0.3:19.6,-19.6:0.3:-0.1);
for k=1:30
    ti=k*10
    titl=sprintf('Time = %g microsec.',ti);
    zn(1:23,1:33)=z(:,k*80);
    zn1=interp2(xo,yo,zn,xi,yi,'cubic');
    surf(xi,yi,zn1); colormap('jet'); caxis(c2); text(-5e-2,9.5e-2,titl,'FontSize',12); shading
interp; axis square; axis off; view(2); colorbar; % caxis(c2);
    M(k)=getframe;
end
movie2avi(M,'vibroexpmfcmovie2.avi','compression','None','Quality',100,'fps',1);

```

B.4.D Spectrograms on Log-Scale with Colors as in LastWave 2.0 (Fig. 42 (b))

```
clear all
yd=load('e11n12ds6cm10cmb12p5cmnoisy.txt'); %Noisy FEM simulation signal file
yds=specgram(yd,max(size(yd)),1/1e-7,90,89);
freq=20:20:600;
time=(10:1e-1:45.75);
for i=1:30
    ydsn(i,:)=yds(31-i,:);
end
atem=abs(max(max(ydsn(1:30,55:412))))^2;
for k=1:30
    for l=55:412
        ate=abs(ydsn(k,l))^2/atem;
        ydsn1(k,l)=20*log10(ate);
    end
end
freq1=1:1:600;
[to,fo]=meshgrid(time,freq);
[tf,ff]=meshgrid(time,freq1);
ydsn2=interp2(to,fo,ydsn1(1:30,55:412),tf,ff);
v=[-30 0];
figure; imagesc(time,freq1,ydsn2); caxis(v);
atest=0:0.0625:1;
atest1=0:0.125:1;
atest2=1:-0.125:0;
atest3=1:-0.0625:0;
atest4=0:0.0625:1;
test(1:17,3)=atest';
test(18:26,3)=1;
test(18:26,2)=atest1';
test(27:43,3)=atest3';
test(27:43,2)=1;
test(44:60,2)=1;
test(44:60,3)=0;
test(44:60,1)=atest4';
test(61:77,1)=1;
test(61:77,3)=0;
test(61:77,2)=atest3';
colormap(test); h=colorbar('vert');
set(h,'FontSize',20);
xlabel('Time ( s)', 'FontSize',24);
ylabel('Frequency (kHz)', 'FontSize',24);
```


B.4.E Transient Out-of-plane Displacements by a Square Piezo Function for Composites

This code uses the kernel function evaluated by the Fortran 90 code in Section B.3 as input and generates out-of-plane displacement surface plots due to excitation by a square piezo.

```
clc
clear all
cpf=load('S0multi045m4590p11mmlayertssymmroot20to800khzallangs.txt');
kern=load('multiQmkernS020to800khz045m4590p11mmlayertssymmre.txt');
for k=1+90:361+90
angle1(k)=-pi+2*pi*(k-91)/360;
end
for k=1:90
angle1(k)=-pi-(91-k)*pi/180;
end
for k=361+91:361+183
angle1(k)=pi+(k-361-91)*pi/180;
end

% These angle changes eliminate computation singularities at 0,90,180,270 and 360
degrees
% since cos( ) and sin( ) functions appear in the denominator
angle1(1)=-3*pi/2-pi/180;
angle1(91)=-pi-pi/180;
angle1(181)=-pi/2-pi/180;
angle1(271)=-pi/180;
angle1(361)=pi/2-pi/180;
angle1(361+91)=pi-pi/180;
angle1(361+182)=3*pi/2-pi/180;
for ko=5:17
    ko
    cpd(1:60)=cpf((ko-2)*60+1:(ko-1)*60);
    cpd(61)=cpd(60);
    for j=1:60
        cp1(3*(j-1)+1)=cpd(j);
        cp1(3*(j-1)+2)=cpd(j)*2/3+cpd(j+1)/3;
        cp1(3*j)=cpd(j)/3+cpd(j+1)*2/3;
    end
    cp1(181)=cp1(180);
    cp(182+90:361+90)=cp1(1:180);
    cp(1+90:181+90)=cp1(1:181);
    cp(1:90)=cp1(91:180);
    cp(361+91:361+183)=cp1(1:93);
```

```

ydd(1:60)=kern((ko-2)*60+1:(ko-1)*60);
ydd(61)=ydd(60);

%Upsampling from 3 deg intervals to 1 deg intervals
for j=1:60
yd(3*(j-1)+1)=ydd(j);
yd(3*(j-1)+2)=ydd(j)*2/3+ydd(j+1)/3;
yd(3*j)=ydd(j)/3+ydd(j+1)*2/3;
end

yd(181)=yd(180);
u3r(1:90)=yd(91:180);
u3r(1+90:181+90)=yd(1:181);
u3r(182+90:361+90)=yd(1:180);
u3r(361+91:361+183)=yd(1:93);
u3=u3r;
omega=2*pi*20e3*(ko-1);

xn(1:80)=0.125e-2*3/2:0.125e-2:10e-2+0.125e-2/2;
yn=-10e-2+0.125e-2*3/2:0.125e-2:10e-2+0.125e-2/2;
[xn1,yn1]=meshgrid(xn,yn);

%Actuator half-size along x1 and x2 directions
a1=0.005;
a2=0.005;

for x1i=4:80
for x1j=1:160
u3f(x1i,x1j,ko)=0.;
x1=0.125e-2*x1i+0.125e-2/2;
x2=0.125e-2*x1j+0.125e-2/2-10e-2;
angc=atan2((x2-a2),(x1-a1));
r=((x1-a1)^2+(x2-a2)^2)^0.5;
kin=round((angc-pi/2)*180/pi)+181+90;
kfin=round((angc+pi/2)*180/pi)+181+90;
for k=kin:kfin
xi=omega/cp(k);
ang=angle1(k);
u3f(x1i,x1j,ko)=u3f(x1i,x1j,ko)+u3(k)*exp(-i*xi*r*cos(angc-ang))/(cos(ang)*sin(ang));
end
angc=atan2((x2+a2),(x1-a1));
r=((x1-a1)^2+(x2+a2)^2)^0.5;
kin=round((angc-pi/2)*180/pi)+181+90;
kfin=round((angc+pi/2)*180/pi)+181+90;
for k=kin:kfin
xi=omega/cp(k);

```

```

ang=angle1(k);
u3f(x1i,x1j,ko)=u3f(x1i,x1j,ko)-u3(k)*exp(-i*xi*r*cos(angc-ang))/(cos(ang)*sin(ang));
end
angc=atan2((x2-a2),(x1+a1));
r=((x1+a1)^2+(x2-a2)^2)^0.5;
kin=round((angc-pi/2)*180/pi)+181+90;
kfin=round((angc+pi/2)*180/pi)+181+90;
for k=kin:kfin
xi=omega/cp(k);
ang=angle1(k);
u3f(x1i,x1j,ko)=u3f(x1i,x1j,ko)-u3(k)*exp(-i*xi*r*cos(angc-ang))/(cos(ang)*sin(ang));
end
angc=atan2((x2+a2),(x1+a1));
r=((x1+a1)^2+(x2+a2)^2)^0.5;
kin=round((angc-pi/2)*180/pi)+181+90;
kfin=round((angc+pi/2)*180/pi)+181+90;
for k=kin:kfin
xi=omega/cp(k);
ang=angle1(k);
u3f(x1i,x1j,ko)=u3f(x1i,x1j,ko)+u3(k)*exp(-i*xi*r*cos(angc-ang))/(cos(ang)*sin(ang));
end
end
end

for x1i=1:3
    x1i
    for x1j=1:77
        u3f(x1i,x1j,ko)=0.;
        x1=0.125e-2*x1i+0.125e-2/2;
        x2=0.125e-2*x1j+0.125e-2/2-10e-2;
        angc=atan2((x2-a2),(x1-a1));
        r=((x1-a1)^2+(x2-a2)^2)^0.5;
        kin=round((angc-pi/2)*180/pi)+181+90;
        kfin=round((angc+pi/2)*180/pi)+181+90;
        for k=kin:kfin
            xi=omega/cp(k);
            ang=angle1(k);
            u3f(x1i,x1j,ko)=u3f(x1i,x1j,ko)+u3(k)*exp(-i*xi*r*cos(angc-ang))/(cos(ang)*sin(ang));
        end
        angc=atan2((x2+a2),(x1-a1));
        r=((x1-a1)^2+(x2+a2)^2)^0.5;
        kin=round((angc-pi/2)*180/pi)+181+90;
        kfin=round((angc+pi/2)*180/pi)+181+90;
        for k=kin:kfin
            xi=omega/cp(k);
            ang=angle1(k);

```

```

u3f(x1i,x1j,ko)=u3f(x1i,x1j,ko)-u3(k)*exp(-i*xi*r*cos(angc-ang))/(cos(ang)*sin(ang));
end
angc=atan2((x2-a2),(x1+a1));
r=((x1+a1)^2+(x2-a2)^2)^0.5;
kin=round((angc-pi/2)*180/pi)+181+90;
kfin=round((angc+pi/2)*180/pi)+181+90;
for k=kin:kfin
xi=omega/cp(k);
ang=angle1(k);
u3f(x1i,x1j,ko)=u3f(x1i,x1j,ko)-u3(k)*exp(-i*xi*r*cos(angc-ang))/(cos(ang)*sin(ang));
end
angc=atan2((x2+a2),(x1+a1));
r=((x1+a1)^2+(x2+a2)^2)^0.5;
kin=round((angc-pi/2)*180/pi)+181+90;
kfin=round((angc+pi/2)*180/pi)+181+90;
for k=kin:kfin
xi=omega/cp(k);
ang=angle1(k);
u3f(x1i,x1j,ko)=u3f(x1i,x1j,ko)+u3(k)*exp(-i*xi*r*cos(angc-ang))/(cos(ang)*sin(ang));
end
end
end

for x1i=1:3
    x1i
    for x1j=84:160
        u3f(x1i,x1j,ko)=0.;
        x1=0.125e-2*x1i+0.125e-2/2;
        x2=0.125e-2*x1j+0.125e-2/2-10e-2;
        angc=atan2((x2-a2),(x1-a1));
        r=((x1-a1)^2+(x2-a2)^2)^0.5;
        kin=round((angc-pi/2)*180/pi)+181+90;
        kfin=round((angc+pi/2)*180/pi)+181+90;
        for k=kin:kfin
            xi=omega/cp(k);
            ang=angle1(k);
            u3f(x1i,x1j,ko)=u3f(x1i,x1j,ko)+u3(k)*exp(-i*xi*r*cos(angc-ang))/(cos(ang)*sin(ang));
        end
        angc=atan2((x2+a2),(x1-a1));
        r=((x1-a1)^2+(x2+a2)^2)^0.5;
        kin=round((angc-pi/2)*180/pi)+181+90;
        kfin=round((angc+pi/2)*180/pi)+181+90;
        for k=kin:kfin
            xi=omega/cp(k);
            ang=angle1(k);
            u3f(x1i,x1j,ko)=u3f(x1i,x1j,ko)-u3(k)*exp(-i*xi*r*cos(angc-ang))/(cos(ang)*sin(ang));
        end
    end
end

```

```

end
angc=atan2((x2-a2),(x1+a1));
r=((x1+a1)^2+(x2-a2)^2)^0.5;
kin=round((angc-pi/2)*180/pi)+181+90;
kfin=round((angc+pi/2)*180/pi)+181+90;
for k=kin:kfin
xi=omega/cp(k);
ang=angle1(k);
u3f(x1i,x1j,ko)=u3f(x1i,x1j,ko)-u3(k)*exp(-i*xi*r*cos(angc-ang))/(cos(ang)*sin(ang));
end
angc=atan2((x2+a2),(x1+a1));
r=((x1+a1)^2+(x2+a2)^2)^0.5;
kin=round((angc-pi/2)*180/pi)+181+90;
kfin=round((angc+pi/2)*180/pi)+181+90;
for k=kin:kfin
xi=omega/cp(k);
ang=angle1(k);
u3f(x1i,x1j,ko)=u3f(x1i,x1j,ko)+u3(k)*exp(-i*xi*r*cos(angc-ang))/(cos(ang)*sin(ang));
end
end
end

```

```

%These lines are used to remove some numerical noise spikes
u3f(4,53+80:61+80,ko)=(u3f(3,53+80:61+80,ko)+u3f(5,53+80:61+80,ko))/2;
u3f(4,80-61:80-53,ko)=(u3f(3,80-61:80-53,ko)+u3f(5,80-61:80-53,ko))/2;
u3f(53:61,84,ko)=(u3f(53:61,85,ko)+u3f(53:61,83,ko))/2;
u3f(53:61,76,ko)=(u3f(53:61,75,ko)+u3f(53:61,77,ko))/2;
u3f(1:3,80-4,ko)=u3f(1:3,80-5,ko)+(u3f(1:3,80-2,ko)-u3f(1:3,80-5,ko))*1/3;
u3f(1:3,80-3,ko)=u3f(1:3,80-5,ko)+(u3f(1:3,80-2,ko)-u3f(1:3,80-5,ko))*2/3;
u3f1=real(u3f);

```

```

figure;
surf(xn,yn,u3f1(:,:,ko)/max(max(abs(u3f1(:,:,ko))))); colormap('jet'); shading interp; axis
equal; axis off; view(2); colorbar; %text(20,-10,titl,'FontSize',9); %title(titl); %
caxis(c2);caxis(c2);
end

```

```

u3f(:,:,18:32)=0;
u3fb(:,:,1:32)=u3f(:,:,1:32);

```

```

% Time vector
t=0:1.6e-6:4.96e-5;

```

```

% Excitation signal (3.5-cycle Hanning windowed toneburst)
y(1:12)=sin(2*pi*200e3*t(1:12)).*(1-cos(2*pi*200e3/3.5*t(1:12)))*0.5;
y(13:32)=0;

```

```

yf=fft(y);
for x1i=1:80
    for x1j=1:160
        for bl=5:17
            u3fte2(bl)=u3fb(x1i,x1j,bl);
        end
        u3fte2(18:32)=0;
        u3tn(x1i,x1j,:)=imag(iffit(u3fte2.*yf));
    end
end

% These points are set to zero to avoid comparison with FEM results very close to the
% actuator
% The discrete nodal shear forces in FEM cause spikes in its immediate vicinity
u3tn(4,77:84,:)=0; u3tn(1:4,84,:)=0; u3tn(1:4,77,:)=0;

[xno,yno]=meshgrid(xn,yn);
figure; surf(xno,yno,u3tn(:,i)'/max(max(max(abs(u3tn))))); axis equal; axis off;
colormap('jet'); shading interp; view(2); h=colorbar; set(h,'FontSize',20); %text(20,-
10,titl,'FontSize',9); %title(titl); % caxis(c2);caxis(c2);
%M(i)=getframe;
end
%movie2avi(M,'s0quasiiso200khzu3theo.avi','compression','None','Quality',100,'fps',1)

```

B.5 Using LastWave 2.0 for Chirplet Matching Pursuits

LastWave 2.0 [215], which is Linux-based freeware, can be downloaded from the website listed. If one is not comfortable in the Linux environment, a system administrator's support might be needed for installation. After installing it, the signal to be analyzed should be saved in the directory where the LastWave executable, "lw", is located. The signal's sampling rate should be such that the chosen scale l_0 (which has to be a power of 2 in the chirplet matching pursuit implemented in LastWave, e.g., 128, 256, 512, etc.) is about 20-30% samples more than the number of samples in the excitation signal toneburst. The Matlab command "resample" can be used to change the signal sampling rate. In addition, the signal file should be a text file with the data in a single column. For this demo, it is assumed that the filename is "testsignal.txt," the signal sampling rate is 0.1 μ s, the scale l_0 is 256, and that four atoms suffice to decompose the signal (this number may have to be revised till atoms below the preset energy threshold described in Chapter IV are obtained).

The LastWave program can be started by typing “lw” at the Linux prompt. At the resulting LastWave prompt, the sequence of commands listed below should be typed to produce an image showing the time-frequency plot of the individual chirplet atoms and to list the properties of the first two chirplet atoms:

```
wtrans a> m
```

```
book m> read 0 ('testsignal.txt')
```

```
book m> 0.dx=1e-7
```

```
book m> mpd 3 '-s' {256} '-O' {'chirp'}
```

```
book m> disp m
```

```
book m> print m[0][0]
```

```
book m> print m[1][0]
```

Further extensive documentation on LastWave is also available on their website.

REFERENCES

- [1] Carlos G.-C., Alan C., and Gordon A., "Health management and automation for future space systems," *Proceedings of the AIAA Space 2005 Conference and Exposition*, p. 1541-1557, Long Beach, CA, August 2005
- [2] Schoess J.N. and Zook J.D., "Test results of Resonant Integrated Microbeam Sensor (RIMS) for acoustic emission monitoring," *Proceedings of the SPIE Conference on Smart Electronics and MEMS*, v. 3328 , p. 326-332, 1998
- [3] Marantidis C., Van Way C.B., and Kudva J.N., "Acoustic-emission sensing in an on-board smart structural health monitoring system for military aircraft," *Proceedings of the SPIE Conference on Smart Structures and Integrated Systems*, v. 2191, p. 258-264, 1994
- [4] Seydel R.E. and Chang F.K., "Implementation of a real-time impact identification technique for stiffened composite panels," *Proceedings of the 2nd International Workshop on Structural Health Monitoring*, Stanford University, California, p. 225-233, 1999
- [5] Kollar L. and Steenkiste R.J., "Calculation of the stresses and strains in embedded fiber optic sensors," *Journal of Composite Materials*, v. 32, p. 1647-1679, 1998
- [6] Rees D., Chiu W.K., and Jones R., "A numerical study of crack monitoring in patched structures using a piezo sensor," *Smart Materials and Structures*, v. 1,p. 202-205, 1992
- [7] Chiu W.K., Galea S.C., Koss L.L., and Rajic N., "Damage detection in bonded repairs using piezoceramics," *Smart Materials and Structures*, v. 9, p. 466-475, 2000
- [8] Hautamaki C., Zurn S., Mantell S.C., and Polla D.L., "Experimental evaluation of MEMS strain sensors embedded in composites," *Journal of Microelectromechanical Systems*, v. 8, p. 272-279, 1999
- [9] Ellerbrock P., "DC-XA Structural Health Monitoring fiber-optic based strain measurement system," *Proceedings of the SPIE*, v. 3044, p. 207-218, 1997

- [10] Auld B.A., "Acoustic fields and waves in solids: Volumes I & II," 2nd ed., R.E. Kreiger Publishing Co., Florida, 1990
- [11] Graff K.F., *Wave motion in elastic solids*, Dover Publications, New York, 1991
- [12] Achenbach J.D., *Wave propagation in elastic solids*, North-Holland, New York, 1984
- [13] Rayleigh J.W.S., "On waves propagated along the plane surface of an elastic solid," *Proceedings of the London Mathematical Society*, v.17, p. 4-11, 1887
- [14] Love A.E.H., *Some problems of geodynamics*, Cambridge University Press, 1926
- [15] Stoneley R., "Elastic waves at the surface of separation of two solids," *Proceedings of the Royal Society of London, Series A*, v. 106, p. 416-428, 1924
- [16] Scholte J.G., "On the Stoneley wave equation," *Proc. Kon. Nederl. Akad. Wetensch*, v. 45 (20-5), p. 159-64, 1942
- [17] Lamb H., "On waves in an elastic plate," *Proceedings of the Royal Society of London Series A*, v. 93, p. 114-128, 1917
- [18] Gazis D.C., "Exact analysis of the plane-strain vibrations of thick-walled hollow cylinders," *Journal of the Acoustical Society of America*, v. 30, 786-794, 1958
- [19] Gazis, D.C., "Three-dimensional investigation of the propagation of waves in hollow circular cylinders," *Journal of the Acoustical Society of America*, v. 31, p. 568-578, 1959
- [20] Worlton D.C., "Experimental confirmation of Lamb waves at megacycle frequencies," *Journal of Applied Physics*, v. 32, p. 967-971, 1961
- [21] Wilcox P.D., Lowe M.J.S. and Cawley P., "Mode and transducer selection for long range Lamb wave inspection," *Journal of Intelligent Material Systems and Structures*, v. 12, p. 553-565, August 2001
- [22] Zhu W., Rose J.L., Barshinger J.N., and Agarwala V.S., "Ultrasonic guided wave NDT for hidden corrosion detection," *Research in Nondestructive Evaluation*, v. 10 (4), p. 205-225, 1998
- [23] Pelts S.P., Jiao D. and Rose J.L., "A comb transducer for guided wave generation and mode selection," *Proceedings of the IEEE Ultrasonics Symposium*, v. 2, p. 857-860, 1996
- [24] Alers G.A. and Burns L.R., "EMAT designs for special applications," *Materials*

Evaluation, v. 45, p. 1184-1194, 1987

- [25] Degerketin F.L. and Khuri-Yakub B.T., "Single mode Lamb wave excitation in thin plates by Hertzian contacts," *Applied Physics Letters*, v. 69(2), p.146-148, 1996
- [26] Pierce S.G. and Culshaw B., "Laser generation of ultrasonic Lamb waves using low power optical sources," *IEE Proceedings: Science, Measurement and Technology*, v 145 (5), p. 244-249, 1998
- [27] Monkhouse R.S.C., Wilcox P.D. and Cawley P., "Flexible interdigital PVDF transducers for the generation of Lamb waves in structures," *Ultrasonics*, v. 35, p. 489-498, 1997
- [28] Monkhouse R.S.C., Wilcox P.D., Lowe M.S.J., Dalton R.P., and Cawley P., "The rapid monitoring of structures using interdigital Lamb wave transducers," *Smart Materials and Structures*, v. 9, p. 304-309, 2000
- [29] Keilers, C. H. and Chang, F.-K., "Identifying delamination in composite Beam using built-in piezoelectrics," *Journal of Intelligent Material Systems and Structures*, v. 6, p. 647-672, 1995
- [30] Diaz Valdes S.H. and Soutis, C., "Health monitoring of composites using Lamb waves generated by piezoelectric devices," *Plastics, Rubber and Composites*, v. 29 (9), p. 475-481, 2000
- [31] Kessler S. and Spearing M., "Design of a piezoelectric-based structural health monitoring system for damage detection in composite materials," *Proceedings of the SPIE*, v. 4701, p. 86-96, 2002
- [32] Kehlenbach M. and Das S., "Identifying damage in plates by analyzing Lamb wave propagation characteristics," *Proceedings of the SPIE*, v. 4702, p. 364-375, 2002
- [33] Osmont D., Devillers D. and Taillade F., "Health monitoring of sandwich plates based on the analysis of the interaction of Lamb waves with damages," *Proceedings of the SPIE*, v. 4327, p. 290-301, 2001
- [34] Wilcox P., Lowe M., and Cawley P., "Lamb and SH wave transducer arrays for the inspection of large areas of thick plates," *Proceedings of the Review of Progress in Quantitative Nondestructive Evaluation*, Montreal, Canada, 25-30 Jun, eds. Thompson D.O. and Chimenti D.E., p. 1049-1056, 1999
- [35] Wilcox P., "Acoustic fields from PVDF interdigital transducers," *IEE*

- Proceedings: Science, Measurement and Technology*, v. 145 (5), p. 250-259, 1998
- [36] Badcock R.A. and Birt E.A., "The use of 0-3 piezocomposite embedded Lamb wave sensors for detection of damage in advanced fibre composites," *Smart Materials and Structures*, v. 9, p. 291-297, 2000
- [37] Egusa S. and Iwasawa N., "Piezoelectric paints as one approach to smart structural materials with health monitoring capabilities," *Smart Materials and Structures*, v. 7(4), 438-445, 1998
- [38] Hayward G., Hailu B., Farlow R., Gachagan A., and McNab A., "The design of embedded transducers for structural health monitoring applications," *Proceedings of the SPIE*, v. 4327, p. 312-323, 2001
- [39] Culshaw B., Pierce S.G. and Staszewski W.J., "Condition monitoring in composite materials: an integrated systems approach," *Proceedings of the Institution of Mechanical Engineers*, v. 212, part I, 1998
- [40] Gordon G.A. and Braunling R., "Quantitative corrosion monitoring and detection using ultrasonic lamb waves," *Proceedings of the SPIE*, v. 5765, p. 504-515, 2005
- [41] Bent A. A. and Hagood N. W., "Piezoelectric fiber composites with interdigitated electrodes," *Journal of Intelligent Material Systems and Structures*, v. 8(11), p. 903-919, 1997
- [42] Schulz M., Sundaresan M.J., Ghoshal A., and Pai P.F., "Active fiber composites for structural health monitoring," *Proceedings of the SPIE*, v. 3992, p. 13-24, 2000
- [43] Wilkie W.K., Bryant R.G., High J.W., Fox R.L., Hellbaum R.F., Jalink A., Little B.D., and Mirick P.H., "Low cost piezocomposite actuator for structural control applications," *Proceedings of the SPIE*, v. 3991, p. 323-334, 2000
- [44] Wilbur M.L., and Wilkie W.K., "Active-twist rotor control applications for UAVs," *Proceedings of the 24th Army Science Conference*, Paper ADM001736, Orlando, Florida, November 29 –December 2, 2004
- [45] Betz D.C., Thursby G., Culshaw B., and Staszewski W.J., "Lamb wave detection and source location using fiber Bragg grating rosettes," *Proceedings of the SPIE*, v. 5050, p. 117-127, 2003
- [46] Kwun H., Light G.M., Kim S.-Y., and Spinks R.L., "Magnetostrictive sensor for

- active health monitoring in structures,” *Proceedings of the SPIE*, v. 4702, p. 282-288, 2002
- [47] Varadan V.K., “Nanotechnology, MEMS and NEMS and their applications to smart systems and devices,” *Proceedings of the SPIE*, v. 5062, p. 20-43, 2003
- [48] Neumann J.J., Greve D.W. and Oppenheim I.J., “Comparison of piezoresistive and capacitive ultrasonic transducers,” *Proceedings of the SPIE*, v. 5391, p. 230-238, 2004
- [49] Schulz M.J., Kirikera G.R., Datta S., and Sundaresan M.J., “Piezoceramics and nanotubes for health monitoring,” *Proceedings of the SPIE*, v. 4702, p. 17-28, 2002
- [50] Lowe M., “Matrix techniques for modeling ultrasonic waves in multilayered media,” *IEEE Transactions on Ultrasonics, Ferroelectrics and Frequency Control*, v. 42(4), p. 525-542, 1995
- [51] Pavlakovic B. and Lowe M., *Disperse software manual Version 2.0.1 6B*, Imperial College, London, UK, 2003
- [52] Adamou A.T.I. and Craster R.V., “Spectral methods for modeling guided waves in elastic media,” *Journal of the Acoustical Society of America*, v. 116(3), p. 1524-1535, 2004
- [53] Kastrzhitskaya E.V. and Meleshko V.V., “Propagation of harmonic waves in an elastic rectangular waveguide,” *Soviet Applied Mechanics (English Translation of Prikladnaya Mekhanika)*, v. 26 (8), p. 773-781, 1991
- [54] Wilcox P., Evans M., Diligent O., Lowe M., and Cawley P., “Dispersion and excitability of guided acoustic waves in isotropic beams with arbitrary cross-section,” *Review of Quantitative Nondestructive Evaluation*, v. 21, eds. D. O. Thompson and D. E. Chimenti, p. 203-210, 2002
- [55] Mukdadi O.M., Desai Y.M., Datta S.K., Shah A.H., and Niklasson A.J., “Elastic guided waves in a layered plate with rectangular cross-section,” v. 112(5), p. 1766-1779, 2002
- [56] Bartoli I., Marzani A., Matt H., di Scalea F.L., and Viola E., “Modeling wave propagation in damped waveguides with arbitrary cross-section,” *Proc. of SPIE*, v. 6177, p. 61770A1-12, 2006
- [57] Viktorov I.A., *Rayleigh and Lamb waves*, Plenum Press, New York, 1967

- [58] Rose J.L., *Ultrasonic waves in solid media*, Cambridge University Press, 1999
- [59] Santosa F. and Pao Y.-H., "Transient axially asymmetric response of an elastic plate," *Wave Motion II*, v. 11, p. 271-295, 1989
- [60] Wilcox P., "Modeling the excitation of Lamb and SH waves by point and line sources," *Review of Quantitative Nondestructive Evaluation*, v. 23, eds. Thompson D.O. and Chimenti D.E., p. 206-213, 2004
- [61] Mal A.K., "Wave propagation in layered composite laminates under periodic surface loads," *Wave Motion*, v. 10, p. 257-266, 1988
- [62] Lih S.-S. and Mal A.K., "On the accuracy of approximate plate theories for wave field calculations in composite laminates," *Wave Motion*, v. 21, p. 17-34, 1995
- [63] Rose J.L., Pilarski A. and Ditri J.J., "An approach to guided wave mode selection for inspection of laminated plate," *Journal of Reinforced Plastics and Composites*, v. 12, p. 536-544, 1993
- [64] Kundu T., Potel C. and de Belleval J.F., "Importance of the near Lamb mode imaging of multilayered composite plates," *Ultrasonics*, v. 39, p. 283-290, 2001
- [65] Guo N. and Cawley P., "The interaction of Lamb waves with delaminations in composite laminates," *Journal of the Acoustical Society of America*, v. 94, p. 2240-2246, 1993
- [66] Alleyne D.N. and Cawley P., "The interaction of Lamb waves with defects," *IEEE Transactions on Ultrasonics, Ferroelectrics and Frequency Control*, v. 39 (3), p. 381-396, 1992
- [67] Maslov K. and Kundu T. "Selection of Lamb modes for detecting internal defects in composite laminates," *Ultrasonics*, v. 35, p. 141-150, 1997
- [68] McKeon J.C.P. and Hinders M.K., "Lamb wave scattering from a through hole," *Journal of Sound and Vibration*, v. 224 (5), p. 843-862, 1999
- [69] Meguid S.A. and Wang X.D., "Wave scattering from cracks and imperfectly bonded inhomogeneities in advanced materials," *Mechanics of Materials*, v. 31, p. 187-195, 1999
- [70] Al-Nassar Y.N., Datta S.K. and Shah A.H., "Scattering of Lamb waves by a normal rectangular strip weldment," *Ultrasonics*, v. 29(2), p. 125-132, 1991
- [71] Veksler N.D., "Phase velocities of Lamb-type and Stoneley-type waves in the problem of acoustic wave scattering by a hollow elastic sphere," *Akusticheskii*

Zurnal, v. 37 (1), p. 42-45,1991

- [72] Chang Z. and Mal A.K., “Scattering of Lamb waves from a rivet hole with edge cracks,” *Mechanics of Materials*, v. 31 (3), p. 197-204, 1999
- [73] Fromme, P., Wilcox, P., Lowe, M. and Cawley, P., “On the scattering and mode conversion of the A_0 Lamb wave mode at circular defects in plates,” *Review of Quantitative Nondestructive Evaluation*, v. 23, eds. D.O. Thompson and D.E. Chimenti, pp. 142-149, 2004
- [74] Lee B.C. and Staszewski W.J., “Modelling of Lamb waves for damage detection in metallic structures: Parts I & II,” *Smart Materials and Structures*, v. 12(5), p. 804-824, 2003
- [75] Liu T, Veidt M. and Kitipornchai S., “Single mode Lamb waves in composite laminated plates generated by piezoelectric transducers.” *Composite Structures*, v. 58(3), p. 381-396, 2002
- [76] Moulin E., Assaad J. and Delebarre C., “Modeling of Lamb waves generated by integrated transducers in composite plates using a coupled finite element–normal modes expansion method,” *Journal of the Acoustical Society of America*, v. 107 (1), p. 87-94, 2000
- [77] Duquenne L., Moulin E., Assaad J., and Grondel S., “Transient modeling of Lamb waves generated in viscoelastic materials by surface bonded piezoelectric transducers,” *Journal of the Acoustical Society of America*, v. 116 (1), p. 133-141, 2004
- [78] Glushkov E.V., Glushkova N.V., Seemann W. and Kvasha O.V., “Elastic wave excitation in a layer by piezoceramic patch actuators,” *Acoustical Physics*, v. 52(4), 2006
- [79] Veidt M., Liu T. and Kitipornchai S., “Experimental investigation of the acousto-ultrasonic transfer characteristics of adhesively bonded piezoceramic transducers,” *Smart Materials and Structures*, v. 9 (1), p. 19-23, 2000
- [80] Veidt M., Liu T. and Kitipornchai S., “Flexural waves transmitted by rectangular piezoceramic transducers,” *Smart Materials and Structures*, v. 10(4), p. 681-688, 2001
- [81] Lin X. and Yuan F. G., “Diagnostic Lamb waves in an integrated piezoelectric sensor/actuator plate: analytical and experimental studies,” *Smart Materials and Structures* v. 10, p. 907–913, 2001

- [82] Rose L.R.F. and Wang C.H., "Mindlin plate theory for damage detection: Source solutions," *Journal of the Acoustical Society of America*, v. 116 (1), p. 154-171, 2004
- [83] Giurgiutiu V., "Lamb wave generation with piezoelectric wafer active sensors for structural health monitoring," *Proceedings of the SPIE*, v. 5056, p. 111-122, 2003
- [84] Bottai G.S., Chrysochoidis N.A., Giurgiutiu V., and Saravanos D.A., "Analytical and experimental evaluation of piezoelectric wafer active sensors for Lamb waves based structural health monitoring in composite laminates," *Proceedings of the SPIE*, v. 6532, p. 65320N-1-N-12, 2007
- [85] Crawley E.F. and de Luis J., "Use of piezoelectric actuators as elements of intelligent structures," *AIAA Journal*, v. 25 (10), 1373-1385, Oct 1987
- [86] Staszewski W. and Worden K., "Signal processing for damage detection," book chapter in *Health Monitoring of Aerospace Structures*, eds. Staszewski W., Boller C. and Tomlinson G., p. 163-206, John Wiley & Sons, UK, 2004
- [87] Yu L., Bao J. and Giurgiutiu V., "Signal processing techniques for damage detection with piezoelectric wafer active sensors and embedded ultrasonic structural radar," *Proceedings of the SPIE*, v. 5391, p. 492-503, 2004
- [88] Rizzo P. and di Scalea F.L., "Discrete wavelet transform to improve guided wave-based health monitoring of tendons and cables," *Proceedings of the SPIE*, v. 5391, p. 523-532, 2004
- [89] Kercel S.W., Klein M.B. and Pouet B., "Wavelet and wavelet-packet analysis of Lamb-wave signatures in laser ultrasonics," *Proceedings of the SPIE*, v. 4056, p. 308-317, 2000
- [90] Hamming R.W., "Digital filters," 3rd ed., Prentice Hall, Englewood Cliffs, USA, 1989
- [91] Staszewski W., "Advanced data pre-processing for damage identification based on pattern recognition," *International Journal of Systems Science*, v. 31(11), p. 1381-1396, 2000
- [92] Prasad M.S., Kumar V.R., Balasubramaniam K., and KrishnaMoorthy C.V., "Imaging of defects in composite structures using guided ultrasonics," *Proceedings of the SPIE*, v. 5062, p. 700-703, 2003
- [93] Ihn J.-B. and Chang F.-K., "Detection and monitoring of hidden fatigue crack growth using a built-in piezoelectric sensor/actuator network: I. Diagnostics,"

Smart Materials and Structures, v. 13, 609-620, 2004

- [94] Prosser W.H., Seale M.D. and Smith B.T., "Time-frequency analysis of the dispersion of Lamb modes," *Journal of the Acoustical Society of America*, v. 105 (5), 2669-2676, 1999
- [95] Niethammer M., Jacobs L., Qu J., and Jarzynski J., "Time frequency representations of Lamb waves," *Journal of the Acoustical Society of America*, v. 109(5), p. 1841-1847, 2001
- [96] Kuttig H., Niethammer M., Hurlebaus S., and Jacobs L.J., "Model-based analysis of dispersion curves using chirplets," *Journal of the Acoustical Society of America*, v. 119(4), 2006
- [97] Hong J.-C., Sun K.H., and Kim Y.Y., "Dispersion-based short-time Fourier transform applied to dispersive wave analysis," *Journal of the Acoustical Society of America*, v. 117, p. 2949-2960, 2005
- [98] Oseguda R., Kreinovich V., Nazarian S., and Roldan E., "Detection of cracks at rivet holes in thin plates using Lamb-wave scanning," *Proceedings of the SPIE*, v. 5047, p. 55-66, 2003
- [99] Quek S.T., Tua P.S. and Wang Q., "Detecting anomalies in beams and plate based on the Hilbert-Huang transform of real signals," *Smart Materials and Structures*, v 12 (3), p. 447-460, 2003
- [100] Salvino L., Purekar A. and Pines D., "Health Monitoring of 2-D Plates Using EMD and Hilbert Phase," *Proc. Fourth International Workshop on Structural Health Monitoring*, Stanford University, California, Sept. 12-14, 2005
- [101] Kerckel S., Klein M. and Pouet B., "Bayesian separation of Lamb wave signatures in laser ultrasonics," *Proceedings of the SPIE*, v. 4055, p. 350-361, 2000
- [102] Staszewski W.J., "Wavelet based compression and feature selection for vibration analysis," *Journal of Sound and Vibration*, v. 211(5), p. 735-760, 1998
- [103] Mallat S., *A wavelet tour of signal processing*, Academic Press, California, USA, 1998
- [104] Rao R.M. and Bopardikar A.S., *Wavelet transforms*, Addison-Wesley, California, USA, 1998
- [105] Strang G. and Nguyen T., *Wavelets and filter banks*, Wellesley-Cambridge, 1997
- [106] Paget C.A., Grondel S., Levin K. and Delebarre C., "Damage assessment in

- composites by Lamb waves and wavelet coefficients,” *Smart Materials and Structures*, v. 12, p. 393-402, 2003
- [107] Lefebvre J.P. and Lasaygues P., “Wavelet analysis for ultrasonic crack detection and modelization,” *Proceedings of the IEEE Ultrasonics Symposium*, v. 2, p. 1143-1146, 1994
- [108] Sohn H., Park G., Wait J.R., Limback N.P., and Farrar C.R., “Wavelet based active sensing for delamination detection in composite structures,” *Smart Materials and Structures*, v. 13, p. 153-160, 2004
- [109] Lemistre M. and Balageas D., “Structural health monitoring system based on diffracted Lamb wave analysis by multiresolution processing,” *Smart Materials and Structures*, v. 10, p. 504-511, 2001
- [110] Sun Z., Mao Y., Jiang W., and Zhang D., “Investigation on interaction of Lamb waves and circumferential notch in pipe by means of wavelet transform,” *Proceedings of the IEEE Ultrasonics Symposium*, v. 1, p. 827-830, 2000
- [111] Legendre S., Massicotte D., Goyette J., and Bose T.K., “Neural classification of Lamb wave ultrasonic weld testing signals using wavelet coefficients,” *IEEE Transactions on Instrumentation and Measurement*, v. 50 (3), p. 672-678, 2001
- [112] Mallat S. and Zhang Z., “Matching pursuits with time-frequency dictionaries,” *IEEE Transactions on Signal Processing*, v. 41(12), 3397-3415, 1993
- [113] Qian S. and Chen D., “Signal representation via adaptive normalized Gaussian functions,” *Signal Processing*, v. 36(1), 1-11, 1994
- [114] Zhang G., Zhang S. and Wang Y., “Application of adaptive time-frequency decomposition in ultrasonic NDE of highly scattering materials,” *Ultrasonics*, v. 38, 961-964, 2000
- [115] Hong J.-C., Sun K.H. and Kim Y.Y., “The matching pursuit approach based on the modulated Gaussian pulse for efficient guided wave inspection,” *Smart Materials and Structures*, v. 14, 548-560, 2005
- [116] Gribonval R., “Fast matching pursuit with a multiscale dictionary of Gaussian chirps,” *IEEE Transactions on Signal Processing*, v. 49 (5), 994-1001, 2001
- [117] Alleyne D. and Cawley P., “A two dimensional Fourier transform method for the quantitative measurement of Lamb modes,” *Proceedings of the IEEE Ultrasonics Symposium*, v. 2, p. 1143-1146, 1990

- [118] El Youbi F., Grondel S. and Assaad J., "Signal processing for damage detection using two different array transducers," *Ultrasonics*, v. 42, p. 803-806, 2004
- [119] Martinez L., Morvan B., Izbicki J.L., "Space-time-wavenumber-frequency $Z(x,t,k,f)$ analysis of SAW generation on fluid filled cylindrical shells," *Ultrasonics*, v. 42, p. 383-389, 2004
- [120] Lin X. and Yuan F. G., "Detection of multiple damages by prestack reverse-time migration," *AIAA Journal*, v. 39, n. 11, Nov. 2001
- [121] Sundararaman S., Adams D.E. and Rigas E.J., "Structural damage identification in homogeneous and heterogeneous structures using beamforming," *Structural Health Monitoring: An International Journal*, v. 4(2), p. 171-190, 2005
- [122] Giurgiutiu V. and Bao J., "Embedded ultrasonic structural radar with piezoelectric wafer active sensors for the NDE of thin-wall structures," IMECE2002-33873, *Proc. of IMECE 2002: 2002 ASME International Mechanical Engineering Congress*, New Orleans, Louisiana, Nov. 17-22, 2002
- [123] Purekar A. and Pines D., "Damage interrogation using a phased piezoelectric sensor/actuator array: simulation results on two dimensional isotropic structures," *Proceedings of the 44th AIAA/ASME/ASCE/AHS Structures, Structural Dynamics, and Materials Conference*, Norfolk, Virginia, Paper 2003-1565, 7-10 Apr. 2003
- [124] Moulin E., Bourasseau N., Assaad J., and Delebarre C., "Lamb wave beam-steering for integrated health monitoring applications," *Proceedings of the SPIE*, v. 5046, p. 124-131, 2003
- [125] Haykin S., *Neural networks: a comprehensive foundation*, Macmillan College Publishing, New York, USA, 1994
- [126] Su Z. and Ye L., "An intelligent signal processing and pattern recognition technique for defect identification using an active sensor network," *Smart Materials and Structures*, v. 13, p. 957-969, 2004
- [127] Challis R.E., Bork U. and Todd P.C.D., "Ultrasonic NDE of adhered T-joints using Lamb waves and intelligent signal processing," *Ultrasonics*, v. 34, p. 455-459, 1996
- [128] Zhao X., Kwan C., Xu R., Qian T., Hay T., Rose J.L., Raju B.B., Maier R., and Hexemer R., "Non destructive inspection of metal matrix composites using guided waves," *Review of Quantitative Nondestructive Evaluation*, v. 23, eds.

Thompson D.O. and Chimenti D.E., p. 914-920, 2004

- [129] Wang C.H., Rose J.T. and Chang F-K, "A computerized time-reversal method for structural health monitoring," *Proceedings of the SPIE*, v. 5046, p. 48-58, 2003
- [130] Ing R.K. and Fink M., "Time recompression of dispersive Lamb waves using a time reversal mirror – Application to flaw detection in thin plates," *Proceedings of the IEEE Ultrasonics Symposium*, v.1, p. 659-663, 1996
- [131] Sohn H., Park H., Law K.H. and Farrar C.R., "Instantaneous online monitoring of unmanned aerial vehicles without baseline signals," *Proceedings of the SEM International Modal Analysis Conference XXIII*, Paper 259, Orlando, Florida, 2005
- [132] Alleyne D.N., Pialucha T.P. and Cawley P., "A signal regeneration technique for long-range propagation of dispersive Lamb waves," *Ultrasonics*, v. 31(3), p. 201-204, 1993
- [133] Kehlenbach M. and Hanselka H., "Automated structural integrity monitoring based on broadband Lamb wave excitation and matched filtering," *Proceedings of the 44th AIAA/ASME/ASCE/AHS Structures, Structural Dynamics and Materials Conference*, Paper AIAA2003-1563, 7-10 Apr, Virginia, USA, 2003
- [134] Lin M., Qing X., Kumar A., and Beard S.J., "SMART layer and SMART suitcase for structural health monitoring applications," *Proceedings of the SPIE*, v. 4332, p. 98-106, 2001
- [135] Kessler S.S., Spearing M.S., Shi Y., and Dunn C., "Packaging of structural health monitoring components," *Proceedings of the SPIE*, v. 5391, p. 219-229, 2004
- [136] Chambers J., Wardle B. and Kessler S., "Durability assessment of Lamb-wave based structural health monitoring nodes," *Proc. 47th AIAA/ASME/ASCE/AHS/ASC Structures, Structural Dynamics, and Materials Conference 14th AIAA/ASME/AHS Adaptive Structures Conference* Paper # AIAA-2006-2263, Newport, Rhode Island, May 1-4, 2006
- [137] Yang J., Chang F.-K., and Derriso M.M., "Design of a built-in health monitoring system for thermal protection panels," *Proceedings of the SPIE*, v. 5046, p. 59-70, 2003
- [138] Lalande F., Chaudhry Z. and Rogers C., "A simplified geometrically nonlinear approach to the analysis of the Moonie actuator," *IEEE Transactions on Ultrasonics, Ferroelectrics and Frequency Control*, v. 42 (1), p. 21-27, 1995

- [139] Haertling, G. H. "Rainbow actuators and sensors: a new smart technology," *Proceedings of the SPIE*, v. 3030, p. 81-92, 1997
- [140] Kugel V. D., Chandran S. and Cross L.E., "A comparative analysis of piezoelectric bending-mode actuators," *Proceedings of the SPIE*, v. 3040, p. 70-80, 1997
- [141] Mossi K.M. and Bishop R.P., "Characterization of different types of high performance THUNDER actuators," *Proceedings of the SPIE*, v. 3675, p. 43-52, 1999
- [142] Pretorius J., Hugo M. and Spangler R., "A comparison of packaged piezoactuators for industrial applications," *Proceedings of the SPIE*, v. 5388, p. 131-142, 2004
- [143] Niezrecki C., Brei D., Balakrishnan S., and Moskalik A., "Piezoelectric actuation: state of the art," *The Shock and Vibration Digest*, v. 33(4), p. 269-280, 2001
- [144] Gorinevsky D., Gordon G.A., Beard S., Kumar A., and Chang F.-K., "Design of integrated SHM system for commercial aircraft applications," *Proceedings of the 5th International Workshop on Structural Health Monitoring*, p. 881-888, Stanford, California, 2005
- [145] Kim H. and Lee K., "Diagnostic network patch system for SHM and intelligent infrastructure," *Proceedings of the SEM International Modal Analysis Conference XXIII*, Paper 274, Orlando, Florida, 2005
- [146] Kim J.S., Vinoy K.J. and Varadan V.K., "Wireless health monitoring of cracks in structures with MEMS-IDT sensors," *Proceedings of the SPIE*, v. 4700, p. 342-353, 2002
- [147] Hay T.R. and Rose J.L., "Interfacing guided wave ultrasound with wireless technology," *Proceedings of the SPIE*, v. 5391, p. 314-320, 2004
- [148] Glaser S.D., "Some real world applications of wireless sensor nodes," *Proceedings of the SPIE*, v. 5391, p. 344-355, 2004
- [149] Ihler E., Zaglauer H.W., Herold-Schmidt U., Dittrich K.W., and Wiesbeck W., "Integrated wireless piezoelectric sensors," *Proceedings of the SPIE*, v. 3991, p. 44-51, 2000
- [150] Lynch J.P., Sundararajan A., Law K.H., Kiremidjian A.S., and Carryer E., "Embedding damage detection algorithms in a wireless sensing unit for operating power efficiency," *Smart Materials and Structures*, v. 13, p. 800-810, 2004

- [151] Lynch J.P. and Loh K.J., "A summary review of wireless sensors and sensor networks for structural health monitoring," *The Shock and Vibration Digest*, v. 38 (2), p. 91-128, 2006
- [152] Sodano H.A., Inman D.J. and Park G., "A review of power harvesting from vibration using piezoelectric materials," *The Shock and Vibration Digest*, v. 36 (3), p. 197-205, 2004
- [153] Schulz M.J., Sundaresan M.J., Mcmichael J., Clayton D., Sadler R., and Nagel B., "Piezoelectric materials at elevated temperature," *Journal of Intelligent Material Systems and Structures*, v. 14(11), p. 693-705, 2003
- [154] Lee B.C., Manson B. and Staszewski W.J., "Environmental effects on Lamb wave responses from piezoceramic sensors," *Materials Science Forum*, v 440-441, p. 195-202, 2003
- [155] Lu Y. and Michaels J.E., "A methodology for structural health monitoring with diffuse ultrasonic waves in the presence of temperature variations," *Ultrasonics*, v. 43, p. 713-731, 2005
- [156] Konstantinidis G., Drinkwater B.W., and Wilcox P.D., "The temperature stability of guided wave structural health monitoring systems," *Smart Materials and Structures*, v. 15, p. 967-976, 2006
- [157] Blaise E. and Chang F.-K., "Built-in diagnostics for debonding in sandwich structures under extreme temperatures," *Proceedings of the 3rd International Workshop on Structural Health Monitoring*, p. 154-163, Stanford, California, USA, 2001
- [158] Paget C.A., Levin K. and Delebarre C., "Behavior of an embedded piezoceramic transducer for Lamb wave generation in mechanical loading," *Proceedings of the SPIE*, v. 3985, p. 510-520, 2000
- [159] Biemans C., Staszewski W.J., Boller C. and Tomlinson G.R., "Crack detection in metallic structures using broadband excitation of acousto-ultrasonics," *Journal of Intelligent Material Systems and Structures*, v. 12, p. 589-597, 2001
- [160] Manson G., Pierce G., Worden K., Monnier T., Guy P., and Atherton K., "Long-term stability of normal condition data for novelty detection," *Proceedings of the SPIE*, v. 3985, p. 323-334, 2000
- [161] Manson G., Pierce G. and Worden K., "On the long-term stability of normal condition for damage detection in a composite panel," *Key Engineering*

Materials, v. 204-205, p. 359-370, 2001

- [162] Giurgiutiu V., Lin B. and Bost J., “Durability and survivability of piezoelectric wafer active sensors for structural health monitoring using the electromechanical impedance technique,” *Proceedings of the ASME International Mechanical Congress*, Paper # IMECE2004-60974, Anaheim, California, 2004
- [163] Blackshire J.L, Giurgiutiu V., Cooney A. and Doane J., “Characterization of sensor performance and durability for structural health monitoring,” *Proceedings of the SPIE 12th Symposium on Smart Structures and Materials*, Paper # 5770-08, San Diego, California, 2005
- [164] Doane J. and Giurgiutiu V., “An initial investigation of the large strain and fatigue loading behavior of piezoelectric wafer active sensors,” *Proceedings of the SPIE 12th Symposium on Smart Structures and Materials*, Paper # 5765-130, 2005
- [165] “Aviation Accident Report,” NTSB\AAR-89/03, National Transport Safety Board, Washington, USA, 1989
- [166] NASA “Columbia Accident Investigation Board Report,” U.S. Government Printing Office, Washington, USA, 2003
- [167] Derriso M.M., Faas P., Calcaterra J., Barnes J.H., and Sotomayer W., “Structural health monitoring for current and future aerospace vehicles,” *Proceedings of the 3rd International Workshop on Structural Health Monitoring*, p. 3-11, Stanford, California, USA, 2001
- [168] Huang J.Q., “Structural health monitoring for reusable launch vehicles – an integrated system and process approach,” *Proceedings of the 3rd International Workshop on Structural Health Monitoring*, p. 113-122, Stanford, California, USA, 2001
- [169] Dalton R.P., Cawley P. and Lowe M.S.J., “The potential of guided waves for monitoring large areas of metallic aircraft fuselage structure,” *Journal of Nondestructive Evaluation*, v. 20 (1), p. 29-46, 2001
- [170] Giurgiutiu V., Zagrai A., Bao J.J., Redmond J.M., Roach D., and Rackow K., “Active sensors for health monitoring of aging aerospace structures,” *International Journal of COMADEM*, v. 6(1), p. 3-21, 2003
- [171] Grondel S., Assaad J., Delebarre C., and Moulin E., “Health monitoring of a composite wingbox structure,” *Ultrasonics*, v. 42, p. 819-824, 2004

- [172] Koh Y.L., Chiu W.K. and Rajic N., "Integrity assessment of composite repair patch using propagating Lamb waves," *Composite Structures*, v. 58(3), p. 363-371, 2002
- [173] Matt H., Marzani A., Restivo G., Oliver J., di Scalea F.L., Kosmatka J., Sohn H., Park G. and Farrar C., "A guided-wave system for monitoring the wing skin-to-spar bond in unmanned aerial vehicles," *Proceedings of the SEM International Modal Analysis Conference XXIII*, Paper 105, Orlando, Florida, 2005
- [174] Blaise E. and Chang F.-K., "Built-in damage detection system for sandwich structures under cryogenic temperatures," *Proceedings of the SPIE*, v. 4701, p. 97-107, 2002
- [175] Derriso M.M., Olson S., Braisted W., DeSimio M., Rosenstengel J., and Brown K., "Detection of fastener failure in a thermal protection system," *Proceedings of the SPIE*, v. 5390, p.585-596, 2004
- [176] Lin M., Kumar A., Qing X., Beard B.J., Russell S.S., Walker J.L., and Delay T.K., "Monitoring the integrity of filament wound structures by built-in sensor networks," *Proceedings of the SPIE*, v. 5054, p. 222-229, 2003
- [177] Lakshmanan K.A. and Pines D.J., "Modeling damage in rotorcraft flexbeams using wave mechanics," *Smart Materials and Structures*, v. 6, p.383-392, 1997
- [178] Chong K.P., Carino N.J. and Washer G., "Health monitoring of civil infrastructures," *Smart Materials and Structures*, v. 12, p. 483-493, 2003
- [179] Shiba K., Kumagai H., Watanabe K., Naruse H., and Ohno H., "Fiber optic distributed sensor for monitoring of concrete structures," *Proceedings of the 3rd International Workshop on Structural Health Monitoring: The Demands and Challenges*, Stanford University, USA, p. 459-468, Sep 2001
- [180] Livingston R.A. and Jin S., "Computational structural mechanics assessment of large-scale fiber optic sensor networks on highway bridges for evaluating damage detection algorithms," *Proceedings of the 3rd International Workshop on Structural Health Monitoring: The Demands and Challenges*, Stanford University, USA, p. 508-516, Sep 2001
- [181] Tennyson R.C., Mufti A.A., Rizkalla S., Tadros G., and Benmokrane B., "Structural health monitoring of innovative bridges in Canada with fiber optic sensors," *Smart Materials and Structures*, v. 10(3), p. 560-573, 2001
- [182] Li H.-N., Li D.-S. and Wang S.-Y., "Study and application of health monitoring by fiber optic sensors in civil engineering," *American Society of Mechanical*

Engineers, Pressure Vessels and Piping Division (Publication) PVP, v. 468, p. 217-224, 2003

- [183] Khazem D.A., Kwun H., Kim S.-Y., and Dynes C., “Long-range inspection of suspender ropes in suspension bridges using the magnetostrictive sensor technology,” *Proceedings of the 3rd International Workshop on Structural Health Monitoring: The Demands and Challenges*, Stanford University, USA, p. 384-392, Sep 2001
- [184] Wu F. and Chang F.-K., “Diagnosis of debonding in steel-reinforced concrete with embedded piezoelectric elements,” *Proceedings of the 3rd International Workshop on Structural Health Monitoring: The Demands and Challenges*, Stanford University, USA, p. 670-679, Sep 2001
- [185] Lovell P.A. and Pines D.J., “Damage assessment in a bolted lap joint,” *Proceedings of the SPIE*, v. 3325, p. 112-126, 1998
- [186] Lin M., Kumar A., Qing X. and Beard S.J., “Advances in utilization of structurally integrated sensor networks for health monitoring in composite applications,” *Proceedings of the SPIE*, v. 4701, p. 167-176, 2002
- [187] Panajott A.V., “The structural health monitoring process at BMW,” *Proceedings of the 3rd International Workshop on Structural Health Monitoring: The Demands and Challenges*, Stanford University, USA, p. 703-712, Sep 2001
- [188] Na W.-B. and Kundu T., “Underwater pipeline inspection using guided waves,” *ASME Journal of Pressure Vessel Technology*, v. 124, p. 196-200, 2002
- [189] Hegeon K., Sang K.Y., and Glenn M.L., “The magnetostrictive sensor technology for long range guided wave testing and monitoring of structures,” *Materials Evaluation*, v. 61(1), p. 80-84, 2003
- [190] Park J.-S., Kim Y.H., Song S.-J., Kim J.-H., Eom H.-S., and Im K.-S., “Towards active monitoring of piping using ultrasonic guided waves,” *Review of Quantitative Nondestructive Evaluation*, v. 23, p. 181-186, 2004
- [191] Hay T.R. and Rose J.L., “Flexible PVDF comb transducers for excitation of axisymmetric guided waves in pipe,” *Sensors and Actuators A (Physical)*, v. A100 (1), p. 18-23, 2002
- [192] Wang W.D., “Applications of guided wave techniques in the petrochemical industry,” *Review of Progress in Quantitative Nondestructive Evaluation*, v. 18A, eds. Thompson D.O. and Chimenti D.E., p. 277-284, Plenum Press, New York,

USA, 1999

- [193] Ghoshal A., Sundaresan M.J., Schulz M.J., and Pai P.F., “Structural health monitoring techniques for wind turbine blades,” *Journal of Wind Engineering and Industrial Aerodynamics*, v. 85, p. 309-324, 2000
- [194] Jones R., Wallbrink C., Tan M., Reichl P., and Dayawansa D., “Health monitoring of draglines using ultrasonic waves,” *Engineering Failure Analysis*, v. 11, p. 257-266, 2004
- [195] Kessler S.S. and Spearing S.M., “Design of a piezoelectric-based structural health monitoring for damage detection in composite materials,” *Proceedings of the SPIE*, v. 4701, p. 86-96, 2002
- [196] Mal A.K., Banerjee S. and Ricci F., “Automated structural health monitoring system using acoustic emission and modal data,” *Proceedings of the SPIE*, v. 5394, p. 1-10, 2004
- [197] Giurgiutiu V., Zagari A. and Bao J., “Damage identification in aging aircraft structures with piezoelectric wafer active sensors,” *Journal of Intelligent Material Systems and Structures*, v. 15, p. 673-687, 2004
- [198] Osmont D. Dupont M., Gouyon R., Lemistre M., and Balageas D., “Piezoelectric transducer network for dual mode (active/passive) detection, localization, and evaluation of impact damages in carbon/epoxy composite plates,” *Proceedings of the SPIE*, v. 4073, p. 130-137, 2000
- [199] Wait J.R., Park G., Sohn H., and Farrar C.R., “Plate damage identification using wave propagation and impedance methods,” *Proceedings of the SPIE*, v. 5394, p. 53-65, 2004
- [200] Monnier T., Jayet Y., Guy P., and Baboux J.C., “Aging and damage assessment of composite structures using embedded piezoelectric sensors,” *Review of Progress in Quantitative NDE*, v. 19, eds. D.O. Thompson and D.E. Chimenti, p. 1269-76, Plenum Press, New York, 2000
- [201] Blanas P. and Das-Gupta D.K., “Composite piezoelectric sensors for smart composite structures,” *Proceedings of the 10th International IEEE Symposium on Electrets*, p. 731-734, 1999
- [202] González A. and Alemany C., “Determination of the frequency dependence of characteristic constants in lossy piezoelectric materials,” *Journal of Physics D: Applied Physics*, v 29 (9), p. 2476-2482, 1996

- [203] Brown J.W. and Churchill R.V., *Complex variables and applications*, 7th ed., McGraw-Hill, New York, 2004
- [204] Miklowitz J., *The theory of elastic waves and waveguides*, North Holland, New York, 1978
- [205] *ABAQUS/Standard user's manual Version 6.2*, Hibbitt, Karlsson and Sorensen, Inc., Rattuck, Rhode Island, USA, 2001
- [206] *IEEE Standard on Piezoelectricity ANSI/IEEE Std 176-1987*, The Institute of Electrical and Electronics Engineers Inc., New York, 1988
- [207] Jordan T., Ounaies Z., Tripp J. and Tchong P., "Electrical properties and power considerations of a piezoelectric actuator," NASA CR-2000-209861/ ICASE Report No. 2000-8, 2000
- [208] Thomas D.T., Welter J.T., and Giurgiutiu V., "Corrosion damage detection with piezoelectric wafer active sensors", *Proc. SPIE Symposium on Smart Structures/NDE*, v. 5394, p. 11-22, San Diego, U.S.A., 2004
- [209] Jones R., Wallbrink C., Tan M., Reichl P., and Dayawansa D., "Health monitoring of draglines using ultrasonic waves," *Engineering Failure Analysis*, v. 11, p. 257-266, 2004
- [210] Papoulis A., *Signal Analysis*, McGraw-Hill, New York, 1984
- [211] Cohen L., *Time-frequency analysis*, Prentice Hall, Englewood Cliffs, New Jersey, 1995
- [212] Mallat S., *A wavelet tour of signal processing*, Academic Press, San Diego, California, 1999
- [213] Bracewell R., *The Fourier transform and its applications*, 3rd edition, McGraw-Hill, New York, 2000
- [214] Hong J.-C., Sun K.H. and Kim Y.Y., "Waveguide damage detection by the matching pursuit approach employing the dispersion-based chirp functions," *IEEE Transactions on Ultrasonics, Ferroelectrics, and Frequency Control*, v. 53(3), p. 592-605, 2006
- [215] Bacry E., *LastWave 2.0* software, <http://www.cmap.polytechnique.fr/~bacry/LastWave>, downloaded in July 2005
- [216] Pines D.J. and Cesnik C.E.S., Private communication concerning collaboration on NASA Constellation University Institutes Project, August 2004

- [217] *NASA's Exploration Systems Architecture Study Final Report*, NASA-TM-2005-214062, NASA Space Transportation Information Network, November 2005
- [218] Myers D.E., Martin C.J., and Blosser M.L., "Parametric weight comparison of advanced metallic, ceramic tile, and ceramic blanket thermal protection systems," NASA-TM-2000-210289, NASA Center for Aerospace Information, June 2000
- [219] Larson W.J. and Wertz J.R., *Space system design and analysis*, 2nd ed., Microcosm, California/Kluwer Academic, The Netherlands, 1995
- [220] 10-3004 adhesive technical datasheet, <http://www.epoxies.com>, Epoxies Etc., Cranston, RI, 2006
- [221] Epoxies 301 and 353ND technical datasheets, <http://www.epotek.com>, Epoxy Technology, Billerica, MA, 2006
- [222] Berlincourt D., Krueger H.H.A., and Near C., "Properties of Morgan electroceramics," Morgan Electroceramics Technical Publication TP-226, <http://www.morganelectroceramics.com>, February 2007
- [223] "Strength of metal aircraft elements," ANC-5 Bulletin, U.S. Munitions Board Aircraft Committee, Mar 1955
- [224] Lord J.D. and Orkney L.P., "Elevated temperature modulus measurements using the impulse excitation technique," National Physical Laboratory Measurement Note, Teddington, UK, July 2000
- [225] Williams B.R., Inman D.J., and Wilkie W.K., "Temperature-dependent thermoelastic properties for macro fiber composite actuators," *Journal of Thermal Stresses*, v. 27, p. 903-915, 2004
- [226] Matweb material property database, <http://www.matweb.com>, February 2007
- [227] Hilton H.H. and Vail C.F., "Bending-torsion flutter of linear viscoelastic wings including structural damping," *Proc. AIAA/ASME Structures, Structural Dynamics and Materials Conference*, Paper # AIAA-93-1475-CP, La Jolla, CA, 1993
- [228] Chaudhry Z. and Rogers C.A., "The pin-force model revisited," *Journal of Intelligent Material Systems and Structures*, v. 5(3), p. 347-354, 1994
- [229] *LAPACK user's guide 3rd edition*, Society for Industrial and Applied Mathematics, Philadelphia, 1999
- [230] Mehra A., Zhang X., Ayon A.A., Waitz I.A., Schmidt M.A., and Spadaccini C.M.,

- “A six-wafer combustion system for a silicon micro gas turbine engine,” *Journal of Microelectromechanical Systems*, v. 9(4), p. 517-527, 2000
- [231] Appleby A.J., “Fuel cell technology: status and future prospects,” *Energy (Oxford)*, v. 21(7-8), 521-653, 1996
- [232] Fuller T.F. and Perry M.L., “A historical perspective of fuel cell technology in the 20th century,” *Journal of the Electrochemical Society*, v. 149 (7), S59-S67, 2002
- [233] *MATLAB R2006a documentation*, The Mathworks, Inc., Natick, Massachusetts, USA, 2006
- [234] *LABVIEW user’s manual Version* , National Instruments Corporation, Austin, Texas, USA, 2002
- [235] Park G., Sohn H., Farrar C.R., and Inman D.J., “Overview of piezoelectric impedance-based health monitoring and path forward,” *The Shock and Vibration Digest*, v. 35(6), p. 451-463, 2003
- [236] Peairs D.M., Park G. and Inman D.J., “Improving the accessibility of the impedance-based structural health monitoring method,” *Journal of Intelligent Material Systems and Structures*, v. 15, p. 129-139, 2004
- [237] *MAPLE Version 10 documentation*, Waterloo Maple Inc., Waterloo, Ontario, Canada, 2005